Computational Investigations of Ionic Liquids: Force Field Development, Gas Solubility and Transport

A Thesis

Submitted For the Degree of

DOCTOR OF PHILOSOPHY

in the Faculty of Science

by

Anirban Mondal

CHEMISTRY AND PHYSICS OF MATERIALS UNIT
JAWAHARLAL NEHRU CENTRE FOR ADVANCED SCIENTIFIC RESEARCH
Bangalore – 560 064, India

AUGUST 2016

To My Parents

DECLARATION

I hereby declare that the matter embodied in the thesis entitled "**Computational Investigations of Ionic Liquids: Force Field Development, Gas Solubility and Transport**" is the result of investigations carried out by me at the Chemistry and Physics of Materials Unit, Jawaharlal Nehru Centre for Advanced Scientific Research, Bangalore, India under the supervision of Prof. S. Balasubramanian and that it has not been submitted elsewhere for the award of any degree or diploma.

In keeping with the general practice in reporting scientific observations, due acknowledgement has been made whenever the work described is based on the findings of other investigators. Any omission that might have occurred by oversight or error of judgement is regretted.

Anirban Mondal

CERTIFICATE

I hereby certify that the matter embodied in this thesis entitled "**Computational Investigations of Ionic Liquids: Force Field Development, Gas Solubility and Transport**" has been carried out by Mr. Anirban Mondal at the Chemistry and Physics of Materials Unit, Jawaharlal Nehru Centre for Advanced Scientific Research, Bangalore, India under my supervision and that it has not been submitted elsewhere for the award of any degree or diploma.

Prof. S. Balasubramanian
(Research Supervisor)

Acknowledgements

It is my immense pleasure to thank my research supervisor, Prof. S. Balasubramanian for giving me an opportunity to explore the interesting area of research on computational materials science. I am extremely thankful to him for his guidance, support, and encouragement throughout the journey of my Ph.D. career. I am greatly thankful to him for providing me excellent computing resources without which the projects would not be successful.

I thank the Jawaharlal Nehru Centre for providing excellent research facilities. I would like to thank the faculty members of CPMU, TSU, NCU, ICMS and EMU for the courses they offered. I acknowledge the present and past coordinators of Int. Ph.D. Materials Science.

I acknowledge JNCASR, TUE-CMS, CDAC-Bangalore and CSIR-4PI for computational facilities.

I am thankful to the open source community for their service in providing the useful softwares and operating systems.

I thank JNCASR, DST and CECAM for funding. I thank all the academic and non-academic staff of JNCASR.

I thank all my friends, especially my Int. Ph.D. batchmates for all the moments I shared with them.

I acknowledge Prof. Pati and his group for their help.

I have enjoyed the company and friendship of my present and past lab mates: Dr. Kanchan, Dr. Sandeep, Dr. Ganga, Dr. Rajdeep, Dr. Chidambar, Dr. Anurag, Dr. Satyanarayana, Pallabi, Promit, Tarak, Karteek, Sudip, Divya, Dr. Saibal, Nimish, Nikhil and Srinath. I thank all of them.

A very special thanks to Dr. Sutapa Roy, Shubhajit and Rajdeep for their company.

Finally, I am thankful to my family members, who have been a source of constant support and strength for years. I thank my parents, brother and Brishti for their patience and encouragement.

Preface

The thesis presents the results of investigations on ionic liquids using computational methods including classical molecular dynamics (MD) simulations, *ab initio* MD simulations, and density functional theory (DFT) based quantum chemical calculations. Free energy profiles to investigate transport and dissolution processes in ionic liquids have been determined.

Chapter 1 presents a general introduction to room temperature ionic liquids describing their physicochemical properties and applications. A concise discussion on prior research on computer simulations of ionic liquids is also presented. A short description of the theoretical methods adopted in this thesis is provided. This chapter ends with a section on 'Scope of the thesis'.

Chapter 2 is divided into two parts. **Chapter 2A** and **Chapter 2B** present the development of an all-atom, non-polarizable force field for room temperature ionic liquids (RTILs). Periodic DFT calculations have been performed on crystalline and liquid phases of RTILs to obtain atomic partial charges that incorporate the effects of charge transfer and electronic polarization. The total charge on the ions is determined to be less than unity. Furthermore, the mean value of the ion charge obtained for the liquid phase compares very well with that determined for the crystal. These partial charges have been adopted within a well established force field to model the condensed state of ionic liquids. Quantum potential energy scans were employed to refine the non-bonded and torsional parameters. Several RTILs have been modeled with the refined force field parameters which showed considerable promise in predicting both intermolecular structure and dynamics, including collective quantities, in near quantitative agreement with experiments.

In **Chapter 3**, periodic DFT calculations and *ab initio* MD simulations have been employed to unravel the effect of cation-anion hydrogen bonding in modulating the low frequency vibrational modes in ammonium-based ionic liquids. Vibrational spectra in both the gas and the crystalline phases of three ionic liquids have been probed via normal-mode analysis within harmonic approximation and power spectra of velocity autocorrelation functions. A blue shift in the far-IR mode is observed with an increase in the number of hydrogen-bonding sites on the cation.

Chapter 4 presents results of atomistic simulations of ammonium-based protic ionic liquids (PILs). Pronounced impact of the length of alkyl tail on the intermolecular structure in trialkylammonium triflate PILs has been elucidated via MD simulations. Vibrational density of states and normal-modes calculated for bulk liquids have revealed that hydrogen bonding interactions between the ions increase with an increase in the bulkiness of the alkyl group attached to the N-atom of ammonium cation.

Chapter 5 is devoted to studies on a protic ionic plastic crystal (POIPC) and is divided into two parts. In **Chapter 5A**, classical MD simulations on a perfect crystal and of a vacancy model of 1,2,4-triazolium perfluorobutanesulfonate are performed, to probe its thermal behavior and electrolytic properties. It is shown that the cations, although translationally ordered are disordered rotationally in the rotator phase and exhibit tumbling motion which leads to a short life-time of N-H$\cdots$O hydrogen bond. One-dimensional vacancy motion has been delineated and free energy calculations have been performed to obtain an estimate of energy barrier for ion hopping.

In **Chapter 5B**, results obtained from Born-Oppenheimer MD simulations of 1,2,4-triazolium perfluorobutanesulfonate in its plastic crystalline phase are presented. Spontaneous autodissociation of –N-$\mathrm{H_N}$ bond in the cation and multiple proton shuttle events between the cation and the anion in the native crystal has been observed. Simulations of a defective crystal with a single proton-hole were carried out to delineate the long-range proton conduction path in the plastic crystalline phase of this POIPC. The free energy barrier for proton transfer was determined using metadynamics simulations which compared well with the experimental value determined using electrical conductivity measurements. Novel variants of the anion which exhibit decreased barrier for proton transfer are proposed.

Chapter 6 is divided into two parts. In **Chapter 6A**, results from MD simulations and quantum chemical calculations investigating the role of cations and anions in the solvation of $\mathrm{SO_2}$ in imidazolium-based ionic liquids are presented. $\mathrm{SO_2}$ exhibits preferential interactions with the anion. Condensed phase MD simulations of $\mathrm{SO_2}$ loaded ILs have demonstrated the formation of a "cage" around the solute by the cations. Free energy calculations offer a microscopic rationale for the experimentally observed $\mathrm{SO_2}$ solubility order in ILs with different anions.

In **Chapter 6B**, six different anion-functionalized ionic liquids with different basicity have been selected, and their $\mathrm{SO_2}$ absorption capacity has been investigated by employing quantum chemical calculations and molecular dynamics simulations. The high uptake of $\mathrm{SO_2}$ in these ILs is shown to originate from multiple-site interactions of $\mathrm{SO_2}$ with the anions. Free energy calculations have been performed to investigate the thermodynamics of gas absorption.

The thesis concludes with a brief outlook for the future directions in this area.

Contents

List of Figures

List of Tables

Chapter 1

Introduction

Classical inorganic salts (e.g. NaCl and KCl) possess high melting temperatures, which inhibit their use as solvents or as reaction media. However, salts composed of organic cations are liquids at relatively moderate temperatures. [1] Following such concept, the past two decades has seen an explosion of interest in "ionic liquids (ILs)" as a new class of solvents. [2–12] Ionic liquids are a group of molten salts with melting points near or around ambient conditions (or, by convention, below 100 °C). [13–15]

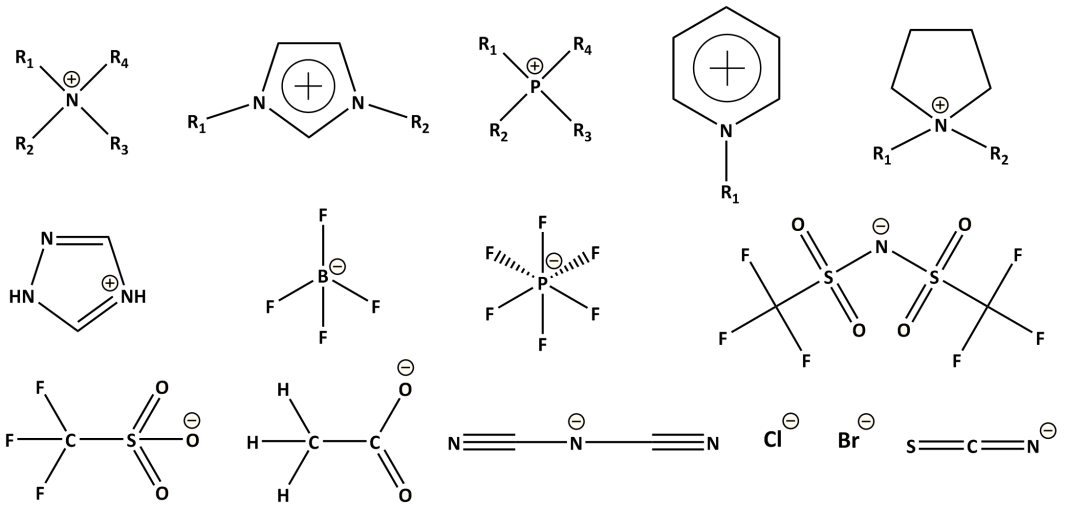

Figure 1.1: Representative cations and anions in ionic liquids.

Room temperature ionic liquids (RTILs) exhibit a large liquidus range at ambient conditions because of their molecular structure. Precise selection of the anion and cation enables the destabilization of the crystal with respect to the liquid, at such conditions. Thus, while there are no explicit set of rules to generate an IL, in principle it is possible to obtain an exponentially large number of ionic liquids by balancing ion–ion interactions and symmetry. [16–20] Thus, any property of interest can be "designed" with the help of this unique variability of the ions and hence, ILs are often referred to as "tailor-made

designer solvents." [21, 22] Figure 1.1 displays few examples of many commonly used cation and anion chemical structures. ILs exhibit unique physicochemical properties, such as low melting points, negligible low vapor pressure (thus, low flammability), high thermal stability, wide liquidus range, tunable electrochemical window and ability to solubilize and process a broad range of materials including organic and inorganic compounds, polymers and biopolymers. [23–30] Due to their non-volatile nature, ILs are being explored as "green" substitutes for volatile organic solvents. [31] The wide range of unique properties favor applications in diverse fields, such as synthesis, catalysis, biocatalysis, separation technology, electrochemistry, analytical chemistry, and nanotechnology. [32–61]

1.1 Classes of Ionic Liquids

The classification of ILs by chemical structure is a challenging task, as ILs possess structural features similar to those of molten salts, ionic crystals, ionic surfactants, and molecular liquids. [62] Based on the presence of proton-donor and proton-acceptor sites, protic [30] and aprotic ILs [28] are known to be the two most common IL types. However, this classification of ILs is not so rigorous as Davis and co-workers characterized dicationic ILs with linked protic and aprotic centers, that exhibit characteristics of both functionalities. [63]

Protic Ionic Liquids. Protic ILs (PILs) are prepared through proton transfer in a stoichiometric neutralization reaction of a Brønsted acid and a Brønsted base. [29, 30] Most PILs display ionic character comparable to that of ideal aqueous KCl solutions. [64] An important aspect of PILs is the presence of hydrogen bond (H-bond) donor and acceptor sites on the ions, through which the protons are transferred from the acid to the base. These proton-donor and proton-acceptor sites are used to build up the hydrogen-bonded network in PILs. The mechanism of proton transfer in PILs is still a subject of debate, however many a times it resembles Grotthuss-like behavior, where labile protons "hop" between sites along the H-bond network. [65, 66] Proton transfer in PILs leads to a number of unique properties such as thermal stability, [67] conductivity, [68] protein stabilization, [69] etc. Thus, a fundamental understanding of H-bond network structures in PILs is extremely important to obtain further insight into their solvent behavior.

Aprotic Ionic Liquids. Aprotic ILs (AILs) share an enormous array of chemical structures which arises from quaternization reactions. AILs extend across a vast domain of cation and anion chemical structures, some of which have H-bonding sites and some which do not. The cations are predominantly organic molecular ions, e.g. resonance stabilized dialkylimidazolium, alkyl pyridinium, cyclic and non-cyclic tetraalkyl ammonium, alkylpyrrolidinium etc. [4, 28, 70, 70, 71] In general, AILs display better thermal and electrochemical stability

than PILs. Further, ionicity of aprotic ILs is higher than protic ILs due to higher ion-pairing in the latter. [29, 72]

Other IL Subclasses. On the basis of distinct structural features, several other IL subclasses are reported in the literature, such as chiral IL, [73] magnetic ILs, [74] divalent ILs, fluorous ILs, [75] polymeric ILs, [76] amino acid ILs, [77] etc. In most instances, they are named from the presence of specific functional groups on the ions. These ILs are relatively less explored but show their promising applications in the fields of spectroscopy, asymmetric synthesis, chromatography, etc. [73]

1.2 Intermolecular Forces

Although RTILs too are composed purely of ions, the Coulombic forces in them are softened, due to the molecular nature. [1] The charge density is lower in RTILs, thus reducing the cohesive energy of the solid. Furthermore, the asymmetric character of the ions too contribute to the relatively lesser cohesive energy of RTILs crystals. [14]

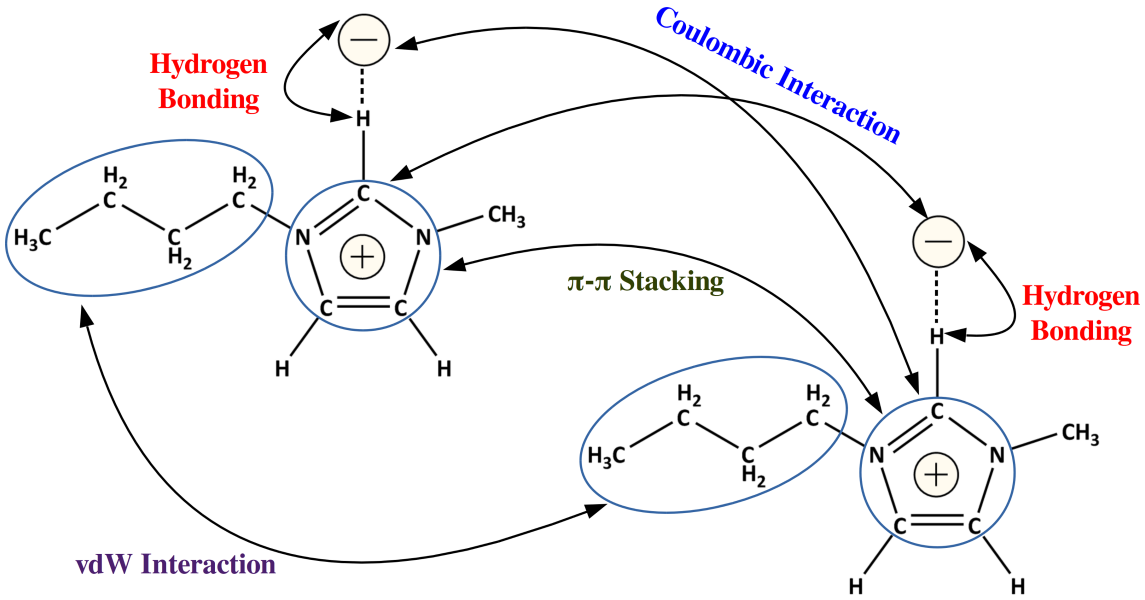

Figure 1.2: Important intermolecular interactions present in ILs.

The electrostatic contribution can be further dissected into terms such as dipole–dipole, ion–dipole, ion–induced dipole and higher electrostatic moments. Among these set of interactions, Coulomb force is at least an order of magnitude stronger than others, [78] and leads to strong binding energies of the order of 500 kJ/mol [79] and therefore, it ensures extremely low vapor pressure in ILs. As the charge is spread over a larger molecular volume than in simple inorganic salts, they are also more polarizable. ILs exhibit charge ordering as well as formation of polar and non-polar domains. [62] These kinds of domain

formation in many ILs is observed because (1) different charged groups try to solvate the other groups with opposite charge and (2) non-polar groups come together for better packing. [80] The preferential arrangement of polar and non-polar domains is controlled by the packing geometry, a quantity which is defined as the relative dimensions of the polar and non-polar groups of cations and anions, [81, 82] and it is well captured in scattering experiments. [62]

Hydrogen bonding is a critical interaction in ILs and determines the local structuring in both solid and liquid phases. A fundamental understanding of H-bonds is crucial for the control of IL solvent properties and transition states in chemical reactions. [83] A spectrum of techniques from both the experimental and computational field have been employed to investigate the H-bonding in ILs. [84–91] While many studies continue to emphasize the formation of three-dimensional H-bonding networks in PILs [92–99] and reference to ion arrangement, it is very common to find statements such as "PILs can build up hydrogen bonding networks similar to water molecules due to their protic nature and general solvent properties." [100] Contrary to this, others refuse to accept the clear-cut existence of such bonds. [101–104]

Hydrogen bonding is mainly attributed to electrostatic interaction, while electron correlation contributes to dispersion also. [105] The strength of hydrogen bond is determined by three main contributions: Coulomb, induction forces due to the dipole–dipole interaction and the dispersion forces due to electron correlation effects. [105] In ionic systems, the leading interaction is electrostatic. [106] Coulomb and induction forces are longer ranged than dispersion (R^{-6}); they are also stronger. For example, ion–dipole interactions decay as R^{-2}; dipole–dipole interactions as R^{-3}; and ion–induced dipole interactions as R^{-4}. [106]

ILs composed of heteroaromatic rings (e.g. imidazolium-based ILs) constitute a family in which $\pi - \pi$ interactions are possible. [107] $\pi - \pi$ stacking of aromatic rings is observed in the crystal structures of $[C_2C_1Im][NO_3]$, [108] $[C_2C_1Im]_2[SO_4]$-H_2O, [108] $[C_2C_1Im][OTf]$, [109] and $[C_2C_1Im][NTf_2]$. [110] The inter-digitation of longer alkyl chains in cations enables the $\pi - \pi$ stacking of imidazolium head groups. Zheng *et al.* proposed such kind of structural alignment in an investigation of the phase behavior of $[C_nC_1Im][Br]$, where n = 12, 14 and 16, with water and p-xylene. [111] Furthermore, $\pi - \pi$ interaction plays an essential role in IL-benzene clathrate formation reported in $[C_2C_1Im][PF_6]$ and $[C_2C_1Im][NTf_2]$. [112] The structuring of ILs near the interface of extended carbon materials such as graphene and carbon nanotube, is chiefly influenced by $\pi - \pi$ interactions between IL and benzene molecule. [36, 53, 113, 114]

In their recent study, MacFarlane *et al.* demonstrated the importance of dispersion interactions in determining the thermodynamic and transport properties of ILs through quantum chemical calculations. [106] Dispersion interactions predominantly emerge as an

effect of electron–electron correlation, and it competes with the Coulombic interactions in systems with long alkyl chain. For bulkier anions (e.g. $[NTf_2]^-$), with multiple non-equivalent interaction sites, dispersion interactions dominate the cohesive energy even for cations with small alkyl chain. [115] More recent studies on ionic liquid crystals manifested the importance of anisotropic dispersion forces in the stabilization of nematic phases of these liquid crystalline systems. [27] The anisometry of the constituent molecules is the cause of the anisotropic dispersion force that aid in the dense molecular packing in the studied systems. Thus, in summary, the short-range structuring of ionic liquids commences as a result of complex interplay of long-range (Coulombic) and short-range (hydrogen bonding, van der Waals, dipole–dipole, $\pi - \pi$) interactions.

1.3 Phenomena at Mesoscopic Length Scales

Mesoscopic organization of ILs has been a long-standing topic of debate, which implies that ILs possess far more complex morphology than initially expected based on the properties of simple inorganic salts. It has been observed that ILs exhibit nanostructures similar to that of concentrated aqueous solutions of surfactants. [116, 117] Moreover, Hamaguchi and Ozawa have asserted that "ILs may not be liquids in the conventional sense, but may rather be considered as mesophases." [118] Formation of liquid-crystalline phases in imidazolium salts with long alkyl chains $C_n \geq 12$, manifested the presence of mesoscopic structures in ILs. [119–121] Existence of such structural domains in the isotropic liquid above the clear point was demonstrated by Hardacre *et al.* using small angle X-ray scattering experiments. [121] Also, evidence for the presence of structural domains came from the crystal structures of salts with shorter alkyl chains. [122]

ILs with shorter alkyl chains (imidazolium salts with $C_n \geq 4$) also exhibit intermediate range structures. Using coarse grain MD simulations, Voth and co-workers showed the aggregation of cations with sufficient tail-length and subsequent formation of spatially heterogeneous domains. [123–125] They suggested that the competition between cumulative short-range interactions between the neutral alkyl moieties and electrostatic interactions between the charged head groups and the anions promote such mesoscopic structures. MD simulation results of Lopes and Padua demonstrated the existence of nonpolar domains that are formed by the tail groups and hydrophilic domains that are formed by the polar head groups of the cations and anions. [126] These domains grow with increase in alkyl chain length and begin to link together. Employing coarse grained MD simulations, Bhargava *et al.* indicated the presence of a bicontinuous morphology in the liquid, whose character is governed by the alkyl tail length. [127] Raju and Balasubramanian explored the intermediate range structure and morphology of symmetric 1,3-didecylimidazolium hexafluorophosphate from coarse grain MD simulations. [128] They showed the formation

of domains in neat IL in the absence of water, within the domains, the ions form a lamellar structure. The emergence of such mesoscopic structures is mainly due to electrostatic and van der Waals forces existing between polar and non-polar components of the IL. [128]

Triolo *et al.* have provided direct experimental support for such mesoscopic structures using X-ray scattering experiments on 1-alkyl-3-methylimidazolium salts ($4 \leq C_n < 10$). [129] Emergence of a diffraction peak due to structural inhomogeneities was revealed by the scattering patterns. The dimensions of the inhomogeneities was found to be proportional to the alkyl chain length. Often, the formation of mesophases in molecular liquids is governed by the shape anisotropy of the molecules and the strong orientation dependence of van der Waals and electrostatic interactions. [21] Dupont suggested that the presence of three–dimensional hydrogen–bonded network may determine the mesoscopic structures in ILs. [117] To dissect the structural dependence of the diffraction peak on alkyl tail length, Triolo *et al.* proposed the following idea. [130] The formation of micelles due to interdigitation of cation tails could be responsible for alkyl tail length dependence on the q value at which the prepeak appears in SAXS experiments. However, recent work by Margulis *et al.* demonstrated that cationic anisotropy imposes certain patterns of coordination along the direction of the longer alkyl tail and is the reason for the prepeak observed in SAXS experiments. [131–134]

The outcome of these mesoscopic structures on the properties of ILs is significant. Many distinct behaviors of ILs can be rationalized in terms of heterogeneous structures. For example, the unusual molecular motions of ILs compared to simple molecular liquids (as discussed in Section 1.4) are primarily due to dynamics processes in a heterogeneous environment. Other possible outcomes involve diffusion-controlled chemical reactions in ILs.

1.4 Molecular Motions in ILs

In low-viscosity ILs, the spectrum of molecular motions expands from time scales of femtoseconds (ultrafast processes) to nanoseconds (diffusive motions). A span of mostly specialized spectroscopic techniques such as dielectric spectroscopy in the microwave [135–138] and far-infrared [139, 140] regime, nuclear magnetic relaxation (NMR), [141–143] optical Kerr effect (OKE) spectroscopy, [144–147] and quasi-elastic neutron scattering (QENS) [148, 149] spectroscopy have been employed to examine the motions of the ionic components in neat ILs. The diffusive processes in simple molecular liquids exhibit exponential relaxation behavior,

$$\phi(t) = exp(-t/\tau_D) \tag{1.1}$$

where τ_D is the "Debye relaxation time." [150] However, in ILs, relaxation process is characterized by strong non-exponential dynamics, as suggested by above mentioned experimental techniques. Although the ILs under consideration have low viscosity, the spectra indicate dynamical behavior similar to that of glassy materials. [135–137, 148, 149] Unlike in molecular liquids, ILs possess a broad spectrum of diffusive processes; which could be accounted for heterogeneity due to mesoscopic structures formed in ILs. Generally, the non-exponential dynamic processes occurring in spatially heterogeneous states are described by the Kohlrausch–Williams–Watts (KWW) stretched exponential function,

$$\phi(t) = exp\Big((-t/\tau_{KWW})^{\beta}\Big) \tag{1.2}$$

with stretching exponents $\beta < 1$ and τ_{KWW} is known as KWW relaxation time. [150, 151] The small values of β suggest the existence of spatial heterogeneities in ILs.

Dynamic heterogeneity in $[C_2C_1Im][NO_3]$ was observed and quantified using a non-Gaussian parameter $\alpha(t)$, by Del Popolo and Voth. [152] They found that $[C_2C_1Im][NO_3]$ exhibited non-Gaussian behavior even at 400 K. Hu and Margulis investigated the dynamics of $[C_4C_1Im][PF_6]$ and showed that the translation mobility is tightly coupled with rotational mobility for $[C_4C_1Im]^+$ cation, while the two are completely decoupled for $[PF_6]^-$ anion. [153] Morrow and Maginn studied the rotational time constants in $[C_4C_1Im][PF_6]$ using classical MD simulations at 298 K. [154] Small anions exhibited rapid rotation with a small rotational time constant ($\sim$ 30 ps), while larger cations exhibited a rotational time constant about their longest axis of several nanoseconds. In imidazolium systems, the translational motion of the larger cation is observed to be slightly faster than that of, the smaller anion. [154–157] Urahata and Ribeiro rationalized this phenomenon in terms of preferential displacement of the cation ring along the direction of the most acidic carbon of the imidazolium ring. [155]

Owing to their major role in chemical reaction dynamics, an emphasis has been placed to characterize ultrafast motions experimentally at the subpicosecond time scale by optical Kerr effect spectroscopy. [61] Also, a handful of experiments have been performed employing terahertz (THz) spectroscopic methods to unveil the intermolecular vibrations and librational motions of ions in the "cage" formed by their neighboring ions. [139, 140]

1.5 IL at Interfaces

Interfacial effects in ionic liquids play a pivotal role in many processes, such as electrochemistry, [158] energy storage, [159] catalysis, [160] etc. It has been demonstrated in a number of experimental and simulation studies that the IL structure perpendicular to the solid interface is characterized by a strong layering of the liquid, which extends up to a few nanometers. [161] The local composition of the layers is observed to possess strong

correlations due to charge-ordering and chiefly depends on the surface charge of the solid. The formation of multilayered structures of ILs at charged interfaces with alternate layers of cations and anions have been reported by a significant number of experiments and molecular simulations. [162–165] Recent AFM studies have shown that the interfacial structure can be tuned by varying the length of alkyl chain of organic cations or anion type. [166, 167] However, at the interface, different arrangement of ions other than multilayer-like structure is also observed for ILs and it has been shown that ILs indeed exhibit monolayer-like interfacial structure at charged surfaces. [168–173] In this context, Kirchner *et al.* have employed coarse-grain model of ILs to demonstrate the formation of both monolayer and multilayer structure by varying the surface charge. [174]

The arrangement of ions at the gas-liquid interface is a subject of fundamental importance. It is observed that IL-vapor ([EMIM][NO_3] or [BMIM][PF_6]) surface layer consists of two regions with different molecular orientations: in the outermost layer, imidazolium rings exhibit parallel orientation to the surface plane, where the ethyl groups are projected into the gas phase and beneath this layer, a dense region where imidazolium rings are oriented perpendicular to surface plane with methyl groups pointing into the bulk. [175, 176] Using MD simulations, Lynden-Bell and Del Pópolo have shown that the surface contains a monolayer of butyl tails with the rings partially aligned. [177] Voth *et al.* performed coarse-grain MD simulations on [C_nMIM][NO_3] with varying alkyl tail length and demonstrated the existence of monolayer to mutilayer structure with an increase in chain length from C_4 to C_{12}. [178] In general, simulation studies offer an explanation that substantiate the orientation observed experimentally and the preferential ordering at the first layer of the IL-vapor interface.

1.6 Macroscopic Properties of ILs

The quantification of the physical properties of ILs and the trends in these properties is of paramount importance in the design of ILs for specific applications. In this section, we will present a brief and non-extensive review of several properties of ILs. Table 1.1 summarizes few important physical properties (experimentally measured) of some common ILs at ambient conditions.

Melting Behavior. The utility of an IL (mainly as a solvent) in several applications depends on its melting temperature (T_m). Aparicio *et al.* demonstrated that the melting point of ILs decreases with increase in size, anisotropy and internal flexibility of ions, whereas T_m increases with higher dispersion interactions between alkyl chains. [193] This trend holds for homologous imidazolium salts with the $[BF_4]^-$ ions. [119–121] ILs with short alkyl chains ($C_n \leq 3$) exhibit crystalline phases with relatively high melting points. Cations comprised of intermediate length alkyl chains ($4 \leq C_n < 12$) show wide liquidus

Table 1.1: Physical properties (experimentally measured) [179–192] of some common ionic liquids at ambient conditions.

Ionic Liquid	Physical Properties				
	Density (g/cm^3)	ΔH_{vap} (kcal/mol)	Viscosity (mPa.s)	Surface Tension (mN/m)	Conductivity ($S.m^{-1}$)
[BMIM][PF_6]	1.365	37.00	182.4	43.52	0.19
[BMIM][BF_4]	1.198	33.78	75.3	44.18	0.45
[BMIM][NTf_2]	1.432	32.17	40.0	33.09	0.46
[BMIM][CF_3SO_3]	1.294	33.22	65.4	35.05	0.36
[BMIM][CF_3CO_2]	1.213	—	58.3	—	0.38
[BMIM][CH_3CO_2]	1.058	26.98	210.0	36.4	0.07
[BMIM][$N(CN)_2$]	1.059	37.57	24.4	48.6	1.05
[BMIM][SCN]	1.069	35.37	40.9	45.4	0.73

range with low melting temperatures and a higher propensity to supercool. [13] Salts with long alkyl chains ($C_n \geq 12$) form complex phase diagrams, implicating ionic liquid-crystalline phases. [27] However, the rationalization of the effects of anions on the T_m is rather difficult, and most often seems to depend on its hydrogen bond acceptor ability. [37] The melting point of an IL can be lowered with an addition of extra salt, e.g. the eutectic mixture of [C_2C_1Im][Cl] and $AlCl_3$ in the mole ratio 1:2 results in a T_m of -96 °C, whereas pure [C_2C_1Im][Cl] melts at 87 °C. [13] Further, Scurto and Leitner showed that the T_m of imidazolium, ammonium, and phosphonium based ILs are lower under CO_2 pressure than their normal melting temperatures. [194]

Enthalpy of Vaporization. The enthalpy of vaporization ($\Delta_{vap}H_m$) is an important quantity for the validation of molecular force fields [195] and in the thermodynamic modeling of equations of state for pure ILs and mixtures. Owing to strong ion–ion interactions, ILs manifest almost an order of magnitude higher $\Delta_{vap}H_m$ than that for molecular liquids. [183] Molar enthalpies and entropies of vaporization are obtained from analysis of vapor-pressure curves. [183]

1.6.1 Transport Coefficients

Viscosity. Viscosity (η) is one of the most important material properties to consider in practical applications. High viscosity can slow down the rate of diffusion-controlled chemical reactions. In general, at room temperatures viscosity of ILs spans between 20 and 40000 cP. [196] Even the lowest viscous IL reported till date at 298 K ($\eta = 21$ cP for [C_2mim][$N(CN)_2$]) [197] has viscosity which is more than one order of magnitude higher than that of water at this temperature (~ 1 cP) [196] and molten organic salts at high

temperatures (1–3 cP). [1] Thus, the design and synthesis of novel ILs with low viscosity is of immense importance. In general, the viscosity of ILs is inversely proportional to the size of ions and temperature. [198] Krossing and co-workers demonstrated the strong dependence of IL viscosity on their molecular volume. [199] Moreover, strong interactive forces such as, Coulombic, van der Waals interactions, and hydrogen bonding greatly influences the IL's viscosity. Extensive hydrogen bonding network results in low mobility of ionic species and high viscosities.

Both experiments and simulations face difficulty in determining accurate values for viscosity coefficients of ILs. In experiments, contaminations by even a small amount of halogen or water can significantly change the measured values. In the case of simulations, calculation of viscosity coefficients in highly viscous systems is a challenging task as it is tough to reach the hydrodynamic limit where the experimental data has been measured. Convergence of viscosity demands large simulation cell sizes and long trajectories. Issues in the calculation of viscosity of ILs in the simulations have been addressed in several studies. [12, 200–203]

Ion Diffusion. The self-diffusion coefficients of the ions in low-viscous ILs at 298 K are of the order of $\approx 10^{-11}\mathrm{m}^2\mathrm{s}^{-1}$, one or two order of magnitude lower than of simple molecular liquids ($\approx 10^{-9}\mathrm{m}^2\mathrm{s}^{-1}$ to $10^{-10}\mathrm{m}^2\mathrm{s}^{-1}$). [156, 157, 204] Experimental results on ion self-diffusion coefficients in ILs suggest that larger cations have higher mobility than smaller anions; [156, 157] this implausible phenomenon can be delineated by the stronger solvation of anions by the cations. [205] Tsuzuki reported that the important factors that govern the ion mobility in ILs are the size and shape of the ions, the charge delocalization in the anion, conformational flexibility, molecular mass of the ions and nanostructure formation in ILs. [206] Often, self-diffusion coefficients are employed to validate the molecular force fields. In simulations, self-diffusion coefficients are computed from the slope of the mean square displacement of ions ($\langle r(t)^2 \rangle$) at long times t, i.e. in the diffusive regime. However, the calculated ion self-diffusion coefficients in several ILs are found to be much lesser than experimental data. [200, 207–212] This deviation could point to either deficiency in the force field and/or reflects the fact that simulation time scales are not enough to reach the true asymptotic linear behavior of $\langle r(t)^2 \rangle$.

Electrical Conductance. Owing to low ion mobility and high viscosity, ILs exhibit electrical conductivities, σ, in the range of 0.1–18 mS cm^{-1} at room temperature; [213] which increase remarkably at high temperatures, and compare well with conductivities of conventional electrolytes used in electrochemistry. The electrical conductivity of ILs is driven by the chemical structures of the constituent ions. $[C_2\mathrm{mim}]^+$ based cations typically possess conductivity of $\sim$ 10 mS cm^{-1} at 298 K, [214, 215] whereas ILs composed of pyrrolidinium

or piperidinium cations show much lower conductivities, 1–2 mS cm^{-1}. [216] Vila and co-workers and Stoppa *et al.* showed that the conductivity at a given temperature in ILs with $[BF_4]^-$ anion decreases as the length of the cation alkyl chain increases. [215, 217] Similar phenomenon is reported by Tokuda *et al.* in homologous imidazolium salts with the $[NTf_2]^-$ anion. [157] Mixing of another solvent with ILs markedly increases the conductivity, e.g. addition of acetonitrile at the concentration of 2 mol/dm with $[C_2mim][BF_4]$ increases the conductivity three times ($\sim$ 50 mS cm^{-1}) at room temperature. [216]

The ion self-diffusion coefficients can be related to the molar conductance $\Lambda = \sigma/C$ via the Nernst-Einstein equation (Eq. 1.3), where C and F represent the molar concentration of the salt and the Faraday constant, respectively. [150]

$$\Lambda_{NE} = \frac{F^2}{RT}(D_{cation} + D_{anion}) \tag{1.3}$$

This relation holds rigorously if the ion movement is independent of each other. Often, it has been observed that measured electrical conductivity differs from the Nernst–Einstein relation. [156, 157, 214, 215, 218] This phenomenon can be rationalized by the effective degree of ion pair association is ILs. The coupled motion of cations and anions in electrically neutral configurations contributes to diffusion, but not to the electrical conductance.

1.7 Applications

Initially, ILs were synthesized for use as catalytic or green solvents in organic chemistry. [2, 219, 220] Later, their potential applications were further extended to electrolytes for batteries and supercapacitors, gas adsorption, as lubricants, materials science, and biochemistry with more and functionalized ILs are produced. [221] To date, ILs are widely employed in multiple fields as illustrated in Figure 1.3.

Solvent. One of the most important application involving ILs is their use as a solvent. [2, 222] ILs have been used as a solvent to dissolve a large number of organic and inorganic materials. For example, dissolution of biomass (such as cellulose) in conventional solvents is very challenging and requires harsh conditions, whereas ILs have been utilized as a preferred solvent to dissolve biomass. [223–226] Another exciting role for ILs is in the storage and manipulation of sensitive biomolecules. [227, 228] Fujita *et al.* have shown the remarkable stability of protein cytochrome c in nontoxic dihydrogen phosphate IL. [229]

Electrolytes. Owing to their high thermal and chemical stability, broad electrochemical window and a wide range of operation temperatures, ILs are utilized as electrolytes in solar cells, Li^+ ion batteries, Li-SO_2 batteries, and supercapacitors. [36, 42, 48, 50] Imidazolium-based ILs are the most frequently investigated as electrolytes and for anions, $[NTf_2]^-$ has

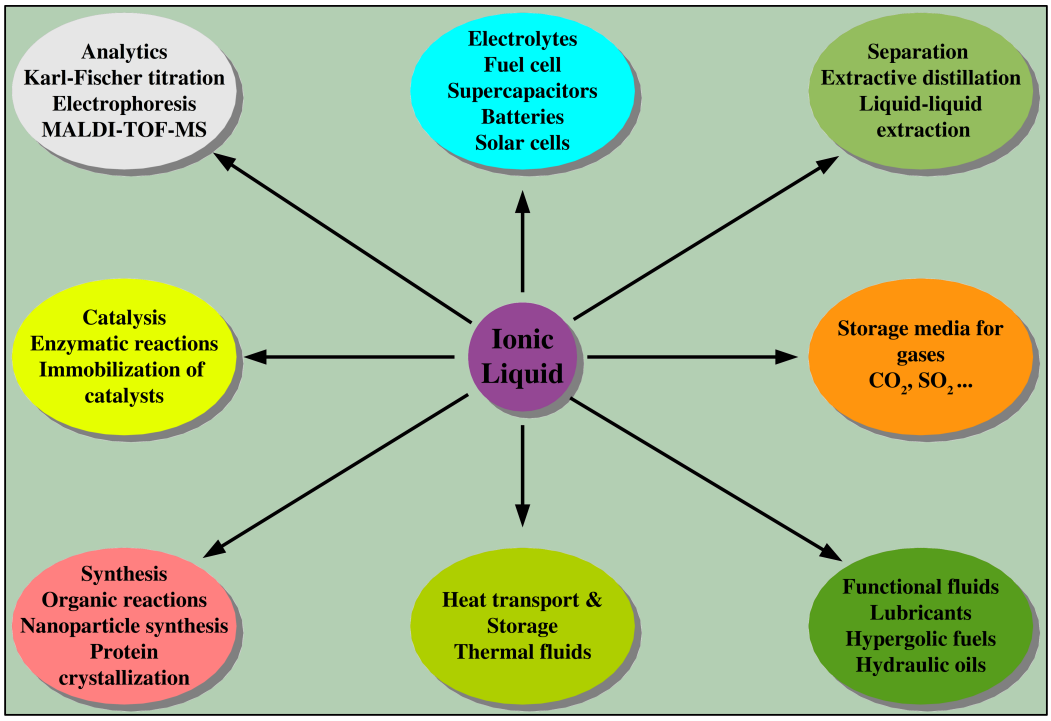

Figure 1.3: Potential applications of ionic liquids.

been a common choice in many studies. [230–232] In a fuel cell, protic ILs are used as electrolytes which serve as proton transport media. Protic ILs consist of proton-donor and proton-acceptor sites, by which proton transport takes place between cathode and anode. [233, 234] Recent development in Protic organic ionic plastic crystals (POIPCs) represent an exciting novel class of solid state proton conductors for fuel cells. [99] Furthermore, ILs are also used as hypergolic fuels. Hypergolic fuels are used in satellite propulsion systems and fuels of choice continue to be hydrazine (N_2H_4) and its derivatives. These materials exhibit high vapor pressures, require expensive handling and safety precautions as they are composed of acutely carcinogenic and toxic substances. [51] Recently, ILs with dicyanamide anion (with cations such as triazolium–, tetrazolium–, tetrazine–, etc.) were shown to exhibit hypergolic properties, thereby meeting some of the requirements of good energetic materials. [51, 235–237]

Gas Solubility. Among others, the solubility of gases in ILs reflects the interactions between simple molecular species and ILs. Following the work of Brennecke and coworkers on the very high solubility of CO_2 in ILs, [238] there have been many studies performed involving gas solubility in ILs. [56, 239–249] Several simulation studies suggested that CO_2 can be intercalated in cavities of the IL structure without markedly affecting it. [247, 250, 251] The electrical quadrupole moment of CO_2 plays a key role in optimizing its interactions with anions. In fact, CO_2 solubility in ILs is seen to be dominated by anions

much more strongly than cations. [252] Without any surprise, polar gases, such as SO_2 and H_2S, exhibit very high solubilities in ILs. [243–246, 249, 252] The solubilities of other gases can also be rationalized based on ion–solute interactions. Simple gases experience weak dispersive interactions with the ions, and therefore, the solubility order indicates the molecular polarizability of the solute, yielding the series $H_2 < O_2 < CH_4 < C_2H_6$ in $[C_2MIM][NTf_2]$ IL. [21]

1.8 Review of Prior Work: Computer Simulations

Modeling the liquid phase – especially of complex liquids such as ILs – is still a non-trivial exercise. [253] Employing quantum chemical methods involving an ion pair in an isolated condition, it is possible to access the gas phase properties, but a single molecule approach of this kind does not effectively capture most properties of the liquid state. This inadequacy arises due to the omission of temperature and environment as well as of the dynamics. In view of these limitations, molecular dynamics (MD) simulations are still the favored approach for condensed-matter investigations. Following the work of Hanke *et al.* [254] there has been an ever-growing number of simulations involving structure, dynamics, and bulk properties of ILs employing classical MD techniques, which were summarized in literature reports. [14, 195, 255–257]

The significance of the simulations is largely determined by the accuracy of the molecular force field used. The main difficulty in developing accurate and transferable force fields is the lack of useful experimental data available, such as enthalpies of vaporization. Most often, derived force field parameters were validated against a limited set of experimentally reported properties, such as crystal cell parameters and liquid densities. [258, 259] Thus, although many of them reproduce well the static intermolecular structure, their ability to predict quantitatively the transport quantities has been a matter of discussion. [157, 260–265] Thus, while a force field may reproduce some thermodynamic quantities of pure IL adequately, care must be taken when applying the same force field to predict dynamic properties, solute–solvent, mixing and interfacial problems.

Moreover, *ab initio* molecular dynamics (AIMD) simulations (such as Car–Parrinello MD), which is a combination of molecular dynamics simulations with electronic structure calculations on the fly, can provide decisive information about the liquid structure. Based on the *ab initio* findings, Del Popolo *et al.* suggested that the Cl^- anion rattles around in a fairly deep potential minima, while the $[C_2C_1im]^+$ cation exhibit significant fluctuations in geometry. [266] Another *ab initio* study employing Car–Parrinello dynamics have shown the subtle but crucial differences in the formation of a hydrogen bond between $C^2 - H$ of the imidazolium ring and Cl^- anion and absence of anion probability density hole above $C^2 - H$ site, when compared with classical simulations. [267] Kirchner and co-workers

delineated the essential aspect of Coulombic stabilization and presence of large positive charge on the most acidic carbon atom in imidazolium cation that drove the formation of hydrogen bonding network in ILs. [85, 268] Lassegues *et al.* utilized *ab initio* methods to detect the various conformers in $[C_2C_1im][NTf_2]$ that contribute to characteristic Raman lines. [269]

Pure $[C_4mim][PF_6]$ and $[C_4mim][PF_6]$-CO_2 mixtures have been studied using CPMD. [270] CPMD simulation of neat IL showed many cation–anion hydrogen bonds in resemblance to the crystal, an aspect which was almost absent in empirical potential MD simulations. The probability of H-bond formation was seen to be increased with the addition of CO_2. In their instantaneous conformations, a CO_2 molecule in the proximity of the IL ions displayed larger deviations from linear geometry. The dissolution of CO_2 in $[C_4mim][PF_6]$ was chiefly driven by the anion, as observed from the computed radial and spatial distribution functions. A tangential alignment of CO_2 molecules with respect to the $[PF_6]^-$ spheres was observed where CO_2 molecules were located in the octahedral voids of the anion. [270] AIMD studies involving $[C_4mim][PF_6]$ and supercritical CO_2 mixture revealed the organization of CO_2 around the terminal carbon atom of the butyl tail. [271] Partial radial distribution functions analysis also indicated the organization of CO_2 molecules around themselves in $[C_4mim][PF_6]$-CO_2 mixtures. [271] CPMD simulations of solution composed of $[C_2mim]^+$ cation and $F(HF)_n^-$ anions were performed by Bhargava and Balasubramanian. [272] The computed structure factor was observed to be in fair accordance with X-ray scattering data. The H–F covalent bond length in polyfluoride moiety was found to be decreased with increasing value of n, as indicated by the blue shift in the frequency of its stretching mode.

Kirchner and co-workers have undertaken CO_2 solvation in a protic ionic liquid, ethylammonium nitrate (EAN) using *ab initio* molecular dynamics simulations. [273] Their data unveiled the presence of microheterogeneity of the alkyl chains and the extended hydrogen bond network between cation and anion in pure PIL. Furthermore, in the mixture of EAN and CO_2, it has been observed that the presence of CO_2 does not break the strong hydrogen bond network between cation and anion, and also the formation of nonpolar domains, i.e. so-called microheterogeneity, was unaltered by the solute molecules. The specific interaction between the solute CO_2 and the solvent was largely dominated by the weak Lewis acid–base interactions between anion and CO_2 and hydrogen bond interactions between oxygens of CO_2 and the cation alkyl hydrogen atoms, in agreement with previous simulation result. [274] In an another work, Kirchner and co-workers investigated the structure of mixtures of ionic liquid, 1-ethyl-3-methylimidazolium acetate ($[C_2C_1im][OAc]$) with water, with the aid of AIMD. [275] Strong hydrogen bond formation between cation and anion were observed in the neat IL, and the presence of water modified and markedly disturbed the hydrogen bond network of the IL. Furthermore, addition of water molecules

resulted in increment in the dipole moment of the $[OAc]^-$ anion, while dipole moment of $[C_2C_1im]^+$ cation was unaffected by the water concentration.

1.9 Theoretical Methods

For computational chemists, modeling ionic liquids represent a prime challenge. This is because ionic liquids exhibit strong intermolecular interactions due to their ionicity. In general, ionic liquids are characterized by the interplay of long–range Coulomb interactions and short–range van der Waals interactions as well as hydrogen bonds. A subtle balance in these interactions plays a key role in ILs, and indeed, results in their unique properties such as structural properties of the liquid and electrostatic properties of the ions. [14] Thus, it implies that to obtain a uniform description on all scales, transfer of the electrostatic and the structural properties consistently from one scale to another is of immense importance. [276, 277] The aim of this section is to provide a schematic protocol to investigate ILs at different scales. Employing a bottom–up approach, the information obtained at each scale shall be consistently transferred to the next scale. In this thesis, the studied scales are the quantum scale involving explicit consideration of electrons, and the classical scale where each molecule is treated as a classical object and possess its explicit chemical identity. Most often, only relatively small systems are considered in quantum chemical calculations, but at an electronic level with higher accuracy. On the other hand, classical simulations are used to describe rather large systems, but at the price of less accurate, empirical molecular description. Thus, it is evident that an ideal compromise between feasibility and accuracy results from the balance between these two approaches.

1.9.1 Quantum Chemical Calculations

The quantum chemical calculations in this thesis were accessed on two different levels: post–Hartree–Fock (post–HF) approaches and density functional theory (DFT) approaches. In most instances, post–HF methods yield explicit, systematically improvable information on the electronic level. On the other hand, DFT methods are more approximate in practice but have the potential to provide a vigorous interpretation of electron density. [278, 279] In post-HF or *ab initio* method, the energy of the molecule and all of its derivative values depend on the determination of the wavefunction. Even though the wavefunction does not exist as a physical, observable property of an atom or molecule, the mathematical interpretation of the wavefunction has shown to predict the energy and other actual properties of the molecule very well. [278, 279] On the contrary, in DFT, the energy of the molecule is a functional of the electron density, which is a physical characteristic of all molecules. [280] Contrary to the wavefunction, for which the complexity increases as the number of electron increases, the determination of the electron density is independent of the number of electrons. Most often, DFT scales as N^3, where N is the number of basis

functions, whereas *ab initio* methods scale as N^4 and as a result DFT calculations are faster. [281]

The smallest building block of ILs that can be examined (e.g. one ion pair) is many times too big, that forbids the use of highly accurate (and expensive) (CCSD(T)) post–HF methods. Moreover, in many studies, it has been demonstrated that standard DFT does not capture accurately the trends in relative energies obtained using *ab initio* methods due to the considerable contribution of dispersion interactions. [276] However, the inclusion of commonly applied dispersion correction schemes results in significant improvement in the quality of DFT results. [277, 282] Apart from this, it should also be noted that Møller-Plesset calculations (MP2) have a much higher basis set requirement than hybrid DFT, which clearly outperforms MP2 when it is dispersion corrected and a triple-zeta-type atomic orbital basis set is employed. [282] Apart from the difficulties in selecting the quantum chemical methods, the cation and the anion are more complex than single atom, and thus several minima occurs on the potential energy surface even of a single IL ion pair. [85] Therefore, it is of immense importance to consider all of these configurations to delineate the local structures of ILs. [85, 277] As an example, in imidazolium-based ionic liquids, it is must to consider the on-top and in-plane configurations while examining optimized configurations.

In this thesis, *ab initio* and DFT methods have been used based on the nature of the system under investigation. In order to take electron correlations into account, *ab initio* techniques such as second-order Møller-Plesset perturbation theory (MP2) combined with correlation consistent basis sets (e.g. aug-cc-pVDZ) was employed in studying optimized configuration, frequency analysis, potential energy surface scan, solute-solvent interactions, etc. in the gas-phase isolated conditions. Computed results such as vibrational spectra or trends in solute-solvent interactions have shown adequate agreement with experimental data. On the other hand, DFT methods have been practiced for both periodic (bulk structure) and non-periodic (gas-phase) calculations. Gas-phase DFT calculations were performed applying hybrid-meta-GGA functional of Minnesota class, e.g. M06. [283] M06 functionals incorporate 27% Hartree-Fock (HF) exchange and have shown to produce relatively accurate results over other functionals in describing non-covalent interactions between molecules. [283] To obtain potential energy surface for large number of systems with several configurations, calculations have been performed at M06/aug-cc-pVDZ level. Often, interaction energies calculated at M06/aug-cc-pVDZ level could able to reproduce the values determined at MP2/aug-cc-pVDZ level, within 1.0–1.5 kcal/mol. In periodic DFT calculations, the well known Perdew, Burke, and Ernzerhof (PBE) functional [284] in combination with triple-ζ double-polarized basis sets and empirical dispersion corrections (D3) [285] was used. The performance of this functional was scrutinized by comparing the

calculated cell parameters against experimentally measured values. The deviation found was less than 1%, which substantiates the applicability of the method.

1.9.2 Classical MD Simulations

The modeling of a liquid phase, the examination of the connections between its macroscopic properties and their nature at a molecular level is a problem that can be thoroughly explored within the framework of statistical mechanics. In this context, MD simulations have been utilized as an explanatory tool to establish relations between the complex structure and interactions of ionic liquids and their fascinating properties.

MD simulation is one of the most celebrated atomistic techniques based on classical Newtonian equation of motion. [286, 287] Compared to other atomistic simulation methods such as Monte Carlo, the time evolution of the interacting atoms is explicitly considered in MD simulations, by which it is possible to access macroscopic properties such as diffusion coefficient, heat of vaporization, viscosity, thermal conductivity, etc. by time-averaging of the behavior of individual atoms. [150] In classical MD simulations, given the initial condition of the system and the inter–atomic potential, the atomic position, velocity, etc. will be updated as the consequence of integration of the equation of motion. Macroscopic properties of interest related to structure and dynamics can then be computed from the trajectory generated in a classical MD simulation.

Determination of a suitable force field is at the heart of molecular modeling at the level of an atomistic resolution. The most commonly used atomistic force field, CL&P, to address the modular nature of ILs has been developed taking into account three basic prescription: transferability, consistency, and compatibility. [288] Transferability is important because cations and anions often belong to homologous series of compounds that can be combined with different counter ions to design new ILs; internal consistency is required because, contrary to molecular species, ILs are comprised of cations and anions that can be considered as distinct units, but whose interactions should be modeled in a consistent way; finally, compatibility is essential because some ions entail organic moieties which have been already parametrized by other well-established force fields.

A general and transferable force field where several ions are modeled in isolation and then integrated to generate the correct IL comes at a price. For example, most importantly it does not rationalize the possibility of charge-transfer between the ions. As already described in Section 1.8, in ILs a significant charge transfer between ions has been observed in both experiments as well as quantum chemical calculations and the importance of inclusion of charge transfer and polarizability in the prediction of transport properties. Therefore, care must be taken in choosing a particular scheme while deriving atomic site charges in ILs.

Atomic Charge Derivation: It has been a long-standing challenge to assign net atomic charges (NACs) to individual atoms from the electron density in a material, $\rho(\vec{r})$ acquired from quantum chemical calculations. Any approach in this regard must meet several criteria in order to gain wide applicability. [289] First, the method should be applicable to both periodic and non-periodic systems. Second, the NACs should be capable of reproducing the electrostatic potential, V, outside the electron distribution; it guarantees the accurate description of electrostatic interactions between chemical species. Third, the NACs should be chemically meaningful. Fourth, the assigned NACs should be independent of the basis sets employed to generate the electron density. Finally, the approach should have direct application to both porous and non-porous materials. Several approaches reported in the literature for computing NACs do not meet one or more of the criteria above. Electrostatic potential (ESP) fitting method uses a set of grid points over which it minimizes the RMS deviation in V outside the van der Waals (vdW) surface of a material relative to V from the full electron density. [290] But, for systems comprised of buried atoms (an atom is buried if the minimum distance between that atom and system's vdW surface is more than the atom's vdW radius), multiple set of atomic charges can reproduce V far from the vdW surface, implying derived ESP charges not to be chemically meaningful. [291] Furthermore, for spatially extended systems, most often, this method requires non-periodic cluster models to generate atomic charges, where the determination of optimal cluster size is painful at times. The recently developed REPEAT [292] method does not require the construction of a non-periodic cluster model and assigns NACs in porous periodic solids, but it has limited applications to non-porous materials. Alternatively, Bader analysis has wide applications to periodic systems and yields chemically meaningful and suitable NACs. [293] However, NACs derived from Bader analysis do not accurately reproduce V outside the electron distribution. On the other hand, Mulliken method has its inherent limitation of explicit basis set dependence. [294] Although natural population analysis (NPA) is devoid of basis set dependence, it is not applicable to periodic systems. [294] In order to overcome all these difficulties in assigning NACs, recently Manz and Sholl introduced a new approach, know as density derived electrostatic and chemical (DDEC) charges. [289, 295] DDEC charges associate known electron density and satisfy all of the criteria defined above. Its application covers a broad range of materials including dense solids, porous solids, surfaces, small molecules, large molecules with buried atoms etc. [289, 295]

Density Derived Electrostatic and Chemical (DDEC) Charges: Theory

A detailed formulation of DDEC method has been given in Ref. [289, 295] In this section, a brief summary of DDEC method is provided. Let us consider an arbitrary material consisting of a set of atoms {A} at position $\{\vec{R}_A\}$, in a reference unit cell, **U**. The total electrostatic potential, V, can be defined as a sum of individual atomic electrostatic

potentials:

$$V(\vec{r}) = \sum_{k_1}\sum_{k_2}\sum_{k_3}\sum_{A} V_A(\vec{r}_A) \tag{1.4}$$

In the periodic direction, k_i spans over all integers involving lattice vector $\vec{v}_i$, while for non-periodic direction, $k_i = 0$ and $\vec{v}_i$ corresponds to boundary of **U**. The electrostatic potential owing to charge distribution on atom A, $V_A(\vec{r}_A)$, can be written as:

$$V_A(\vec{r}_A) = \frac{z_A}{r_A} - \oint \frac{\rho_A(\vec{r'}_A)d^3\vec{r'}_A}{|\vec{r}_A - \vec{r'}_A|} = \frac{q_A}{r_A} + B + C \tag{1.5}$$

where $\rho_A(\vec{r}_A)$ is the electron density on atom A, the nuclear charge is denoted as z_A, q_A is the NAC, and $r_A = |\vec{r}_A|$. Since atomic multipole expansion can be used to express $V_A(\vec{r}_A)$ outside the charge distribution, [296] $V_A(\vec{r}_A)$ can be rewritten as Eq. 1.5, where B and C are terms due to atomic multipoles (AMs) and penetration of the atom's electron density, respectively. [289] The penetration term, C, exhibits exponential decay with increasing r_A and finally becomes zero for r_A higher than a threshold value where ρ_A becomes negligible. On the other hand, atomic multipoles can be calculated using methods already reported in the literature. [296] Following the convention of atoms-in-molecule (AIM) approach, the total electron density is incorporated in the collection of atomic densities, which implies $\Theta(\vec{r}) = 0$ where

$$\Theta(\vec{r}) = \rho(\vec{r}) - \sum_{k_1}\sum_{k_2}\sum_{k_3}\sum_{A} \rho_A(\vec{r}_A) \tag{1.6}$$

Derived NACs should demonstrate the amount of charge transfer in order to be chemically meaningful. The obvious question arises at this point is, how to account for the different types of charge transfer in interacting systems?

We begin with electron density on atom A in the interacting system to be $\rho_A(\vec{r}_A)$. In case of ionic charge transfer, this quantity should approximately equal to the electron density of same atom in a noninteracting reference state, $\rho_{\mathrm{A}}^{\mathrm{ref}}(\mathrm{r_A}, \mathrm{n_A})$, provided number of electrons, n_A are same. To attain this, one can minimize the distance between $\rho_A(\vec{r}_A)$ and $\rho_{\mathrm{A}}^{\mathrm{ref}}(\mathrm{r_A}, \mathrm{n_A})$ subject to the constraint $\Theta(\vec{r}) = 0$. The iterative Hirshfeld (IH) method provides us with a suitable distance measure; [297]

$$\mathrm{F_{chem}} = \sum_{A} \oint \rho_A(\vec{r}_A) ln\left(\frac{\rho_A(\vec{r}_A)}{\rho_{\mathrm{A}}^{\mathrm{ref}}(\mathrm{r_A}, \mathrm{n_A})}\right) d^3\vec{r} \tag{1.7}$$

Setting $\partial \mathrm{F_{chem}}/\partial\rho_A(\vec{r}_A) = 0$ results in a proportional distribution of electrons between atoms, $\rho_A(\vec{r}_A)/\rho_{\mathrm{A}}^{\mathrm{ref}}(\mathrm{r_A}, \mathrm{n_A}) = \rho_B(\vec{r}_B)/\rho_{\mathrm{B}}^{\mathrm{ref}}(\mathrm{r_B}, \mathrm{n_B})$. On the other hand, in case of charge transfer in covalent bonding, electron density of each atom exhibit non-spherical distortion.

For spherically symmetric charge distributions, multipole contributions sum to zero and thus, Eq. 1.4 shows rapid convergence if each $\rho_A(\vec{r}_A)$ is optimized to be as close to spherically symmetric as possible. This is achieved by following Iterative Stockholder Atom (ISA) method [298] which minimizes the distance ($\mathrm{F_{ESP}}$) between $\rho_A(\vec{r}_A)$ and its spherical average, $\rho_{\mathrm{A}}^{\mathrm{avg}}(\mathrm{r_A})$, subject to the constraint $\Theta(\vec{r}) = 0$, where

$$\mathrm{F_{ESP}} = \sum_A \oint \rho_A(\vec{r}_A) ln \left(\frac{\rho_A(\vec{r}_A)}{\rho_{\mathrm{A}}^{\mathrm{avg}}(\mathrm{r_A})} \right) d^3\vec{r} \tag{1.8}$$

Setting $\partial \mathrm{F_{ESP}}/\partial \rho_A(\vec{r}_A) = 0$ yields $\rho_A(\vec{r}_A)/\rho_{\mathrm{A}}^{\mathrm{avg}}(\mathrm{r_A}) = \rho_B(\vec{r}_B)/\rho_{\mathrm{B}}^{\mathrm{avg}}(\mathrm{r_B}, \mathrm{n_B})$, where electron density of atom A is proportional to $\rho_{\mathrm{A}}^{\mathrm{avg}}(\mathrm{r_A})$.

For a system where all the atoms are located near the surface, only one set of NACs closely reproduces V. In this scenario, NACs for a force field are those which minimize $\mathrm{F_{ESP}}$ regardless of $\mathrm{F_{chem}}$ and equivalent to well-determined ESP charges. On the other hand, for a system comprised of buried atoms, many different combination of charges can reproduce V with comparable accuracy. Inclusion of $\mathrm{F_{chem}}$ in the minimization functional will confirm that derived NACs are chemically meaningful, because optimization of atomic distributions are performed in such a way that it resembles those of real atoms in appropriate reference states. Thus for convenient tackling of systems with and without buried atoms, the optimization functional should have weighted contribution from both $\mathrm{F_{chem}}$ and $\mathrm{F_{ESP}}$;

$$G = \chi \mathrm{F_{chem}} + (1 - \chi)\mathrm{F_{ESP}} + \int_U \lambda(\vec{r})\Theta(\vec{r}) d^3\vec{r} \tag{1.9}$$

where the Lagrange multiplier $\lambda(\vec{r})$ imposes the constraint $\Theta(\vec{r}) = 0$ and χ is the weight factor. Atomic charges are then computed employing an iterative scheme. Setting $\partial G/\partial \rho_A(\vec{r}_A) = 0$ for constant $\rho_{\mathrm{A}}^{\mathrm{ref}}(\mathrm{r_A}, \mathrm{n_A})$ yields

$$\frac{\partial G}{\partial \rho_A(\vec{r}_A)} = (1 - \chi) ln \left(\frac{\rho_A(\vec{r}_A)}{\rho_{\mathrm{A}}^{\mathrm{avg}}(\mathrm{r_A})} \right) + \chi ln \left(\frac{\rho_A(\vec{r}_A)}{\rho_{\mathrm{A}}^{\mathrm{ref}}(\mathrm{r_A}, \mathrm{n_A})} \right) + \chi - \lambda(\vec{r}) \tag{1.10}$$

Exponentiating Eq. 1.10 results

$$e^{\lambda(\vec{r}) - \chi} = \frac{\rho_A(\vec{r}_A)}{w_A(r_A)} = \frac{\rho_B(\vec{r}_B)}{w_B(r_B)} \tag{1.11}$$

where the relative weight factor for atom A is

$$w_A(r_A) = (\rho_{\mathrm{A}}^{\mathrm{avg}}(\mathrm{r_A}))^{(1-\chi)} (\rho_{\mathrm{A}}^{\mathrm{ref}}(\mathrm{r_A}, \mathrm{n_A}))^{\chi} \tag{1.12}$$

Eq. 1.11 can be more appropriately written as;

$$\rho_A(\vec{r}_A) = w_A(r_A)\rho(\vec{r}) / \sum_{k_1}\sum_{k_2}\sum_{k_3}\sum_{B} w_B(r_B) \tag{1.13}$$

As an initial estimate, neutral atom densities, $\rho_{\mathrm{A}}^{\mathrm{ref}}(\mathrm{r_A}, 0)$, are employed and the current estimate of $\{w_A(r_A)\}$ in present iteration is applied to calculate $\{\rho_A(\vec{r}_A)\}$ by Eq. 1.13 followed by determination of n_A as;

$$n_A = \oint \rho_A(\vec{r}_A) d^3\vec{r}_A = z_A - q_A \tag{1.14}$$

Finally improved estimate of $\{w_A(r_A)\}$ is obtained by combining reference density, $\rho_{\mathrm{A}}^{\mathrm{ref}}(\mathrm{r_A}, \mathrm{n_A})$, and the spherical average of $\rho_A(\vec{r}_A)$ in Eq. 1.12. This process is reiterated until the NACs for consecutive iterations vary by less than a chosen tolerance. A scheme to calculate DDEC/c3 charges is displayed in Figure 1.4.

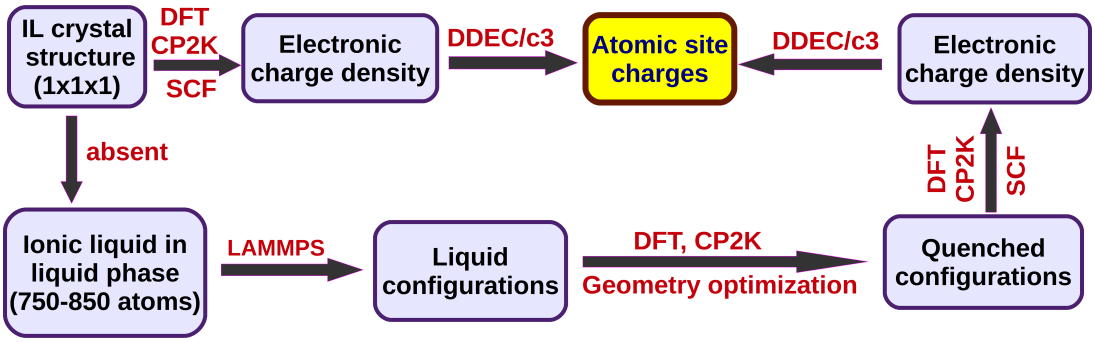

Figure 1.4: Scheme to calculate DDEC charges from crystalline and liquid phases of ILs.

1.9.3 *Ab Initio* MD Simulations

Classical molecular dynamics simulations often provide useful insights into the structure and dynamics. However, the empirical potential approach usually cannot account for events such as chemical reactions. Thus, to address this issue, *ab initio* MD (AIMD) simulations can be employed, which incorporates the explicit treatment of the electronic structure, on-the-fly during the MD simulations of a larger assembly of molecules (compared to gas phase quantum chemical calculations) with three-dimensional periodic boundary conditions. [299–301]

An important aspect involving ILs that can be studied employing AIMD simulations is the proton transfer reactions in protic ionic liquids. Whether proton diffusion in PILs follows Grotthus or a Vehicle mechanism, is a long-standing challenge in computational chemistry; [302] although many experimental reports suggest the fact that proton transfer occurs in PILs via a Grotthus mechanism. [99, 303] In the present thesis, AIMD simulations

have been performed in order to delineate the proton transfer mechanism in protic organic ionic plastic crystalline material.

At this point, it is noteworthy that equilibrium MD and AIMD simulations are in general too short to examine rare events unless the process is associated with very low energy barrier (2–3 kJ/mol at room temperature). Also, another issue arises that ionic liquids are generally very viscous, and thus to attain ample sampling of conformations, long simulations are needed. Therefore, rare events involving ionic liquids must be explored by employing free energy methods, such as adaptive biasing force (ABF), [304] metadynamics, [305] and others. Here, in this thesis, rare events were also studied employing free energy techniques. ABF method has been utilized to determine i) the solvation free energy of a solute molecule in bulk IL and ii) the energy barrier for an ion (cation or anion) to hop from one site to another site in a protic organic ionic plastic crystalline material. On the other hand, metadynamics simulations have been performed to compute the associated energy barrier in proton transfer reactions.

1.10 Software Used

Classical MD simulations have been performed using LAMMPS program. [306] *Ab initio* MD simulations have been carried out using CP2K [307] and CPMD [308] softwares. Gaussian 09 [309] package was employed to perform gas phase DFT calculations. Atomic site charges have been computed using DDEC/c3 program. [289, 295] Systems are visualized in VMD, [310] Mercury [311] and Jmol. [312]

1.11 Scope of the Thesis

Chapter 1 presents a general introduction to room temperature ionic liquids describing their physicochemical properties and applications. A concise discussion on prior research on computer simulations of ionic liquids is also presented. A short description of the theoretical methods adopted in this thesis is provided.

Chapter 2 is divided into two parts. **Chapter 2A** and **Chapter 2B** present the development of an all-atom, non-polarizable force field for room temperature ionic liquids (RTILs). Periodic DFT calculations have been performed on crystalline and liquid phases of RTILs to obtain atomic partial charges that incorporate the effects of charge transfer and electronic polarization. The total charge on the ions is determined to be less than unity. Furthermore, the mean value of the ion charge obtained for the liquid phase compares very well with that determined for the crystal. These partial charges have been adopted within a well established force field to model the condensed state of ionic liquids. Quantum potential energy scans were employed to refine the non-bonded and torsional parameters. Several RTILs have been modeled with the refined force field parameters which showed

considerable promise in predicting both intermolecular structure and dynamics, including collective quantities, in near quantitative agreement with experiments.

In **Chapter 3**, periodic DFT calculations and *ab initio* MD simulations have been employed to unravel the effect of cation-anion hydrogen bonding in modulating the low frequency vibrational modes in ammonium-based ionic liquids. Vibrational spectra in both the gas and the crystalline phases of three ionic liquids have been probed via normal-mode analysis within harmonic approximation and power spectra of velocity autocorrelation functions. A blue shift in the far-IR mode is observed with an increase in the number of hydrogen-bonding sites on the cation.

Chapter 4 presents results of atomistic simulations of ammonium-based protic ionic liquids (PILs). Pronounced impact of the length of alkyl tail on the intermolecular structure in trialkylammonium triflate PILs has been elucidated via MD simulations. Vibrational density of states and normal-modes calculated for bulk liquids have revealed that hydrogen bonding interactions between the ions increase with an increase in the bulkiness of the alkyl group attached to the N-atom of ammonium cation.

Chapter 5 is devoted to studies on a protic ionic plastic crystal (POIPC) and is divided into two parts. In **Chapter 5A**, classical MD simulations on a perfect crystal and of a vacancy model of 1,2,4-triazolium perfluorobutanesulfonate performed, to probe its thermal behavior and electrolytic properties are described. It is shown that the cations, although translationally ordered are disordered rotationally in the rotator phase and exhibit tumbling motion which leads to a short life-time of N-H$\cdots$O hydrogen bond. One-dimensional vacancy motion has been delineated and free energy calculations have been performed to obtain an estimate of energy barrier for ion hopping.

In **Chapter 5B**, results obtained from Born-Oppenheimer MD simulations of 1,2,4-triazolium perfluorobutanesulfonate in its plastic crystalline phase are presented. Spontaneous autodissociation of –N-H_N bond in the cation and multiple proton shuttle events between the cation and the anion in the native crystal has been observed. Simulations of a defective crystal with a single proton-hole were carried out to delineate the long-range proton conduction path in the plastic crystalline phase of this POIPC. The free energy barrier for proton transfer was determined using metadynamics simulations which compared well with the experimental value determined using electrical conductivity measurements. Novel variants of the anion which exhibit decreased barrier for proton transfer are proposed.

Chapter 6 is divided into two parts. In **Chapter 6A**, results from MD simulations and quantum chemical calculations investigating the role of cations and anions in the solvation of SO_2 in imidazolium-based ionic liquids are presented. SO_2 exhibits preferential interactions with the anion. Condensed phase MD simulations of SO_2 loaded ILs have demonstrated the formation of a "cage" around the solute by the cations. Free energy calculations offer

a microscopic rationale for the experimentally observed SO_2 solubility order in ILs with different anions.

In **Chapter 6B**, six different anion-functionalized ionic liquids with different basicity have been selected, and their SO_2 absorption capacity has been investigated by employing quantum chemical calculations and molecular dynamics simulations. The high uptake of SO_2 in these ILs is shown to originate from multiple-site interactions of SO_2 with the anions. Free energy calculations have been performed to investigate the thermodynamics of gas absorption.

Bibliography

[1] Freyland, W. *Coulombic Fluids: Bulk and Interfaces*; Springer Series in Solid-State Sciences; 2011.

[2] Welton, T. *Chem. Rev.* **1999**, *99*, 2071–2084.

[3] Hallett, J. P.; Welton, T. *Chem. Rev.* **2011**, *111*, 3508–3576.

[4] Angell, C. A.; Ansari, Y.; Zhao, Z. *Faraday Discuss.* **2012**, *154*, 9–27.

[5] Sangoro, J. R.; Kremer, F. *Acc. Chem. Res.* **2012**, *45*, 525–532.

[6] Santos, C. S.; Baldelli, S. *Chem. Soc. Rev.* **2010**, *39*, 2136–2145.

[7] Hunt, P. A.; Ashworth, C. R.; Matthews, R. P. *Chem. Soc. Rev.* **2015**, *44*, 1257–1288.

[8] Amde, M.; Liu, J.-F.; Pang, L. *Environ. Sci. Technol.* **2015**, *49*, 12611–12627.

[9] Dupont, J. *Acc. Chem. Res.* **2011**, *44*, 1223–1231.

[10] Chatel, G.; MacFarlane, D. R. *Chem. Soc. Rev.* **2014**, *43*, 8132–8149.

[11] Petkovic, M.; Seddon, K. R.; Rebelo, L. P. N.; Pereira, C. S. *Chem. Soc. Rev.* **2011**, *40*, 1383–1403.

[12] Hu, Z.; Margulis, C. J. *Acc. Chem. Res.* **2007**, *40*, 1097–1105.

[13] Freemantle, M. *An Introduction to Ionic Liquids*; The Royal Society of Chemistry, 2009.

[14] Kirchner, B.; Clare, B. *Ionic Liquids*; Topics in Current Chemistry; 2009.

[15] Rollet, A.-L.; Bessada, C. *NMR Studies of Molten Salt and Room Temperature Ionic Liquids*; Annual Reports on NMR Spectroscopy; Academic Press, 2013.

[16] Wasserscheid, P.; Welton, T. *Ionic Liquids in Synthesis*; Wiley-VCH, 2008; Vol. 1.

[17] Wasserscheid, P.; Welton, T. *Ionic Liquids in Synthesis*; Wiley-VCH, 2008; Vol. 2.

[18] Li, H. *Microstructure Study of Ionic Liquids by Spectroscopy*; Springer Berlin Heidelberg, 2014.

[19] Hu, Y.; Peng, X. *Effect of the Structures of Ionic Liquids on Their Physical Chemical Properties*; Springer Berlin Heidelberg, 2014.

[20] Chiappe, C.; Marra, A.; Mele, A. *Synthesis and Applications of Ionic Liquids Derived from Natural Sugars*; Springer Berlin Heidelberg, 2010.

[21] Weingärtner, H. *Angew. Chem. Int. Ed.* **2008**, *47*, 654–670.

[22] Mu, T.; Han, B. *Structures and Thermodynamic Properties of Ionic Liquids*; Springer Berlin Heidelberg, 2014.

[23] Greaves, T. L.; Drummond, C. J. *Chem. Soc. Rev.* **2008**, *37*, 1709–1726.

[24] Rehman, A.; Zeng, X. *Acc. Chem. Res.* **2012**, *45*, 1667–1677.

[25] Niedermeyer, H.; Hallett, J. P.; Villar-Garcia, I. J.; Hunt, P. A.; Welton, T. *Chem. Soc. Rev.* **2012**, *41*, 7780–7802.

[26] Maton, C.; Vos, N. D.; Stevens, C. V. *Chem. Soc. Rev.* **2013**, *42*, 5963–5977.

[27] Goossens, K.; Lava, K.; Bielawski, C. W.; Binnemans, K. *Chem. Rev.* **2016**, *116*, 4643–4807.

[28] Angell, C. A.; Byrne, N.; Belieres, J.-P. *Acc. Chem. Res.* **2007**, *40*, 1228–1236.

[29] Greaves, T. L.; Drummond, C. J. *Chem. Rev.* **2015**, *115*, 11379–11448.

[30] Greaves, T. L.; Drummond, C. J. *Chem. Rev.* **2008**, *108*, 206–237.

[31] Kerton, F.; Marriott, R. *Alternative Solvents for Green Chemistry*; The Royal Society of Chemistry, 2013.

[32] Wang, H.; Gurau, G.; Rogers, R. D. *Dissolution of Biomass Using Ionic Liquids*; Springer Berlin Heidelberg, 2014.

[33] Wang, J.; Wang, H. *Aggregation in Systems of Ionic Liquids*; Springer Berlin Heidelberg, 2014.

[34] Kerscher, B.; Schüler, F.; Appel, A.-K.; Schadt, K.; Mülhaupt, R. *Nanostructured Polymeric Ionic Liquids*; Springer International Publishing, 2013.

[35] Hollóczki, O.; Nyulászi, L. *Carbenes from Ionic Liquids*; Springer Berlin Heidelberg, 2014.

[36] Eshetu, G. G.; Armand, M.; Scrosati, B.; Passerini, S. *Angew. Chem. Int. Ed.* **2014**, *53*, 13342–13359.

[37] Zhang, Q.; Shreeve, J. M. *Chem. Rev.* **2014**, *114*, 10527–10574.

[38] Ananikov, V. P. *Chem. Rev.* **2011**, *111*, 418–454.

[39] Tang, S.; Baker, G. A.; Zhao, H. *Chem. Soc. Rev.* **2012**, *41*, 4030–4066.

[40] Lei, Z.; Dai, C.; Chen, B. *Chem. Rev.* **2014**, *114*, 1289–1326.

[41] Sun, X.; Luo, H.; Dai, S. *Chem. Rev.* **2012**, *112*, 2100–2128.

[42] Osada, I.; Vries, H.; Scrosati, B.; Passerini, S. *Angew. Chem. Int. Ed.* **2016**, *55*, 500–513.

[43] Zhang, S.; Sun, J.; Zhang, X.; Xin, J.; Miao, Q.; Wang, J. *Chem. Soc. Rev.* **2014**, *43*, 7838–7869.

[44] Wang, H.; Gurau, G.; Rogers, R. D. *Chem. Soc. Rev.* **2012**, *41*, 1519–1537.

[45] Freudenmann, D.; Wolf, S.; Wolff, M.; Feldmann, C. *Angew. Chem. Int. Ed.* **2011**, *50*, 11050–11060.

[46] Werner, S.; Haumann, M.; Wasserscheid, P. *Ann. Rev. Chem. Biomol. Eng.* **2010**, *1*, 203–230.

[47] Marrucho, I.; Branco, L.; Rebelo, L. *Ann. Rev. Chem. Biomol. Eng.* **2014**, *5*, 527–546.

[48] Eshetu, G. G.; Armand, M.; Ohno, H.; Scrosati, B.; Passerini, S. *Energy Environ. Sci.* **2016**, *9*, 49–61.

[49] Jutz, F.; Andanson, J.-M.; Baiker, A. *Chem. Rev.* **2011**, *111*, 322–353.

[50] Fedorov, M. V.; Kornyshev, A. A. *Chem. Rev.* **2014**, *114*, 2978–3036.

[51] Zhang, Y.; Gao, H.; Joo, Y.-H.; Shreeve, J. M. *Angew. Chem. Int. Ed.* **2011**, *50*, 9554–9562.

[52] Jr., E. W. C.; Margulis, C. J.; Maroncelli, M.; Wishart, J. F. *Ann. Rev. Phys. Chem.* **2011**, *62*, 85–105.

[53] Xin, B.; Hao, J. *Chem. Soc. Rev.* **2014**, *43*, 7171–7187.

[54] Le Bideau, J.; Viau, L.; Vioux, A. *Chem. Soc. Rev.* **2011**, *40*, 907–925.

[55] Isambert, N.; Duque, M. d. M. S.; Plaquevent, J.-C.; Genisson, Y.; Rodriguez, J.; Constantieux, T. *Chem. Soc. Rev.* **2011**, *40*, 1347–1357.

[56] Bara, J. E.; Camper, D. E.; Gin, D. L.; Noble, R. D. *Acc. Chem. Res.* **2010**, *43*, 152–159.

[57] Lee, J. W.; Shin, J. Y.; Chun, Y. S.; Jang, H. B.; Song, C. E.; Lee, S. *Acc. Chem. Res.* **2010**, *43*, 985–994.

[58] Giernoth, R. *Angew. Chem. Int. Ed.* **2010**, *49*, 2834–2839.

[59] Hu, Y.-F.; Liu, Z.-C.; Xu, C.-M.; Zhang, X.-M. *Chem. Soc. Rev.* **2011**, *40*, 3802–3823.

[60] Greaves, T. L.; Drummond, C. J. *Chem. Soc. Rev.* **2013**, *42*, 1096–1120.

[61] Hubbard, C. D.; Illner, P.; van Eldik, R. *Chem. Soc. Rev.* **2011**, *40*, 272–290.

[62] Hayes, R.; Warr, G. G.; Atkin, R. *Chem. Rev.* **2015**, *115*, 6357–6426.

[63] Mirjafari, A.; Pham, L. N.; McCabe, J. R.; Mobarrez, N.; Salter, E. A.; Wierzbicki, A.; West, K. N.; Sykora, R. E.; Davis, J. H. *RSC Adv.* **2013**, *3*, 337–340.

[64] Xu, W.; Angell, C. A. *Science* **2003**, *302*, 422–425.

[65] Noda, A.; Susan, M. A. B. H.; Kudo, K.; Mitsushima, S.; Hayamizu, K.; Watanabe, M. *J. Phys. Chem. B* **2003**, *107*, 4024–4033.

[66] Miran, M. S.; Yasuda, T.; Susan, M. A. B. H.; Dokko, K.; Watanabe, M. *J. Phys. Chem. C* **2014**, *118*, 27631–27639.

[67] Yoshizawa, M.; Xu, W.; Angell, C. A. *J. Am. Chem. Soc.* **2003**, *125*, 15411–15419.

[68] Belieres, J.-P.; Angell, C. A. *J. Phys. Chem. B* **2007**, *111*, 4926–4937.

[69] Mann, J. P.; M Cluskey, A.; Atkin, R. *Green Chem.* **2009**, *11*, 785–792.

[70] Sun, J.; Forsyth, M.; MacFarlane, D. R. *J. Phys. Chem. B* **1998**, *102*, 8858–8864.

[71] MacFarlane, D. R.; Forsyth, S. A.; Golding, J.; Deacon, G. B. *Green Chem.* **2002**, *4*, 444–448.

[72] Zaitsau, D. H.; Emel'yanenko, V. N.; Stange, P.; Schick, C.; Verevkin, S. P.; Ludwig, R. *Angew. Chem. Int. Ed.* **2016**, doi:10.1002/anie.201605633.

[73] Ding, J.; Armstrong, D. W. *Chirality* **2005**, *17*, 281–292.

[74] Santos, E.; Albo, J.; Irabien, A. *RSC Adv.* **2014**, *4*, 40008–40018.

[75] Shen, Y.; Kennedy, D. F.; Greaves, T. L.; Weerawardena, A.; Mulder, R. J.; Kirby, N.; Song, G.; Drummond, C. J. *Phys. Chem. Chem. Phys.* **2012**, *14*, 7981–7992.

[76] Mecerreyes, D. *Prog. Polym. Sci.* **2011**, *36*, 1629–1648.

[77] Ohno, H.; Fukumoto, K. *Acc. Chem. Res.* **2007**, *40*, 1122–1129.

[78] Israelachvili, J. N. *Unifying Concepts in Intermolecular and Interparticle Forces*; Academic Press, 2011.

[79] Zahn, S.; Bruns, G.; Thar, J.; Kirchner, B. *Phys. Chem. Chem. Phys.* **2008**, *10*, 6921–6924.

[80] Lopes, J. N. C.; Gomes, M. F. C.; Pádua, A. A. H. *J. Phys. Chem. B* **2006**, *110*, 16816–16818.

[81] Israelachvili, J. N.; Marčelja, S.; Horn, R. G. *Q. Rev. Biophys.* **1980**, *13*, 121–200.

[82] Israelachvili, J. N.; Mitchell, D. J.; Ninham, B. W. *J. Chem. Soc., Faraday Trans. 2* **1976**, *72*, 1525–1568.

[83] Landini, D.; Maia, A. *Tetrahedron Lett.* **2005**, *46*, 3961 – 3963.

[84] Hanke, C. G.; Lynden-Bell, R. M. *J. Phys. Chem. B* **2003**, *107*, 10873–10878.

[85] Hunt, P. A.; Kirchner, B.; Welton, T. *Chem. Eur. J.* **2006**, *12*, 6762–6775.

[86] Skarmoutsos, I.; Dellis, D.; Matthews, R. P.; Welton, T.; Hunt, P. A. *J. Phys. Chem. B* **2012**, *116*, 4921–4933.

[87] Kempter, V.; Kirchner, B. *J. Mol. Struct.* **2010**, *972*, 22–34.

[88] Sarangi, S. S.; Reddy, S. K.; Balasubramanian, S. *J. Phys. Chem. B* **2011**, *115*, 1874–1880.

[89] Fumino, K.; Wulf, A.; Ludwig, R. *Angew. Chem. Int. Ed.* **2009**, *48*, 3184–3186.

[90] Fumino, K.; Peppel, T.; Geppert-Rybczynska, M.; Zaitsau, D. H.; Lehmann, J. K.; Verevkin, S. P.; Kockerling, M.; Ludwig, R. *Phys. Chem. Chem. Phys.* **2011**, *13*, 14064–14075.

[91] Hunt, P. A. *J. Phys. Chem. B* **2007**, *111*, 4844–4853.

[92] López-Barrón, C. R.; Li, D.; DeRita, L.; Basavaraj, M. G.; Wagner, N. J. *J. Am. Chem. Soc.* **2012**, *134*, 20728–20732.

[93] Debeljuh, N. J.; Sutti, A.; Barrow, C. J.; Byrne, N. *J. Phys. Chem. B* **2013**, *117*, 8430–8435.

[94] Wang, X.; Chen, X.; Zhao, Y.; Yue, X.; Li, Q.; Li, Z. *Langmuir* **2012**, *28*, 2476–2484.

[95] Jiang, W.; Hao, J.; Wu, Z. *Langmuir* **2008**, *24*, 3150–3156.

[96] Shi, L.; Zheng, L. *J. Phys. Chem. B* **2012**, *116*, 2162–2172.

[97] Zhao, M.; Gao, Y.; Zheng, L. *J. Phys. Chem. B* **2010**, *114*, 11382–11389.

[98] Zhang, G.; Chen, X.; Zhao, Y.; Ma, F.; Jing, B.; Qiu, H. *J. Phys. Chem. B* **2008**, *112*, 6578–6584.

[99] Luo, J. et al. *Energy Environ. Sci.* **2015**, *8*, 1276–1291.

[100] Lu, F.; Shi, L.; Gu, Y.; Yang, X.; Zheng, L. *Colloid. Polym. Sci.* **2013**, *291*, 2375–2384.

[101] Dear, R. D.; Worrall, E. K.; Gault, W. D.; Ritchie, G. A. D. *J. Phys. Chem. B* **2013**, *117*, 10567–10571.

[102] Bicak, N. *J. Mol. Liq.* **2005**, *116*, 15–18.

[103] Malham, I. B.; Letellier, P.; Mayaffre, A.; Turmine, M. *J. Chem. Thermodyn.* **2007**, *39*, 1132 – 1143.

[104] Bouguerra, S.; Malham, I. B.; Letellier, P.; Mayaffre, A.; Turmine, M. *J. Chem. Thermodyn.* **2008**, *40*, 146 – 154.

[105] Jeffrey, G. A. *An Introduction to Hydrogen Bonding*; Oxford University Press, 1997.

[106] Izgorodina, E. I.; Golze, D.; Maganti, R.; Armel, V.; Taige, M.; Schubert, T. J. S.; MacFarlane, D. R. *Phys. Chem. Chem. Phys.* **2014**, *16*, 7209–7221.

[107] Matthews, R. P.; Welton, T.; Hunt, P. A. *Phys. Chem. Chem. Phys.* **2014**, *16*, 3238–3253.

[108] Wilkes, J. S.; Zaworotko, M. J. *J. Chem. Soc., Chem. Commun.* **1992**, 965–967.

[109] Wilkes, J. S.; Zaworotko, M. J. *Supramol. Chem.* **1993**, *1*, 191–193.

[110] Deetlefs, M.; Hardacre, C.; Nieuwenhuyzen, M.; Padua, A. A. H.; Sheppard, O.; Soper, A. K. *J. Phys. Chem. B* **2006**, *110*, 12055–12061.

[111] Li, X.-W.; Zhang, J.; Dong, B.; Zheng, L.-Q.; Tung, C.-H. *Colloids Surf., A* **2009**, *335*, 80–87.

[112] Deetlefs, M.; Hardacre, C.; Nieuwenhuyzen, M.; Sheppard, O.; Soper, A. K. *J. Phys. Chem. B* **2005**, *109*, 1593–1598.

[113] Frolov, A. I.; Kirchner, K.; Kirchner, T.; Fedorov, M. V. *Faraday Discuss.* **2012**, *154*, 235–247.

[114] Fedorov, M. V.; Lynden-Bell, R. M. *Phys. Chem. Chem. Phys.* **2012**, *14*, 2552–2556.

[115] Shimizu, K.; Tariq, M.; Gomes, M. F. C.; Rebelo, L. P. N.; Lopes, J. N. C. *J. Phys. Chem. B* **2010**, *114*, 5831–5834.

[116] Schroder, U.; Wadhawan, J. D.; Compton, R. G.; Marken, F.; Suarez, P. A. Z.; Consorti, C. S.; de Souza, R. F.; Dupont, J. *New J. Chem.* **2000**, *24*, 1009–1015.

[117] Dupont, J. *J. Braz. Chem. Soc.* **2004**, *15*, 341 – 350.

[118] Hamaguchi, H.-O.; Ozawa, R. *Structure of Ionic Liquids and Ionic Liquid Compounds: Are Ionic Liquids Genuine Liquids in the Conventional Sense?*; John Wiley & Sons, Inc., 2005.

[119] D. Holbrey, J.; R. Seddon, K. *J. Chem. Soc., Dalton Trans.* **1999**, 2133–2140.

[120] Bowlas, C. J.; Bruce, D. W.; Seddon, K. R. *Chem. Commun.* **1996**, 1625–1626.

[121] Hardacre, C.; Holbrey, J. D.; McMath, S. E. J.; Nieuwenhuyzen, M. *Small-Angle Scattering from Long-Chain Alkylimidazolium-Based Ionic Liquids*; American Chemical Society, 2002.

[122] van den Broeke, J.; Stam, M.; Lutz, M.; Kooijman, H.; Spek, A.; Deelman, B.-J.; van Koten, G. *Eur. J. Inorg. Chem.* **2003**, *2003*, 2798–2811.

[123] Wang, Y.; Voth, G. A. *J. Am. Chem. Soc.* **2005**, *127*, 12192–12193.

[124] Wang, Y.; Voth, G. A. *J. Phys. Chem. B* **2006**, *110*, 18601–18608.

[125] Wang, Y.; Jiang, W.; Yan, T.; Voth, G. A. *Acc. Chem. Res.* **2007**, *40*, 1193–1199.

[126] Lopes, J. N. C.; Pádua, A. A. H. *J. Phys. Chem. B* **2006**, *110*, 3330–3335.

[127] Bhargava, B. L.; Devane, R.; Klein, M. L.; Balasubramanian, S. *Soft Matter* **2007**, *3*, 1395–1400.

[128] Raju, S. G.; Balasubramanian, S. *J. Mater. Chem.* **2009**, *19*, 4343–4347.

[129] Triolo, A.; Russina, O.; Bleif, H.-J.; Cola, E. D. *J. Phys. Chem. B* **2007**, *111*, 4641–4644.

[130] Triolo, A.; Russina, O.; Fazio, B.; Triolo, R.; Cola, E. D. *Chem. Phys. Lett.* **2008**, *457*, 362 – 365.

[131] Annapureddy, H. V. R.; Kashyap, H. K.; Biase, P. M. D.; Margulis, C. J. *J. Phys. Chem. B* **2010**, *114*, 16838–16846.

[132] Kashyap, H. K.; Hettige, J. J.; Annapureddy, H. V. R.; Margulis, C. J. *Chem. Commun.* **2012**, *48*, 5103–5105.

[133] Kashyap, H. K.; Santos, C. S.; Annapureddy, H. V. R.; Murthy, N. S.; Margulis, C. J.; Castner, Jr, E. W. *Faraday Discuss.* **2012**, *154*, 133–143.

[134] Santos, C. S.; Annapureddy, H. V. R.; Murthy, N. S.; Kashyap, H. K.; Castner, E. W.; Margulis, C. J. *J. Chem. Phys.* **2011**, *134*, 064501.

[135] Daguenet, C.; Dyson, P. J.; Krossing, I.; Oleinikova, A.; Slattery, J.; Wakai, C.; Weingärtner, H. *J. Phys. Chem. B* **2006**, *110*, 12682–12688.

[136] Weingärtner, H.; Sasisanker, P.; Daguenet, C.; Dyson, P. J.; Krossing, I.; Slattery, J. M.; Schubert, T. *J. Phys. Chem. B* **2007**, *111*, 4775–4780.

[137] Schröder, C.; Wakai, C.; Weingärtner, H.; Steinhauser, O. *J. Chem. Phys.* **2007**, *126*, 084511.

[138] Schrodle, S.; Annat, G.; MacFarlane, D. R.; Forsyth, M.; Buchner, R.; Hefter, G. *Chem. Commun.* **2006**, 1748–1750.

[139] Yamamoto, K.; Tani, M.; Hangyo, M. *J. Phys. Chem. B* **2007**, *111*, 4854–4859.

[140] Asaki, M. L. T.; Redondo, A.; Zawodzinski, T. A.; Taylor, A. J. *J. Chem. Phys.* **2002**, *116*, 10377–10385.

[141] Antony, J. H.; Dölle, A.; Mertens, D.; Wasserscheid, P.; Carper, W. R.; Wahlbeck, G. P. *J. Phys. Chem. A* **2005**, *109*, 6676–6682.

[142] Heimer, N. E.; Wilkes, J. S.; Wahlbeck, P. G.; Carper, W. R. *J. Phys. Chem. A* **2006**, *110*, 868–874.

[143] Wulf, A.; Ludwig, R.; Sasisanker, P.; Weingärtner, H. *Chem. Phys. Lett.* **2007**, *439*, 323 – 326.

[144] Hyun, B.-R.; Dzyuba, S. V.; Bartsch, R. A.; Quitevis, E. L. *J. Phys. Chem. A* **2002**, *106*, 7579–7585.

[145] Turton, D. A.; Hunger, J.; Stoppa, A.; Hefter, G.; Thoman, A.; Walther, M.; Buchner, R.; Wynne, K. *J. Am. Chem. Soc.* **2009**, *131*, 11140–11146.

[146] Giraud, G.; Gordon, C. M.; Dunkin, I. R.; Wynne, K. *J. Chem. Phys.* **2003**, *119*, 464–477.

[147] Shirota, H.; Funston, A. M.; Wishart, J. F.; Castner, E. W. *J. Chem. Phys.* **2005**, *122*, 184512.

[148] Triolo, A.; Russina, O.; Arrighi, V.; Juranyi, F.; Janssen, S.; Gordon, C. M. *J. Chem. Phys.* **2003**, *119*, 8549–8557.

[149] Triolo, A.; Russina, O.; Hardacre, C.; Nieuwenhuyzen, M.; Gonzalez, M. A.; Grimm, H. *J. Phys. Chem. B* **2005**, *109*, 22061–22066.

[150] Hansen, J.-P.; McDonald, I. R. *Theory of Simple Liquids, Third Edition*; Academic Press: San Diego, CA, 2006.

[151] Ediger, M. D. *Annu. Rev. Phys. Chem.* **2000**, *51*, 99–128.

[152] Pópolo, M. G. D.; Voth, G. A. *J. Phys. Chem. B* **2004**, *108*, 1744–1752.

[153] Hu, Z.; Margulis, C. J. *Proc. Natl. Acad. Sci.* **2006**, *103*, 831–836.

[154] Morrow, T. I.; Maginn, E. J. *J. Phys. Chem. B* **2002**, *106*, 12807–12813.

[155] Urahata, S. M.; Ribeiro, M. C. C. *J. Chem. Phys.* **2005**, *122*, 024511.

[156] Tokuda, H.; Hayamizu, K.; Ishii, K.; Susan, M. A. B. H.; Watanabe, M. *J. Phys. Chem. B* **2004**, *108*, 16593–16600.

[157] Tokuda, H.; Hayamizu, K.; Ishii, K.; Susan, M. A. B. H.; Watanabe, M. *J. Phys. Chem. B* **2005**, *109*, 6103–6110.

[158] Armand, M.; Endres, F.; MacFarlane, D. R.; Ohno, H.; Scrosati, B. *Nat. Mater.* **2009**, *8*, 621–629.

[159] MacFarlane, D. R.; Tachikawa, N.; Forsyth, M.; Pringle, J. M.; Howlett, P. C.; Elliott, G. D.; Davis, J. H.; Watanabe, M.; Simon, P.; Angell, C. A. *Energy Environ. Sci.* **2014**, *7*, 232–250.

[160] Hapiot, P.; Lagrost, C. *Chem. Rev.* **2008**, *108*, 2238–2264.

[161] Rotenberg, B.; Salanne, M. *J. Phys. Chem. Lett.* **2015**, *6*, 4978–4985.

[162] Mezger, M.; Schröder, H.; Reichert, H.; Schramm, S.; Okasinski, J. S.; Schöder, S.; Honkimäki, V.; Deutsch, M.; Ocko, B. M.; Ralston, J.; Rohwerder, M.; Stratmann, M.; Dosch, H. *Science* **2008**, *322*, 424–428.

[163] Yokota, Y.; Harada, T.; Fukui, K. *Chem. Commun.* **2010**, *46*, 8627–8629.

[164] Payal, R. S.; Balasubramanian, S. *ChemPhysChem* **2012**, *13*, 1764–1771.

[165] Merlet, C.; Rotenberg, B.; Madden, P. A.; Salanne, M. *Phys. Chem. Chem. Phys.* **2013**, *15*, 15781–15792.

[166] Li, H.; Rutland, M. W.; Atkin, R. *Phys. Chem. Chem. Phys.* **2013**, *15*, 14616–14623.

[167] Li, H.; Endres, F.; Atkin, R. *Phys. Chem. Chem. Phys.* **2013**, *15*, 14624–14633.

[168] Baldelli, S. *J. Phys. Chem. Lett.* **2013**, *4*, 244–252.

[169] Baldelli, S. *J. Phys. Chem. B* **2003**, *107*, 6148–6152.

[170] Rivera-Rubero, S.; Baldelli, S. *J. Am. Chem. Soc.* **2004**, *126*, 11788–11789.

[171] Rivera-Rubero, S.; Baldelli, S. *J. Phys. Chem. B* **2006**, *110*, 15499–15505.

[172] Smith, E. F.; Villar Garcia, I. J.; Briggs, D.; Licence, P. *Chem. Commun.* **2005**, 5633–5635.

[173] Smith, E. F.; Rutten, F. J. M.; Villar-Garcia, I. J.; Briggs, D.; ; Licence, P. *Langmuir* **2006**, *22*, 9386–9392.

[174] Kirchner, K.; Kirchner, T.; Ivaništšev, V.; Fedorov, M. *Electrochim. Acta* **2013**, *110*, 762–771.

[175] Yan, T.; Li, S.; Jiang, W.; Gao, X.; Xiang, B.; ; Voth, G. A. *J. Phys. Chem. B* **2006**, *110*, 1800–1806.

[176] Bhargava, B. L.; Balasubramanian, S. *J. Am. Chem. Soc.* **2006**, *128*, 10073–10078.

[177] Lynden-Bell, R. M.; Pópolo, M. G. D. *Phys. Chem. Chem. Phys.* **2006**, *8*, 949–954.

[178] Jiang, W.; Wang, Y.; Yan, T.; Voth, G. A. *J. Phys. Chem. C* **2008**, *112*, 1132–1139.

[179] Tokuda, H.; Tsuzuki, S.; Susan, M. A. B. H.; Hayamizu, K.; Watanabe, M. *J. Phys. Chem. B* **2006**, *110*, 19593–19600.

[180] Xu, W.-G.; Li, L.; Ma, X.-X.; Wei, J.; Duan, W.-B.; Guan, W.; Yang, J.-Z. *J. Chem. Eng. Data* **2012**, *57*, 2177–2184.

[181] Deyko, A.; Hessey, S. G.; Licence, P.; Chernikova, E. A.; Krasovskiy, V. G.; Kustov, L. M.; Jones, R. G. *Phys. Chem. Chem. Phys.* **2012**, *14*, 3181–3193.

[182] Deyko, A.; Lovelock, K. R. J.; Corfield, J.-A.; Taylor, A. W.; Gooden, P. N.; Villar-Garcia, I. J.; Licence, P.; Jones, R. G.; Krasovskiy, V. G.; Chernikova, E. A.; Kustov, L. M. *Phys. Chem. Chem. Phys.* **2009**, *11*, 8544–8555.

[183] Zaitsau, D. H.; Kabo, G. J.; Strechan, A. A.; Paulechka, Y. U.; Tschersich, A.; Verevkin, S. P.; Heintz, A. *J. Phys. Chem. A* **2006**, *110*, 7303–7306.

[184] Freire, M. G.; Carvalho, P. J.; Fernandes, A. M.; Marrucho, I. M.; Queimada, A. J.; Coutinho, J. A. *J. Colloid Interface Sci.* **2007**, *314*, 621 – 630.

[185] Almeida, H. F. D.; Passos, H.; Lopes-da Silva, J. A.; Fernandes, A. M.; Freire, M. G.; Coutinho, J. A. P. *J. Chem. Eng. Data* **2012**, *57*, 3005–3013.

[186] Sánchez, L. G.; Espel, J. R.; Onink, F.; Meindersma, G. W.; Haan, A. B. *J. Chem. Eng. Data* **2009**, *54*, 2803–2812.

[187] Vakili-Nezhaad, G.; Vatani, M.; Asghari, M.; Ashour, I. *J. Chem. Thermodyn.* **2012**, *54*, 148–154.

[188] Xu, A.; Zhang, Y.; Li, Z.; Wang, J. *J. Chem. Eng. Data* **2012**, *57*, 3102–3108.

[189] Yoshida, Y.; Baba, O.; Saito, G. *J. Phys. Chem. B* **2007**, *111*, 4742–4749.

[190] Sterner, E. S.; Rosol, Z. P.; Gross, E. M.; Gross, S. M. *J. Appl. Polym. Sci.* **2009**, *114*, 2963–2970.

[191] Ma, X.-X.; Wei, J.; Zhang, Q.-B.; Tian, F.; Feng, Y.-Y.; Guan, W. *Ind. Eng. Chem. Res.* **2013**, *52*, 9490–9496.

[192] Chambreau, S. D.; Vaghjiani, G. L.; To, A.; Koh, C.; Strasser, D.; Kostko, O.; Leone, S. R. *J. Phys. Chem. B* **2010**, *114*, 1361–1367.

[193] Aparicio, S.; Atilhan, M.; Karadas, F. *Ind. Eng. Chem. Res.* **2010**, *49*, 9580–9595.

[194] Scurto, A. M.; Leitner, W. *Chem. Commun.* **2006**, 3681–3683.

[195] Hunt, P. A. *Mol. Simul.* **2006**, *32*, 1–10.

[196] Plechkova, N. V.; Seddon, K. R. *Chem. Soc. Rev.* **2008**, *37*, 123–150.

[197] MacFarlane, D. R.; Golding, J.; Forsyth, S.; Forsyth, M.; Deacon, G. B. *Chem. Commun.* **2001**, 1430–1431.

[198] Coutinho, J. A. P.; Carvalho, P. J.; Oliveira, N. M. C. *RSC Adv.* **2012**, *2*, 7322–7346.

[199] Slattery, J.; Daguenet, C.; Dyson, P.; Schubert, T.; Krossing, I. *Angew. Chem. Int. Ed.* **2007**, *46*, 5384–5388.

[200] Yan, T.; Burnham, C. J.; Pópolo, M. G. D.; Voth, G. A. *J. Phys. Chem. B* **2004**, *108*, 11877–11881.

[201] Urahata, S. M.; Ribeiro, M. C. *J. Chem. Phys.* **2006**, *124*, 074513.

[202] Rey-Castro, C.; Vega, L. F. *J. Phys. Chem. B* **2006**, *110*, 14426–14435.

[203] Hu, Z.; Margulis, C. J. *J. Phys. Chem. B* **2007**, *111*, 4705–4714.

[204] Every, H. A.; Bishop, A. G.; MacFarlane, D. R.; Oradd, G.; Forsyth, M. *Phys. Chem. Chem. Phys.* **2004**, *6*, 1758–1765.

[205] Pádua, A. A. H.; Gomes, M. F. C.; Lopes, J. N. C. *Acc. Chem. Res.* **2007**, *40*, 1087–1096.

[206] Tsuzuki, S. *ChemPhysChem* **2012**, *13*, 1664–1670.

[207] Liu, Z.; Huang, S.; Wang, W. *J. Phys. Chem. B* **2004**, *108*, 12978–12989.

[208] Liu, Z.; Wu, X.; Wang, W. *Phys. Chem. Chem. Phys.* **2006**, *8*, 1096–1104.

[209] Zhong, X.; Liu, Z.; Cao, D. *J. Phys. Chem. B* **2011**, *115*, 10027–10040.

[210] Tsuzuki, S.; Matsumoto, H.; Shinoda, W.; Mikami, M. *Phys. Chem. Chem. Phys.* **2011**, *13*, 5987–5993.

[211] Bagno, A.; D'Amico, F.; Saielli, G. *J. Mol. Liq.* **2007**, *131-132*, 17–23.

[212] Bedrov, D.; Borodin, O.; Li, Z.; Smith, G. D. *J. Phys. Chem. B* **2010**, *114*, 4984–4997.

[213] Lewandowski, A.; Świderska-Mocek, A. *J. Power Sources* **2009**, *194*, 601–609.

[214] Vila, J.; Ginés, P.; Rilo, E.; Cabeza, O.; Varela, L. *Fluid Phase Equilib.* **2006**, *247*, 32–39.

[215] Vila, J.; Varela, L.; Cabeza, O. *Electrochim. Acta* **2007**, *52*, 7413–7417.

[216] Galiński, M.; Lewandowski, A.; Stepniak, I. *Electrochim. Acta* **2006**, *51*, 5567–5580.

[217] Stoppa, A.; Zech, O.; Kunz, W.; Buchner, R. *J. Chem. Eng. Data* **2010**, *55*, 1768–1773.

[218] Tokuda, H.; Ishii, K.; Susan, M. A. B. H.; Tsuzuki, S.; Hayamizu, K.; Watanabe, M. *J. Phys. Chem. B* **2006**, *110*, 2833–2839.

[219] Welton, T. *Coord. Chem. Rev.* **2004**, *248*, 2459–2477.

[220] Gordon, C. M. *Appl. Catal., A* **2001**, *222*, 101–117.

[221] Sawant, A.; Raut, D.; Darvatkar, N.; Salunkhe, M. *Green Chem. Lett. Rev.* **2011**, *4*, 41–54.

[222] Rogers, R. D.; Seddon, K. R. *Science* **2003**, *302*, 792–793.

[223] Swatloski, R. P.; Spear, S. K.; Holbrey, J. D.; Rogers, R. D. *J. Am. Chem. Soc.* **2002**, *124*, 4974–4975.

[224] Rogers, R. D.; Seddon, K. R.; Volkov, S. *Green Industrial Applications of Ionic Liquids*; Springer, 2002.

[225] Payal, R. S.; Bharath, R.; Periyasamy, G.; Balasubramanian, S. *J. Phys. Chem. B* **2012**, *116*, 833–840.

[226] Payal, R. S.; Balasubramanian, S. *Phys. Chem. Chem. Phys.* **2014**, *16*, 17458–17465.

[227] Vijayaraghavan, R.; Izgorodin, A.; Ganesh, V.; Surianarayanan, M.; MacFarlane, D. *Angew. Chem. Int. Ed.* **2010**, *49*, 1631–1633.

[228] Chandran, A.; Ghoshdastidar, D.; Senapati, S. *J. Am. Chem. Soc.* **2012**, *134*, 20330–20339.

[229] Fujita, K.; MacFarlane, D. R.; Forsyth, M. *Chem. Commun.* **2005**, 4804–4806.

[230] Vatamanu, J.; Borodin, O.; Smith, G. D. *J. Am. Chem. Soc.* **2010**, *132*, 14825–14833.

[231] Vatamanu, J.; Borodin, O.; Smith, G. D. *J. Phys. Chem. B* **2011**, *115*, 3073–3084.

[232] Vatamanu, J.; Borodin, O.; Bedrov, D.; Smith, G. D. *J. Phys. Chem. C* **2012**, *116*, 7940–7951.

[233] Susan, M. A. B. H.; Noda, A.; Mitsushima, S.; Watanabe, M. *Chem. Commun.* **2003**, 938–939.

[234] Nakamoto, H.; Watanabe, M. *Chem. Commun.* **2007**, 2539–2541.

[235] Singh, R. P.; Verma, R. D.; Meshri, D. T.; Shreeve, J. M. *Angew. Chem. Int. Ed.* **2006**, *45*, 3584–3601.

[236] Schneider, S.; Hawkins, T.; Rosander, M.; Vaghjiani, G.; Chambreau, S.; Drake, G. *Energy Fuels* **2008**, *22*, 2871–2872.

[237] Chambreau, S. D.; Schneider, S.; Rosander, M.; Hawkins, T.; Gallegos, C. J.; Pastewait, M. F.; Vaghjiani, G. L. *J. Phys. Chem. A* **2008**, *112*, 7816–7824.

[238] Blanchard, L. A.; Hancu, D.; Beckman, E. J.; Brennecke, J. F. *Nature* **1999**, *399*, 28–29.

[239] Wang, C.; Luo, H.; Jiang, D.-e.; Li, H.; Dai, S. *Angew. Chem. Int. Ed.* **2010**, *49*, 5978–5981.

[240] Wang, C.; Luo, X.; Luo, H.; Jiang, D.-e.; Li, H.; Dai, S. *Angew. Chem. Int. Ed.* **2011**, *50*, 4918–4922.

[241] Bates, E. D.; Mayton, R. D.; Ntai, I.; Davis, J. H. *J. Am. Chem. Soc.* **2002**, *124*, 926–927.

[242] Zhang, Y.; Zhang, S.; Lu, X.; Zhou, Q.; Fan, W.; Zhang, X. *Chem. Eur. J.* **2009**, *15*, 3003–3011.

[243] Wu, W.; Han, B.; Gao, H.; Liu, Z.; Jiang, T.; Huang, J. *Angew. Chem. Int. Ed.* **2004**, *43*, 2415–2417.

[244] Cui, G.; Wang, C.; Zheng, J.; Guo, Y.; Luo, X.; Li, H. *Chem. Commun.* **2012**, *48*, 2633–2635.

[245] Huang, J.; Riisager, A.; Wasserscheid, P.; Fehrmann, R. *Chem. Commun.* **2006**, 4027–4029.

[246] Ren, S.; Hou, Y.; Wu, W.; Liu, Q.; Xiao, Y.; Chen, X. *J. Phys. Chem. B* **2010**, *114*, 2175–2179.

[247] Shah, J. K.; Maginn, E. J. *J. Phys. Chem. B* **2005**, *109*, 10395–10405.

[248] Zhang, X.; Huo, F.; Liu, Z.; Wang, W.; Shi, W.; Maginn, E. J. *J. Phys. Chem. B* **2009**, *113*, 7591–7598.

[249] Anderson, J. L.; Dixon, J. K.; Maginn, E. J.; Brennecke, J. F. *J. Phys. Chem. B* **2006**, *110*, 15059–15062.

[250] Huang, X.; Margulis, C. J.; Li, Y.; Berne, B. J. *J. Am. Chem. Soc.* **2005**, *127*, 17842–17851.

[251] Cadena, C.; Anthony, J. L.; Shah, J. K.; Morrow, T. I.; Brennecke, J. F.; Maginn, E. J. *J. Am. Chem. Soc.* **2004**, *126*, 5300–5308.

[252] Anthony, J. L.; Maginn, E. J.; Brennecke, J. F. *J. Phys. Chem. B* **2002**, *106*, 7315–7320.

[253] Kirchner, B. *Phys. Rep.* **2007**, *440*, 1–111.

[254] Hanke, C. G.; Price, S. L.; Lynden-Bell, R. M. *Mol. Phys.* **2001**, *99*, 801–809.

[255] Maginn, E. J. *Acc. Chem. Res.* **2007**, *40*, 1200–1207.

[256] Lynden-Bell, R. M.; Pópolo, M. G. D.; Youngs, T. G. A.; Kohanoff, J.; Hanke, C. G.; Harper, J. B.; Pinilla, C. C. *Acc. Chem. Res.* **2007**, *40*, 1138–1145.

[257] Bhargava, B. L.; Balasubramanian, S.; Klein, M. L. *Chem. Commun.* **2008**, 3339–3351.

[258] Lopes, J. N. C.; Pádua, A. A. H. *J. Phys. Chem. B* **2004**, *108*, 2038–2047.

[259] Lopes, J. N. C.; Pádua, A. A. H. *J. Phys. Chem. B* **2004**, *108*, 16893–16898.

[260] Qiao, B.; Krekeler, C.; Berger, R.; Site, L. D.; Holm, C. *J. Phys. Chem. B* **2008**, *112*, 1743–1751.

[261] Dommert, F.; Schmidt, J.; Qiao, B.; Zhao, Y.; Krekeler, C.; Site, L. D.; Berger, R.; Holm, C. *J. Chem. Phys.* **2008**, *129*, 224501.

[262] Bhargava, B. L.; Balasubramanian, S. *J. Chem. Phys.* **2007**, *127*, 114510.

[263] Köddermann, T.; Paschek, D.; Ludwig, R. *ChemPhysChem* **2007**, *8*, 2464–2470.

[264] Cadena, C.; Zhao, Q.; Snurr, R. Q.; Maginn, E. J. *J. Phys. Chem. B* **2006**, *110*, 2821–2832.

[265] Santos, L.; Lopes, J. N. C.; Coutinho, J. A. P.; Esperança, J. M. S. S.; Gomes, L. R.; Marrucho, I. M.; Rebelo, L. P. N. *J. Am. Chem. Soc.* **2007**, *129*, 284–285.

[266] Pópolo, M. G. D.; Lynden-Bell, R. M.; Kohanoff, J. *J. Phys. Chem. B* **2005**, *109*, 5895–5902.

[267] Bhargava, B.; Balasubramanian, S. *Chem. Phys. Lett.* **2006**, *417*, 486–491.

[268] Hunt, P. A.; Gould, I. R.; Kirchner, B. *Aust. J. Chem.* **2007**, *60*, 9–14.

[269] Lasségues, J. C.; Grondin, J.; Holomb, R.; Johansson, P. *J. Raman Spectrosc.* **2007**, *38*, 551–558.

[270] Bhargava, B. L.; Balasubramanian, S. *J. Phys. Chem. B* **2007**, *111*, 4477–4487.

[271] Bhargava, B. L.; Saharay, M.; Balasubramanian, S. *Bull. Mater. Sci.* **2008**, *31*, 327–334.

[272] Bhargava, B. L.; Balasubramanian, S. *J. Phys. Chem. B* **2008**, *112*, 7566–7573.

[273] Firaha, D. S.; Kirchner, B. *J. Chem. Eng. Data* **2014**, *59*, 3098–3104.

[274] Hollóczki, O.; Kelemen, Z.; Könczöl, L.; Szieberth, D.; Nyulászi, L.; Stark, A.; Kirchner, B. *ChemPhysChem* **2013**, *14*, 315–320.

[275] Brehm, M.; Weber, H.; Pensado, A. S.; Stark, A.; Kirchner, B. *Phys. Chem. Chem. Phys.* **2012**, *14*, 5030–5044.

[276] Kirchner, B.; Hollóczki, O.; Lopes, J. N. C.; Pádua, A. A. H. *WIREs. Comput. Mol. Sci.* **2015**, *5*, 202–214.

[277] Wendler, K.; Dommert, F.; Zhao, Y. Y.; Berger, R.; Holm, C.; Site, L. D. *Faraday Discuss.* **2012**, *154*, 111–132.

[278] Kohanoff, J. *Electronic Structure Calculations for Solids and Molecules: Theory and Computational Methods*; Cambridge University Press, 2006.

[279] Martin, R. M. *Electronic Structure: Basic Theory and Practical Methods (Vol 1)*; Cambridge University Press, 2004.

[280] Capelle, K. *A bird's-eye view of density-functional theory*; cond-mat/0211443, 2002.

[281] Szabó, A.; Ostlund, N. S. *Modern quantum chemistry : introduction to advanced electronic structure theory*; Dover Publications, 1996.

[282] Grimme, S.; Hujo, W.; Kirchner, B. *Phys. Chem. Chem. Phys.* **2012**, *14*, 4875–4883.

[283] Zhao, Y.; Truhlar, D. G. *Theor. Chem. Acc.* **2008**, *120*, 215–241.

[284] Perdew, J. P.; Burke, K.; Ernzerhof, M. *Phys. Rev. Lett.* **1996**, *77*, 3865–3868.

[285] Grimme, S.; Antony, J.; Ehrlich, S.; Krieg, H. *J. Chem. Phys.* **2010**, *132*, 154104.

[286] Allen, M. P.; Tildesley, D. J. *Computer Simulation of Liquids*; Oxford University Press, USA, 1989.

[287] Frenkel, D.; Smit, B. *Understanding Molecular Simulation: From Algorithms to Applications*; Academic Press, Inc., 1996.

[288] Lopes, J. N. C.; Pádua, A. A. H. *Theor. Chem. Acc.* **2012**, *131*, 1–11.

[289] Manz, T. A.; Sholl, D. S. *J. Chem. Theory Comput.* **2010**, *6*, 2455–2468.

[290] Sigfridsson, E.; Ryde, U. *J. Comput. Chem.* **1998**, *19*, 377–395.

[291] Dognon, J.-P.; Durand, S.; Granucci, G.; Lévy, B.; Millié, P.; Rabbe, C. *J. Mol. Struct.* **2000**, *507*, 17–23.

[292] Campañá, C.; Mussard, B.; Woo, T. K. *J. Chem. Theory Comput.* **2009**, *5*, 2866–2878.

[293] Bader, R. F. W.; MacDougall, P. J.; Lau, C. D. H. *J. Am. Chem. Soc.* **1984**, *106*, 1594–1605.

[294] Reed, A. E.; Weinstock, R. B.; Weinhold, F. *J. Chem. Phys.* **1985**, *83*, 735–746.

[295] Manz, T. A.; Sholl, D. S. *J. Chem. Theory Comput.* **2012**, *8*, 2844–2867.

[296] Kosov, D. S.; Popelier, P. L. A. *J. Phys. Chem. A* **2000**, *104*, 7339–7345.

[297] Bultinck, P.; Alsenoy, C. V.; Ayers, P. W.; Carbó-Dorca, R. *J. Chem. Phys.* **2007**, *126*, 144111.

[298] Bultinck, P.; Cooper, D. L.; Dimitri, V. N. *Phys. Chem. Chem. Phys.* **2009**, *11*, 3424–3429.

[299] Marx, D.; Hutter, J. *Ab Initio Molecular Dynamics : Basic Theory and Advanced Methods*; Cambridge University Press, 2009.

[300] Car, R.; Parrinello, M. *Phys. Rev. Lett.* **1985**, *55*, 2471–2474.

[301] VandeVondele, J.; Krack, M.; Mohamed, F.; Parrinello, M.; Chassaing, T.; Hutter, J. *Comput. Phys. Commun.* **2005**, *167*, 103–128.

[302] Pringle, J. M. *Phys. Chem. Chem. Phys.* **2013**, *15*, 1339–1351.

[303] Luo, J.; Conrad, O.; Vankelecom, I. F. J. *J. Mater. Chem. A* **2013**, *1*, 2238–2247.

[304] Darve, E.; Rodríguez-Gómez, D.; Pohorille, A. *J. Chem. Phys.* **2008**, *128*, 144120.

[305] Laio, A.; Gervasio, F. L. *Rep. Prog. Phys.* **2008**, *71*, 126601–126623.

[306] Plimpton, S. *J. Comput. Phys.* **1995**, *117*, 1–19.

[307] Hutter, J.; Iannuzzi, M.; Schiffmann, F.; VandeVondele, J. *Wiley Interdiscip. Rev. Comput. Mol. Sci.* **2014**, *4*, 15–25.

[308] Hutter, J.; Ballone, J. P.; Bernasconi, M.; Focher, P.; Fois, E.; Goedecker, S.; Marx, D.; Parrinello, M.; Tuckerman, M. E. CPMD Version 3.13.2. Max Planck Institut fuer Festkoerperforschung and IBM Zurich Research Laboratory: Stuttgart, Germany, and Zurich, 1990.

[309] Frisch, M. J. et al. Gaussian 09 Revision D.01. Gaussian Inc. Wallingford CT **2009**.

[310] Humphrey, W.; Dalke, A.; Schulten, K. *J. Mol. Graphics* **1996**, *14*, 33–38.

[311] Macrae, C. F.; Edgington, P. R.; McCabe, P.; Pidcock, E.; Shields, G. P.; Taylor, R.; Towler, M.; van de Streek, J. *J. Appl. Crystallogr.* **2006**, *39*, 453–457.

[312] Jmol: an open-source Java viewer for chemical structures in 3D. http://www.jmol.org/.

Chapter 2A

Refinement of Molecular Force Field for Imidazolium-Based Room Temperature Ionic Liquids

2A.1 Introduction

Molecular simulation methods have been widely used to obtain atomic-level understanding of room temperature ionic liquids. These include *ab initio* molecular dynamics (AIMD), [1–9] molecular dynamics (MD) simulations using polarizable force fields [10–14] and those employing non-polarizable, empirical potentials. [15–20] While AIMD simulations can possibly provide an accurate picture of cation-anion hydrogen bonding and anion polarization, they are computationally expensive. They can also suffer from inadequate representation of dispersive interactions. Force fields which include terms that include ion polarizations do offer an improvement over those with fixed charges; however, they too can be computationally demanding and are not available for a wide class of compounds.

Nonpolarizable force fields for several ILs based on the imidazolium, pyridinium, and phosphonium cations were developed by Lopes, Padua and co-workers using the OPLS-AA and AMBER framework. [21–24] In a similar approach, Wang and co-workers developed a force field for a few ILs based on the imidazolium cation. [25] Other force fields developed for ILs are a few united atom models, [26, 27] the OPLS-AA model, [28] coarse grained

models [29–31] etc. While many of them reproduce well the density and to a large extent the intermolecular structure, their ability to quantitatively reproduce surface tension and transport quantities such as the diffusion coefficient, has been a matter of discussion. [32–38]. Ludwig *et al.* [32] developed a force field for $[\mathrm{C_nMIM}][\mathrm{NTf_2}]$ which describes the thermodynamic and transport properties reasonably well, in particular for ILs with short alkyl tails. [39]

Properties of ILs such as their low vapor pressure, ionic conductivity, shear viscosity etc. are largely determined by the electrostatic interactions between the ions. Charge transfer and polarization of ionic species determine their effective charges in bulk ILs. Thus, one observes a net decrease in the effective charges on ions in bulk liquids, [10, 40, 41] in good agreement with recent photoelectron spectroscopy experiments of Licence and co-workers. [42, 43] Atomic charges used in many force fields have mostly been derived from quantum chemical calculations of an ion or an ion pair studied in gas phase. The charges calculated thus do not capture these condensed phase effects and their use often leads to overbinding of ions in bulk. Such an approach was also found to diminish values of diffusion coefficients of ions in the liquid phase, relative to experimentally determined values. [14, 17, 25, 44–47]

Voth and co-workers introduced polarizable force fields for ILs to capture the effect of electronic polarizability in condensed phases of ILs, [14] which resulted in a much faster diffusion of ions compared with the nonpolarizable model. Borodin and co-workers have contributed significantly to the development of both polarizable and nonpolarizable force fields for several ILs whose prediction of properties are in quantitative agreement with experiments. [12, 47–50] A simpler (mean field level) treatment of charge transfer and polarizability within a nonpolarizable force field model is to scale the overall atomic charges and allowing for ion charges to deviate from values of $\pm$1e. The dynamics in the liquid consequently is speeded up due to the lower electrostatic binding and this procedure has been implemented for ionic liquids by several groups. [37, 40, 41] However, the scale factors used so far have been empirical in nature.

Kossmann *et al.* [51] have employed second-order Møller-Plesset perturbation theory (MP2) and density functional theory (DFT) techniques to study clusters of [MMIM][Cl] and obtained a reduced charge for the chloride ion of -0.823e. An *ab initio* molecular dynamics simulation of liquid [MMIM][Cl] followed by a Mulliken population analysis of snapshots performed by Bühl *et al.*, [2] also yielded a reduced charge for the chloride anion to be between -0.7 and -0.8e. More recently, Delle Site and co-workers developed a protocol to calculate atomic partial charges to account for bulk phase charge transfer and polarization. [52–54] They have carried out a liquid phase AIMD simulation and used the Blöchl [55] method to calculate site charges for snapshots selected from the CPMD

trajectory.

Starting from CL&P parameters as an initial guess along with the atomic charges calculated using the Blöchl method, Holm *et al.* refined the force field for [MMIM][Cl]. [56] The density of the simulated liquid reproduced the experimental value reasonably well. At low temperature, the calculated ionic conductivity overestimated the experimental value, but the deviation from experiment vanishes in the high temperature region. Very recently Holm *et al.* described a design of transferable force field for [MMIM], [EMIM] and [BMIM] cations with a combination of thiocyanate [SCN], chloride [Cl] and dicyanamide [DCA] as anions. [57] A similar refinement procedure as before was adopted. However, the density of simulated liquid [EMIM][DCA] was less than the experimental value by about 5% which was attributed to an artifact of reduced net charge. The ionic conductivity too was underestimated by 50%.

Although attractive, this approach requires a AIMD simulation of the liquid to be performed which is forbidding due to the computational cost. In a recent work, Zhang and Maginn proposed a novel idea to calculate atomic site charges for an IL from its crystalline phase. [58] They fitted a periodic electrostatic potential for crystalline 1-*n*-butyl-3-methylimidazolium hexafluorophosphate ([BMIM][PF_6]) and 1-ethyl-3-methylimidazolium hexafluorophosphate ([EMIM][PF_6]) and derived atom charges from it. Using these charges within the General AMBER force field (GAFF) framework, they concluded that charges calculated from crystalline phases are better in reproducing the dynamics of ILs than those obtained using the Blöchl method or that from scaling the unit charges calculated from gas phase quantum chemical calculation of one ion pair.

The local coordination shell of a cation in an ionic liquid shares much commonality with its crystalline counterpart. One should thus be able to exploit this aspect and generalize the approach delineated by Zhang and Maginn [58] for other ionic liquids. In the present Chapter, we present a direct and systematic method to derive atomic charges for imidazolium based room temperature ionic liquids. Motivated by the work of Zhang and Maginn, we come up with a consistent set of site charges for cations and anions in six different ionic liquids by studying their crystalline counterparts using density functional theory. We have employed the density-derived electrostatic and chemical (DDEC/c3) charge partitioning method [59, 60] to calculate atomic charges of ions. The DDEC/c3 method has been proven earlier to be very accurate to calculate charges for periodic systems. It has been used to calculate charges for various porous and non-porous periodic systems such as, metal organic framework, zeolites etc. [61, 62] In the present Chapter, dihedral and non-bonded interaction parameters have been refined taking into consideration the revised charges. This procedure is shown to reproduce the experimental density, heat of vaporization, surface tension, ion diffusion coefficients, viscosity, and electrical conductivity for several ionic

liquids in nearly a quantitative fashion. In this Chapter 2A, the charges are derived from DFT calculations of the crystalline phase of ionic liquids. The case of deriving charges from the liquid state itself (in cases where the crystal structure is not available), is discussed in Chapter 2B.

2A.2 Methodology and Simulation Details

The force field developed by Lopes, Padua and co-workers (CL&P) [21–24] covers a wide range of ILs and it reproduces static properties reliably [36] and is thus widely used. However, transport properties such as diffusion coefficient (and thus electrical conductivity) appears to be underpredicted by this model. [32, 36–38] Thus, we have chosen the CL&P force field as an initial framework for our refinement procedure. The bond and angle parameters of CL&P have been retained; however, the partial charges on the atoms have been derived using the DDEC/c3 method as applied to electron density of either crystals (whose experimentally determined structures are known) or liquids. The electron density itself was obtained using DFT calculations. The proposed set of partial charges would have an effect on the short-range (SR) interactions and thus the non-bonded potential parameters too need to be refitted. Revision of the charges and non-bonded parameters demands a revision of dihedral parameters as the two are related through 1-4 interactions which are present in the CL&P force field.

2A.2.1 Derivation of Atomic Charges

1-alkyl-3-methylimidazolium based ionic liquids containing six different anions were considered for calculation of site charges. These were hexafluorophosphate (PF_6), tetrafluoroborate (BF_4), bis(trifluoromethylsulfonyl)imide (NTf_2), chloride (Cl), nitrate (NO_3) and trifluoromethane sulfonate or triflate (CF_3SO_3). For each anion, three ILs with different lengths of pendant alkyl tails ranging from methyl to butyl were chosen for the calculations.

The nomenclature used to describe sites on the imidazolium ring is shown in Figure 2A.1.

Crystalline Phase Charges: Atomic charges were calculated from crystalline phases of ILs wherever experimental crystal structures are available. Initial cell parameters and atomic positions were taken from Cambridge crystal structure database. [63–65] The size of the simulation cell considered for all the crystals was $1\times1\times1$. A description of all the systems studied here is provided in Table 2A.1.

DFT calculations were carried out using CP2K software. [66] All valence electrons were treated with triple-ζ double-polarized basis and a density cutoff of 280 Ry was used. Exchange and correlation effects were considered through the Perdew, Burke and Ernzerhof (PBE) functional. [67] Geodecker-Teter-Hutter (GTH) pseudopotentials [68]

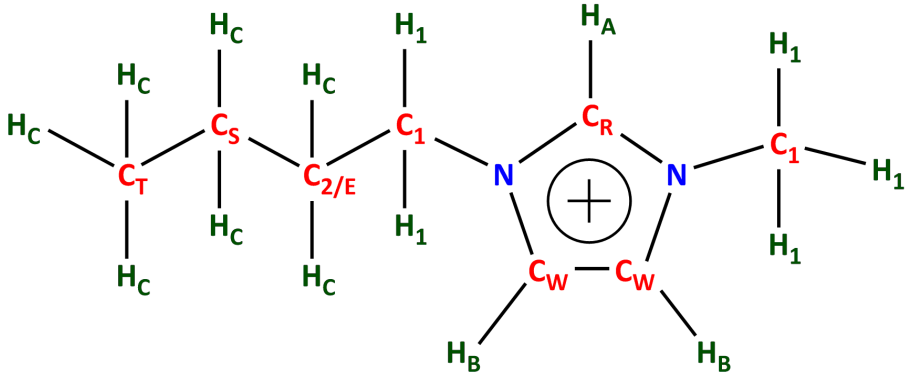

Figure 2A.1: Atom labeling in imidazolium ring.

were used to consider the effect of core electrons and nuclei. Neither the coordinates nor the cell parameters were optimized. The wave functions were optimized with a convergence criterion of 10^{-7} on its gradient. Cube files of valence electron density were saved. DDEC charges were computed with the codes available at http://ddec.sourceforge.net as described by Manz and Sholl using the DDEC/c3 method. [59, 60] We have tried to calculate atomic charges using some other methods also, such as the Blöchl, [55] REPEAT [69] and RESP. [70] However, charges obtained through these methods were not always consistent across different IL compounds and thus were discarded.

Table 2A.1: Summary of the cell parameters and supercell dimension of all the crystalline systems studied.

System	Cell parameter						Reference
	a (Å)	b (Å)	c (Å)	$\alpha(^o)$	$\beta\ (^o)$	$\gamma\ (^o)$	
[MMIM][Cl]	8.652	7.858	10.539	90.0	106.3	90.0	Ref. [71]
[BMIM][Cl]	10.113	11.411	8.328	90.0	90.0	90.0	Ref. [72]
[MMIM][PF_6]	11.254	9.361	17.986	90.0	90.0	90.0	Ref. [73]
[EMIM][PF_6]	8.627	9.035	13.469	90.0	101.9	90.0	Ref. [74]
[BMIM][PF_6]	8.755	8.904	9.013	95.8	114.9	103.1	Ref. [75]
[EMIM][CF_3SO_3]	10.183	12.384	18.294	90.0	90.0	90.0	Ref. [76]
[BMIM][CF_3SO_3]	10.222	12.534	22.541	90.0	93.3	90.0	Ref. [77]
[EMIM][BF_4]	8.762	9.396	11.425	90.0	98.7	90.0	Ref. [77]
[EMIM][NO_3]	4.540	14.810	13.445	90.0	95.7	90.0	Ref. [78]
[MMIM][NTf_2]	8.535	12.681	13.502	88.1	80.2	79.8	Ref. [79]
[EMIM][NTf_2]	18.499	8.626	19.255	90.0	90.0	90.0	Ref. [76]

Charges Derived from Liquid Phase: In order to check the transferability of the charges derived from a crystal and its corresponding liquid, simulations of the liquid phase was also carried out with the following protocol. A number of snapshots were chosen from a classical molecular dynamics (MD) simulation of an IL, carried out primarily using the CL&P force field. Liquid [BMIM][BF_4] alone was modelled using the Wang force field. [25] These configurations were then taken into DFT framework. The basis set, density cutoff and pseudopotentials used were the same as mentioned previously. For each of these configurations, the gradient of the electronic wave functions and the force on the nuclei were optimized with convergence criteria of 10^{-7} and 10^{-3}, respectively. Using these quenched configurations, atomic charges were calculated following the same procedure as described earlier for crystal systems. The charges thus obtained were averaged over all ions and configurations. A full description of these systems are provided in Table 2A.2.

Table 2A.2: Summary of all the liquid systems studied for calculating atomic charges.

System	Number of ion pairs
[MMIM][BF_4]	38
[MMIM][NO_3]	45
[EMIM][Cl]	40
[BMIM][BF_4]	28
[BMIM][NO_3]	30
[BMIM][NTf_2]	18

The force field developed by Lopes and co-workers [21–24] was employed and MD simulations were carried out using the LAMMPS [80] software. Furthermore, since the interaction cutoff has to be less than half box length, we have used a pairwise cutoff distance of 10 Å in these classical MD simulations. Initial positions of all atoms were generated by placing the molecules randomly in a box of length 20 Å. Equations of motion were integrated with the velocity Verlet algorithm with a time step of 1 fs. All C-H covalent bonds were constrained using the SHAKE algorithm as implemented in LAMMPS software. [80] Long range electrostatic interactions were computed using the particle-particle particle-mesh (PPPM) solver with a precision of 10^{-5}. As prescribed in the force field, a multiplication factor of 0.5 was used to scale down the non-bonded interactions calculated for pair of atoms which were separated by three bonds. The parameters for cross interactions between different molecular species (atomic groups) were derived using standard Lorentz-Berthelot rules. Cubic periodic boundary conditions were applied.

Constant-pressure and constant-temperature ensemble (NPT) simulations were carried out until the volume converged. Temperature and pressure of the system were maintained at 300 K and 1 atm using Nosé-Hoover thermostat and barostat, respectively, with a damping

factor of 1 ps. [81–83] The densities of the systems compared well against experimental data. The final coordinates of the NPT run were taken to the constant-volume and constant-temperature (NVT) ensemble for a further equilibration for 5 ns under constant NVT conditions. Finally, an analysis run was generated for 10 ns. Configurations at every 1 ns were selected for coarse geometry optimization within DFT (as described earlier) and further for the calculation of atomic charges using the DDEC/c3 method.

2A.2.2 Optimization of Short-Range Interactions

The accurate representation of short-range (SR) interactions is quite important in reproducing intermolecular structure accurately which can have a bearing even on long time dynamics. [84] Here, the SR interactions between the particle types i and j are described through the standard 12-6 LJ potential with σ and ϵ as parameters.

Given that the site charges as well as the total ion charges are changed from values associated with the CL&P force field, one needs to adjust the parameters of both the non-bonded and dihedral interaction terms. Towards this purpose, we have carried out quantum chemical calculations of six different ion pairs in gas phase with [BMIM] as a common cation. For each anion, these calculations involved three potential energy scan runs in each of which the cation-anion distance was varied along a certain direction. Such potential energy surfaces (PES) were taken as references against which those obtained using the refined force field were benchmarked. Non-bonded parameters (typically of sites in the anion) were refined so as to reproduce the PES of the quantum calculation. The latter were carried out using Gaussian09, [85] for which the initial structures were constructed using GaussView. [86] These reference calculations were calculated at M06/aug-cc-pVDZ level of theory whose binding energy was within 2 kcal/mol of that obtained through MP2/aug-cc-pVDZ level of theory. In the scan runs, the cation was held fixed while the anions were displaced along the (I) $C_R - H_A$ vector, (II) $C_W - H_B$ vector (closer to the methyl) and (III) perpendicular to the center of the imidazolium ring as illustrated in Figure 2A.2.

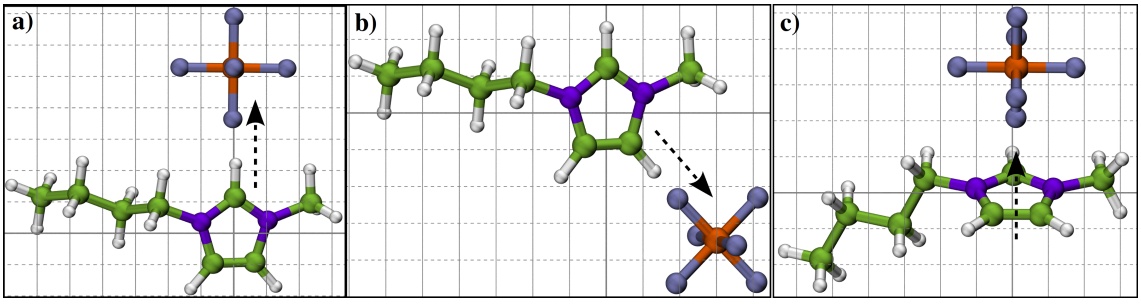

Figure 2A.2: Directions along which the cation-anion distance was varied, shown here for [BMIM][PF_6]: (a) along the $C_R - H_A$ bond; (b) along the $C_W - H_B$ bond; (c) perpendicular to the imidazolium ring plane. Color scheme: nitrogen, violet; carbon, green; hydrogen, white; phosphorus, orange; and fluorine, iceblue.

Scan runs with the same coordinates as used in the quantum run were initiated to obtain the PES from the empirical force field. These were carried out using LAMMPS. [80] In these gas phase scan runs alone, CL&P force field parameters were used to model the IL pairs with a unit ion charge value and with site charges as per CL&P. As these scan runs were conducted in gas phase, the ions can be expected to be unaffected by polarization which is present in the condensed phase. Thus, the original site charges of CL&P were used. The box length was set to 200 Å in these calculations and the interaction sphere of a site included all other sites irrespective of distance. Non-bonded interaction parameters were iterated manually until the surfaces obtained from the force field best matched those from the quantum runs. To achieve this, the LJ parameters of the three hydrogen atoms directly attached to imidazolium ring (H_A and H_B) as well as of the sites on the anions were tuned. Parameters involving other atom types in the cation were unaltered from their CL&P values.

The first ion pair to be studied was [BMIM][PF_6] and the procedure described above was followed. However, while refining the LJ parameters of other anions, the cation parameters were left unchanged and those of the sites on the anion alone were refined. Thus, in the refined force field, the LJ parameters of the cation are independent of cation tail length or of the anion type. The LJ parameters of the anion are independent of the cation tail length too. In Figure 2A.3 we show results of scan runs performed in case of [BMIM][PF_6]. In all the three directions, the potential well obtained from the CL&P model was seen to be marginally shallower and to be present at slightly larger distances relative to the quantum result. By refining the parameters, the location of the minimum in all the three scan runs for a given anion was obtained within 0.05 Å of the M06/aug-cc-pVDZ result. The difference in the well depth between the quantum data and that of the refined force field was within 2.5 kcal/mol, for all the IL systems studied here. The tuned LJ potentials are provided in Table 2A.3.

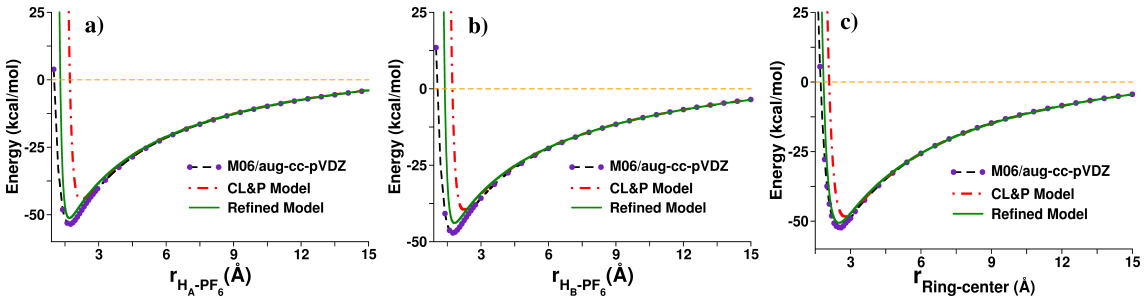

Figure 2A.3: Potential energy as a function of distance between cation site and anion from quantum calculation (M06/aug-cc-pVDZ), the CL&P model [22, 23] and from our refined model for [BMIM][PF_6]. The three directions are described Figure 2A.2.

Table 2A.3: Lennard-Jones parameters for 1-alkyl-3-methylimidazolium cation and selected anions according to the refined model. Atoms separated by three covalent bonds interact via 1-4 interactions with the following scale factors: 0.5 for Lennard-Jones and zero for Coulomb.

Atom	ε (kJ mol^{-1})	σ (Å)
N	0.71128	3.25
C_R	0.29288	3.55
C_W	0.29288	3.55
H_A	0.04184	1.70
H_B	0.12552	2.00
C_1	0.27614	3.50
H_1	0.12552	2.50
C_2/C_E	0.27614	3.50
H_C	0.12552	2.50
C_S	0.27614	3.50
C_T	0.27614	3.50
P ([PF_6])	0.83680	3.74
F ([PF_6])	0.17152	2.75
B ([BF_4])	0.25104	3.68
F ([BF_4])	0.08368	2.80
N ([NO_3])	0.33800	3.06
O ([NO_3])	0.56816	2.70
S ([CF_3SO_3])	0.75312	3.55
O ([CF_3SO_3])	0.41840	2.80
C ([CF_3SO_3])	0.15062	3.50
F ([CF_3SO_3])	0.17991	2.95
N ([NTf_2])	0.41840	3.25
S ([NTf_2])	0.54392	3.55
O ([NTf_2])	1.04600	2.96
C ([NTf_2])	0.10878	3.50
F ([NTf_2])	0.09623	2.95
Cl ([Cl])	1.25452	3.30

2A.2.3 Dihedral Interactions

The 1-4 term (12-6 LJ and Coulomb with a scale factor) acts between atoms separated by three covalent bonds. Since the non-bonded interaction parameters have been altered, the 1-4 energy will also be changed. The effect of reparametrization of non-bonded interactions

needs to be reflected in the 1-4 interactions as well which will affect the dihedral energy too. Hence, the dihedral potential needs to be reparametrized. In this process, we found it convenient (within LAMMPS) to employ the multi-harmonic function to describe the dihedral potential, expressed as,

$$\mathrm{E}^{\mathrm{MH}}_{\mathrm{dihedral}} = \sum_{n=1}^{5} A_n cos^{n-1}(\phi) \tag{2A.1}$$

The dihedral interaction parameters A_n were refitted in a manner so as to reproduce the dihedral profile obtained from quantum chemical calculations. For the latter, we adopt the dihedral potential profile of the CL&P model. The procedure we follow is identical to that described in Ref. [56] The potential energy between sites 1 and 4 defined according to CL&P can be split as, [56]

$$\mathrm{E}^{\mathrm{CL\&P}} = \mathrm{E}^{\mathrm{CL\&P}}_{1-4,\mathrm{LJ}} + \mathrm{E}^{\mathrm{CL\&P}}_{1-4,\mathrm{Coulomb}} + \mathrm{E}^{\mathrm{CL\&P}}_{\mathrm{dihedral}} \tag{2A.2}$$

Coulombic and LJ contributions to the 1-4 interactions in the CL&P model are scaled by a factor of 0.5. In our model, we employ this factor for 1-4 LJ interactions while that for 1-4 Coulomb interactions is zero (i.e., 1-4 pairs do not interact via Coulomb forces). This procedure aids in introducing better transferability to the force field. Note that the total 1-4 interaction energy in our force field for ions in gas phase is the same as that of the CL&P (Eq. 2A.2). The dihedral energies in our refined model, E^{MH} can be obtained from

$$\mathrm{E}^{\mathrm{refined}} = \mathrm{E}^{\mathrm{refined}}_{1-4,\mathrm{LJ}} + \mathrm{E}^{\mathrm{MH}}_{\mathrm{dihedral}} = \mathrm{E}^{\mathrm{CL\&P}} \tag{2A.3}$$

We demand that $\mathrm{E}^{\mathrm{refined}}$ be the same as $\mathrm{E}^{\mathrm{CL\&P}}$. Thus,

$$\mathrm{E}^{\mathrm{refined}}_{1-4,\mathrm{LJ}} + \mathrm{E}^{\mathrm{MH}}_{\mathrm{dihedral}} = \mathrm{E}^{\mathrm{CL\&P}}_{1-4,\mathrm{LJ}} + \mathrm{E}^{\mathrm{CL\&P}}_{1-4,\mathrm{Coulomb}} + \mathrm{E}^{\mathrm{CL\&P}}_{\mathrm{dihedral}} \tag{2A.4}$$

and

$$\mathrm{E}^{\mathrm{MH}}_{\mathrm{dihedral}} = \mathrm{E}^{\mathrm{CL\&P}}_{1-4,\mathrm{LJ}} + \mathrm{E}^{\mathrm{CL\&P}}_{1-4,\mathrm{Coulomb}} + \mathrm{E}^{\mathrm{CL\&P}}_{\mathrm{dihedral}} - \mathrm{E}^{\mathrm{refined}}_{1-4,\mathrm{LJ}} \tag{2A.5}$$

In order to obtain the dihedral interaction parameters A_n, we have calculated the energies of every type of dihedral angle. Later $\mathrm{E}^{\mathrm{MH}}_{\mathrm{dihedral}}$ was fitted to Equation 2A.5. In this procedure, the positions of the first and last atoms of all the dihedral angles were stored with a step size of 5° over the range -180° to +180°. OPLS potential was used to calculate $\mathrm{E}^{\mathrm{CL\&P}}_{\mathrm{dihedral}}$. The OPLS potential parameters for all the dihedral angles were taken from the CL&P model. At each step, $\mathrm{E}^{\mathrm{MH}}_{\mathrm{dihedral}}$ energy was calculated. The multi-harmonic dihedral potential for two dihedral types, e.g. $\mathrm{N}-\mathrm{C_R}-\mathrm{N}-\mathrm{C_1}$ and $\mathrm{C_R}-\mathrm{N}-\mathrm{C_1}-\mathrm{C_2}$ are shown in Figure 2A.4(a) and 2A.4(b), respectively, for purposes of illustration. From

the first two plots, we can see that $E^{CL\&P}_{dihedral}$ and $E^{MH}_{dihedral}$ energies are different. The E_{1-4} energies for those two dihedrals were also found to be different by about a few kcal/mol. Hence, it is evident that the reparametrization of short-range interactions does affect the dihedral potentials. Hence, it is important to adapt the dihedral potentials such that it would reproduce the dihedral energies obtained from quantum chemical calculations.

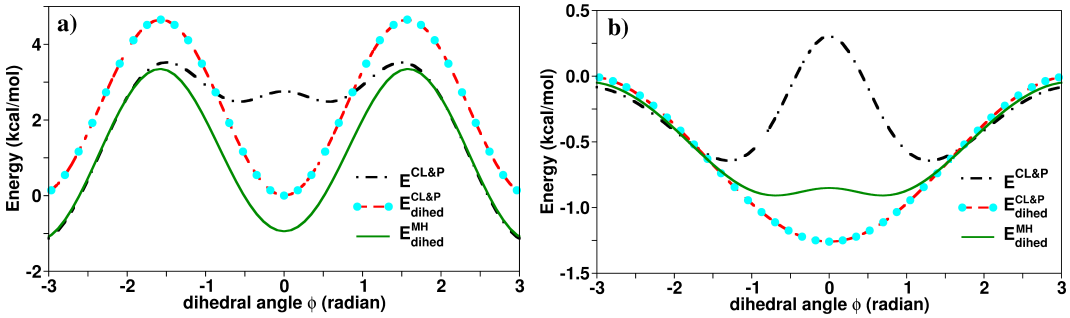

Figure 2A.4: Energy profiles of the dihedral interaction for (a) $N - C_R - N - C_1$ and (b) $C_R - N - C_1 - C_2$. Black (dash-dotted) line, $E^{CL\&P}$ is the reference energy between 1 and 4 sites. The green solid line is $E^{MH}_{dihedral}$ derived using Eq. 2A.5.

As discussed earlier, the LJ potential parameters for sites on the cation are independent of the IL that they constitute. Hence, in this dihedral refitting method, the set of LJ parameters used to calculate $E^{refined}_{1-4,LJ}$ are also the same for any IL. As $E^{refined}_{1-4,Coulomb}$ is chosen to be zero, the dihedral potential parameters for the cation too are independent of the specific IL. This characteristic imbues a general and transferable nature to the refined force field. Dihedral potentials for polyatomic anions containing dihedral angles, such as, bis(trifluoromethylsulfonyl)imide (NTf_2) or triflate (CF_3SO_3), were also refined in a similar fashion. The dihedral interaction potentials for different types of dihedral angles are tabulated in Table 2A.4.

2A.2.4 Molecular Dynamics Simulations

The refined set of force field parameters were used to model various ILs. Following the CL&P convention, real space cutoff distances were defined at 11, 12 and 13 Å for the [EMIM], [BMIM] and [HMIM] salts, respectively. All systems were simulated at 300 K except [BMIM][Cl], which was studied at 353 K. Each IL was studied with 512 ion pairs. Initial atomic coordinates were set up using Packmol software. [87] The systems were equilibrated in the NPT ensemble for 10 ns. This was followed by production runs lasting 25 ns, generated in the NVT ensemble. All other simulation protocols were the same as used in the simulation of liquid phases of ILs for charge calculation. All the systems are visualized using Mercury [88] and VMD. [89]

The crystalline phase of two ionic liquids, [BMIM][PF_6] and [BMIM][Cl] were also simulated using the refined set of force field parameters. Initial cell parameters and atom

Table 2A.4: Proper dihedral parameters in Multi/harmonic form according to the refined model: $E^{MH}_{dihedral} = \sum_{n=1}^{5} A_n cos^{n-1}(\phi)$. Improper dihedral parameters are the same as in the CL&P model. [22, 23] C^* represents a generic aliphatic carbon, C_1, C_2, C_E, C_S or C_T. H^* represents either H_1 or H_C.

	A/kJ mol^{-1}				
Dihedrals	A_1	A_2	A_3	A_4	A_5
$N-C_R-N-C_W$	14.7099	-0.95885	-19.7501	-0.11816	-0.04368
$N-C_R-N-C_1$	13.7712	-0.89994	-19.6735	-0.06280	-0.01782
$N-C_W-C_W-N$	50.4243	1.14629	-44.6186	0.15686	0.06079
$N-C_W-C_W-H_B$	52.7715	1.33905	-44.6014	3.97756	3.62251
$N-C_1-C_2-H_C$	2.27225	-0.21912	0.08213	0.75320	0.00109
$N-C_1-C_2-C_S$	-4.97220	-2.63207	-3.35502	-2.47295	-0.02335
$C_R-N-C_1-H_1$	-3.21080	-0.23108	0.08841	0.15008	0.08769
$C_R-N-C_1-C_2$	-2.86520	-2.66755	-0.00707	-0.00184	-0.00046
$C_R-N-C_W-C_W$	16.0210	0.69856	-12.3393	0.08548	0.03146
$C_R-N-C_W-H_B$	7.12874	-0.35581	-12.2003	0.74643	0.49777
$C_W-N-C_R-H_A$	13.0390	-0.40932	-19.0264	0.87567	0.57367
$C_W-C_W-N-C_1$	17.3763	0.74241	-12.3787	0.04866	0.01339
$C_W-N-C_1-H_1$	-3.53060	-1.10516	0.05991	1.17817	0.08523
$C_W-N-C_1-C_2$	2.66194	-4.80344	-6.11366	1.58603	-0.00042
$H_B-C_W-N-C_1$	4.77081	-0.77312	-12.6223	0.02983	0.02272
$H_B-C_W-C_W-H_B$	55.1903	0.74542	-44.8956	0.01226	0.00218
$H_A-C_R-N-C_1$	11.6353	-0.77517	-19.5152	0.05171	0.03464
$C^*-C^*-C^*-H^*$	-1.80660	-2.29693	0.00000	3.06260	0.00000
$C^*-C^*-C^*-C^*$	11.2836	1.88903	0.65689	2.33459	0.00000
$H^*-C^*-C^*-H^*$	1.59553	-1.86226	0.02908	2.66964	0.00197
			[CF_3SO_3]		
$O-S-C-F$	20.9362	1.17315	0.889769	3.46649	0.324511
			[NTf_2]		
$N-S-C-F$	21.8644	1.56059	0.96483	3.29636	0.38304
$S-N-S-C$	76.4973	33.7603	14.4047	-2.45383	2.57709
$S-N-S-O$	-109.112	-18.3380	-4.46968	-0.77684	0.13012
$O-S-C-F$	17.7697	0.66526	0.73270	3.25009	0.16869

positions were taken from the experimentally determined crystal structures. [72, 75] The size of the simulation cell considered for [BMIM][PF_6] and [BMIM][Cl] crystals was 4×4×4 and 3×3×4 respectively, consisting of 4096 and 3744 atoms. Classical MD

simulations were carried out in the fully flexible, isothermal-isobaric (NPT) ensemble at 173 and 200 K, respectively using the LAMMPS [80] package. The ewald/n solver was used to calculate the long-range interactions with a precision of 10^{-5}. All other simulation protocols were the same as used in the simulation of liquid phases of ILs. The systems were equilibrated in the NPT ensemble for 3 ns and this was followed by production runs lasting 5 ns. Details of simulated cell parameters and their comparison with experiment are provided in Table 2A.5. The crystal structures were found to be stable in the simulations employing the refined force field.

Table 2A.5: Simulated cell parameters using the refined force field and compared against the experimental data. Uncertainty in simulated values were of the order of 0.002.

System	Method	a (Å)	b (Å)	c (Å)	α (^{o})	β (^{o})	γ (^{o})	ρ (g/cm^3)
[BMIM][PF_6]	exp.	8.755	8.904	9.013	95.810	114.955	103.061	1.56
	sim.	8.714	8.862	8.971	95.809	114.954	103.061	1.57
[BMIM][Cl]	exp.	10.113	11.411	8.328	90.000	90.000	90.000	1.21
	sim.	10.169	11.474	8.375	89.999	89.999	89.999	1.19

Surface tension was calculated using a simulation of the liquid-vapor interface. A pre-equilibrated configuration of the bulk liquid containing 512 molecules in the NVT ensemble was taken. The length of the simulation box along the z-axis was increased to 120 Å to generate two liquid-vapor interfaces. A 10 ns trajectory was generated and the pressure tensor of the system was stored at every time step. The surface tension γ was calculated from the diagonal components of the pressure tensor P_{ii} using Equation 2A.6 at 300 K ([BMIM][Cl] at 353 K).

$$\gamma = \frac{l_z}{4}(2P_{zz} - P_{xx} - P_{yy}) \tag{2A.6}$$

where l_z is the length of simulation box in the direction parallel to the interface normal, here the z- axis.

Shear viscosity was calculated through the equilibrium Green-Kubo relation using the full stress (pressure) tensor, [90]

$$\eta(t) = \frac{V}{10k_BT}\int_0^t \langle Tr[\tilde{\mathbf{P}}(t'')\tilde{\mathbf{P}}(t'+t'')]\rangle dt' \tag{2A.7}$$

where V is the volume of the simulation cell and $\tilde{\mathbf{P}}$ is the symmetric, traceless part of the pressure tensor. Angular brackets denote averaging over t''. Eq. 2A.7 uses all the elements of the pressure tensor and has been found to be more accurate providing a better statistics over the one which uses only the off-diagonal elements [91] or other non-equilibrium methods. [92]

The long time value of the integral in Eq. 2A.7 yields the shear viscosity, η. The integrand is the stress-stress time correlation function, $C_P(t)$. This autocorrelation function decays rapidly at short times but can exhibit a rather slow decay, thus making the convergence of its integral a tedious one. It is a well known fact that ionic liquids exhibit sluggish dynamic behavior [93], and therefore it is very important to integrate the long time behavior accurately to obtain a reliable value of viscosity. Pressure tensor at every time step was stored from nine independent MD runs each of length 8 ns. The stress-stress autocorrelation function was calculated from the block average of these runs from which the shear viscosity was obtained.

The zero-frequency electrical conductivity, σ was computed using the time integral of electric-current autocorrelation function defined as [94, 95]

$$\sigma = \frac{1}{3k_BTV}\int_0^\infty \langle \mathbf{j}(t)\cdot\mathbf{j}(0)\rangle dt = \frac{1}{3k_BTV}\int_0^\infty J(t)dt, \tag{2A.8}$$

where $\mathbf{j}(t)$ is the electric-current function,

$$\mathbf{j}(t) = \sum_{i=1}^{N} q_i \mathbf{v}_i(t) \tag{2A.9}$$

and q_i and $\mathbf{v}_i(t)$ represent the charge and velocity of atom i at time t. N is the total number of atoms in the system. The electric-current autocorrelation function, $J(t)$ can be expressed as [96]

$$\begin{aligned} J(t) &= \left\langle \sum_{i=1}^{N}\sum_{j=1}^{N} q_i q_j \mathbf{v}_i(t)\cdot\mathbf{v}_j(0)\right\rangle \\ &= \left\langle \sum_{i=1}^{N_c}\sum_{j=1}^{N_c} q_i q_j \mathbf{v}_i(t)\cdot\mathbf{v}_j(0)\right\rangle + \left\langle \sum_{i=1}^{N_a}\sum_{j=1}^{N_a} q_i q_j \mathbf{v}_i(t)\cdot\mathbf{v}_j(0)\right\rangle + \left\langle 2\sum_{i=1}^{N_a}\sum_{j=1}^{N_c} q_i q_j \mathbf{v}_i(t)\cdot\mathbf{v}_j(0)\right\rangle \\ &= J_{++}(t) + J_{--}(t) + 2J_{+-}(t) \end{aligned} \tag{2A.10}$$

where, N_c and N_a are the number of atoms belonging to all cations and anions respectively and $N = N_c + N_a$. The electric current autocorrelation function can thus be expressed as the sum of three terms: J_{++} is the cation electric current autocorrelation function, J_{--} is the anion electric current autocorrelation function and J_{+-} is the cation-anion electric current cross correlation function.

Atom velocities were stored at every time step from nine independent MD runs each of length of 2 ns. The electric-current autocorrelation function was calculated from each run and these were averaged. The integral of stress time correlation function required

longer duration to converge than what is required for the integral of the electric current time correlation function.

Ionic conductivity can also be calculated using the Nernst-Einstein relation, [95]

$$\sigma_{NE} = \frac{N_i q^2}{V k_B T}(D^+ + D^-) \tag{2A.11}$$

where V is the volume, temperature is T, the number of ion pairs is N_i, q is the effective net charge of the ions and k_B is the Boltzmann constant.

The cross correlation function in Eq. 2A.10 is thus the deviation from ideal Nernst-Einstein behavior (independent ion motion) and provides a measure of ion pairing in the liquids.

2A.3 Results and Discussion

2A.3.1 Atomic Charges

Charges calculated either from the crystal or the corresponding liquid show a decrease in the total ion charge from unity, which accounts for the polarization and charge transfer effects in the bulk environment, as shown in Figure 2A.5. The net ion charge varies from a value of $\pm$ 0.64e for the chloride to one of $\pm$ 0.79e for [BF_4].

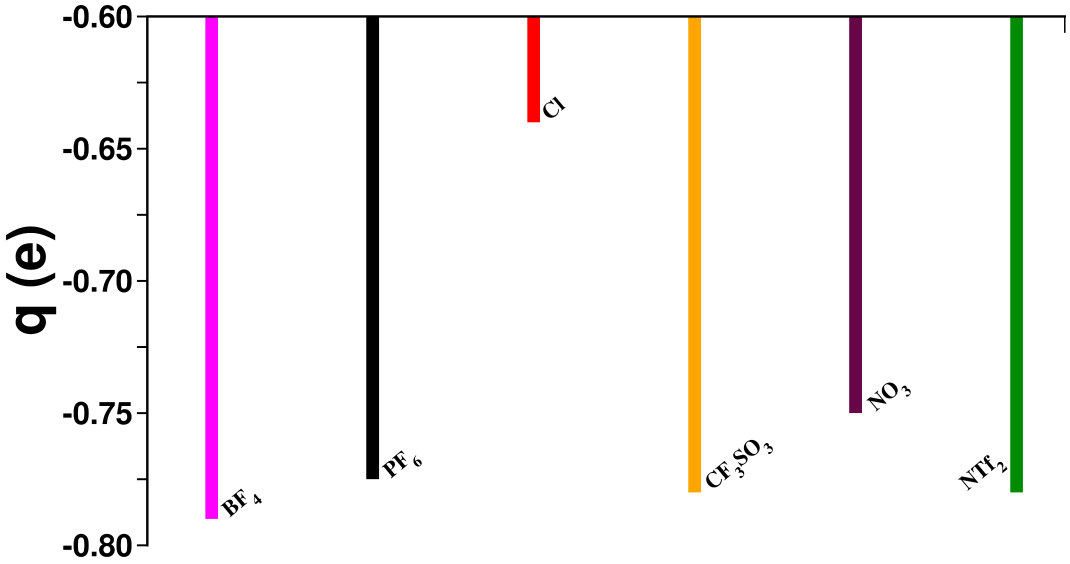

Figure 2A.5: Ion charges of anions [BF_4], [PF_6], [Cl], [CF_3SO_3], [NO_3], and [NTf_2] in imidazolium based ILs obtained from their crystalline state.

An interesting observation in the atomic charge distribution as well as in the total ion charges was noticed. Total ion charges calculated from the three crystalline compounds containing the same anion, [MMIM][PF_6], [EMIM][PF_6] and [BMIM][PF_6] ILs were nearly identical. In this specific instance, these were found to be $\pm$ 0.78, $\pm$ 0.77 and $\pm$

0.78e, respectively. Similar behaviour was observed in the atomic site charges for these ILs as well. Furthermore, atoms related to each other by crystal symmetry carried the same charge. In fact, this criterion was one of the vital ones which persuaded us to use the DDEC/c3 method over the ESP or Blöchl methods. Furthermore, nitrogen atoms present in the imidazolium ring of the above three ILs possess nearly the same charge values. Also, site charges on the cation were found to be comparable in ILs containing different anion types. The largest difference was for sites present on the imidazolium ring. In addition, it was observed that the charges of methyl or methylene groups lying beyond the second carbon atom (C_2) on the alkyl tail were quite small. In the liquid phase, the charges on specific atoms in an IL too showed a spread of around 0.04e around respective mean values.

A comparison of the atomic charges obtained from the crystal and liquid phases was enlightening. As mentioned earlier, liquid phase atomic charges were calculated using a number of snapshots generated from classical MD simulation, which were subsequently optimized for their geometries (albeit to a coarse extent) within DFT. The ion charge distribution in the liquid phase of [BMIM][BF_4] and [BMIM][NO_3] are shown in Figure 2A.6a and Figure 2A.6b, respectively. The ion charge from the crystal compares very well with the mean of the distribution from the liquid phase. Furthermore, the average charge values on every atomic site was found to be very close to atomic charges of the crystalline phase. Thus, for salts whose crystal structures have not been determined, one can employ this procedure to obtain the atomic site charges from the corresponding liquid. It is much less expensive than performing a full fledged AIMD simulation.

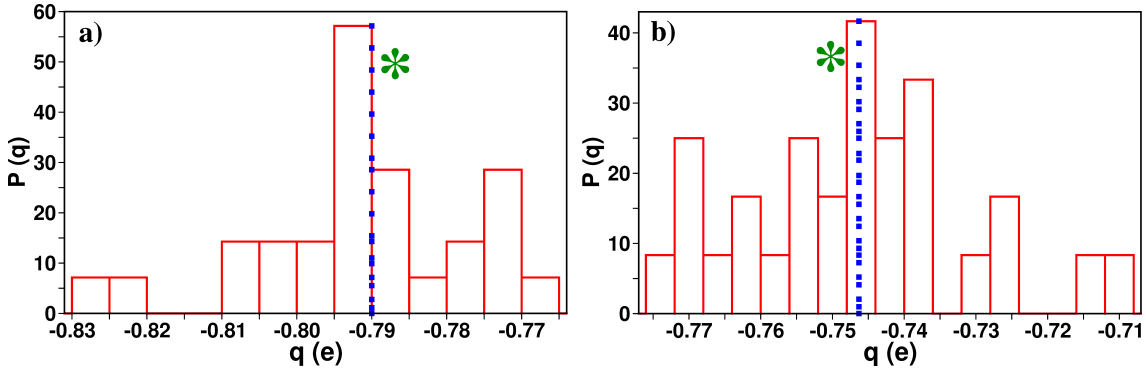

Figure 2A.6: Distribution of ion charges calculated from snapshots of a MD simulation trajectory of liquid phase of (a) [BMIM][BF_4] and (b) [BMIM][NO_3]. The thin blue line is the mean of this distribution while the star is the charge value in the crystalline phase.

Our aim was to employ the same atom typing scheme of CL&P. In order to achieve a force field that is transferable across ILs, a few practical solutions were adopted. The site charges on the cation were revised keeping their total charges unchanged. Firstly, for a particular type of anion, the total ion charges were taken to be the mean of ion charges of ILs containing this specific anion but with varying alkyl tail length on the imidazolium cation.

Table 2A.6: Atomic site charges for the cation according to the refined model.

Atom type	Charge (e)					
	$[PF_6]$	$[BF_4]$	$[NO_3]$	$[CF_3SO_3]$	[Cl]	$[NTf_2]$
N	0.145	0.140	0.145	0.145	0.130	0.145
C_R	-0.005	-0.010	-0.005	-0.030	-0.010	-0.005
C_W	-0.110	-0.110	-0.120	-0.110	-0.130	-0.120
H_A	0.170	0.180	0.165	0.180	0.150	0.175
H_B	0.160	0.170	0.160	0.170	0.140	0.170
C_1	-0.250	-0.250	-0.250	-0.250	-0.250	-0.250
H_1	0.120	0.120	0.120	0.120	0.120	0.120
C_2	-0.076	-0.076	-0.076	-0.076	-0.076	-0.076
C_E	-0.174	-0.174	-0.174	-0.174	-0.174	-0.174
H_C	0.098	0.098	0.098	0.098	0.098	0.098
C_S	-0.196	-0.196	-0.196	-0.196	-0.196	-0.196
C_T	-0.294	-0.294	-0.294	-0.294	-0.294	-0.294

Site charges of all different atom types were also averaged over in this fashion. Given that the total charge on the anions depended on their type, the charge on the imidazolium cation too would depend on the specific IL that it is present in. It is also desirable that the charges on the methylene group present beyond two bonds from the nitrogen of the ring are neutral; this will enable the use of same atom types as that of CL&P. In an IL, the anions are located closer to the imidazolium ring than to the alkyl group of the cation. Thus, the total charge of methyl as well as methylene groups which are located beyond the $C_{2/E}$ carbon atom were changed to zero from the values calculated using DDEC/c3 method. The difference in the charges was distributed equally over all the sites on the imidazolium ring.

This procedure of a marginal reassignment of charges provides the advantage of having the same charge distribution within the alkyl part of the cation across all the ILs, independent of the anion type. Thus, the only difference in cation site charges in different ILs lies in the atoms of the imidazolium ring. Charges obtained through the DDEC/c3 method as applied to crystals as well as those recommended by us after reassignment for the sake of transferability are provided in Table 2A.6 and Table 2A.7. These charges together with the non-bonded parameters provided in Table 2A.3, constitute our refined force field.

In summary, the site charges on the imidazolium cation depend on the specific anion type that is present in the ionic liquid, as it would in a polarizable force field. However, the non-bonded, 1-4, and torsional parameters of the cation are independent of the anion type present in the IL.

Table 2A.7: Atomic site charges for the anion according to the refined model.

Atom	Charge (e)
P ([PF_6])	1.589
F ([PF_6])	-0.394
B ([BF_4])	1.010
F ([BF_4])	-0.450
N ([NO_3])	0.780
O ([NO_3])	-0.510
S ([CF_3SO_3])	1.090
O ([CF_3SO_3])	-0.600
C ([CF_3SO_3])	0.440
F ([CF_3SO_3])	-0.170
N ([NTf_2])	-0.740
S ([NTf_2])	1.090
O ([NTf_2])	-0.545
C ([NTf_2])	0.445
F ([NTf_2])	-0.155
Cl ([Cl])	-0.640

2A.3.2 Density

The liquid phase of seven IL systems were simulated using these refined set of partial charges combined with tuned LJ parameters and refitted dihedral interaction potentials. All of them were studied at 300 K, except for [BMIM][Cl] which was studied at 353 K due to its higher melting point.

Table 2A.8: Liquid phase densities (g/cm^3) of ILs obtained from simulations using the refined force field compared with experimental data at 300 K. [97–100] †The temperature is 348 K. Uncertainty in the simulated density is around 0.002 g/cm^3.

System	ρ_{exp}	ρ_{sim}	$\Delta\rho(\%)$
[BMIM][BF_4]	1.202	1.206	+0.33
[BMIM][PF_6]	1.368	1.388	+1.31
[HMIM][PF_6]	1.293	1.310	+1.31
[BMIM][NO_3]	1.154	1.164	+0.86
[BMIM][CF_3SO_3]	1.298	1.317	+1.45
[BMIM][NTf_2]	1.437	1.446	+0.62
[BMIM][Cl]†	1.050	1.038	-1.14

The computed densities are within 2% of experimental results (see Table 2A.8) and are compared in Figure 2A.7a. The CL&P model has been documented to reproduce liquid phase density well. [36] However, an earlier attempt to employ partial charges (obtained from the crystalline phase) for liquid [BMIM][PF_6] and [EMIM][PF_6] [58] yielded differences in density of around 6%. This example shows the importance of refining the non-bonded and torsional interaction parameters along with the site charges.

2A.3.3 Heat of Vaporization

Vaporization enthalpy is an important physical property which is a signature of the strength of intermolecular interactions. The strong electrostatic interaction between the ions is a major reason for the higher heat of vaporization of ILs relative to those of molecular liquids. Heats of vaporization (ΔH_{vap}) can be computed from simulations using the following equation 2A.12.

$$\Delta H_{vap} = \Delta H_{gas} - \Delta H_{liquid} = E_{total}^{gas} - E_{total}^{liquid} + RT \qquad (2A.12)$$

E_{total}^{gas} is the average potential energy for an ion pair in the gas phase while E_{total}^{liquid} is the corresponding value in the liquid phase. The vaporization enthalpy was computed for all these IL systems parameterised by the refined force field and the results are summarized in Table 2A.9. It is very difficult to compare the computed and experimental heats of vaporization values as the values reported using different experimental techniques differ from each other significantly. [101, 102] It is evident that the values obtained from simulations show satisfactory agreement with experimental results. Experimental ΔH_{vap} value for [BMIM][Cl] are not available, but our estimates compare well with the value of 29.1 kcal/mol obtained by simulations earlier. [28]

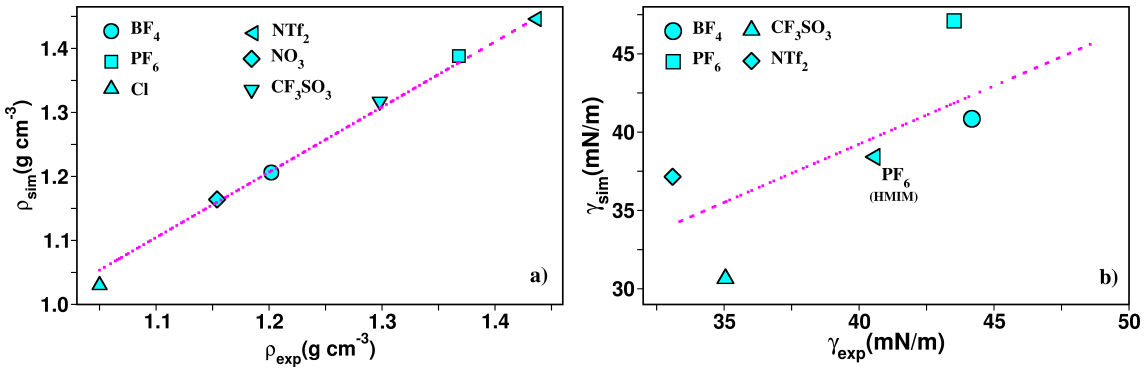

Figure 2A.7: Scatter plot for the comparison of (a) density and (b) surface tension of ILs between experiment and simulations. The common cation is [BMIM]. The dashed line is the target.

Table 2A.9: Heat of vaporization (kcal/mol) at 300 K of ILs obtained from simulations compared against experimental data at 298 K. [103–107] †The temperature is 353 K. Estimated standard error on the mean in the simulated heat of vaporization is around 0.02 kcal/mol.

System	ΔH_{vap}^{exp}	ΔH_{vap}^{sim}	$\Delta\Delta H_{vap}(\%)$	$\Delta H_{vap}^{Lit.}$
[BMIM][BF_4]	33.78	31.90	-5.56	27.8 [28], 33.6 [108]
[BMIM][PF_6]	37.00	33.00	-10.81	31.9 [28], 35.9 [108]
[HMIM][PF_6]	33.41	34.70	+3.86	40.1 [28]
[BMIM][NO_3]	37.52	33.57	-10.52	36.2 [108]
[BMIM][CF_3SO_3]	33.22	32.94	-0.84	31.1 [28], 34.1 [108]
[BMIM][NTf_2]	32.17	31.23	-2.92	31.9 [108]
[BMIM][Cl]†	—	28.02	—	29.1 [28]

2A.3.4 Surface Tension

The calculated values of surface tension are compared against experimental data in Table 2A.10 and the agreement is quite reasonable (see Figure 2A.7b).

Table 2A.10: Surface tension (mN/m) of ILs at 300 K calculated using the refined force field compared with experimental results. [109] † The temperature is 353 K. Uncertainty in the calculated surface tension is around 0.06 mN/m.

System	γ_{exp}	γ_{sim}	$\Delta\gamma$ (%)
[BMIM][BF_4]	44.18±0.02	40.85	-7.5
[BMIM][PF_6]	43.52±0.04	47.10	8.2
[HMIM][PF_6]	38.35±0.02	40.21	4.5
[BMIM][NO_3]	—	51.20	—
[BMIM][CF_3SO_3]	35.05±0.03	31.65	-4.2
[BMIM][NTf_2]	33.09±0.02	36.15	9.1
[BMIM][Cl]†	—	39.52	—

2A.3.5 Radial Distribution Functions

Radial distribution functions (RDFs) of anion around cation and of anion around the acidic proton (H_A) were obtained from the refined model and a few of them are shown in Figure 2A.8. For all the ILs, the cation-anion RDFs show a well structured first peak, and a shoulder between 5 and 7 Å. Such features have been observed and discussed in earlier simulations. [25, 37] These effects are due to charge ordering [110] and van der Waals interactions and are observed up to a distance of 20 Å. In earlier reports, it was found that the anion prefers to locate itself around the acidic hydrogen (H_A), rather than near H_B or H

sites present in the methyl (H_1) or alkyl group (H_C). [25] Moreover, such an arrangement leads to the formation of a hydrogen bond between the acidic hydrogen and the anion. The anion-(H_A) RDF obtained from the refined model is able to well reproduce this important feature. The RDF of (H_A)-Cl in [BMIM][Cl] shows the highest peak amongst all ILs and [BF_4] anion was found to have interact strongly with (H_A) than [PF_6] or [NO_3] does. These observations are in good agreement with earlier results. [25, 111]

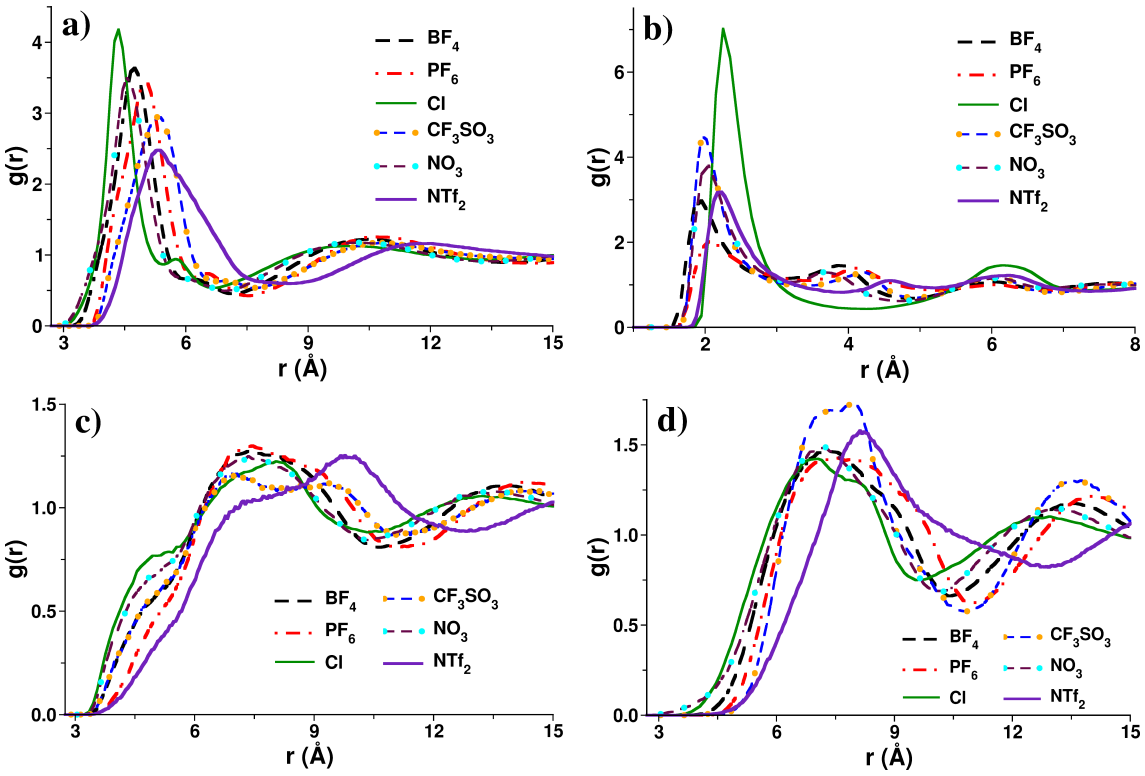

Figure 2A.8: Radial distribution functions for (a) cation-anion, (b) H_A-anion, (c) cation-cation, and (d) anion-anion for ILs obtained using the refined model.

2A.3.6 Spatial Distribution Functions

Spatial distribution functions (SDFs) were used for further characterization of intermolecular structure in the liquid. The spatial density map of anion around the cation center of mass are shown in Figure 2A.9.

Anions have three preferred binding sites around the cation. These are positioned around the three ring hydrogens – one H_A and two H_B atoms. Among these three, the most preferred one is the former. Anions are also present above and below the ring plane. Between the two H_B atoms, anions favour the methyl side rather than the butyl (alkyl) side, as the conformational flexibility of the latter can cause steric hindrance to the anion.

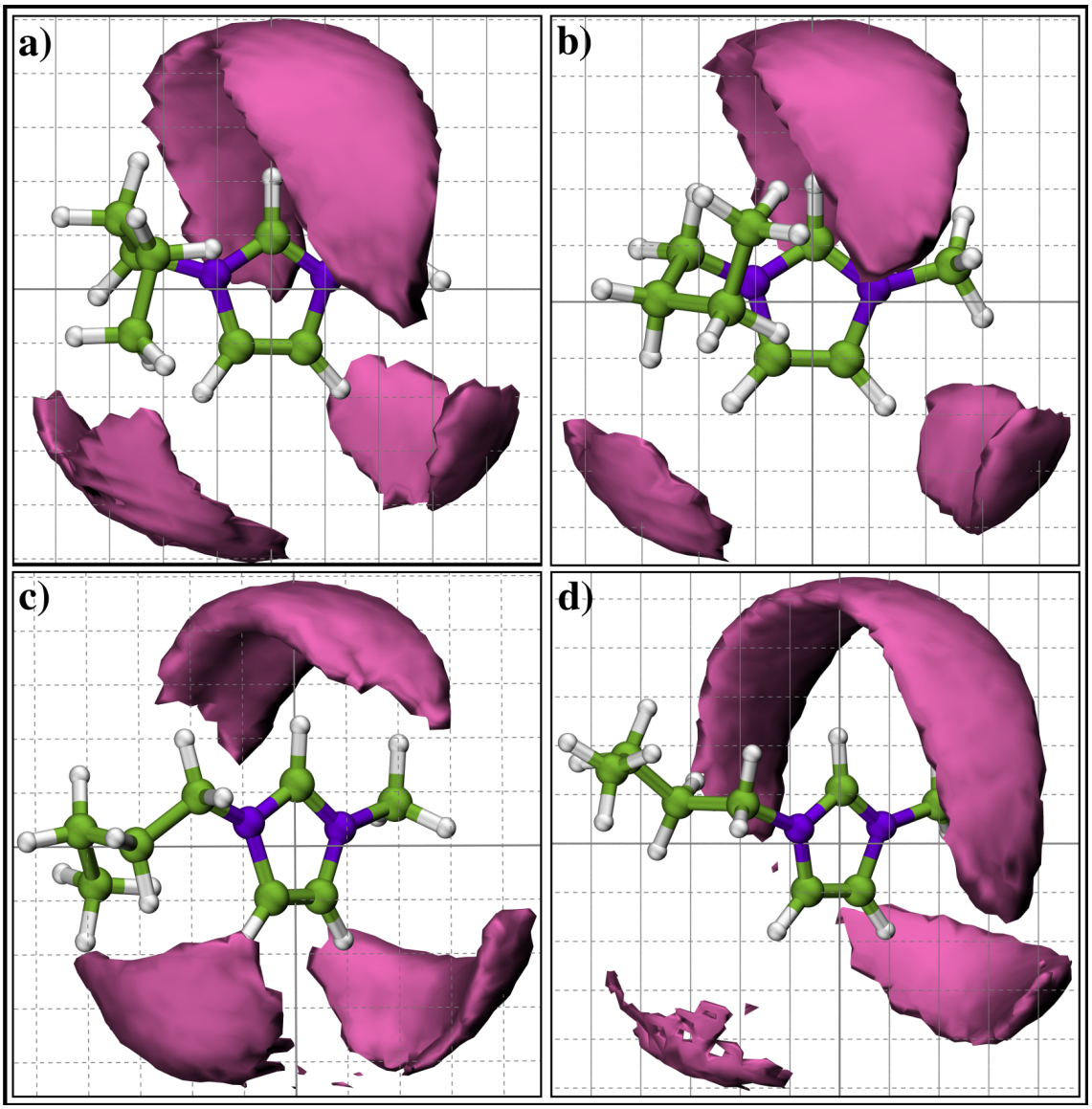

Figure 2A.9: Spatial distribution function of anions around the cation at an isosurface value of 0.021 $Å^{-3}$: (a) [BMIM][BF_4]; (b) [BMIM][NO_3]; (c) [BMIM][Cl]; (d) [BMIM][PF_6]. Color scheme: nitrogen, violet; carbon, green; hydrogen, white.

2A.3.7 Mean Square Displacement and Self-Diffusion Coefficients

Transport properties of ILs were determined from a calculation of mean square displacement (MSD) of the center of mass of ions. MSD was calculated for the ILs at 300 K (except for [BMIM][Cl] at 353 K) on the basis of a 25 ns NVT trajectory and are shown in Figure 2A.10a. Consistent with experiments [112, 113] and many simulations, [37, 41, 114] the cations diffuse faster than anions.

In order to check whether the system is in the diffusive regime, we have calculated the

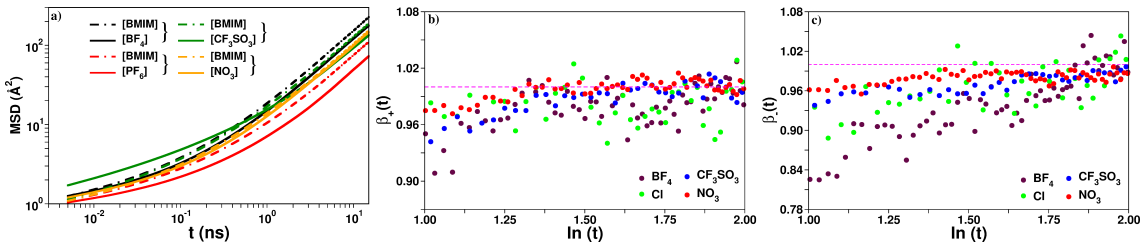

Figure 2A.10: Computed (a) center of mass MSD, $\beta(t)$ values for (b) cation, and (c) anion for different ionic liquids at 300 K.

Table 2A.11: Time window over which the slope of MSD was calculated and obtained self-diffusion coefficients ($\times 10^{-7}$cm^{2}s^{-1}) of ions in various ILs at 300 K using the refined force field compared against experimental values reported at 303 K. [100] †The temperature is 353 K. Uncertainty in the calculated values is around 0.02×10^{-7}cm^{2}s^{-1}.

System	Time (ns)		D_+		ΔD_+ (%)	D_-		ΔD_- (%)
	cation	anion	exp.	sim.		exp.	sim.	
[BMIM][BF_4]	2.2-16.1	2.5-15.8	1.80	2.30	27.7	1.70	1.83	7.6
[BMIM][PF_6]	4.9-14.9	4.1-9.9	0.89	1.05	17.9	0.71	0.74	4.2
[HMIM][PF_6]	5.8-20.1	7.4-20.1	—	0.54	—	—	0.47	—
[BMIM][NO_3]	3.3-13.5	4.3-12.2	—	1.65	—	—	1.51	—
[BMIM][CF_3SO_3]	4.2-13.5	5.8-15.6	2.10	2.08	-0.95	1.60	1.41	-11.8
[BMIM][NTf_2]	5.8-9.9	6.7-16.4	3.40	2.70	-20.5	2.60	2.10	-19.2
[BMIM][Cl]†	4.1-12.2	5.5-11.1	—	14.1	—	—	17.3	—

exponent $\beta(t)$, defined as

$$\beta(t) = \frac{dln\langle \Delta r^2(t)\rangle}{dln(t)} \tag{2A.13}$$

where $\Delta r^2(t)$ is the mean square displacement at time t. $\beta(t) < 1$ implies that the dynamics of the system is subdiffusive, while $\beta(t) = 1$ implies diffusive motion. $\beta(t)$ values for each ion type were computed as a function of time and these are shown in Figure 2A.10b,c. The self-diffusion coefficients were obtained from the slope of the MSD data for the ions in the diffusive regime. The time window over which the slope was calculated for each system are provided in Table 2A.11. The calculated values of self-diffusion coefficients are given in Table 2A.11. The values reported here shows a significant increase in the ion dynamics over the CL&P force field and are within 20% of experimental results in many systems.

2A.3.8 Viscosity

The initial decay of the normalized stress-stress time correlation function (TCF) $C_P(t)$ for [BMIM][PF_6] and [BMIM][BF_4] are shown in Figure 2A.11. The decay of this TCF is characterized by rapid, high amplitude oscillations followed by a slow decay. The

oscillations can be inferred as due to the high-frequency intramolecular vibrational modes of the cations. The timescales involved in the relaxation of stress of these systems are evident from the slow decaying nature of $C_P(t)$.

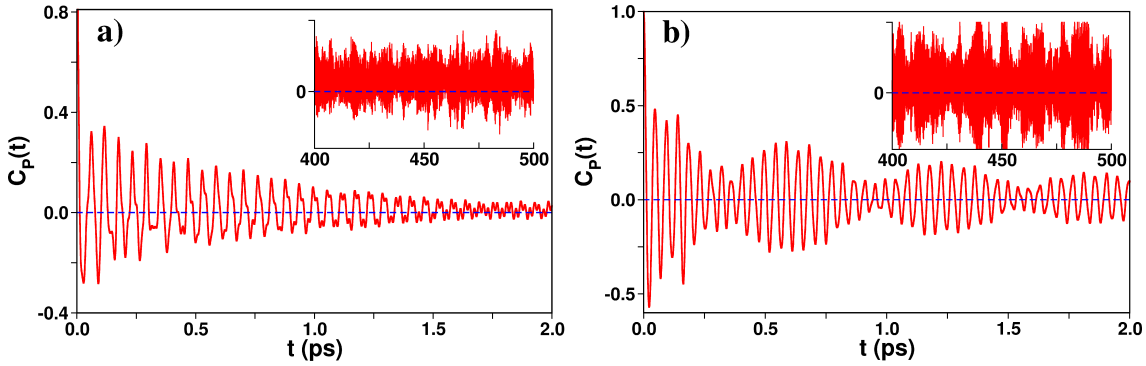

Figure 2A.11: Normalized full stress tensor autocorrelation functions for (a) [BMIM][PF_6] and (b) [BMIM][BF_4] at 300 K. The inset shows the same quantities between 400 and 500 ps.

The running integral of the stress correlation function whose converged value corresponds to shear viscosity is plotted for different ionic liquids at 300 K in Figure 2A.12. The values of shear viscosities for all these systems are tabulated in Table 2A.12 and are compared against experimental results. The observed trend in the simulated viscosities is η[BMIM][PF_6] > η[BMIM][NO_3] > η[BMIM][BF_4] > η[BMIM][CF_3SO_3] > η[BMIM][NTf_2]. Results from simulation are in good agreement with experiment and follow the same trend. [115] Gardas and Coutinho [116] proposed that ILs with highly symmetric, nearly spherical anions are more viscous. In the family of imidazolium based ILs, viscosity increases with anion in the order [NTf_2] < [CF_3SO_3] < [BF_4] < [PF_6] which trend is reproduced by our simulations. This ranking for different anions can be attributed to both the strength of hydrogen bonding interactions between cation and anion as well as to their electrostatic interaction. Anions in which the negative charge is more delocalized in space exhibit weaker interactions with the cation [117] and consequently could reduce the viscosity of the IL. Ludwig and co-workers [118] as well as Hunt [119] have discussed that hydrogen bonding between cation-anion increases the fluidity of the liquid.

2A.3.9 Electrical Conductivity

Electrical conductivity at 300 K was computed from both the Green-Kubo relation, Eq. 2A.8 and the Nernst-Einstein relation, Eq. 2A.11 and are provided in Table 2A.13. The influence of size, shape and mass of the anions on the computed electrical conductivities can be observed (see Table 2A.13). Two opposing effects of anions operate in the determination of electrical conductivity. Anions which are larger in size have smaller charge density and consequently exhibit higher mobility. On the other hand, transport of larger anions

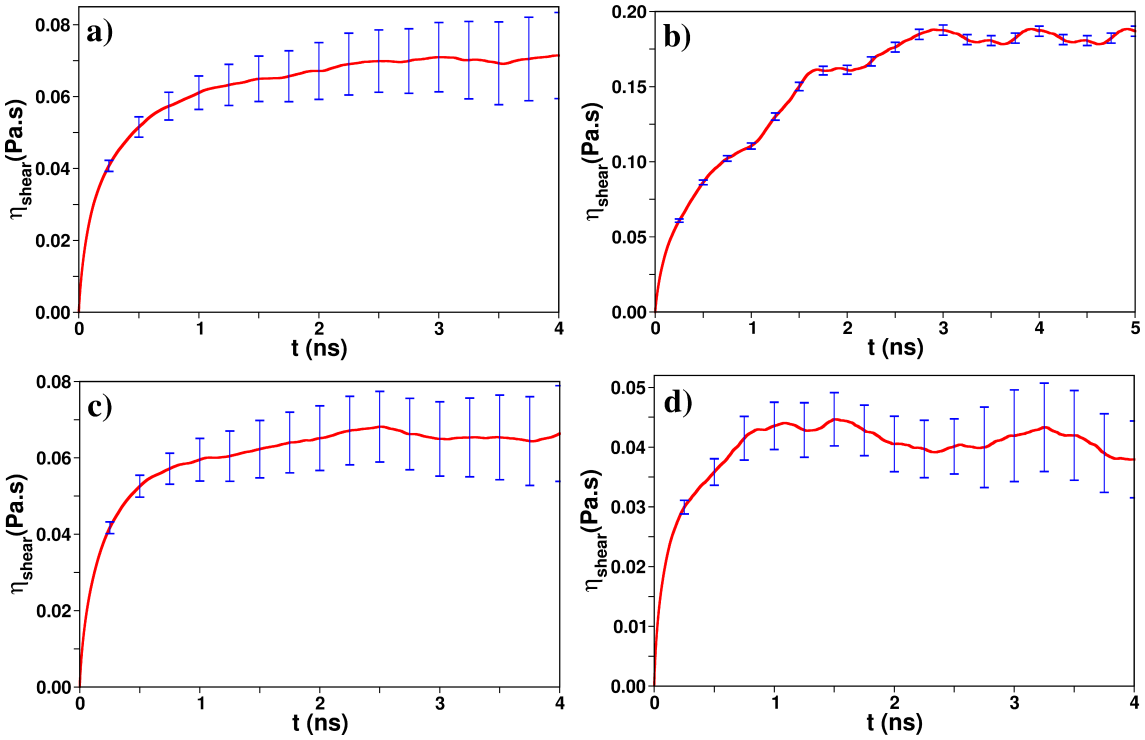

Figure 2A.12: Running integral (see Eq. 2A.7) representing the shear viscosities of (a) [BMIM][BF_4], (b) [BMIM][PF_6], (c) [BMIM][CF_3SO_3], and (d) [BMIM][NTf_2] from nine independent trajectories at 300 K. The bars are standard error on the mean.

Table 2A.12: Shear viscosity (mPa.s) of ILs obtained from simulation (η_{sim}) compared against experimental data (η_{exp}) at 303 K. [100, 120] Estimated standard error on the mean in η_{sim} is around 5 mPa.s. Values determined from other experimental (303 K) and simulation (298 K) reports are also provided.

System	η_{exp}	η_{sim}	$\Delta\eta(\%)$	Literature data	
				exp.	sim.
[BMIM][PF_6]	182.4	185	1.2	209.1 [121],209.2 [122]	181.8 [123]
[BMIM][NO_3]	123.5	129	4.2	144.1 [99]	135.4 [123]
[BMIM][BF_4]	75.3	71	-5.4	75.4 [121],73.42, [124]	98 [125]
[BMIM][CF_3SO_3]	65.4	65	-0.3	63.19 [126],64.2 [99]	90 [12]
[BMIM][NTf_2]	40.0	42	3.7	40.6 [121],40.64 [127]	65.1 [128]

is not facile because of their large size, which in turn decreases the electrical conductivity. [129] The observed trend in the calculated electrical conductivity is: σ[BMIM][BF_4] $>$ σ[BMIM][NO_3] $>$ σ[BMIM][NTf_2] $>$ σ[BMIM][CF_3SO_3] $>$ σ[BMIM][PF_6]. From these simulated values, one can see that the conductivity of [BMIM][BF_4] does not follow the experimentally obtained conductivity order. [112] But, for other three ionic liquids, it follows the same, e.g. this trend is partially supported by the experimental observations of

Rivera and co-workers: σ[BMIM][NTf_2] > σ[BMIM][CF_3SO_3] > σ[BMIM][PF_6]. [130] Among the ILs studied in this work, the one with the [BF_4] anion shows the highest electrical conductivity. Table 2A.13 lists conductivities reported in the literature determined through experiments. Reported conductivity values do show variations among themselves (as the temperature at which the experimental measurements were carried out are also different); however, to compare with our simulation results, we have chosen the results obtained by Tokuda *et al.*, [100] as their work also reports some other physical properties (e.g. density, viscosity, etc.) of these ILs which are consistent with previously reported values.

Table 2A.13: Electrical conductivity (S.m^{-1}) of ILs at 300 K obtained from simulation (σ_{GK}) compared against experimental (σ_{exp}) data at 303 K. [100] Estimated standard error on the mean in the simulated value is around 0.05 S.m^{-1}. Literature data are at 298 K. [a]303 K.

System	σ_{exp}	σ_{GK}	σ_{NE}	σ_{GK}/σ_{NE}	$\Delta\sigma$(%)	Literature data	
						exp.	sim.
[BMIM][BF_4]	0.45	0.42	0.51	0.82	-6.6	0.35 [131],0.36 [132]	0.28 [12]
[BMIM][NTf_2]	0.46	0.29	0.38	0.76	-36.9	0.45 [133],0.39 [134]	0.42 [12]
[BMIM][CF_3SO_3]	0.36	0.25	0.36	0.69	-30.5	0.23 [135][a],0.29 [136]	0.20 [12]
[BMIM][PF_6]	0.19	0.17	0.19	0.89	-10.5	0.15 [133],0.15 [131]	0.08 [12]
[BMIM][NO_3]	—	0.31	0.39	0.79	—	—	0.07 [12]

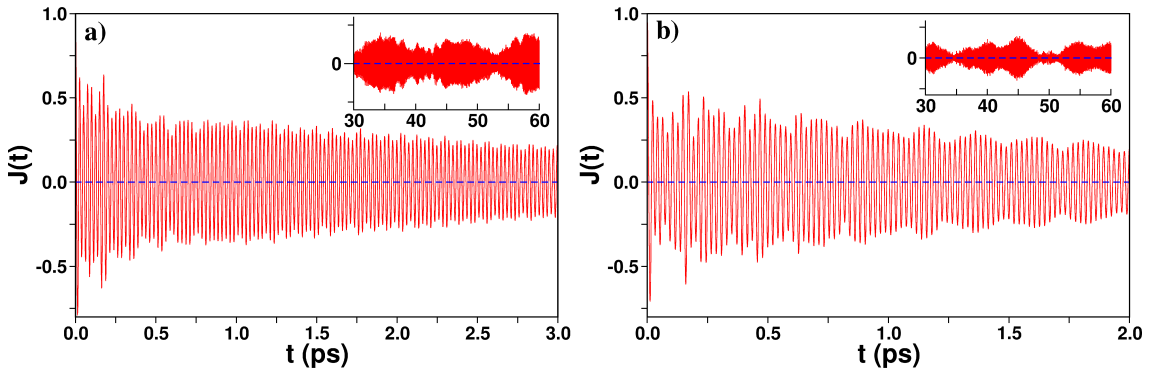

Figure 2A.13: Normalized electric-current autocorrelation functions of (a) [BMIM][PF_6] and (b) [BMIM][BF_4]. Inset shows the magnified region of these autocorrelation functions between 30 and 60 ps.

In Figure 2A.13, we provide the electric-current autocorrelation functions for [BMIM][PF_6] and [BMIM][BF_4]. The running integral of electric-current autocorrelation functions for ILs are provided in Figure 2A.14.

The calculated electrical conductivity values from Green-Kubo relation shows the same

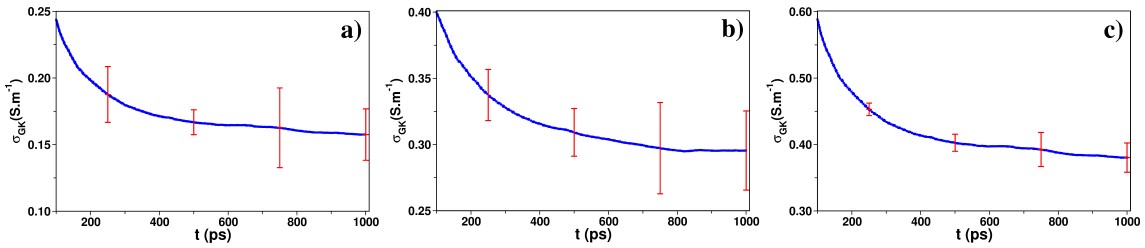

Figure 2A.14: Running integral representing electrical conductivity of (a) [BMIM][PF_6], (b) [BMIM][NO_3], and (c) [BMIM][BF_4]. The bars are standard error on the mean.

trend as observed from Nernst-Einstein conductivities. Values obtained from the Green-Kubo relation are lower than the Nernst-Einstein conductivity, as the latter method assumes uncorrelated motion of the ions (say, formation of neutral ion clusters) in the liquids. The ratio of σ_{GK} to σ_{NE} gives a measure of correlated ion motion in ILs. In our study, it follows the trend: σ[BMIM][PF_6] $>$ σ[BMIM][BF_4] $>$ σ[BMIM][NO_3] $>$ σ[BMIM][NTf_2] $>$ σ[BMIM][CF_3SO_3]. For [BMIM][PF_6], the ion-pair association between cation and anion is the least, whereas for σ[BMIM][CF_3SO_3], it is the most.

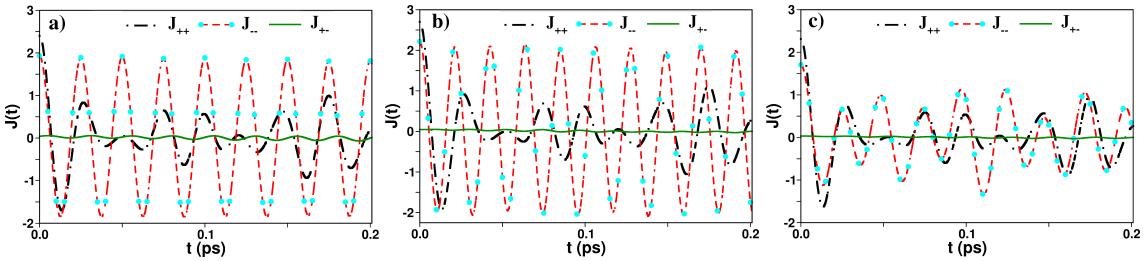

Figure 2A.15: Electric-current correlation functions for cation-cation, anion-anion and cation-anion of liquid (a) [BMIM][PF_6], (b) [BMIM][BF_4], and (c) [BMIM][CF_3SO_3] at 300 K.

In Figure 2A.15, we show different contributions to the total electric-current correlation function, such as cation-cation, anion-anion and the cross (cation-anion) correlation functions of various ILs. In general, the cation-cation current time correlation function decays faster than the corresponding anion-anion one. The magnitude of $J_{+-}(t)$ too is much lesser than that of $J_{++}(t)$ or $J_{--}(t)$. In an earlier work on [BMIM][Cl], Urahata and Ribeiro [137] observed that the main contribution to electrical conductivity comes from the anions, while the cross correlation also contributed significantly. The larger diffusion coefficients of chloride ion than that of the cation could be a reason for this observation. In the current study, we observe the contribution from cations and anions to be almost the same.

The centre of mass electric-current correlation functions defined as:

$$\mathrm{J}^{\mathrm{COM}}(t) = \left\langle \sum_{i=1}^{N_p} \sum_{j=1}^{N_p} q_i q_j \mathbf{v}_{\mathrm{i}}^{\mathrm{COM}}(t) \cdot \mathbf{v}_{\mathrm{j}}^{\mathrm{COM}}(0) \right\rangle \tag{2A.14}$$

where, $\mathbf{v}_{\mathrm{i}}^{\mathrm{COM}}$ is the velocity of the center of mass of ion i and N_p is the number of ion pairs.

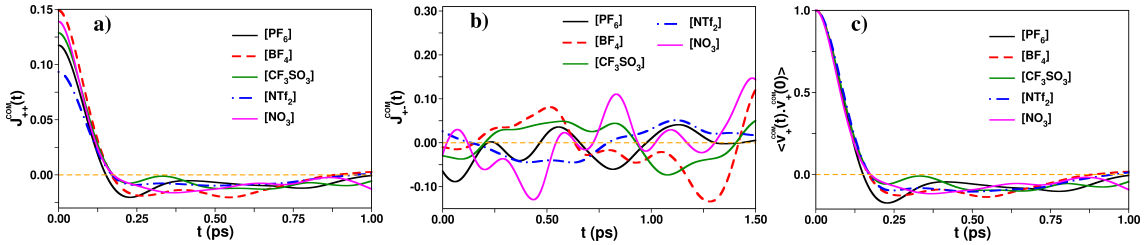

Figure 2A.16: Centre of mass (a) cation-cation and (b) cation-anion (cross) electric-current autocorrelation functions, and (c) centre of mass velocity autocorrelation functions of cations for different ILs at 300 K.

The centre of mass cation-cation ($\mathrm{J}_{++}^{\mathrm{COM}}$) and cation-anion electric-current correlation function ($\mathrm{J}_{+-}^{\mathrm{COM}}$) for different ILs are compared in Figure 2A.16 at 300 K. The former function exhibits oscillations with different frequencies which arises from different vibrational modes in the cation. $\mathrm{J}_{++}^{\mathrm{COM}}$ for [BMIM][PF_6] shows the deepest first minimum indicating the strength of the anion cage within which the cation rattles. In a similar fashion, the electric-current time correlation function, J(t) can also be recognized as the sum of $J_{++}(t)$, $J_{--}(t)$, and $2J_{+-}(t)$. The integral of these quantities were found to be nearly identical (see Table 2A.14), signifying that all of them contribute equally to the electrical conductivity. To understand this further, we computed the normalized cation-cation velocity autocorrelation functions for different liquids (Figure 2A.16). [PF_6] anion forms the strongest cage among all anions, inside which the cation resident. This is likely the reason for the high viscosity of [BMIM][PF_6] compared to other ILs. The sign and magnitude of the first peak of the cross-correlation term (Figure 2A.16b) provides an idea of cation-anion pairing at short times. [138] The most negative value is seen for [BMIM][PF_6] which implies that the anions forming the cage around a cation move in a concerted manner (i.e., they have the same direction of center of mass velocity).

Temperature dependence of electrical conductivity: In this subsection, we discuss the temperature dependence of the electrical conductivity for four liquids. To this end, electrical conductivities were derived using the Green-Kubo relation (Eq. 2A.8) at temperatures T = 300, 330, 360 and 400 K for [BMIM][PF_6] and [BMIM][BF_4], while for [BMIM][CF_3SO_3] and [BMIM][NTf_2], the conductivities were calculated at T = 330, 333, 353 and 373 K.

Table 2A.14: Contribution of cation-cation ($\sigma_{GK}{}^{++}$), anion-anion ($\sigma_{GK}{}^{--}$), and cation-anion ($\sigma_{GK}{}^{+-}$) electric-current correlation functions to the total electrical conductivity (σ_{GK}, S.m^{-1}) of ILs at 300 K obtained from simulation.

System	σ_{GK}	$\sigma_{GK}{}^{++}$	$\sigma_{GK}{}^{--}$	$2\times\sigma_{GK}{}^{+-}$
[BMIM][PF_6]	0.17	0.061	0.051	0.058
[BMIM][BF_4]	0.42	0.132	0.113	0.180
[BMIM][CF_3SO_3]	0.25	0.085	0.084	0.084
[BMIM][NTf_2]	0.29	0.105	0.086	0.098
[BMIM][NO_3]	0.31	0.106	0.103	0.100

In Figure 2A.17, electrical conductivity obtained from simulations are compared against experimental results at different temperatures. For [BMIM][PF_6] and [BMIM][BF_4], the simulations reproduce experimental data rather well over the entire temperature range. The calculated results for [BMIM][CF_3SO_3] and [BMIM][NTf_2] are within 30% of experiment and the temperature dependence is well reproduced.

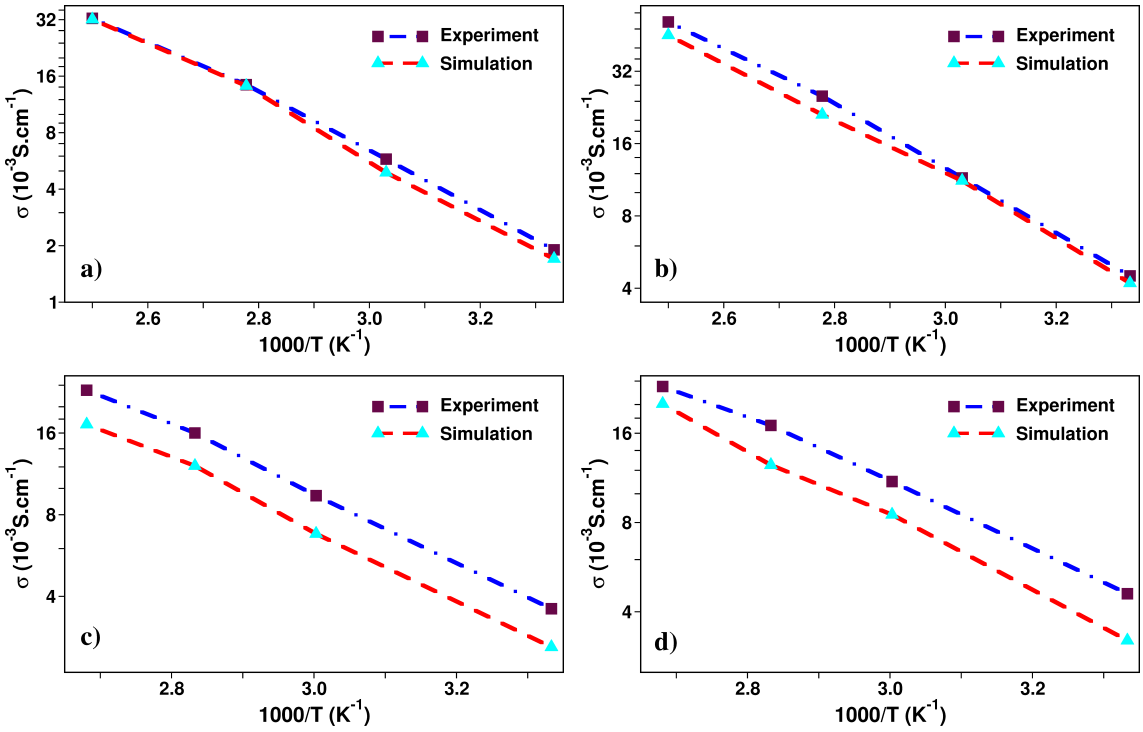

Figure 2A.17: Electrical conductivity obtained from simulations compared against experimental data [100] (a) [BMIM][PF_6], (b) [BMIM][BF_4], (c) [BMIM][CF_3SO_3], and (d) [BMIM][NTf_2].

2A.4 Conclusions

Periodic density functional theory calculations have been carried out for crystalline and liquid phases of various room temperature ionic liquids. The electronic charge density obtained from such calculations have been used to determine site charges on atoms through the robust DDEC/c3 [59, 60] method. Atomic site charges were obtained from both these phases for ILs containing six different anion types, [PF_6], [BF_4], [Cl], [NO_3], [CF_3SO_3], and [NTf_2]. The set of partial charges are crucial in the refinement of the force field, as electrostatic interactions are dominant in these liquids. The total ion charges obtained through this procedure were less than unity, which captures the effect of polarization and charge transfer from neighboring ions in the bulk environment. Surprisingly, for the five molecular anions studied here, the total ion charge varied over a narrow range – from 0.75 to 0.8e. The charge on the chloride as obtained from crystalline [BMIM][Cl] was -0.6e, implying the greater extent of charge transfer in this system due to its relatively smaller size.

Although the charges obtained here are from crystals, we have demonstrated that the mean ion charge in the liquid state is nearly the same as that obtained from the crystal. Further, the ion charge distribution in the liquid is rather narrow as well. This observation offers the possibility of charge determination by first carrying out a MD simulation of the desired liquid using a reasonable force field followed by coarse geometry optimizations within DFT of a few snapshots derived therefrom. The procedure to obtain site charges either from the crystal or from the liquid is quite tractable. These procedures are much less expensive than performing a full-blown *ab initio* MD simulation and are thus attractive.

A transferable force field for ILs was derived using these set of partial charges as a basis. We adapted the well established CL&P force field for this purpose – its non-bonded, 1-4, and torsional parameters were refined. This refinement procedure was carried out using three potential energy surfaces established by gas phase quantum chemical calculations of ion pairs, as benchmarks.

With the combination of refined site charges obtained from condensed phase DFT calculations and the fine-tuned non-bonded and torsional parameters, classical MD simulations of various ILs were carried out. The calculated physical properties (density, heat of vaporization, surface tension, diffusion coefficients) are in nearly quantitative agreement with experimental data. The equilibrium Green-Kubo relation was employed to calculate the shear viscosity and electrical conductivity from the long-time integral of stress autocorrelation and electric-current autocorrelation function, respectively. An estimate of correlated ion motion in these liquids was obtained through a comparison of the Green-Kubo and Nernst-Einstein conductivities. The force field is able to reproduce the experimental values of shear viscosity of these liquids rather accurately. The prediction of

electrical conductivity of [BMIM][PF_6] and [BMIM][BF_4] is remarkably good while that for [BMIM][CF_3SO_3] and [BMIM][NTf_2] is fair. Reconciliation of the conductivity of the latter between simulation and experiments needs further study.

In principle, this procedure can be extended to other imidazolium based ILs with other anion types, as well as to pyridinium or amino acid based salts. This approach will constitute our endeavour in the next Chapter.

Bibliography

[1] Pópolo, D. M. G.; Lynden-Bell, R. M.; Kohanoff, J. *J. Phys. Chem. B* **2005**, *109*, 5895–5902.

[2] Bühl, M.; Chaumont, A.; Schurhammer, R.; Wipff, G. *J. Phys. Chem. B* **2005**, *109*, 18591–18599.

[3] Bhargava, B.; Balasubramanian, S. *Chem. Phys. Lett.* **2006**, *417*, 486 – 491.

[4] Bagno, A.; D'Amico, F.; Saielli, G. *ChemPhysChem* **2007**, *8*, 873–881.

[5] Spickermann, C.; Thar, J.; Lehmann, S. B. C.; Zahn, S.; Hunger, J.; Buchner, R.; Hunt, P. A.; Welton, T.; Kirchner, B. *J. Chem. Phys.* **2008**, *129*, 104505.

[6] Kirchner, B.; Seitsonen, A. P. *Inorg. Chem.* **2007**, *46*, 2751–2754.

[7] Thar, J.; Brehm, M.; Seitsonen, A. P.; Kirchner, B. *J. Phys. Chem. B* **2009**, *113*, 15129–15132.

[8] Mallik, B. S.; Siepmann, J. I. *J. Phys. Chem. B* **2010**, *114*, 12577–12584.

[9] Zahn, S.; Wendler, K.; Site, L. D.; Kirchner, B. *Phys. Chem. Chem. Phys.* **2011**, *13*, 15083–15093.

[10] Schröder, C. *Phys. Chem. Chem. Phys.* **2012**, *14*, 3089–3102.

[11] Yan, T.; Wang, Y.; Knox, C. *J. Phys. Chem. B* **2010**, *114*, 6905–6921.

[12] Borodin, O. *J. Phys. Chem. B* **2009**, *113*, 11463–11478.

[13] Schröder, C.; Steinhauser, O. *J. Chem. Phys.* **2010**, *133*, 154511.

[14] Yan, T.; Burnham, C. J.; Pópolo, D. M. G.; Voth, G. A. *J. Phys. Chem. B* **2004**, *108*, 11877–11881.

[15] Maginn, E. J. *J. Phys.: Condens. Matter* **2009**, *21*, 373101.

[16] Zhao, W.; Leroy, F.; Heggen, B.; Zahn, S.; Kirchner, B.; Balasubramanian, S.; Müller-Plathe, F. *J. Am. Chem. Soc.* **2009**, *131*, 15825–15833.

[17] Tsuzuki, S.; Matsumoto, H.; Shinoda, W.; Mikami, M. *Phys. Chem. Chem. Phys.* **2011**, *13*, 5987–5993.

[18] Pensado, A. S.; Gomes, M. F. C.; Lopes, J. N. C.; Malfreyt, P.; Pádua, A. A. H. *Phys. Chem. Chem. Phys.* **2011**, *13*, 13518–13526.

[19] Lynden-Bell, R. M.; Atamas, N. A.; Vasilyuk, A.; Hanke, C. G. *Mol. Phys.* **2002**, *100*, 3225–3229.

[20] Maginn, E. J. *Acc. Chem. Res.* **2007**, *40*, 1200–1207.

[21] Lopes, J. N. C.; Pádua, A. A. H.; Shimizu, K. *J. Phys. Chem. B* **2008**, *112*, 5039–5046.

[22] Lopes, J. N. C.; Deschamps, J.; Pádua, A. A. H. *J. Phys. Chem. B* **2004**, *108*, 2038–2047.

[23] Lopes, J. N. C.; Pádua, A. A. H. *J. Phys. Chem. B* **2004**, *108*, 16893–16898.

[24] Lopes, J. N. C.; Pádua, A. A. H. *J. Phys. Chem. B* **2006**, *110*, 19586–19592.

[25] Liu, Z.; Huang, S.; Wang, W. *J. Phys. Chem. B* **2004**, *108*, 12978–12989.

[26] Liu, Z.; Chen, T.; Bell, A.; Smit, B. *J. Phys. Chem. B* **2010**, *114*, 4572–4582.

[27] Zhong, X.; Liu, Z.; Cao, D. *J. Phys. Chem. B* **2011**, *115*, 10027–10040.

[28] Sambasivarao, S. V.; Acevedo, O. *J. Chem. Theory Comput.* **2009**, *5*, 1038–1050.

[29] Roy, D.; Maroncelli, M. *J. Phys. Chem. B* **2010**, *114*, 12629–12631.

[30] Wang, Y.; Izvekov, S.; Yan, T.; Voth, G. A. *J. Phys. Chem. B* **2006**, *110*, 3564–3575.

[31] Bhargava, B. L.; Balasubramanian, S.; Klein, M. L. *Chem. Commun.* **2008**, 3339–3351.

[32] Köddermann, T.; Paschek, D.; Ludwig, R. *ChemPhysChem* **2007**, *8*, 2464–2470.

[33] Santos, L. M. N. B. F.; Lopes, J. N. C.; Coutinho, J. A. P.; Esperança, J. M. S. S.; Gomes, L. R.; Marrucho, I. M.; Rebelo, L. P. N. *J. Am. Chem. Soc.* **2007**, *129*, 284–285.

[34] Tokuda, H.; Hayamizu, K.; Ishii, K.; Susan, M. A. B. H.; Watanabe, M. *J. Phys. Chem. B* **2005**, *109*, 6103–6110.

[35] Qiao, B.; Krekeler, C.; Berger, R.; Luigi, D. S.; Holm, C. *J. Phys. Chem. B* **2008**, *112*, 1743–1751.

[36] Dommert, F.; Schmidt, J.; Qiao, B.; Zhao, Y.; Krekeler, C.; Luigi, D. S.; Berger, R.; Holm, C. *J. Chem. Phys.* **2008**, *129*, 224501.

[37] Bhargava, B. L.; Balasubramanian, S. *J. Chem. Phys.* **2007**, *127*, 114510.

[38] Cadena, C.; Zhao, Q.; Snurr, R. Q.; Maginn, E. J. *J. Phys. Chem. B* **2006**, *110*, 2821–2832.

[39] Köddermann, T.; Paschek, D.; Ludwig, R. *ChemPhysChem* **2008**, *9*, 549–555.

[40] Chaban, V. *Phys. Chem. Chem. Phys.* **2011**, *13*, 16055–16062.

[41] Morrow, T. I.; Maginn, E. J. *J. Phys. Chem. B* **2002**, *106*, 12807–12813.

[42] Men, S.; Lovelock, K. R. J.; Licence, P. *Phys. Chem. Chem. Phys.* **2011**, *13*, 15244–15255.

[43] Hurisso, B. B.; Lovelock, K. R. J.; Licence, P. *Phys. Chem. Chem. Phys.* **2011**, *13*, 17737–17748.

[44] Bagno, A.; D'Amico, F.; Saielli, G. *J. Mol. Liq.* **2007**, *131-132*, 17–23.

[45] Liu, Z.; Wu, X.; Wang, W. *Phys. Chem. Chem. Phys.* **2006**, *8*, 1096–1104.

[46] Zhong, X.; Liu, Z.; Cao, D. *J. Phys. Chem. B* **2011**, *115*, 10027–10040.

[47] Bedrov, D.; Borodin, O.; Li, Z.; Smith, G. D. *J. Phys. Chem. B* **2010**, *114*, 4984–4997.

[48] Vatamanu, J.; Borodin, O.; Smith, G. D. *J. Am. Chem. Soc.* **2010**, *132*, 14825–14833.

[49] Vatamanu, J.; Borodin, O.; Smith, G. D. *J. Phys. Chem. B* **2011**, *115*, 3073–3084.

[50] Vatamanu, J.; Borodin, O.; Bedrov, D.; Smith, G. D. *J. Phys. Chem. C* **2012**, *116*, 7940–7951.

[51] Koßmann, S.; Thar, J.; Kirchner, B.; Hunt, P. A.; Welton, T. *J. Chem. Phys.* **2006**, *124*, 174506.

[52] Schmidt, J.; Krekeler, C.; Dommert, F.; Zhao, Y.; Berger, R.; Luigi, D. S.; Holm, C. *J. Phys. Chem. B* **2010**, *114*, 6150–6155.

[53] Wendler, K.; Zahn, S.; Dommert, F.; Berger, R.; Holm, C.; Kirchner, B.; Luigi, D. S. *J. Chem. Theory Comput.* **2011**, *7*, 3040–3044.

[54] Wendler, K.; Dommert, F.; Zhao, Y. Y.; Berger, R.; Holm, C.; Luigi, D. S. *Faraday Discuss.* **2012**, *154*, 111–132.

[55] Blöchl, P. E. *J. Chem. Phys.* **1995**, *103*, 7422–7428.

[56] Dommert, F.; Holm, C. *Phys. Chem. Chem. Phys.* **2013**, *15*, 2037–2049.

[57] Dommert, F.; Wendler, K.; Qiao, B.; Luigi, D. S.; Holm, C. *J. Mol. Liq.* **2014**, *192*, 32 – 37.

[58] Zhang, Y.; Maginn, E. J. *J. Phys. Chem. B* **2012**, *116*, 10036–10048.

[59] Manz, T. A.; Sholl, D. S. *J. Chem. Theory Comput.* **2010**, *6*, 2455–2468.

[60] Manz, T. A.; Sholl, D. S. *J. Chem. Theory Comput.* **2012**, *8*, 2844–2867.

[61] Jasuja, H.; Zang, J.; Sholl, D. S.; Walton, K. S. *J. Phys. Chem. C* **2012**, *116*, 23526–23532.

[62] Fang, H.; Kamakoti, P.; Ravikovitch, P. I.; Aronson, M.; Paur, C.; Sholl, D. S. *Phys. Chem. Chem. Phys.* **2013**, *15*, 12882–12894.

[63] Allen, F. H. *Acta Crystallogr., Sect. B: Struct. Sci* **2002**, *58*, 380–388.

[64] Bruno, I. J.; Cole, J. C.; Edgington, P. R.; Kessler, M.; Macrae, C. F.; McCabe, P.; Pearson, J.; Taylor, R. *Acta Crystallogr., Sect. B: Struct. Sci* **2002**, *58*, 389–397.

[65] Bruno, I.; Cole, J.; Lommerse, J.; Rowland, R.; Taylor, R.; Verdonk, M. *J. Comput. Aided Mol. Des.* **1997**, *11*, 525–537.

[66] Hutter, J.; Iannuzzi, M.; Schiffmann, F.; VandeVondele, J. *WIREs Comput. Mol. Sci.* **2014**, *4*, 15–25.

[67] Perdew, J. P.; Burke, K.; Ernzerhof, M. *Phys. Rev. Lett.* **1996**, *77*, 3865–3868.

[68] Goedecker, S.; Teter, M.; Hutter, J. *Phys. Rev. B* **1996**, *54*, 1703–1710.

[69] Campañá, C.; Mussard, B.; Woo, T. K. *J. Chem. Theory Comput.* **2009**, *5*, 2866–2878.

[70] Bayly, C. I.; Cieplak, P.; Cornell, W.; Kollman, P. A. *J. Phys. Chem.* **1993**, *97*, 10269–10280.

[71] Arduengo, A. J.; Dias, H. V. R.; Harlow, R. L.; Kline, M. *J. Am. Chem. Soc.* **1992**, *114*, 5530–5534.

[72] Holbrey, J. D.; Reichert, W. M.; Nieuwenhuyzen, M.; Johnson, S.; Seddon, K. R.; Rogers, R. D. *Chem. Commun.* **2003**, 1636–1637.

[73] Holbrey, J. D.; Reichert, W. M.; Nieuwenhuyzen, M.; Sheppard, O.; Hardacre, C.; Rogers, R. D. *Chem. Commun.* **2003**, 476–477.

[74] Reichert, W. M.; Holbrey, J. D.; Swatloski, R. P.; Gutowski, K. E.; Visser, A. E.; Nieuwenhuyzen, M.; Seddon, K. R.; Rogers, R. D. *Cryst. Growth Des.* **2007**, *7*, 1106–1114.

[75] Dibrov, S. M.; Kochi, J. K. *Acta Crystallogr., Sect. C* **2006**, *62*, 19–21.

[76] Choudhury, A. R.; Winterton, N.; Steiner, A.; Cooper, A. I.; Johnson, K. A. *CrystEngComm* **2006**, *8*, 742–745.

[77] Choudhury, A. R.; Winterton, N.; Steiner, A.; Cooper, A. I.; Johnson, K. A. *J. Am. Chem. Soc.* **2005**, *127*, 16792–16793.

[78] Wilkes, J. S.; Zaworotko, M. J. *Chem. Commun.* **1992**, 965–967.

[79] Holbrey, J. D.; Richert, W. M.; Rogers, R. D. *Dalton Trans.* **2004**, 2267–2271.

[80] Plimpton, S. *J. Comput. Phys.* **1995**, *117*, 1–19.

[81] Nosé, S. *J. Chem. Phys.* **1984**, *81*, 511–519.

[82] Nosé, S. *Mol. Phys.* **1984**, *52*, 255–268.

[83] Martyna, G. J.; Klein, M. L.; Tuckerman, M. *J. Chem. Phys.* **1992**, *97*, 2635–2643.

[84] Zahn, S.; Bruns, G.; Thar, J.; Kirchner, B. *Phys. Chem. Chem. Phys.* **2008**, *10*, 6921–6924.

[85] Frisch, M. J. et al. Gaussian 09 Revision D.01. Gaussian Inc. Wallingford CT **2009**.

[86] Dennington, R.; Keith, T.; Millam, J. GaussView Version 5. Semichem Inc., Shawnee Mission, KS, 2009.

[87] Martínez, L.; Andrade, R.; Birgin, E. G.; Martínez, J. M. *J. Comp. Chem.* **2009**, *30*, 2157–2164.

[88] Macrae, C. F.; Edgington, P. R.; McCabe, P.; Pidcock, E.; Shields, G. P.; Taylor, R.; Towler, M.; van de Streek, J. *J. Appl. Crystallogr.* **2006**, *39*, 453–457.

[89] Humphrey, W.; Dalke, A.; Schulten, K. *J. Mol. Graphics* **1996**, *14*, 33–38.

[90] Daivis, P. J.; Evans, D. J. *J. Chem. Phys.* **1994**, *100*, 541–547.

[91] Mundy, C. J.; Siepmann, J. I.; Klein, M. L. *J. Chem. Phys.* **1995**, *103*, 10192–10200.

[92] Chen, T.; Smit, B.; Bell, A. T. *J. Chem. Phys.* **2009**, *131*, 246101.

[93] Sarangi, S. S.; Zhao, W.; Müller-Plathe, F.; Balasubramanian, S. *ChemPhysChem* **2010**, *11*, 2001–2010.

[94] Harada, M.; Yamanaka, A.; Tanigaki, M.; Tada, Y. *J. Chem. Phys.* **1982**, *76*, 1550–1556.

[95] Hansen, J.-P.; McDonald, I. R. *Theory of Simple Liquids, Third Edition*; 2006.

[96] Pópolo, D. M. G.; Voth, G. A. *J. Phys. Chem. B* **2004**, *108*, 1744–1752.

[97] Li, J.-G.; Hu, Y.-F.; Ling, S.; Zhang, J.-Z. *J. Chem. Eng. Data* **2011**, *56*, 3068–3072.

[98] He, R.-H.; Long, B.-W.; Lu, Y.-Z.; Meng, H.; Li, C.-X. *J. Chem. Eng. Data* **2012**, *57*, 2936–2941.

[99] Seddon, K. R.; Annegret, S.; María-José, T. *Viscosity and Density of 1-Alkyl-3-methylimidazolium Ionic Liquids*; American Chemical Society, 2002.

[100] Tokuda, H.; Tsuzuki, S.; Susan, M. A. B. H.; Hayamizu, K.; Watanabe, M. *J. Phys. Chem. B* **2006**, *110*, 19593–19600.

[101] Swiderski, K.; McLean, A.; Gordon, C. M.; Vaughan, D. H. *Chem. Commun.* **2004**, 2178–2179.

[102] Lee, S. H.; Lee, S. B. *Chem. Commun.* **2005**, 3469–3471.

[103] Xu, W.-G.; Li, L.; Ma, X.-X.; Wei, J.; Duan, W.-B.; Guan, W.; Yang, J.-Z. *J. Chem. Eng. Data* **2012**, *57*, 2177–2184.

[104] Emel'yanenko, V. N.; Verevkin, S. P.; Heintz, A.; Schick, C. *J. Phys. Chem. B* **2008**, *112*, 8095–8098.

[105] Deyko, A.; Hessey, S. G.; Licence, P.; Chernikova, E. A.; Krasovskiy, V. G.; Kustov, L. M.; Jones, R. G. *Phys. Chem. Chem. Phys.* **2012**, *14*, 3181–3193.

[106] Zaitsau, D. H.; Kabo, G. J.; Strechan, A. A.; Paulechka, Y. U.; Tschersich, A.; Verevkin, S. P.; Heintz, A. *J. Phys. Chem. A* **2006**, *110*, 7303–7306.

[107] Deyko, A.; Lovelock, K. R. J.; Corfield, J.-A.; Taylor, A. W.; Gooden, P. N.; Villar-Garcia, I. J.; Licence, P.; Jones, R. G.; Krasovskiy, V. G.; Chernikova, E. A.; Kustov, L. M. *Phys. Chem. Chem. Phys.* **2009**, *11*, 8544–8555.

[108] Borodin, O. *J. Phys. Chem. B* **2009**, *113*, 12353–12357.

[109] Freire, M. G.; Carvalho, P. J.; Fernandes, A. M.; Marrucho, I. M.; Queimada, A. J.; Coutinho, J. A. *J. Colloid Interface Sci.* **2007**, *314*, 621 – 630.

[110] Bhargava, B. L.; Klein, M. L.; Balasubramanian, S. *ChemPhysChem* **2008**, *9*, 67–70.

[111] Payal, R. S.; Balasubramanian, S. *Phys. Chem. Chem. Phys.* **2013**, *15*, 21077–21083.

[112] Tokuda, H.; Hayamizu, K.; Ishii, K.; Susan, M. A. B. H.; Watanabe, M. *J. Phys. Chem. B* **2004**, *108*, 16593–16600.

[113] Kanakubo, M.; Harris, K. R.; Tsuchihashi, N.; Ibuki, K.; Ueno, M. *J. Phys. Chem. B* **2007**, *111*, 2062–2069.

[114] Urahata, S. M.; Ribeiro, M. C. C. *J. Chem. Phys.* **2005**, *122*, 024511.

[115] Jin, H.; O'Hare, B.; Dong, J.; Arzhantsev, S.; Baker, G. A.; Wishart, J. F.; Benesi, A. J.; Maroncelli, M. *J. Phys. Chem. B* **2008**, *112*, 81–92.

[116] Gardas, R. L.; Coutinho, J. A. *Fluid Phase Equilib.* **2008**, *266*, 195 – 201.

[117] Bonhôte, P.; Dias, A.-P.; Papageorgiou, N.; Kalyanasundaram, K.; Grätzel, M. *Inorg. Chem.* **1996**, *35*, 1168–1178.

[118] Fumino, K.; Peppel, T.; Geppert-Rybczynska, M.; Zaitsau, D. H.; Lehmann, J. K.; Verevkin, S. P.; Kockerling, M.; Ludwig, R. *Phys. Chem. Chem. Phys.* **2011**, *13*, 14064–14075.

[119] Hunt, P. A. *J. Phys. Chem. B* **2007**, *111*, 4844–4853.

[120] Mokhtarani, B.; Sharifi, A.; Mortaheb, H. R.; Mirzaei, M.; Mafi, M.; Sadeghian, F. *J. Chem. Thermodyn.* **2009**, *41*, 1432–1438.

[121] Jacquemin, J.; Husson, P.; Padua, A. A. H.; Majer, V. *Green Chem.* **2006**, *8*, 172–180.

[122] Fan, W.; Zhou, Q.; Sun, J.; Zhang, S. *J. Chem. Eng. Data* **2009**, *54*, 2307–2311.

[123] Micaelo, N. M.; Baptista, A. M.; Soares, C. M. *J. Phys. Chem. B* **2006**, *110*, 14444–14451.

[124] Vakili-Nezhaad, G.; Vatani, M.; Asghari, M.; Ashour, I. *J. Chem. Thermodyn.* **2012**, *54*, 148–154.

[125] Chaban, V. V.; Voroshylova, I. V.; Kalugin, O. N.; Prezhdo, O. V. *J. Phys. Chem. B* **2012**, *116*, 7719–7727.

[126] Ge, M.-L.; Zhao, R.-S.; Yi, Y.-F.; Zhang, Q.; Wang, L.-S. *J. Chem. Eng. Data* **2008**, *53*, 2408–2411.

[127] Katsuta, S.; Shiozawa, Y.; Imai, K.; Kudo, Y.; Takeda, Y. *J. Chem. Eng. Data* **2010**, *55*, 1588–1593.

[128] Androulaki, E.; Vergadou, N.; Ramos, J.; Economou, I. G. *Mol. Phys.* **2012**, *110*, 1139–1152.

[129] Vila, J.; Varela, L.; Cabeza, O. *Electrochim. Acta* **2007**, *52*, 7413–7417.

[130] Rivera, A.; Brodin, A.; Pugachev, A.; Rössler, E. A. *J. Chem. Phys.* **2007**, *126*, 114503.

[131] Stoppa, A.; Hunger, J.; Buchner, R. *J. Chem. Eng. Data* **2009**, *54*, 472–479.

[132] Schreiner, C.; Zugmann, S.; Hartl, R.; Gores, H. J. *J. Chem. Eng. Data* **2010**, *55*, 1784–1788.

[133] Widegren, J. A.; Saurer, E. M.; Marsh, K. N.; Magee, J. W. *J. Chem. Thermodyn.* **2005**, *37*, 569 – 575.

[134] Vranes, M.; Dozic, S.; Djeric, V.; Gadzuric, S. *J. Chem. Eng. Data* **2012**, *57*, 1072–1077.

[135] Yu, Y.-H.; Soriano, A. N.; Li, M.-H. *Thermochim. Acta* **2009**, *482*, 42 – 48.

[136] Zech, O.; Stoppa, A.; Buchner, R.; Kunz, W. *J. Chem. Eng. Data* **2010**, *55*, 1774–1778.

[137] Urahata, S. M.; Ribeiro, M. C. C. *J. Chem. Phys.* **2006**, *124*, 074513.

[138] Kowsari, M. H.; Alavi, S.; Ashrafizaadeh, M.; Najafi, B. *J. Chem. Phys.* **2009**, *130*, 014703.

Chapter 2B

A Refined All-Atom Potential for Imidazolium-Based Room Temperature Ionic Liquids: Acetate, Dicyanamide, and Thiocyanate Anions

2B.1 Introduction

An important aspect of force field for ionic liquids (ILs) is the transferability of site parameters across ILs. Charge transfer between ions [1] as well as polarization (in particular, that of the anion) in ILs need to be accounted for in an effective manner. Both photoelectron spectroscopy experiments [2–4] as well as quantum density functional theory (DFT) based simulations [5–9] have demonstrated the nature and magnitude of charge transfer in the condensed state. To capture these effects, in the last Chapter (Chapter 2A), a protocol that combines electron density data of an IL in its condensed phase with gas phase quantum chemical calculations, to yield suitable interaction parameters within a nonpolarizable force field was outlined.

In this approach, a charge partitioning method (DDEC/c3) developed by Manz and Sholl [10, 11] was employed to obtain the ion charges from crystalline, as well as bulk liquid phases of these salts. It was shown that the ions in condensed phases possess fractional charges (between 0.6e to 0.8e). The fractional charges were adapted into the well-established CL&P [12, 13] force field. Subsequently, the non-bonded and torsional

Reprinted with permission from "A Refined All-Atom Potential for Imidazolium-Based Room Temperature Ionic Liquids: Acetate, Dicyanamide, and Thiocyanate Anions" *J. Phys. Chem. B* **2015**, *119*, 11041–11051.

parameters were refined so as to make them be in accord with the partial charges. This approach showed substantial improvement in predicting the physical properties of seven RTILs, containing different anions. The good agreement with experimental data on a wide range of properties gives us confidence in expanding these calculations to other anions commonly used in ILs.

In the present Chapter, refined force field parameters are determined for the IL anions, acetate ([CH_3COO] or [OAc]), thiocyanate ([SCN]) and dicyanamide ([$N(CN)_2$] or [DCA]) which can be combined with imidazolium cation to form respective ILs. The methodology of parametrization is the same as described in Chapter 2A. It consists of (i) derivation of atomic partial charges from condensed phase quantum calculations, (ii) reparametrization of non-bonded and torsional potentials via gas phase quantum calculations, and (iii) molecular dynamics (MD) simulations of bulk ILs to validate the force field against experimentally determined observables. With the present work, the charge derivation and IL force field refinement scheme is extended to ionic liquids whose crystal structure is unknown.

2B.2 Methodology and Simulation Details

The cation and anion of ILs used in this work and the nomenclature used to describe sites on the imidazolium ring and on the anions are shown in Figure 2B.1. For cation, the initial set of parameters were taken from the CL&P force field. [12] To provide the initial framework for refinement, force fields of Lopes *et al.*, [14] Senapati *et al.*, [15] and Chaumont and Wipff [16] for the anions [$N(CN)_2$], [CH_3COO], and [SCN], respectively, were employed.

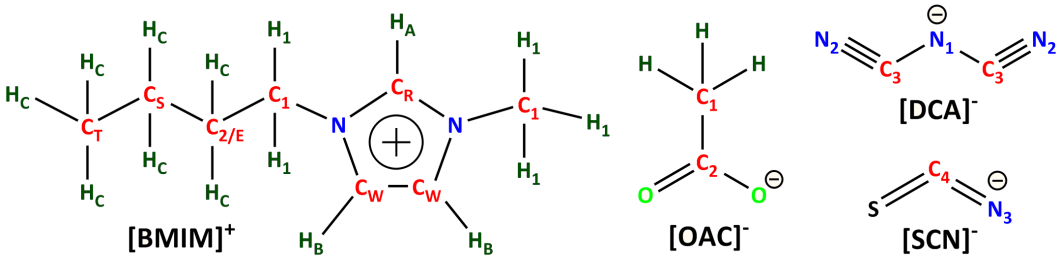

Figure 2B.1: Atom labeling in cation and anions used in simulations.

2B.2.1 Charge derivation from bulk IL

In Chapter 2A, calculations were primarily based on charges derived from DFT calculations of crystalline phases. It was also shown that the ion charges derived thus matched the mean values of the ion charge distributions obtained through DFT calculations of the corresponding liquid phase. Thus, if the crystal structure of an IL compound is not available, the electron density distribution of its liquid phase can be obtained from a DFT calculation

Table 2B.1: Summary of all the liquid systems studied for calculating atomic charges.

System	Number of ion pairs	Box length (Å)
[BMIM][OAc]	25	19.96
[BMIM][DCA]	25	20.04
[BMIM][SCN]	27	19.98

from which the atomic site charges can be obtained. It is this approach that comes in handy for the ILs studied here, for which 1-butyl-3-methylimidazolium is chosen as the common cation.

Classical MD simulations of these liquid systems were carried out with typically around 30 ion pairs using force fields based on literature as mentioned earlier. A full description of these systems is provided in Table 2B.1. The liquid configurations acquired from MD trajectories were then quenched to their minimum energy positions within DFT framework using CP2K software. [17] The convergence criteria used for the gradient of electronic wave functions and force on the nuclei were 10^{-7} and 10^{-3}, respectively. Perdew, Burke, and Ernzerhof (PBE) exchange-correlation functional was employed. [18] The effect of core electrons and nuclei were treated with Geodecker-Teter-Hutter (GTH) pseudopotentials. [19] Triple-ζ double-polarized basis sets with an energy cutoff of 280 Ry was used to represent all the valence electrons. The optimized coordinates were used to generate the valence electron density at the same level of theory and were saved in a cube file. This density information was used as an input to the DDEC/c3 code [10, 11] to obtain the atomic charges. The charges were averaged over all ions present in all the configurations quenched similarly from a liquid phase classical MD trajectory.

2B.2.2 Short-Range and Torsional Interactions

Another important aspect of modeling ILs is to represent the non-bonded interaction parameters accurately. That for the imidazolium cation have already been described in Chapter 2A. Thus, such parameters were refined only for those atoms belonging to the anions studied here. The quantum chemical potential energy surfaces (PES) for ion pairs in gas phase across three different directions (see Figure 2B.2) have been used as benchmarks. The Lennard-Jones parameters of anions were then iteratively adjusted to reproduce these three different quantum PES. The refined Lennard-Jones parameters for anions are tabulated in Table 2B.2. As changes in non-bonded parameters affect 1-4 interactions as well, the torsional parameters too need to be reworked. These torsional parameters for anions are tabulated in Table 2B.3.

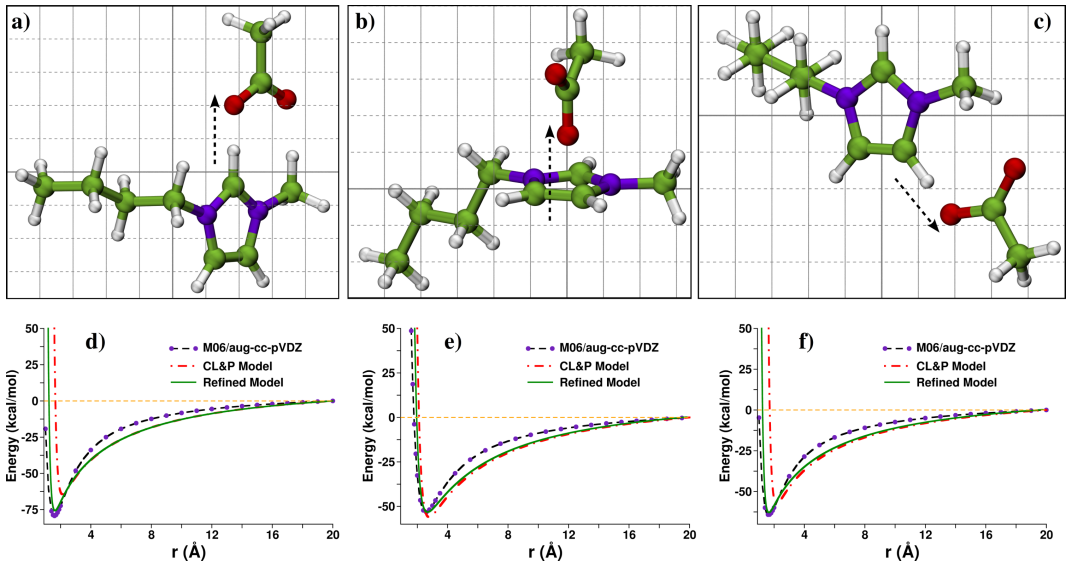

Figure 2B.2: Directions along which potential energy surfaces were obtained using M06/aug-cc-pVDZ level of theory for [BMIM][OAc]: (a) along C-H_A bond; (b) perpendicular to the imidazolium ring plane; (c) along C-H_B bond. Color scheme: nitrogen, violet; carbon, green; hydrogen, white; oxygen, red. Potential energy as a function of distance between cation site and anion in three different directions are shown in bottom panels (d-f). Potential energy surfaces for [BMIM][DCA] and [BMIM][SCN] as well were obtained in a similar manner.

2B.2.3 Molecular Dynamics Simulations

1-butyl-3-methylimidazolium based ionic liquids containing any of the three anions ([$N(CN)_2$], [CH_3COO], and [SCN]) were modeled using these refined set of force field parameters. Classical MD simulations were performed on their liquid phases using LAMMPS package. [20] Long-range interactions were computed using the particle-particle particle mesh Ewald (PPPM) solver with a precision of 10^{-5}. Velocity Verlet algorithm was used to calculate the equations of motion with a time step of 1 fs. All C-H covalent bonds were constrained using SHAKE algorithm as implemented in LAMMPS. The Nosé-Hoover thermostat and barostat were employed to control the temperature and pressure of the system. [21–23] Cross interactions between different atom types were computed using standard Lorentz-Berthelot rules.

All the systems were simulated using 512 ion pairs. Initial configurations were generated using Packmol software. [24] The simulations have been carried out at the same temperatures where experimental data were available in the literature. These were 300, 313, 333 and 343 K for [BMIM][CH_3COO] and [BMIM][$N(CN)_2$], while for [BMIM][SCN] system, the temperatures were 300, 313, 323 and 333 K. All the systems were equilibrated for 10 ns in the constant-NPT ensemble followed by a duration of 5 ns in the constant-NVT ensemble. This procedure was followed by a 48 ns production run in the constant-NVT

Table 2B.2: Lennard-Jones parameters for anions according to the refined model. Atoms separated by three covalent bonds interact via 1-4 interactions with the following scale factors: 0.5 for Lennard-Jones and zero for Coulomb.

Atom	ε (kcal mol^{-1})	σ (Å)
C_1	0.10939	3.15
C_2	0.07599	3.00
O	0.10999	2.56
H	0.01270	2.45
N_1	0.16500	3.05
C_3	0.06500	3.10
N_2	0.16500	3.00
S	0.22000	3.34
C_4	0.18000	3.25
N_3	0.20000	2.78

Table 2B.3: Proper dihedral parameters (kcal/mol) in Multi/harmonic form according to the refined model: $\mathrm{E}^{\mathrm{MH}}_{\mathrm{dihedral}} = \sum_{n=1}^{5} A_n cos^{n-1}(\phi)$.

Dihedrals	A_1	A_2	A_3	A_4	A_5
$O-C_2-C_1-H$	0.12146	0.11818	-0.00109	0.08951	0.01109
$N_2-C_3-N_1-C_3$	0.00000	0.00000	0.00000	0.00000	0.00000

ensemble. The systems were visualized in VMD. [25]

Transport properties such as self-diffusion coefficient, shear viscosity and electrical conductivity were calculated using equilibrium Green-Kubo relations discussed in Chapter 2A.

2B.3 Results and Discussion

2B.3.1 Atomic Charges

The effect of electronic polarization and charge transfer between ions are reflected in the calculated ion charges. The net ion charge showed a reduction from unity in all the three liquids. The mean ion charges were $\pm$0.74e, $\pm$0.65e, and $\pm$0.78e for ILs composed of [CH_3COO], [SCN], and [$N(CN)_2$] anions, respectively. The smaller anion, [SCN] exhibits a larger charge transfer effect, nearly similar to the charge of the chloride determined in [BMIM][Cl] liquid in Chapter 2A. A few important observations: (i) site charges on atoms in butyl tail as well as in methyl group attached to the imidazolium cation were similar in nature through different ILs, (ii) the methylene groups present beyond C_2 carbon were found to be charge neutral, (iii) symmetry related atoms in both anion and cations possessed

Table 2B.4: Atomic site charges (e) for the cation according to the refined model.

Atom	[OAc]	[SCN]	[DCA]
N	0.135	0.120	0.140
C_R	-0.015	-0.005	-0.005
C_W	-0.120	-0.110	-0.120
H_A	0.175	0.145	0.185
H_B	0.165	0.135	0.170
C_1	-0.250	-0.250	-0.250
H_1	0.120	0.120	0.120
C_2	-0.076	-0.076	-0.076
C_E	-0.174	-0.174	-0.174
H_C	0.098	0.098	0.098
C_S	-0.196	-0.196	-0.196
C_T	-0.294	-0.294	-0.294

similar charge values. For the sake of transferability, as before (see Chapter 2A), minor reassignments were made in the atomic site charges. For a particular type of anion, site charges of different atom types were averaged over the number of anions present in each system. The residual charge on terminal methyl group and methylene groups beyond the C_2 carbon were redistributed to other sites on the imidazolium ring so that these non-polar groups could be assigned a charge of zero. Revised site charges are provided in Table 2B.4 and Table 2B.5.

2B.3.2 Density

These refined set of potential parameters were used to simulate the liquid phases of these salts at four different temperature. Simulations were carried out in the constant-temperature constant-pressure (NPT) ensemble, and the mean box length was used to compute the density of these ILs. The temperature dependence of density compares well with experiment (within 2% deviation) and are presented in Table 2B.6.

2B.3.3 Heat of Vaporization

The enthalpy of vaporization has been computed as

$$\Delta \mathrm{H}_{\mathrm{vap}} = \mathrm{E}_{\mathrm{Ion-pair}} - \mathrm{E}_{\mathrm{liq}} + RT \tag{2B.1}$$

where $\mathrm{E}_{\mathrm{Ion-pair}}$ is the total energy of an ion pair in gas phase, $\mathrm{E}_{\mathrm{liq}}$ represents the total energy per mole of ion pair in the liquid and R is the universal gas constant. Vaporization enthalpy ($\Delta \mathrm{H}_{\mathrm{vap}}$) was calculated for these ILs using the refined model. The results are

Table 2B.5: Atomic site charges (e) for the anion according to the refined model.

Atom	Charge (e)
C_1	-0.54
C_2	0.73
O	-0.66
H	0.13
N_1	-0.56
C_3	0.50
N_2	-0.61
S	-0.38
C_4	0.26
N_3	-0.53

summarized in Table 2B.7. Values obtained from simulations show good agreement with experiment. The heat of vaporization computed for [BMIM][DCA] using the current model is comparable to that estimated from a polarizable model (ΔH_{vap} = 31.5 kcal/mol). [26]

Table 2B.6: Density of ionic liquids (gm/cm^3) obtained from MD simulation using the refined force field, compared against experiment. [27–29] Estimated uncertainty in computed density is around 0.004 gm/cm^3. $\Delta\rho = (\rho^{sim} - \rho^{exp})/\rho^{exp}$.

Ionic Liquid	T (K)	ρ^{exp}	ρ^{sim}	$\Delta\rho$ (%)
[BMIM][OAc]	300	1.058	1.056	-0.18
	313	1.049	1.046	-0.28
	333	1.031	1.030	-0.09
	343	1.025	1.023	-0.19
[BMIM][DCA]	300	1.059	1.071	1.13
	313	1.049	1.061	1.14
	333	1.037	1.045	0.77
	343	1.031	1.037	0.58
[BMIM][SCN]	300	1.069	1.082	1.21
	313	1.060	1.070	0.94
	323	1.049	1.062	1.23
	333	1.043	1.053	0.95

2B.3.4 Structure

To understand the intermolecular structure in the liquid, site-site radial distribution functions (RDF) were analyzed. Figure 2B.3a shows the RDFs between the geometric

Table 2B.7: Heat of vaporization (kcal/mol) at 300 K of ILs obtained from simulations compared against experimental data at 298 K. [30–32] The uncertainty in the computed heat of vaporization is around 0.03 kcal/mol. $\Delta(\Delta H_{vap}) = (\Delta H_{vap}^{Sim} - \Delta H_{vap}^{Exp})/\Delta H_{vap}^{Exp}$.

Ionic Liquid	ΔH_{vap}^{Exp}	ΔH_{vap}^{Sim}	$\Delta(\Delta H_{vap})$ (%)
[BMIM][OAc]	26.98	30.01	+11.14
[BMIM][DCA]	37.57	33.71	-10.27
[BMIM][SCN]	35.37	30.12	-14.13

center of the imidazolium ring and the central atom of the corresponding anion. The RDFs between anion (anion atom that have largest negative partial charge and act as hydrogen bond acceptor; O in [OAc], N2 in [DCA], and N3 in [SCN]) and the acidic hydrogen (H_A) on imidazolium cation are displayed in Figure 2B.3b.

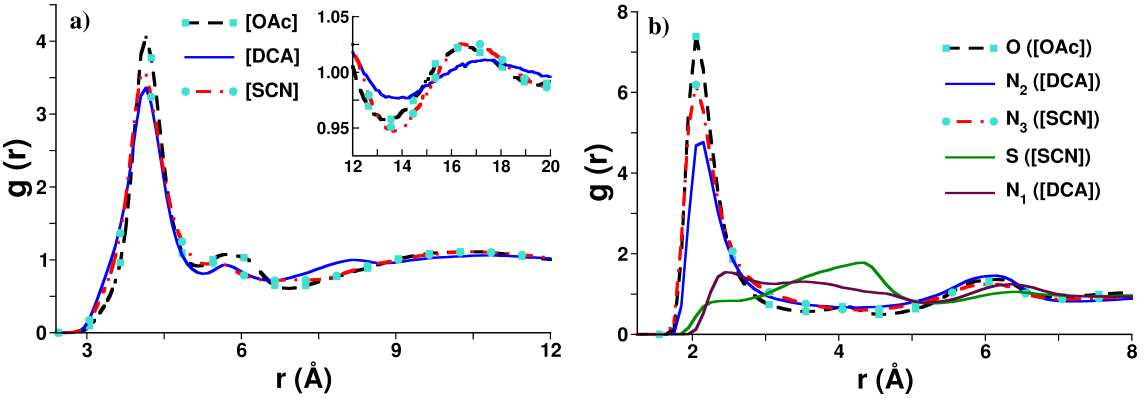

Figure 2B.3: Radial distribution functions for (a) cation–anion and (b) anion–H_A for ILs modeled with refined parameters.

The intense first peak of cation–anion $g(r)$ indicates a strong structural correlation between cation and anion which is observed even at distances of 20 Å (see inset of Figure 2B.3a). As can be seen from Figure 2B.3b, the anion–H_A $g(r)$ have a strong, sharp peak around 2 Å, typical of hydrogen bonding. Within a sphere of 4 Å radius, the acidic proton on imidazolium cation has an average of 2.2 oxygen atoms of [CH_3COO], 2.0 and 1.4 nitrogen atoms of [$N(CN)_2$], and [SCN], respectively.

The central nitrogen atom (N_1) in [$N(CN)_2$] and sulfur atom in [SCN] also possess negative partial charge as shown in Table 2B.5, and hence, in principle both of them can form hydrogen bonds with the acidic proton of the imidazolium cation. We calculated the $g(r)$ between these two pairs of atoms as well which are displayed in Figure 2B.3b. These $g(r)$ show no sign of strong interaction between nitrogen atom (N_1) in [$N(CN)_2$] or sulfur atom in [SCN] with the [BMIM] acidic hydrogen atom, which is consistent with the results obtained earlier. [33–35]

The structural correlations were further investigated by examining the spatial density

distribution of anion atoms around the cation. Figure 2B.4 displays the spatial density map of anion around cation center of mass at an isosurface value of 0.011 $Å^{-3}$. Three well-defined, preferred locations for anions were seen in all the systems and they are in the proximity of the three ring hydrogen atoms: one H_A and two H_B atoms. The former, i.e., the acidic hydrogen site (H_A) being more favored.

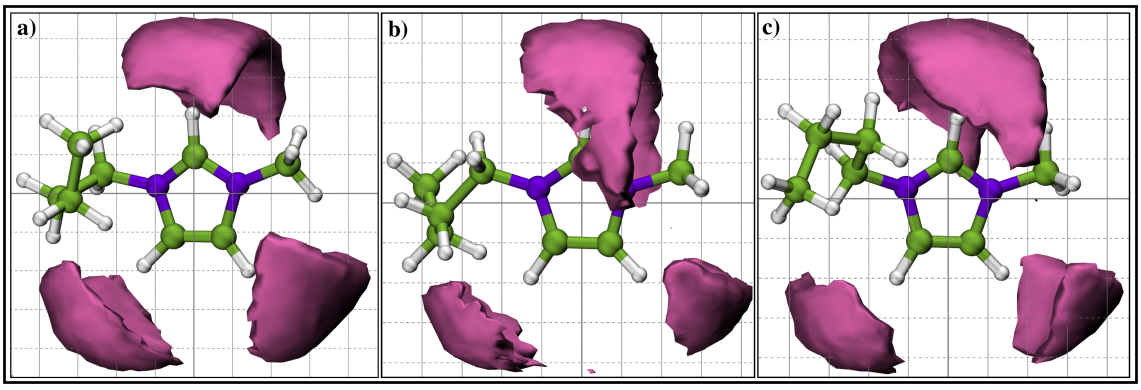

Figure 2B.4: Spatial distribution function of anions around the cation at an isosurface value of 0.011 $Å^{-3}$: (a) [BMIM][CH_3COO]; (b) [BMIM][$N(CN)_2$]; (c) [BMIM][SCN]. Color scheme: violet, nitrogen; green, carbon; white, hydrogen.

2B.3.5 Surface Tension

Calculated surface tension values are compared against experimental data in Table 2B.8. Computed results showed adequate consistency with experimental observations over the set of state points.

2B.3.6 Mean Square Displacement and Self-Diffusion Coefficients

Transport properties are analysed by calculating self-diffusion coefficient of ions at different temperature. The mean square displacement (MSD) of the center of mass of ions were calculated based on three MD runs each of 30 ns, whose average is presented in Figure 2B.5a. At any given time, the lighter anions diffuse faster than cations as expected. [15, 36]

The signature of diffusive nature of molecular motions can be determined from the exponent $\gamma(t)$ defined as,

$$\gamma(t) = \frac{dln\langle \Delta r^2(t) \rangle}{dln(t)} \tag{2B.2}$$

where $\Delta r^2(t)$ is the mean square displacement at time t. The diffusive regime is characterised by $\gamma(t) = 1$.

We have considered the last 20 ns of the simulation data to acquire ion diffusion coefficients. The computed self-diffusion coefficient of ions at four different temperatures

Table 2B.8: Surface tension (mN/m) obtained from MD simulation compared against experiment. [27–29] The estimated standard error on the mean in the calculated surface tension is around 0.07 mN/m. $\Delta\gamma = (\gamma^{\mathrm{sim}} - \gamma^{\mathrm{exp}})/\gamma^{\mathrm{exp}}$.

Ionic Liquid	T (K)	γ^{exp}	γ^{sim}	$\Delta\gamma$ (%)
[BMIM][OAc]	300	36.4	36.7	+0.94
	313	35.5	34.2	-3.51
	333	34.7	33.5	-3.52
	343	34.4	32.5	-5.21
[BMIM][DCA]	300	48.6	43.9	-8.21
	313	47.2	43.3	-7.81
	333	45.5	41.9	-6.82
	343	45.0	41.2	-8.43
[BMIM][SCN]	300	45.4	41.3	-8.22
	313	43.3	39.7	-7.64
	323	39.2	37.3	-4.84
	333	—	35.9	—

are tabulated in Table 2B.9. The ion self-diffusion coefficients are consistently higher for [BMIM][SCN] compared to [BMIM][OAc] or [BMIM][DCA]. This may be due to the smaller size of [SCN] anion and the reduced total ion charge ($\pm$0.65e) in [BMIM][SCN], which results in diminished electrostatic interactions between the ions. A similar trend in ion diffusion coefficients was observed in earlier simulations as well. [15, 36]

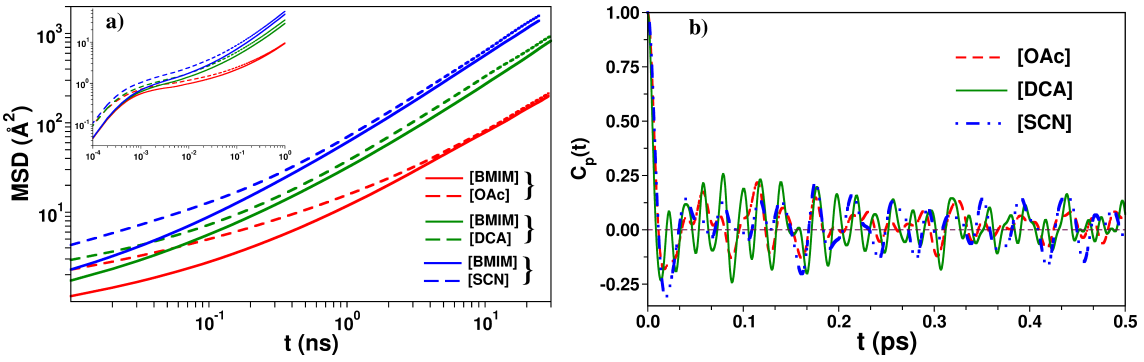

Figure 2B.5: (a) Mean square displacement (MSD) of ions as a function of time at 300 K. Inset shows the MSD at short times focussing on the sub-diffusive nature of transport at those time scales. (b) Normalized full stress tensor autocorrelation functions for ILs at 300 K. [BMIM] is the common cation.

Table 2B.9: Ion self-diffusion coefficients ($\times 10^{-7}$ cm^2/s) calculated employing the refined force field.

Ionic Liquid	T (K)	D_+	D_-
[BMIM][OAc]	300	1.27	1.32
	313	2.39	2.71
	333	5.49	6.52
	343	7.98	8.61
[BMIM][DCA]	300	4.47	5.23
	313	7.04	8.52
	333	12.67	16.27
	343	17.56	19.65
[BMIM][SCN]	300	9.48	9.97
	313	14.65	16.69
	323	18.23	19.44
	333	23.16	26.61

2B.3.7 Viscosity

The initial decay of the stress autocorrelation functions is shown in Figure 2B.5b. The equilibrium viscosity was evaluated from the converged value of the running integral of stress time autocorrelation function. Shear viscosity extracted from MD simulations at different temperature for the systems investigated here are tabulated in Table 2B.10.

The running integral of stress time correlation function for ILs [BMIM][OAc] and [BMIM][DCA] are displayed in Figure 2B.6 demonstrate its convergence.

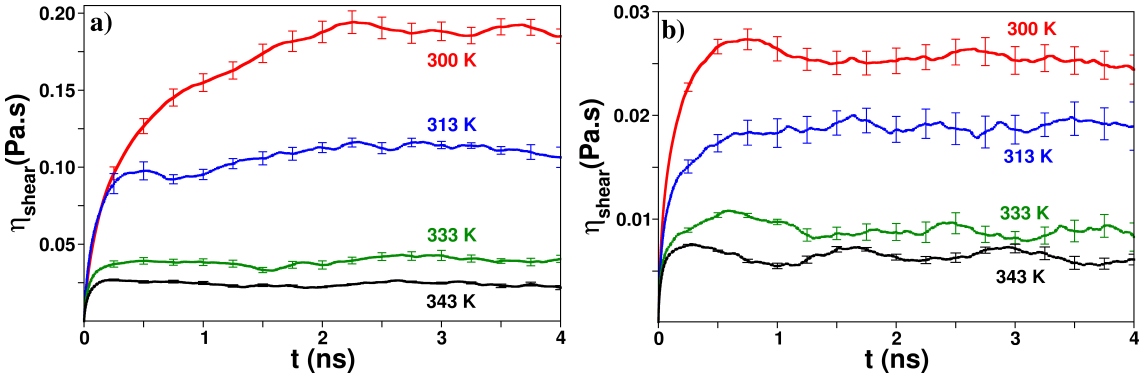

Figure 2B.6: Running values of shear viscosities from the stress time autocorrelation functions for (a) [BMIM][OAc] and (b) [BMIM][DCA]. The standard error on the mean is shown by the bars.

Shear viscosity obtained using this refined potential showed satisfactory agreement with experiments with deviations much less than 20% as shown in Table 2B.10. The

Table 2B.10: Shear viscosity (mPa·s) of ILs obtained from MD simulations, experimental values. [27–29] $\Delta\eta = (\eta^{\mathrm{sim}} - \eta^{\mathrm{exp}})/\eta^{\mathrm{exp}}$.

Ionic Liquid	T (K)	η^{exp}	η^{sim}	$\Delta\eta$ (%)
[BMIM][OAc]	300	210.0	191.5 ±7.0	-8.8
	313	112.0	104.3 ±6.2	-6.8
	333	42.7	38.4 ±3.2	-10.0
	343	28.7	24.1 ±3.0	-16.0
[BMIM][DCA]	300	24.4	25.1 ±3.1	2.8
	313	16.8	18.2 ±2.0	8.3
	333	8.9	8.7 ±1.8	-2.2
	343	6.6	6.4 ±1.6	-3.0
[BMIM][SCN]	300	40.9	35.2 ±4.3	-13.9
	313	27.2	24.1 ±3.3	-11.3
	323	14.1	12.6 ±2.0	-10.5
	333	10.7	8.1 ±1.7	-24.2

maximum deviation (around 24%) was observed for [BMIM][SCN], for which the computed enthalpy of vaporization was also found to be underpredicted by maximum margin (14%). This may be due to the under binding nature of this potential as the electrostatic interaction is much diminished by the total ion charge (±0.65e) as extracted from DDEC/c3 method. The observed trend in computed viscosities; η[BMIM][OAc] > η[BMIM][SCN] > η[BMIM][DCA], showed good agreement with experiment as well. [27–29] The temperature dependence of viscosities obtained from MD simulations showed acceptable consistency with experiment and is displayed in Figure 2B.7a.

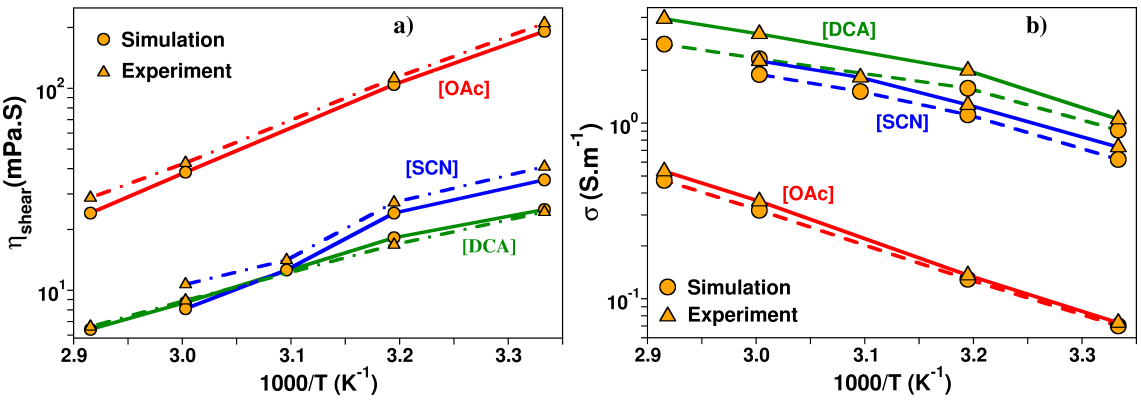

Figure 2B.7: Temperature dependence of (a) shear viscosity and (b) electrical conductivity obtained from simulation and plotted against experiment. [27–29, 37–39] [BMIM] is the common cation.

2B.3.8 Electrical Conductivity

The zero frequency electrical conductivity (σ_{GK}) was estimated from the integral of electric current time autocorrelation function through the Green-Kubo relation. A set of twenty independent trajectories, each of 2 ns in length was used to compute the electric-current autocorrelation functions and finally, the electrical conductivity was averaged over these trajectories. Computed electrical conductivity for these ILs are provided in Table 2B.11.

Table 2B.11: Electrical conductivity (S·m^{-1}) of ILs evaluated from MD simulations and experimental values. [37–39] The uncertainty in computed conductivity is around 0.04 S.m^{-1}. $\Delta\sigma = (\sigma^{\mathrm{Sim}} - \sigma^{\mathrm{Exp}})/\sigma^{\mathrm{Exp}}$.

Ionic Liquid	T (K)	σ^{Exp}	σ^{GK}	$\Delta\sigma$ (%)
[BMIM][OAc]	300	0.073	0.070	-4.11
	313	0.136	0.129	-5.14
	333	0.359	0.319	-11.14
	343	0.532	0.472	-11.27
[BMIM][DCA]	300	1.052	0.912	-13.30
	313	1.570	1.520	-3.18
	333	2.410	2.324	-3.57
	343	2.850	2.716	-4.71
[BMIM][SCN]	300	0.730	0.621	-14.93
	313	1.270	1.115	-12.20
	323	1.820	1.514	-16.81
	333	2.260	1.892	-16.28

In correspondence to its low viscosity, [BMIM][DCA] showed the highest electrical conductivity among the three ILs. The order of electrical conductivity from MD simulation: σ[BMIM][DCA] > σ[BMIM][SCN] >σ[BMIM][OAc], agrees with experiment. [37–39] The temperature dependence of electrical conductivities for these ionic liquids are shown in Figure 2B.7b. The calculated electrical conductivity values are also able to reproduce the experimentally measured conductivities at different temperatures, with the maximum deviation (less than 20%) observed for [BMIM][SCN]. An earlier simulation result obtained for [BMIM][DCA] from a polarizable model [26] underestimated the experiment by only -3% at 298 K, compared to the 13 % deviation obtained by us. However, at 333 K, the polarizable model overestimated the conductivity by 24 %. The origin of these differences between the models and experiment need to be investigated further.

2B.3.9 Incoherent Intermediate Scattering Function

The self part of van Hove function, [40] also known as incoherent (self) intermediate scattering function [F_s(Q,t)], was investigated to discern the nature of relaxation of density correlations of individual ions at different time and length scales (wave vector). This function is defined as [41]

$$F_s(\mathbf{Q},t) = \frac{1}{N}\sum_i \langle exp\{-i\mathbf{Q}[\mathbf{r}_i(t) - \mathbf{r}_i(0)]\}\rangle \tag{2B.3}$$

here, N is the number of ions, $\mathbf{r}_i(t)$ is the position of ion center at time t, and $\mathbf{Q}$ is the reciprocal lattice vector.

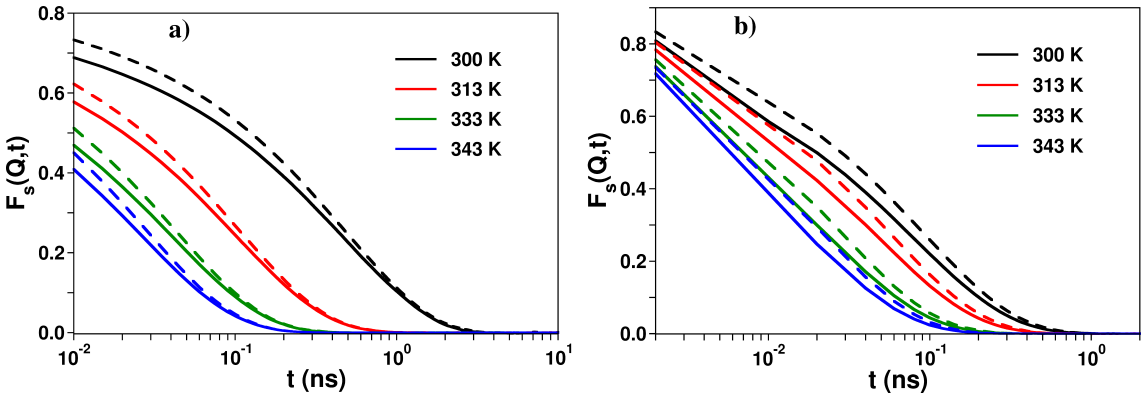

Figure 2B.8: Self-intermediate scattering functions F_s(Q,t) of cations (dashed line) and anions (solid line) of (a) [BMIM][OAc] and (b) [BMIM][DCA] at different temperatures and at Q = 1.4 Å^{-1}.

F_s(Q,t) captures the structural relaxation of ILs. At short timescales, F_s(Q,t) exhibits a fast relaxation (β relaxation) followed by a plateau signifying ions trapped in a cage of counterions. At longer timescales, ions diffuse out leading to the complete relaxation of F_s(Q,t) (α relaxation). [42–49] The decay of F_s(Q,t) for cation and anion of different ILs at a wave vector value of 1.4 Å^{-1} obtained from simulations are displayed in Figure 2B.8. At all temperatures, the structural relaxation of anions is faster than that of cations in all three ILs, consistent with the trend in self-diffusion. [50]

In order to estimate the timescales associated with β (τ_β) and α relaxations (τ_β), F_s(Q,t) were fitted to a modified Kohlrausch-Williams-Watts function [48]

$$F_s(\mathbf{Q},t) = Aexp(-t/\tau_\beta) + (1-A)exp[-(t/\tau_\alpha)^\beta]. \tag{2B.4}$$

The mean relaxation time for the α process is given by [48, 51]

$$\langle\tau_\alpha\rangle = \frac{\tau_\alpha}{\beta}\Gamma\left(\frac{1}{\beta}\right), \tag{2B.5}$$

where Γ is the Gamma function. The top panel of Figure 2B.9a and Figure 2B.9b display the estimated relaxation times $\langle\tau_\alpha\rangle$ and τ_β as a function of temperature in different ILs. A closer investigation showed that τ_α for anions was lower than that of cations, which suggests that the average time to escape from the "cage" formed by their neighboring ions is smaller for anions than that of cations. Similar kind of behavior was also observed in the case of τ_β. The bottom panel of Figure 2B.9a and Figure 2B.9b displays the temperature dependence of the stretching parameters (β) for α relaxation in different ILs. For both cations and anions, β increased with increase in system temperature. Again, values of β for cations were larger than those of anions. β values for these ILs are larger than that reported for [BMIM][PF_6], [47] presumably due to the lower viscosity of ILs studied here. Further β^- is marginally smaller than β^+, implying the larger dynamical heterogeneity of anions.

The dependence of F_s(**Q**,t) on wave vector is shown in Figure 2B.10. At large **Q**, the relaxation behaviour for cations and anions in [BMIM][OAc] are quite similar, while in [BMIM][DCA] or in [BMIM][SCN], their relaxations are decoupled. At smaller **Q**, anions show a faster relaxation than cations. Thus, these observations suggest that the "caging" dynamics is critical in these systems, consistent with earlier results obtained from both experiment and simulation. [52, 53]

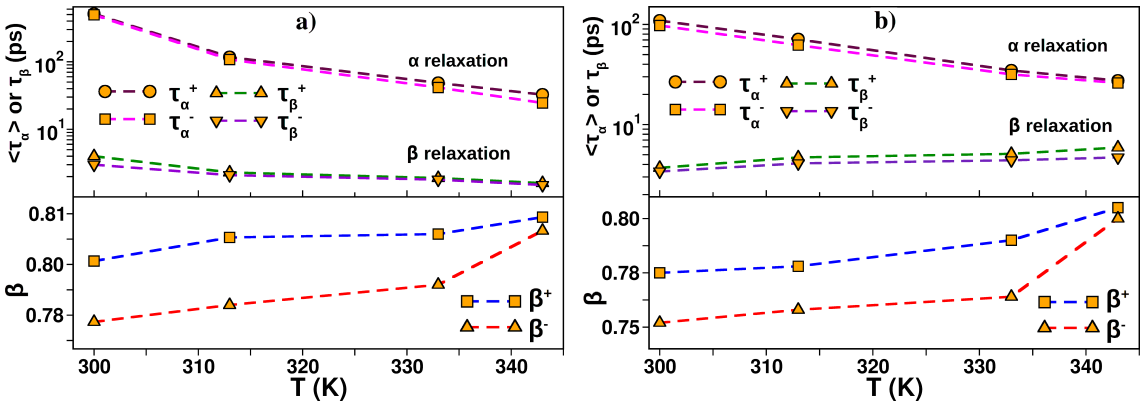

Figure 2B.9: Structural relaxation times τ_β and $\langle\tau_\alpha\rangle$ and the stretching parameter (β) of α relaxation for cations and anions of (a) [BMIM][OAc] and (b) [BMIM][DCA] as a function of temperature.

2B.3.10 Coherent Intermediate Scattering Function

In order to investigate the collective behavior of the system, we have computed the coherent intermediate scattering function F(**Q**,t) defined as; [41]

$$F(\mathbf{Q},t) = \frac{1}{N}\sum_i\sum_j \langle exp\{-i\mathbf{Q}[\mathbf{r}_i(t) - \mathbf{r}_j(0)]\}\rangle. \tag{2B.6}$$

The relaxation of $F(\mathbf{Q},t)$ at different wave vectors (**Q**) at 300 K are displayed in

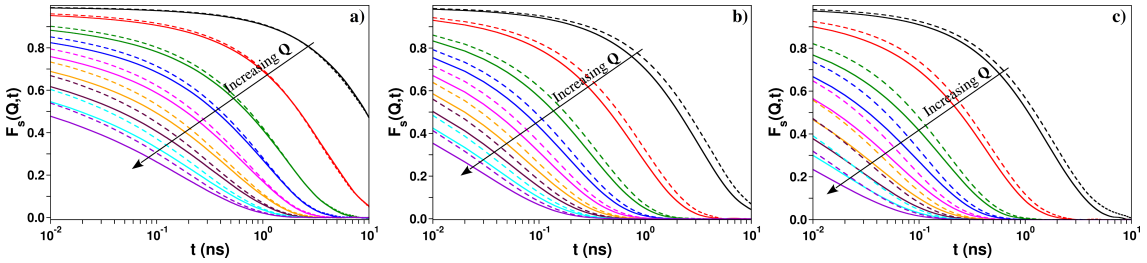

Figure 2B.10: F_s(**Q**,t) of cations (dashed lines) and anions (solid lines) of (a) [BMIM][OAc], (b) [BMIM][DCA], and (c) [BMIM][SCN] at 300 K and at different wave vectors. Following are the values of **Q** (from top to bottom, in $\mathrm{\AA}^{-1}$): 0.25, 0.5, 0.8, 1.0, 1.2, 1.4, 1.6, 1.8, and 2.0.

Figure 2B.11. $F(\mathbf{Q},t)$ showed a two-step relaxation process similar to what was observed in the case of $F_s(\mathbf{Q},t)$.

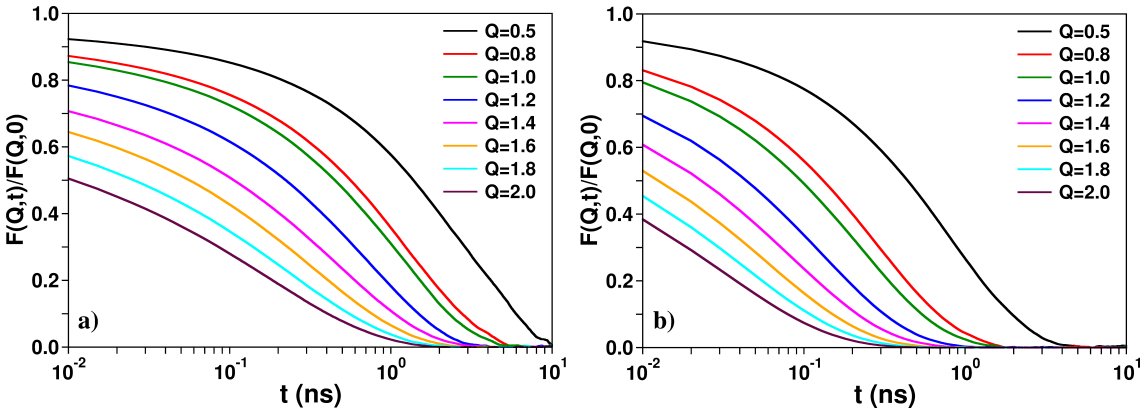

Figure 2B.11: Wave vector dependence of normalized F(**Q**,t) at 300 K for (a) [BMIM][OAc] and (b) [BMIM][DCA].

2B.4 Conclusions

We have prescribed a method to obtain atomic site charges employing periodic density functional theory on the liquid phase of ionic liquids. This approach extends our earlier work (Chapter 2A) which used the DDEC/c3 method [10, 11] on both the crystalline and liquid phases of ILs to obtain atomic charges. The electronic polarization and charge transfer effects are accounted in an effective manner. 1-butyl-3-methylimidazolium based cation combined with three different anion types; acetate ([CH_3COO]), dicyanamide ([$N(CN)_2$]), and thiocyanate ([SCN]) were considered. As before, charges on ions were lesser than unity and were calculated to be -0.78e, -0.74e and -0.65e for DCA, OAc and SCN, respectively.

In order to obtain a transferable force field, these set of partial charges were combined with the well established CL&P force field developed by Lopes and co-workers. [12–14] Consequently, its non-bonded, 1-4 and torsional interaction parameters were refined. In

this refinement procedure, we have adopted three potential energy surface scans in the gas phase for isolated ion pairs as our benchmark. Lennard-Jones parameters which best fitted all these three scans was taken for the condensed phase simulations.

The current scheme considers explicitly the effect of charge transfer between ions, while the effect of polarization in the condensed state is captured in an effective, mean field sense. The exact contribution of each of these effects which resulted in bettering the prediction of transport properties is unknown and could be an object of study in future. The force field parameters are transferable and it is possible to study ILs containing imidazolium cations with varying alkyl tail length. The transferability of the parameters across temperature has been demonstrated to the best extent possible – through the nearly quantitative reproduction of density, surface tension, shear viscosity, and electrical conductivity. Thus, we are confident that the parameters are robust.

Classical molecular dynamics simulations have been carried out for the three ILs modeled with this new set of potential parameters at four different state points. Computed static properties, such as densities, heat of vaporization, surface tension were in good agreement with experimental data. Various methods were employed to compute transport properties including self-diffusion coefficients, ionic conductivity, and shear viscosity. Results from simulations were consistent with the experimental findings. Cations were observed to diffuse slower than anions, consistent with previous simulations. [15, 36] Single ion dynamics were investigated through incoherent intermediate scattering function. The results suggested that the anions possess a marginally higher dynamically heterogeneous environment than the cations.

Green-Kubo formulation was employed to calculate the ionic conductivity and shear viscosity of the liquids. These collective quantities were predicted to within 20-25% of experimental results, which is not unreasonable given the complexity of these fluids. Despite these differences, this nonpolarizable force field can reproduce the experimental trends with temperature remarkably well. A drawback of the current approach is in modeling mixtures of ILs having the same cation but different anions. In the current framework, the cation charge in the two pure ILs are different, which poses an issue when the ILs are mixed. We hope to address such challenges in the future.

Bibliography

[1] Dommert, F.; Wendler, K.; Berger, R.; Luigi, D. S.; Holm, C. *ChemPhysChem* **2012**, *13*, 1625–1637.

[2] Blundell, R. K.; Licence, P. *Chem. Commun.* **2014**, *50*, 12080–12083.

[3] Hurisso, B. B.; Lovelock, K. R. J.; Licence, P. *Phys. Chem. Chem. Phys.* **2011**, *13*, 17737–17748.

[4] Men, S.; Lovelock, K. R. J.; Licence, P. *Phys. Chem. Chem. Phys.* **2011**, *13*, 15244–15255.

[5] Chaban, V. *Phys. Chem. Chem. Phys.* **2011**, *13*, 16055–16062.

[6] Morrow, T. I.; Maginn, E. J. *J. Phys. Chem. B* **2002**, *106*, 12807–12813.

[7] Schröder, C. *Phys. Chem. Chem. Phys.* **2012**, *14*, 3089–3102.

[8] Dommert, F.; Wendler, K.; Qiao, B.; Site, L. D.; Holm, C. *J. Mol. Liq.* **2014**, *192*, 32 – 37.

[9] Zhang, Y.; Maginn, E. J. *J. Phys. Chem. B* **2012**, *116*, 10036–10048.

[10] Manz, T. A.; Sholl, D. S. *J. Chem. Theory Comput.* **2010**, *6*, 2455–2468.

[11] Manz, T. A.; Sholl, D. S. *J. Chem. Theory Comput.* **2012**, *8*, 2844–2867.

[12] Lopes, J. N. C.; Pádua, A. A. H. *J. Phys. Chem. B* **2004**, *108*, 2038–2047.

[13] Lopes, J. N. C.; Pádua, A. A. H. *J. Phys. Chem. B* **2004**, *108*, 16893–16898.

[14] Lopes, J. N. C.; Pádua, A. A. H. *J. Phys. Chem. B* **2006**, *110*, 19586–19592.

[15] Chandran, A.; Prakash, K.; Senapati, S. *Chem. Phys.* **2010**, *374*, 46–54.

[16] Chaumont, A.; Wipff, G. *Inorg. Chem.* **2009**, *48*, 4277–4289.

[17] Hutter, J.; Iannuzzi, M.; Schiffmann, F.; VandeVondele, J. *WIREs Comput. Mol. Sci.* **2014**, *4*, 15–25.

[18] Perdew, J. P.; Burke, K.; Ernzerhof, M. *Phys. Rev. Lett.* **1996**, *77*, 3865–3868.

[19] Goedecker, S.; Teter, M.; Hutter, J. *Phys. Rev. B* **1996**, *54*, 1703–1710.

[20] Plimpton, S. *J. Comput. Phys.* **1995**, *117*, 1–19.

[21] Nosé, S. *J. Chem. Phys.* **1984**, *81*, 511–519.

[22] Nosé, S. *Mol. Phys.* **1984**, *52*, 255–268.

[23] Martyna, G. J.; Klein, M. L.; Tuckerman, M. *J. Chem. Phys.* **1992**, *97*, 2635–2643.

[24] Martínez, L.; Andrade, R.; Birgin, E. G.; Martínez, J. M. *J. Comp. Chem.* **2009**, *30*, 2157–2164.

[25] Humphrey, W.; Dalke, A.; Schulten, K. *J. Mol. Graphics* **1996**, *14*, 33–38.

[26] Borodin, O. *J. Phys. Chem. B* **2009**, *113*, 11463–11478.

[27] Almeida, H. F. D.; Passos, H.; da Silva, J. A. L.; Fernandes, A. M.; Freire, M. G.; Coutinho, J. A. P. *J. Chem. Eng. Data* **2012**, *57*, 3005–3013.

[28] Sánchez, L. G.; Espel, J. R.; Onink, F.; Meindersma, G. W.; Haan, A. B. *J. Chem. Eng. Data* **2009**, *54*, 2803–2812.

[29] Vakili-Nezhaad, G.; Vatani, M.; Asghari, M.; Ashour, I. *J. Chem. Thermodyn.* **2012**, *54*, 148–154.

[30] Ma, X.-X.; Wei, J.; Zhang, Q.-B.; Tian, F.; Feng, Y.-Y.; Guan, W. *Ind. Eng. Chem. Res.* **2013**, *52*, 9490–9496.

[31] Chambreau, S. D.; Vaghjiani, G. L.; To, A.; Koh, C.; Strasser, D.; Kostko, O.; Leone, S. R. *J. Phys. Chem. B* **2010**, *114*, 1361–1367.

[32] Deyko, A.; Lovelock, K. R. J.; Corfield, J.-A.; Taylor, A. W.; Gooden, P. N.; Villar-Garcia, I. J.; Licence, P.; Jones, R. G.; Krasovskiy, V. G.; Chernikova, E. A.; Kustov, L. M. *Phys. Chem. Chem. Phys.* **2009**, *11*, 8544–8555.

[33] Liu, Z.; Huang, S.; Wang, W. *J. Phys. Chem. B* **2004**, *108*, 12978–12989.

[34] Bhargava, B. L.; Balasubramanian, S. *J. Chem. Phys.* **2007**, *127*, 114510.

[35] Payal, R. S.; Balasubramanian, S. *Phys. Chem. Chem. Phys.* **2013**, *15*, 21077–21083.

[36] Bedrov, D.; Borodin, O. *J. Phys. Chem. B* **2010**, *114*, 12802–12810.

[37] Sterner, E. S.; Rosol, Z. P.; Gross, E. M.; Gross, S. M. *J. Appl. Polym. Sci.* **2009**, *114*, 2963–2970.

[38] Xu, A.; Zhang, Y.; Li, Z.; Wang, J. *J. Chem. Eng. Data* **2012**, *57*, 3102–3108.

[39] Yoshida, Y.; Baba, O.; Saito, G. *J. Phys. Chem. B* **2007**, *111*, 4742–4749.

[40] Van Hove, L. *Phys. Rev.* **1954**, *95*, 249–262.

[41] Herwig, K. W.; Wu, Z.; Dai, P.; Taub, H.; Hansen, F. Y. *J. Chem. Phys.* **1997**, *107*, 5186–5196.

[42] Habasaki, J.; Ngai, K. L. *J. Chem. Phys.* **2008**, *129*, 194501.

[43] Liu, H.; Maginn, E. *J. Chem. Phys.* **2011**, *135*, 124507.

[44] Ishida, T.; Shirota, H. *J. Phys. Chem. B* **2013**, *117*, 1136–1150.

[45] Pal, T.; Biswas, R. *J. Chem. Phys.* **2014**, *141*, 104501.

[46] Del Pópolo, M. G.; Voth, G. A. *J. Phys. Chem. B* **2004**, *108*, 1744–1752.

[47] Sarangi, S. S.; Zhao, W.; Müller-Plathe, F.; Balasubramanian, S. *ChemPhysChem* **2010**, *11*, 2001–2010.

[48] Triolo, A.; Russina, O.; Arrighi, V.; Juranyi, F.; Janssen, S.; Gordon, C. M. *J. Chem. Phys.* **2003**, *119*, 8549–8557.

[49] Hu, Z.; Margulis, C. J. **2006**, *103*, 831–836.

[50] Zhang, Y.; Maginn, E. J. *J. Phys. Chem. Lett.* **2015**, *6*, 700–705.

[51] Müller-Plathe, F.; van Gunsteren, W. F. *J. Chem. Phys.* **1995**, *103*, 4745–4756.

[52] Shirota, H.; Castner, E. W. *J. Phys. Chem. A* **2005**, *109*, 9388–9392.

[53] Hu, Z.; Huang, X.; Annapureddy, H. V. R.; Margulis, C. J. *J. Phys. Chem. B* **2008**, *112*, 7837–7849.

Chapter 3

Vibrational Signatures of Cation-Anion Hydrogen Bonding in Ionic Liquids: A Periodic Density Functional Theory and Molecular Dynamics Study

3.1 Introduction

Knowledge of intermolecular forces is a requisite for understanding the structure and properties of ionic liquids (ILs). In particular, the subtle balance between Coulomb forces, hydrogen bonds, and dispersion forces plays a crucial role in determining their unique properties. [1, 2] Ionic motions in ILs have been characterised by a variety of experimental methods. [3–15] In a molten salt, the cation rattles within a cage formed by the anions and vice versa. The rattling frequency is typically in the far infrared (FIR) region and can be studied using vibrational spectroscopy. It carries the signature of cation-anion interactions; the band position, although strictly related to the curvature of the potential energy surface, is also usually correlated with the strength of the interaction. Naturally, hydrogen bonded ion partners exhibit a far-IR band at higher wave numbers than ones which do not. [1]

Many intermolecular interactions contribute to this region of frequency, making it difficult to distinguish their contributions properly. Some research groups have suggested that long-range electrostatic interactions contribute to these bands rather than hydrogen

bonding. [16, 17] Sarangi *et al.* [18] proposed that the low frequency band arises primarily from interionic interactions and demonstrated that short-range interactions alone can reproduce it.

Recently, Ludwig *et al.* have studied the FIR spectra of protic ionic liquids (PILs) such as tetramethylammonium nitrate and trimethylammonium nitrate. [19] In $[Me_3NH][NO_3]$, they observed a distinct vibrational mode at 171 cm^{-1} which was not present in $[Me_4N][NO_3]$. They have also performed zero temperature, density functional theory (DFT) calculations of small clusters of neutral ion pairs in gas phase. Combining these with NMR data, they concluded that this band represents vibrations associated with anion-cation interaction and can specifically be assigned to the $^{+}$N-H$\cdots NO_3^{-}$ hydrogen bond stretching mode. Hayes *et al.* studied hydrogen bonding in various ammonium ion based PILs using neutron diffraction. [20] Two types of H-bond were observed; one with a short H-bond distance (1.6 Å to 1.7 Å) and largely linear. The other one had a longer H-bond distance (2.4 Å to 2.6 Å) and was bent, causing the ionic liquid to melt at a lower temperature. Fumino *et al.* have combined FIR vibrational spectroscopy with *ab initio* and DFT calculations to investigate cation-anion interactions in PILs in terms of hydrogen bonding. [21–24] They suggested that the vibrational band representing the cation-anion interaction can be identified from other low-frequency vibrational modes. While *ab initio* quantum chemical or DFT calculations have been performed on ion-pair clusters (in gas phase) to interpret experimental observations, it is imperative that condensed phase vibrational spectra too are explored theoretically, which to our knowledge, has not been attempted yet.

In general, while quantum chemical calculations are carried out in gas phase and empirical potential based molecular dynamics (MD) simulations on the condensed phase, *ab initio* molecular dynamics (AIMD) simulations provide a route to study intermolecular vibrations in condensed systems with little in-built empiricism. Here, our main objective is to study the crystalline states of ILs wherein the coordination environment of an ion is quite similar to that in bulk ILs. We have carried out Hessian calculations (using periodic DFT as well as force field) of the crystalline states of three alkylammonium based ILs, dimethylammonium bromide ($[(CH_3)_2NH_2][Br]$), trimethylammonium bromide ($[(CH_3)_3NH][Br]$) and tetramethylammonium bromide ($[(CH_3)_4N][Br]$). Results from these simulations are reinforced by quantum chemical calculations of ion pairs and of ion pair dimers in gas phase. These calculations are also augmented by calculations of NMR chemical shifts of hydrogen atoms obtained from crystalline and gas phase ion pair calculations. Empirical force field based MD simulations have also been employed to compute the power spectrum of the crystalline form of these ILs.

3.2 Methodology and Simulation Details

3.2.1 Gas Phase

Calculations using atom-centered basis sets. Geometries and vibrational spectra of ion pairs of these salts in gas phase were obtained using the Gaussian09 code. [25] In order to have a complete description of electron correlation, geometry optimizations were performed at MP2/aug-cc-pVDZ level of theory. Gaussview [26] was used to model the initial geometries. Optimization was performed by employing the keywords "opt= verytight" and "scf=verytight". Furthermore, an ultrafine grid was used in the DFT calculations. Normal mode calculations of these systems at the harmonic level showed no imaginary frequencies, indicating that they were indeed at a minimum. We have also studied clusters of two ion pairs for all these salts at the same level of theory as mentioned above.

Calculations using plane-wave basis sets. DFT calculations for isolated ion pairs were performed using CPMD-3.13.2 package. [27] The energy and density cutoff were 150 Ry and 900 Ry, respectively. Norm conserving Troullier-Martins pseudopotentials [28] were used to account for the effect of all the core electrons and of the nucleus on the valence electrons. Exchange and correlation effects were treated through the Perdew, Burke and Ernzerhof (PBE) functional. [29] The effect of van der Waals interactions (vdW) was considered through Grimme's method. [30] Optimizations under isolated conditions were carried out in a cubic box of length 12 Å and the Poisson equation was solved using the Hockney method. [31] The gradient on the wave functions and on the nuclear positions were optimized with convergence criteria of 10^{-7} and 10^{-5} au, respectively. The minimized structure was used to obtain the vibrational spectrum.

3.2.2 Crystalline Phase

Periodic DFT calculations. Initial cell parameters and atom positions were taken from Cambridge crystal structure database. [32–34] A description of all the systems studied here is provided in Table 3.1. Other details of the calculations are the same as discussed in DFT calculations for ion pairs. Each of these systems was optimized by varying the cell parameters and coordinates iteratively until the energy minimum was found. Calculated cell parameters differed by less than 0.5% of their experimental values (see Table 3.2). Forces on atoms were optimized with a convergence criterion of 10^{-5} au. Normal mode analysis within the harmonic approximation were carried out on the final geometries.

Classical MD simulations. Classical molecular dynamics simulations of crystalline phases of these salts have been carried out using LAMMPS [38]. Interaction parameters to model the PILs have been taken from the work of Lopes and Padua. [39] The simulations

Table 3.1: Summary of cell parameters and supercell dimensions of all the crystalline systems employed in AIMD simulations.

System	Cell parameter						Supercell	Reference
	a (Å)	b (Å)	c (Å)	$\alpha(^o)$	β (^{o})	γ (^{o})		
$[(CH_3)_2NH_2][Br]$	13.861	5.469	13.359	90.0	93.09	90.0	(1x2x1)	Ref. [35]
$[(CH_3)_3NH][Br]$	5.349	8.023	6.790	90.0	105.70	90.0	(2x2x2)	Ref. [36]
$[(CH_3)_4N][Br]$	7.708	7.708	5.498	90.0	90.00	90.0	(2x2x2)	Ref. [37]

Table 3.2: Calculated cell parameters of crystals compared with experimental data. References for the experimental data are as provided in Table 3.1.

System	Method	a (Å)	b (Å)	c (Å)	β (^{o})
$[(CH_3)_2NH_2][Br]$	exp.	13.861	10.938	13.359	93.09
	calc.	13.782	10.854	13.274	92.90
$[(CH_3)_3NH][Br]$	exp.	10.698	16.046	13.580	105.70
	calc.	10.583	15.885	13.460	105.67
$[(CH_3)_4N][Br]$	exp.	15.416	15.416	10.996	90.00
	calc.	15.266	15.266	10.936	90.00

were performed in the canonical ensemble using the Nosé-Hoover thermostat. [40–42] Equations of motion were integrated using the velocity Verlet algorithm with a time step of 1 fs. All C-H covalent bonds were constrained using the SHAKE algorithm as implemented in LAMMPS. [38] The ewald/disp solver was used to calculate the long-range interactions with a precision of 10^{-5}. The real space cutoff distance was 11 Å. Each system was equilibrated for 5 ns (in NPT ensemble) which was followed by 10 ns production run in the NVT ensemble. Atom coordinates were stored every 100 ps to obtain 100 snapshots for each PIL. Details of simulation cell parameters and simulation conditions are described in Table 3.3.

Energy minimizations were performed on the 100 configurations selected from the classical MD trajectory for each ionic liquid using the conjugate gradient method in

Table 3.3: Summary of supercell dimensions, number of ion pairs and temperature in classical molecular dynamics simulations of different PILs in their crystalline states.

System	Supercell	No. of ion pairs	No. of atoms	Temperature (K)
$[(CH_3)_2NH_2][Br]$	2x5x2	160	1920	143
$[(CH_3)_3NH][Br]$	5x3x4	120	1800	100
$[(CH_3)_4N][Br]$	3x3x5	90	1620	293

LAMMPS. A normal-mode analysis (NMA) code developed earlier within our group was used to calculate the Hessian matrix of the potential energy with respect to the atom coordinates. [43] While the eigenvalues of the Hessian are related to frequencies, the eigenvectors correspond to atomic displacements in a mode. The frequency spectrum was calculated using a bin width of 2 cm^{-1} and was averaged over the results for the 100 quenched configurations.

We have also calculated the vibrational density of states (VDOS) from the MD trajectory as the Fourier transform of the time autocorrelation functions of the atomic velocities (VACF). This can be expressed as

$$I(\omega) = \frac{1}{k_B T} \sum_j m_j \left[\frac{1}{2\pi} \int_{-\infty}^{\infty} exp(-i\omega t) \langle \mathbf{v}_j(0).\mathbf{v}_j(t) \rangle dt \right] \tag{3.1}$$

where $\mathbf{v}_j(t)$ is the velocity of atom type j at time t. To calculate this VACF, a separate MD trajectory was generated for a duration of 100 ps and atomic velocities were stored at each time step.

***Ab initio* MD simulations.** Born-Oppenheimer molecular dynamics (BOMD) simulations of crystalline phases of these salts were performed using CPMD-3.13.2 software. [27] The temperature of ions was set to that value at which the crystal structures were determined experimentally (143 K, 100 K and 293 K for $[Me_2NH_2][Br]$, $[Me_3NH][Br]$ and $[Me_4N][Br]$, respectively). A Nosé-Hoover chain thermostat [42] was used with a coupling constant of 1500 cm^{-1}. Equations of motion were integrated with a time step of 15 au. For these simulations, an energy cutoff of 85 Ry was used to expand the wave function, and four times this value was used for the electronic density. The systems were equilibrated for 2 ps followed by production runs for 12 ps. Velocity autocorrelation function of the ions were calculated and VDOS was obtained from the Fourier transform of this function.

All the systems were visualized using Mercury, [44] VMD, [45] and Jmol [46]. Atomic displacements were visualized in Jmol [46] for the assignment of modes.

3.2.3 NMR Chemical Shift

Gas phase. Geometries of ion pairs were optimized at B3LYP/6-311++G(d,p) level of theory using Gaussian09 [25] software. The quenched geometries were used to obtain ^1H NMR chemical shielding at the same level of theory. Chemical shifts were also calculated for the crystals using the periodic DFT code CPMD-3.13.2. [27] Chemical shift calculations for gas phase ion pairs obtained from CPMD-3.13.2. were benchmarked against those from Gaussian in Table 3.4. The $\delta(^1H)$ values calculated using plane-wave basis sets is able to reproduce the chemical shifts obtained from atom-centered basis sets.

Table 3.4: Comparison of $\delta(^1\mathrm{H})$ values in ion-pair of alkylammonium salts in their gas phase calculated using atom-centered basis sets and plane-wave basis sets.

System	$\delta(^1\mathrm{H})$	
	atom-centered basis set	plane-wave basis set
$[(CH_3)_2NH_2][I]$	12.04	17.56
$[(CH_3)_2NH_2][Br]$	17.37	18.53
$[(CH_3)_2NH_2][Cl]$	18.75	19.68
$[(CH_3)_3NH][I]$	11.76	16.62
$[(CH_3)_3NH][Br]$	16.56	17.79
$[(CH_3)_3NH][Cl]$	17.82	18.72

Crystalline phase. NMR chemical shifts were also studied for the crystalline systems consisting of 1 unit cell. Geometry optimization was performed under periodic boundary condition, with a convergence criterion of 10^{-4} au for the forces on atoms. In these calculations which employed the PBE functional, [29] an energy cutoff of 80 Ry was used for the wave function. NMR resonance frequencies were obtained using a method [47] that is implemented in CPMD. It has been proven to capture the effect of hydrogen bonding and has yielded results in good agreement with experiments. [48–51]

The shielding constant of tetramethylsilane (TMS) was used as reference; thus, $\delta(\mathrm{H}) = \sigma(\mathrm{TMS}) - \sigma(\mathrm{H})$, where $\sigma(\mathrm{TMS})$ is the shielding calculated for an isolated TMS molecule at the same level of theory.

3.3 Results and Discussion

Gas Phase. Normal mode analysis was performed for three alkylammonium salts in gas phase. Frequencies which are present above 400 cm^{-1} can be attributed to intramolecular modes and hence are not of interest here. The calculated spectra exhibit bands at sub-200 cm^{-1} which are usually attributed to unspecific librational motions. [19] The far-infrared absorption band red shifts with decreasing propensity for the formation of cation-anion hydrogen bond i.e., from dimethyl based cation to the tetramethyl based one.

Vibrational spectra obtained at MP2/aug-cc-pVDZ level for an ion pair of $[(CH_3)_2NH_2][Br]$ showed a characteristic mode at 221 cm^{-1}, whereas for $[(CH_3)_3NH][Br]$ and $[(CH_3)_4N][Br]$, it was present at 193 cm^{-1} and 146 cm^{-1}, respectively. Harmonic frequencies obtained from gas phase calculations using the plane wave basis set (i.e., within CPMD) were consistent with the values calculated with localised basis set. The optimized geometries of ion pairs of these three alkylammonium salts are compared in Figure 3.1. The corresponding frequencies for the three ion pairs calculated with CPMD were found to be: 212 cm^{-1}, 201 cm^{-1}, and 148 cm^{-1}, respectively. The calculated spectra (up to 300 cm^{-1}) of these

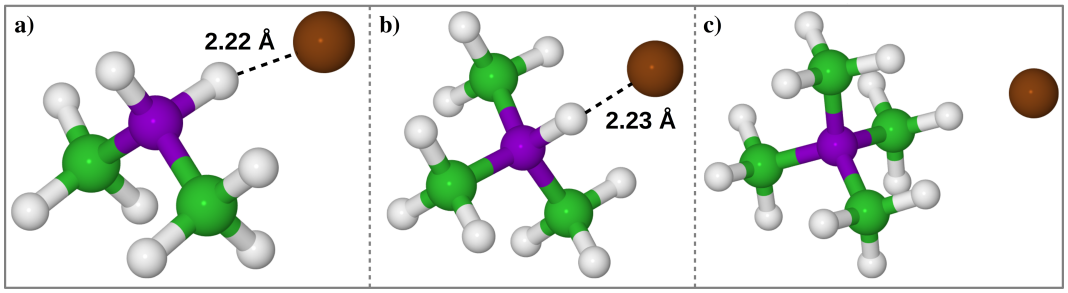

Figure 3.1: Optimized geometries of ion pairs of three alkylammonium salts at MP2/aug-cc-pVDZ level of theory. (a) $[(CH_3)_2NH_2][Br]$, (b) $[(CH_3)_3NH][Br]$, and (c) $[(CH_3)_4N][Br]$. Color scheme: nitrogen, violet; carbon, green; hydrogen, white; bromine, ochure.

alkylammonium salts are plotted in Figure 3.2a. Harmonic frequencies for clusters of two ion pairs of each of these salts were also calculated at MP2/aug-cc-pVDZ level. A similar trend in frequencies in the low wave number region was observed with increasing number of methyl groups on the cation; however, the frequencies were distinctly lower than those obtained for a single ion pair. Frequencies obtained for dimers of $[(CH_3)_2NH_2][Br]$, $[(CH_3)_3NH][Br]$, and $[(CH_3)_4N][Br]$ are 197 cm^{-1}, 181 cm^{-1}, and 144 cm^{-1}, respectively. The red shift in the frequencies with increasing numbers of ion pairs points to the necessity to study either large clusters in gas phase (computationally forbidding) or adopt periodic DFT calculations.

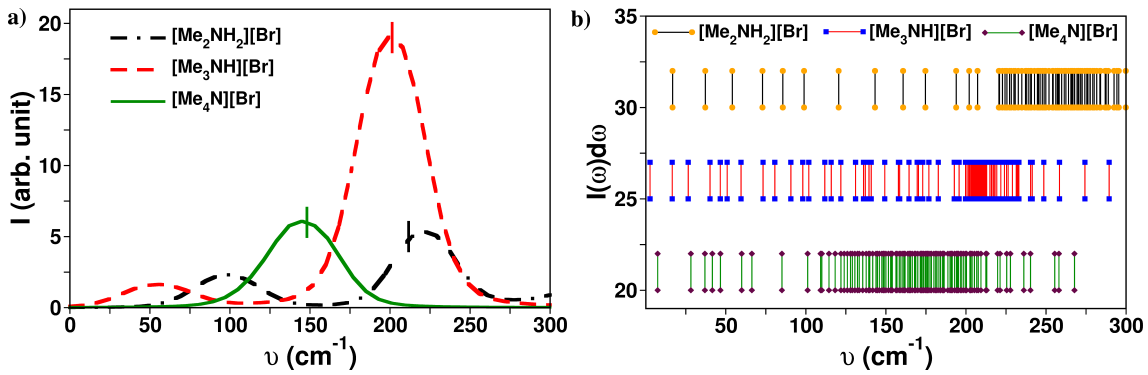

Figure 3.2: (a) Far-IR spectra of different alkylammonium salts obtained from ion pair calculations at MP2/aug-cc-pVDZ level. Short vertical lines are values of frequencies obtained from DFT calculations of ion pairs using CPMD. (b) Stick pattern of calculated far-IR spectra obtained through Hessian calculations of crystalline (based on periodic DFT calculations) phases of alkylammonium ILs.

We examine the data in terms of cation-anion hydrogen bonding. In $[Me_2NH_2][Br]$, there are two acidic protons on the nitrogen atom, whereas in $[Me_3NH][Br]$, only one such acidic hydrogen is present. In $[Me_4N][Br]$, there are no acidic protons, thus depriving it

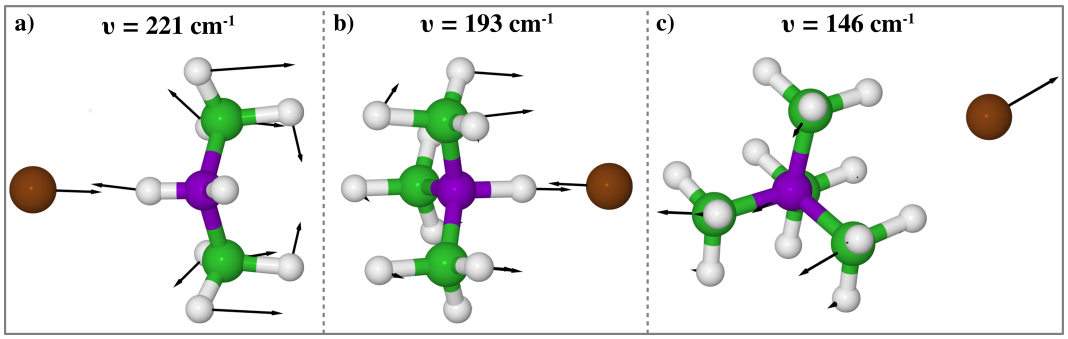

Figure 3.3: Inter-ionic low frequency modes in ion pair of (a) $[(CH_3)_2NH_2][Br]$, (b) $[(CH_3)_3NH][Br]$, and (c) $[(CH_3)_4N][Br]$ as studied through MP2/aug-cc-pVDZ level calculations in gas phase. The atomic displacement vectors are shown as arrows and are scaled by a factor for better visualization. Color scheme: nitrogen, violet; carbon, green; hydrogen, white; bromine, ochure.

of any hydrogen bonding interaction with the anion. Going from the dimethyl- to tetramethylammonium cation, the hydrogen bond formation ability decreases, which considerably influences the far-IR band position. The "inductive effect" also plays a crucial role here. The transmission of charge in a molecule through a chain of atoms by electrostatic induction is known as inductive effect, which can be either positive or negative in character. From the dimethyl- to the tetramethyl- group, the electron releasing character increases. This would lead to lesser charge transfer into the N-H antibonding orbital, as the electron density at ammonium nitrogen increases - indicating a weaker hydrogen bond. This leads to a red shift in the frequency of the intermolecular mode as the hydrogen bond weakens. Therefore, it is clear that the characteristic frequency band represents anion-cation interaction and can be assigned to $^{+}$N-H$\cdots$Br^{-} hydrogen bond. Visualization of the atomic displacements of these vibrational modes clearly indicate the H-bonding stretching characteristic as shown in Figure 3.3.

Crystal Phase - DFT. Thus far, we discussed the FIR vibrational modes of one ion pair in gas phase. As mentioned earlier, condensed phase effects are significant and discernible in the far-IR region of the vibrational spectrum. Thus, we have performed Hessian calculations on the crystalline phase of these three salts as well. These intermolecular mode frequencies were found to be consistently higher than ones calculated for isolated ion pairs. A stick pattern of the calculated spectra for these salts is shown in Figure 3.2b. A group of vibrational frequencies for dimethyl-, trimethyl-, and tetramethylammonium bromide, are located around 248 cm^{-1}, 209 cm^{-1}, and 162 cm^{-1}, respectively. Thus, the trend observed in the gas phase vibrational analysis is present in the crystalline phase of these ammonium salts as well. In both set of calculations, an increase in the number of H-bonding sites on

the cation blue shifts the intermolecular vibrational mode. Atomic displacement vectors corresponding to a specific cation-anion vibrational mode at low wave numbers in the three different salts in their crystalline states are shown in Figure 3.4.

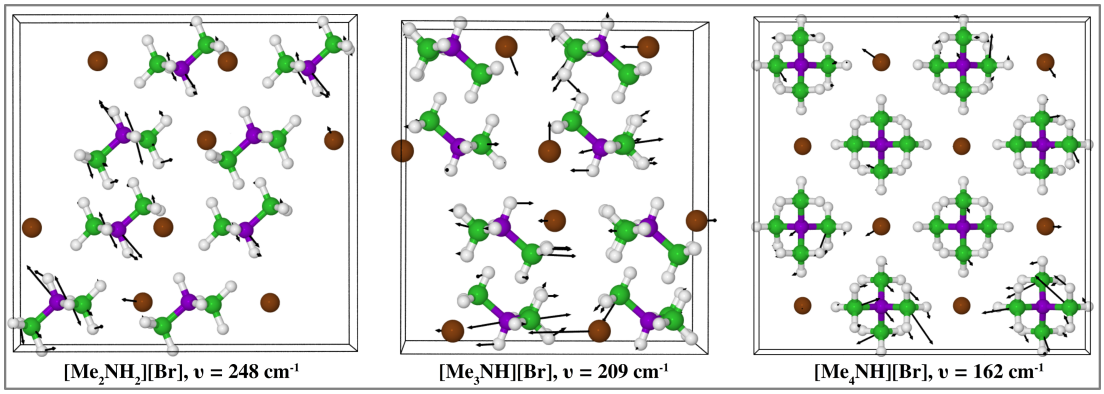

Figure 3.4: Inter-ionic character of selected modes in crystalline alkylammonium salts calculated using periodic DFT calculations through a diagonalization of the Hessian within the harmonic approximation. Atomic displacement vectors are shown as arrows and are scaled by an arbitrary factor for clarity. Color scheme: nitrogen, violet; carbon, green; hydrogen, white; bromine, ochure.

The interionic character of the modes at low frequencies for these alkylammonium salts have so far been examined through zero temperature Hessian calculations. In order to substantiate our observations, we have also performed finite temperature MD simulations of these salts in their crystalline states.

Crystal Phase - Empirical Potential. As described in the earlier section, the VDOS were obtained from both normal-mode analysis (NMA) and as the power spectrum of autocorrelation functions of atomic velocities from a classical MD (generated with empirical potential) trajectory. The density of states for the three crystals obtained from these two approaches are shown in Figure 3.5. The number and intensity of such imaginary frequencies is insignificant (see inset of Figure 3.5a). A prominent feature around 200 cm^{-1} is observed for $[(CH_3)_2NH_2][Br]$ and $[(CH_3)_3NH][Br]$, which is absent in the spectrum of $[(CH_3)_4N][Br]$. Instead, we can clearly see a gap in the VDOS for $[(CH_3)_4N][Br]$. A similar, but narrower gap is observed for $[(CH_3)_3NH][Br]$. The VDOS for $[(CH_3)_2NH_2][Br]$ is devoid of such a gap.

Figure 3.6 displays atomic displacements of modes obtained by diagonalizing the Hessian determined via the empirical force field. The acidic protons (N-H) mainly contribute to the modes in the frequency range 200-240 cm^{-1} (Figure 3.6a) for $[(CH_3)_2NH_2][Br]$; while for $[(CH_3)_3NH][Br]$, similar protons contribute to modes in the range 185-200 cm^{-1} (Figure 3.6b).

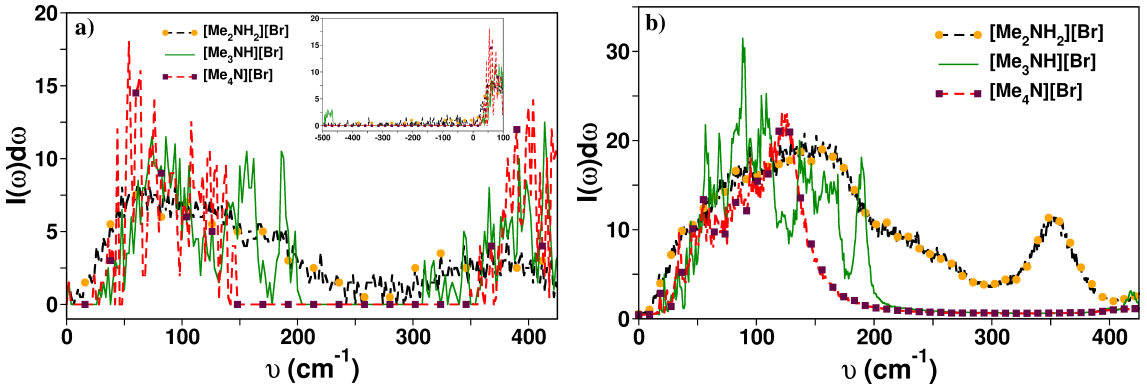

Figure 3.5: Comparison of the low frequency region of vibrational density of states (VDOS) obtained from (a) a normal-mode analysis (NMA) and (b) as the power spectrum of time autocorrelation functions of atomic velocities from a classical MD trajectory, for the three PILs in their crystalline states. Inset in (a) shows imaginary modes present in the power spectrum obtained from NMA calculations.

The hydrogen bond network in the PILs are displayed in Figure 3.6c and Figure 3.6d. Each bromide anion in $[(CH_3)_2NH_2][Br]$ forms hydrogen bonds with two acidic hydrogens while in $[(CH_3)_3NH][Br]$, it can form only one. The radial distribution function between bromide and the acidic hydrogen atom (N_H) obtained from the experimental crystal structure (single configuration) are shown in Figure 3.7a. The mean Br-H distance in $[(CH_3)_3NH][Br]$ is slightly larger than in $[(CH_3)_2NH_2][Br]$; as expected, the coordination number is two and one for $[(CH_3)_2NH_2][Br]$ and $[(CH_3)_3NH][Br]$, respectively. The atomic displacements obtained using NMA code in the region 50 - 100 cm^{-1} are shown in Figure 3.7b, and it can be seen that the bromide anions mainly contribute to the modes present in this range.

Crystal Phase - *Ab initio* MD Simulations. The AIMD trajectory was used to calculate the autocorrelation function of the ion velocities and the Fourier transform of this function yields the VDOS. The density of states for the three salts in their crystalline states obtained from finite temperature AIMD simulations are shown in Figure 3.8. Consistent with the results from Hessian calculations, the low frequency band red shifts as the number of N_H protons is reduced. The trend in the position of the low frequency band observed in the Hessian calculations is also present in the VDOS of these salts in their crystalline states. As $[(CH_3)_4N][Br]$ does not have any cation-anion hydrogen bonding, the low wave number peaks are a signature of only electrostatic and other short-range interactions between the ions. The bands for $[(CH_3)_3NH][Br]$ and $[(CH_3)_2NH_2][Br]$ are modulated further by the cation-anion hydrogen bond. The influence of the cation-anion hydrogen bond is also reflected in the high wave number region (> 3000 cm^{-1}). Due to the formation of more hydrogen bonds in $[(CH_3)_2NH_2][Br]$ than in $[(CH_3)_3NH][Br]$, the N-H covalent bond in

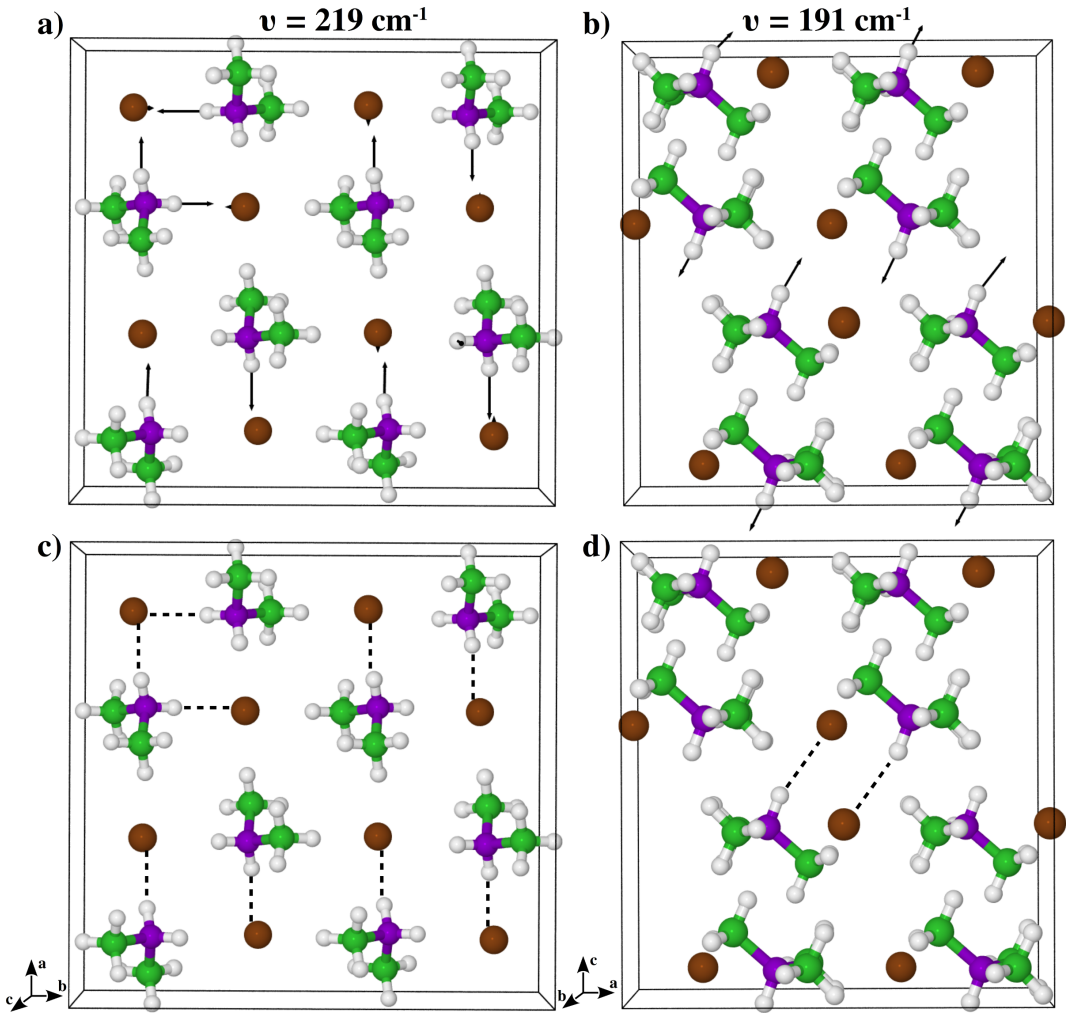

Figure 3.6: Inter-ionic character of selected modes in crystalline alkylammonium salts calculated using NMA; (a) $[(CH_3)_2NH_2][Br]$ and (b) $[(CH_3)_3NH][Br]$. Atomic displacement vectors are shown as arrows and are scaled by an arbitrary factor for clarity. Hydrogen bond network in PILs: (c) $[(CH_3)_2NH_2][Br]$ and (d) $[(CH_3)_3NH][Br]$ as obtained from experimental crystal structure. Color scheme: nitrogen, violet; carbon, green; hydrogen, white; bromine, ochure.

$[(CH_3)_3NH][Br]$ was expected to be stronger than in $[(CH_3)_2NH_2][Br]$. Therefore, the N-H stretching frequency in $[(CH_3)_3NH][Br]$ can be expected to be present at a higher wave number compared to $[(CH_3)_2NH_2][Br]$. These observations are confirmed in Figure 3.8 which provides the VDOS in the high frequency region. In Figure 3.8, modes present around 2900 cm^{-1} correspond to the C-H stretching frequencies while N-H stretching vibrations are present around 3100 cm^{-1}.

The effect of cation-anion hydrogen bond on the vibrational spectrum was analysed further from the AIMD trajectories. The velocities of the acidic proton(s) that forms hydrogen bond with the bromide anion were projected along the N-H$\cdots$Br bond vector.

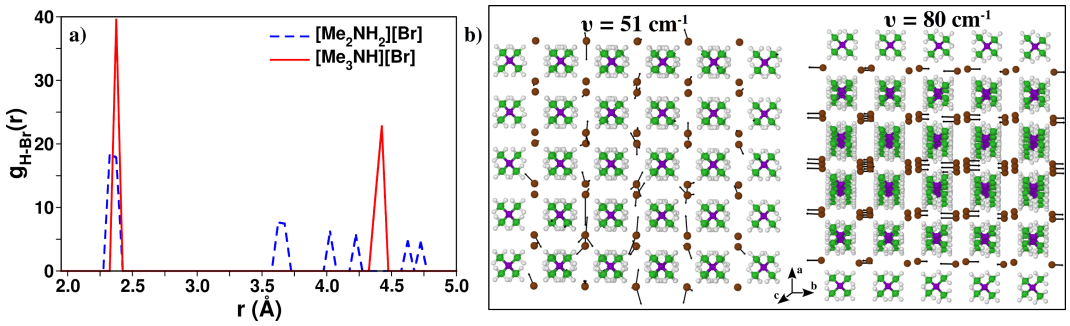

Figure 3.7: (a) Radial distribution functions of acidic hydrogen atoms around the bromide anion in crystalline phases of PILs obtained from the experimental crystal structure. (b) Interionic character of selected modes in crystalline $[(CH_3)_4N][Br]$ calculated using NMA within a classical force field. Atomic displacement vectors are shown as arrows and are scaled by an arbitrary factor for clarity.

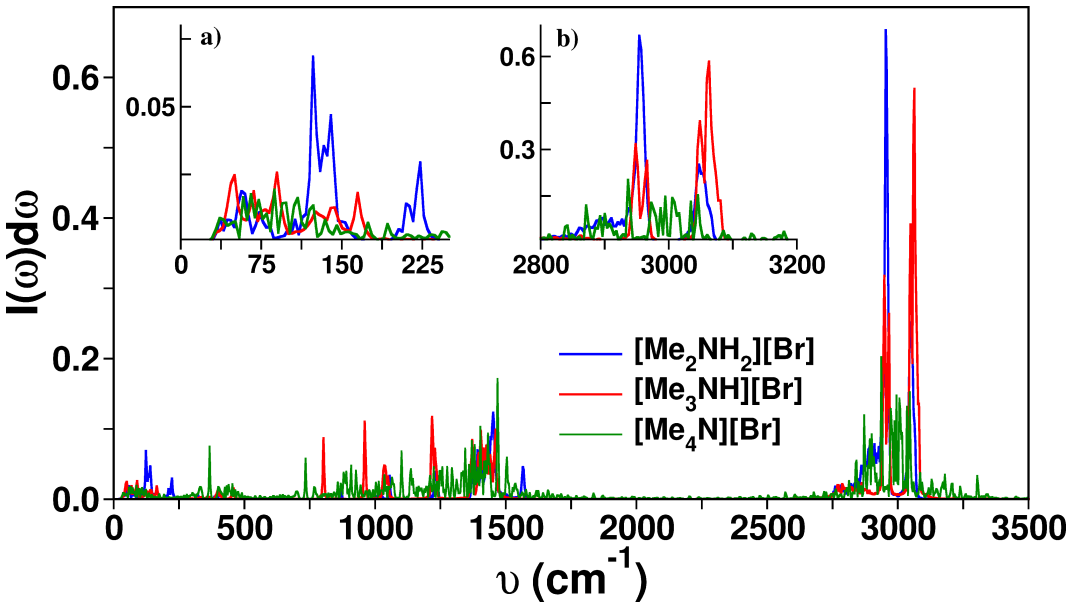

Figure 3.8: Power spectra of velocity autocorrelation function obtained from AIMD simulation of different alkylammonium salts in their crystalline states. In inset: (a) magnified low frequency region corresponding to cation-anion hydrogen bonding; (b) high frequency region of VDOS corresponding to C-H and N-H stretching vibrations.

The autocorrelation function of this component was analyzed through its Fourier transform. This quantity is thus the power spectrum specifically for the hydrogen bond stretching mode. A schematic of these calculations is provided in Figure 3.9 along with the corresponding spectra for $[(CH_3)_2NH_2][Br]$ and $[(CH_3)_3NH][Br]$. In $[(CH_3)_2NH_2][Br]$, the low wave number peak is present at around 220 cm^{-1} arising due to strong $^{+}$N-H$\cdots$Br^{-} interaction. On the other hand, the weaker interaction between the same pair in $[(CH_3)_3NH][Br]$ results in a red shift in that mode and the same is located at 165 cm^{-1}. The three methyl groups

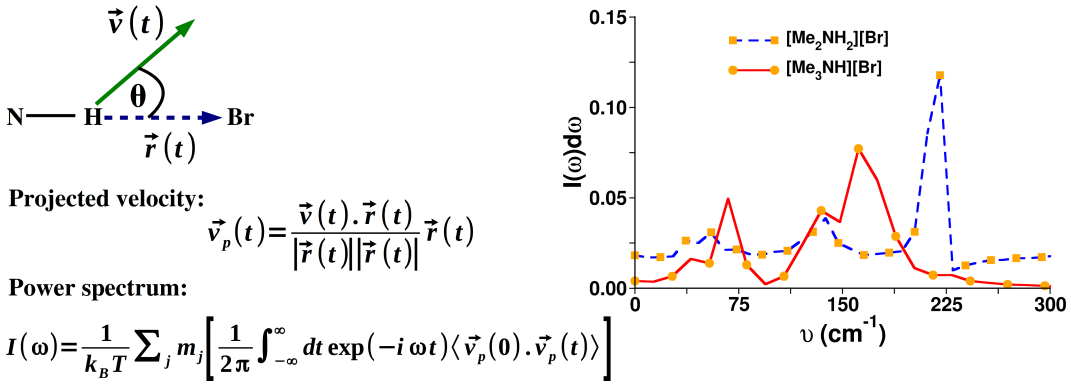

Figure 3.9: Left panel: Scheme shows the projection of acidic hydrogen velocities along the cation-anion hydrogen bond axis. Right panel: Power spectra of velocity autocorrelation function of acidic hydrogen projected along the cation-anion hydrogen bond axis.

provide a large positive inductive effect, resulting in a less acidic N_H proton (where the nitrogen atom is more electron rich) in $[(CH_3)_3NH][Br]$. On the contrary, the N_H proton of $[(CH_3)_2NH_2][Br]$ is found to be more acidic in nature due to a less electron rich N center. A more acidic hydrogen atom interacts stronger with the bromide anion which results in a blue shift in the low frequency vibrational band in $[(CH_3)_2NH_2][Br]$. This analysis conclusively demonstrates these modes to possess hydrogen bond stretching character.

The presence and strength of hydrogen bonding in PILs was further investigated in terms of hydrogen bond length and angle. The distribution of hydrogen bond length and hydrogen bond angle in $[(CH_3)_2NH_2][Br]$ and $[(CH_3)_3NH][Br]$ were calculated from the AIMD trajectories and are compared in Figure 3.10. The mean hydrogen bond distance in $[(CH_3)_2NH_2][Br]$ is marginally shorter than in $[(CH_3)_3NH][Br]$. On the other hand, the difference in hydrogen bond angle was more prominent. In the case of $[(CH_3)_2NH_2][Br]$, the cation-anion hydrogen bond was found to be more linear and the N-H$\cdots$Br angle is close to 180°. However, the mean angle in $[(CH_3)_3NH][Br]$ is around 165°. Hence, these observations also suggests stronger intermolecular interaction in $[(CH_3)_2NH_2][Br]$ than in $[(CH_3)_3NH][Br]$.

$\delta(^1H)$ NMR. The NMR chemical shifts $\delta(^1H)$ in these alkylammonium salts were calculated both in the gas phase as well as in the crystalline phase. The calculations have also been carried out for chloride (Cl^-) and iodide (I^-) anion based salts in their gas phase for the sake of comparison. The chemical shifts for the salts are plotted against their corresponding ($^+$N-H$\cdots$anion) far-IR frequencies in Figure 3.11. As the $^+$N-H$\cdots$anion interaction increases, a blue shift in far-IR frequency is observed, with a corresponding increase in $\delta(^1H)$. The interaction strength is the highest for chloride which leads to a large NMR downfield proton chemical shift and high far-IR frequencies. On the other hand,

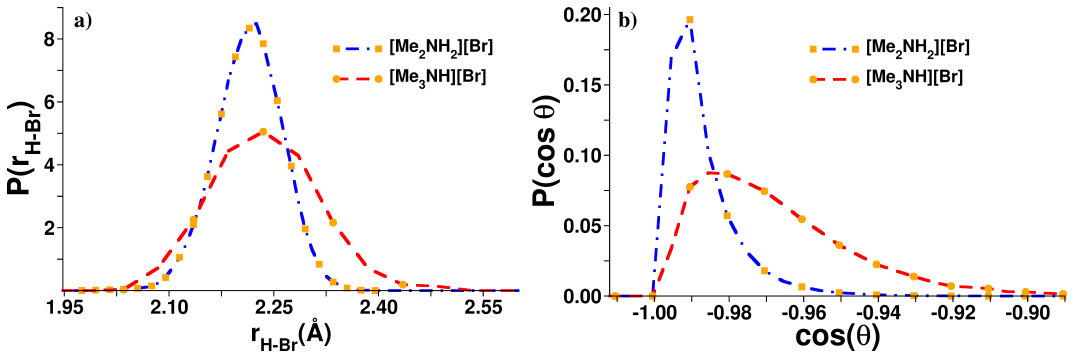

Figure 3.10: Normalized distribution of (a) NH$\cdots$Br bond length and (b) N-H$\cdots$Br angle in crystalline $[(CH_3)_2NH_2][Br]$ and $[(CH_3)_3NH][Br]$ calculated from the AIMD trajectory.

iodide anion showed an upfield shift and a red shift in the far-IR frequency relative to chloride and bromide anion. The difference in the number of electron releasing groups in the two types of cations results in differences in the interaction strength and the $\delta(^1H)$ values. The $\delta(^1H)$ values obtained for the bromide based crystals are comparable to those obtained for the corresponding ion pairs in gas phase. Thus, at least as far as chemical shift values are concerned, gas phase calculations appear sufficient.

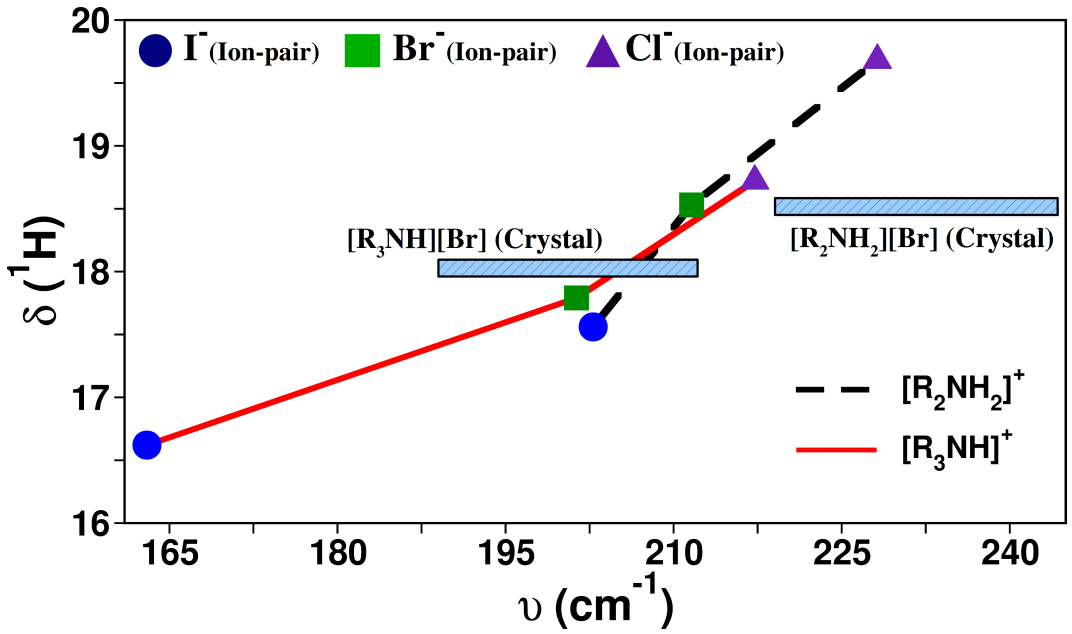

Figure 3.11: Chemical shifts $\delta(^1H)$ for the N_H proton plotted against $^+$N-H$\cdots$anion far-IR frequencies of alkylammonium salts in their gas phase. For crystalline systems, $\delta(^1H)$ values are plotted against a group of vibrational frequencies that correspond to $^+$N-H$\cdots$anion interionic vibrational band (as depicted in Figure 3.2b). Data presented here are obtained from CPMD code. [27]

To examine further the hydrogen bond donor-acceptor properties in these PILs, the

total electron density difference map was calculated using GaussView [26] and visualized in VMD. [45] The electron density of each fragment in gas phase (cation and anion) at MP2/aug-cc-pVDZ level of theory was also calculated. The sum of the electron density of each fragment was then subtracted from the total electron density of the ion pair in gas phase. This difference is shown in Figure 3.12.

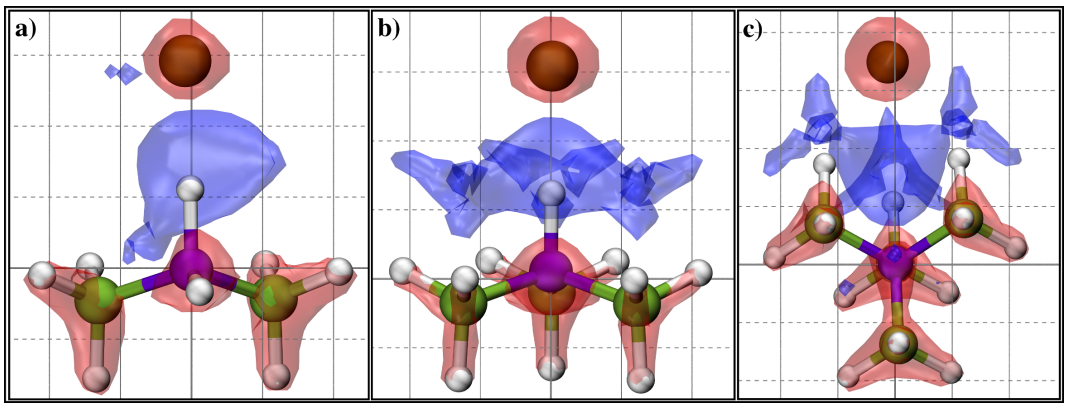

Figure 3.12: Electron density difference maps for (a) $[(CH_3)_2NH_2][Br]$, (b) $[(CH_3)_3NH][Br]$, and (c) $[(CH_3)_4N][Br]$.

In Figure 3.12, blue (red) represents the loss (gain) of electron density. In $[(CH_3)_2NH_2][Br]$ and $[(CH_3)_3NH][Br]$, the acidic hydrogen acts as the electron deficient center while the bromide anion acts as the electron rich center (hydrogen bond acceptor). The presence of these two centers with different electron densities can enable charge transfer between ions in these salts. The atomic charges of these salts in their crystalline states were calculated using the density-derived electrostatic and chemical (DDEC) charge partitioning method. [52, 53] Details of these calculations have been described in Chapter 2A. The total ion charges were found to be ± 0.647, ± 0.658, and ± 0.667e for $[(CH_3)_2NH_2][Br]$, $[(CH_3)_3NH][Br]$, and $[(CH_3)_4N][Br]$. Thus, the extent of charge transfer in these salts follows the same trend as the strength of interionic interactions.

Figure 3.13 summarizes the frequency spectra for $[(CH_3)_2NH_2][Br]$ obtained using the different techniques.

3.4 Conclusions

We have reviewed the far-infrared region of the vibrational spectrum of alkylammonium based PILs using a set of computational techniques. Harmonic frequencies were calculated for isolated ion pairs as well as for the crystalline states of these salts. Both classical and *ab initio* molecular dynamics simulations were performed for three different PILs in their crystalline states. The time correlation function for ion velocities were used to obtain the vibrational power spectra of these crystals. Normal-mode analyses were also performed

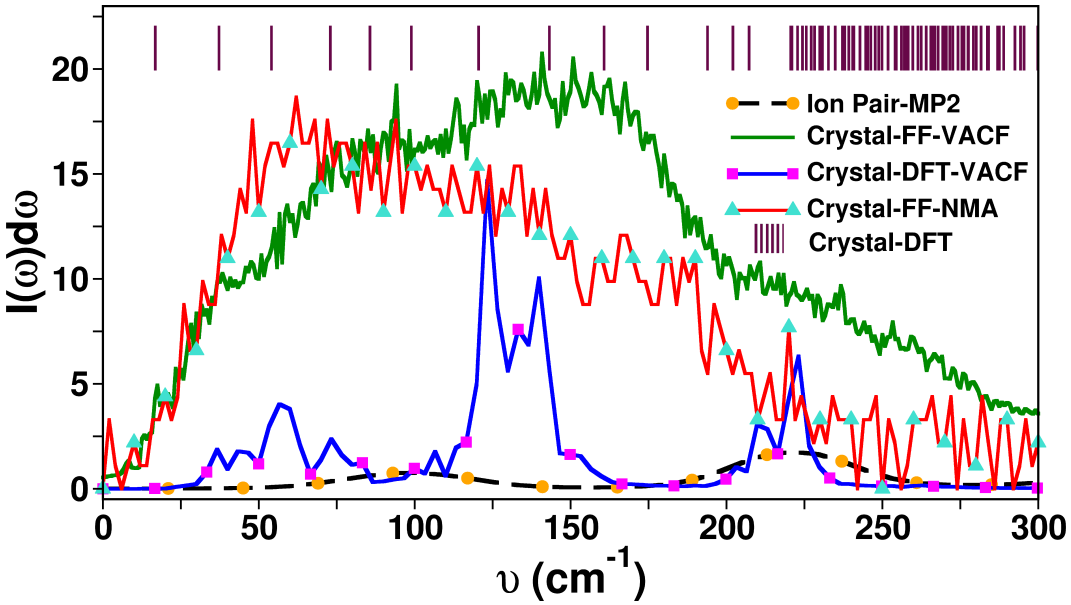

Figure 3.13: Frequency spectra of crystalline $[(CH_3)_2NH_2][Br]$ calculated through different methods. The spectra calculated from density functional theory (DFT) within the harmonic approximation for an "ion-pair" and of a "crystal supercell" (stick pattern, marked Crystal-DFT) are shown for comparison. "Crystal-FF-VACF" and "Crystal-DFT-VACF" stand for the power spectrum of velocity autocorrelation function calculated from classical MD and AIMD trajectories respectively. "Crystal-FF-NMA" is the frequency spectrum obtained by performing normal-mode analysis (NMA) on configurations selected from the trajectory generated in classical MD simulation.

using the classical MD trajectory to obtain the vibrational density of states within the harmonic approximation.

We have observed distinct vibrational modes located in the 150-240 cm^{-1} region of the spectra, corresponding to near neighbor cation-anion interactions. Vibrational analysis has provided rich information on the nature of these modes. Specifically, we find a blue shift in the far-IR mode with increasing number of hydrogen bonding sites on the cation. This frequency shift was related to the difference in interaction strength arising as a result of inductive effects caused by different number of alkyl groups present on the cation. The difference in the strength of cation-anion hydrogen bond was further probed with the help of geometrical parameters such as the hydrogen bond distance and hydrogen bond angle. In $[(CH_3)_2NH_2][Br]$, the hydrogen bond is more linear than in $[(CH_3)_3NH][Br]$, alluding to the former's strength. Such low frequency modes were also observed in ILs containing different anions such as $[CH_3SO_3]^-$, $[CF_3SO_3]^-$, $[NTf_2^-$, $[NO_3]^-$, etc., coupled with $[R_3NH]^+$ cation. [24, 54] The position of the peak was found be modulated by the interaction strength between ion-pairs in these PILs. Such a modulation in the peak position with change in the interaction strength between ions was also observed in many

spectroscopic investigations. [23, 24, 54] We have also examined the vibrational modes located below 100 cm^{-1} region of spectra. The modes present in this region of spectra are mainly due to the rattling motions of bromide anions. Similar interionic modes of cations are observed in the range 100-200 cm^{-1}.

Results from these vibrational analyses were further supported by NMR chemical shift values of acidic hydrogen atoms in different PILs. The $\delta(^1H)$ values is correlated with the characteristic low frequency peak position. The hydrogen bond donor-acceptor properties were further examined through electron density difference maps. The charge transfer effects in the crystalline phase of these salts were probed through the DDEC/c3 charge partitioning method, [52, 53] which predicts a fractional ion charge for all these systems and the values are consistent with trends exhibited by the position of the low frequency band in these PILs. Furthermore, the influence of the alkyl group on the intermolecular structure and $^+$N-H$\cdots$anion hydrogen bond needs to be addressed. It will be the topic in the next Chapter.

Bibliography

[1] Wulf, A.; Fumino, K.; Ludwig, R. *Angew. Chem. Int. Ed.* **2010**, *49*, 449–453.

[2] Fumino, K.; Peppel, T.; Geppert-Rybczynska, M.; Zaitsau, D. H.; Lehmann, J. K.; Verevkin, S. P.; Kockerling, M.; Ludwig, R. *Phys. Chem. Chem. Phys.* **2011**, *13*, 14064–14075.

[3] Stoppa, A.; Hunger, J.; Buchner, R.; Hefter, G.; Thoman, A.; Helm, H. *J. Phys. Chem. B* **2008**, *112*, 4854–4858.

[4] Daguenet, C.; Dyson, P. J.; Krossing, I.; Oleinikova, A.; Slattery, J.; Wakai, C.; Weingärtner, H. *J. Phys. Chem. B* **2006**, *110*, 12682–12688.

[5] Turton, D. A.; Hunger, J.; Stoppa, A.; Hefter, G.; Thoman, A.; Walther, M.; Buchner, R.; Wynne, K. *J. Am. Chem. Soc.* **2009**, *131*, 11140–11146.

[6] Nakamura, K.; Shikata, T. *ChemPhysChem* **2010**, *11*, 285–294.

[7] Shirota, H.; Castner, E. W. *J. Phys. Chem. A* **2005**, *109*, 9388–9392.

[8] Xiao, D.; Rajian, J. R.; Hines, L. G.; Li, S.; Bartsch, R. A.; Quitevis, E. L. *J. Phys. Chem. B* **2008**, *112*, 13316–13325.

[9] Fujisawa, T.; Nishikawa, K.; Shirota, H. *J. Chem. Phys.* **2009**, *131*, 244519.

[10] Dominguez-Vidal, A.; Kaun, N.; Ayora-Cañada, M. J.; Lendl, B. *J. Phys. Chem. B* **2007**, *111*, 4446–4452.

[11] Yokozeki, A.; Kasprzak, D. J.; Shiflett, M. B. *Phys. Chem. Chem. Phys.* **2007**, *9*, 5018–5026.

[12] Roth, C.; Chatzipapadopoulos, S.; Kerlé, D.; Friedriszik, F.; Lütgens, M.; Lochbrunner, S.; Kühn, O.; Ludwig, R. *New J. Phys.* **2012**, *14*, 105026.

[13] Katsyuba, S. A.; Vener, M. V.; Zvereva, E. E.; Fei, Z.; Scopelliti, R.; Laurenczy, G.; Yan, N.; Paunescu, E.; Dyson, P. J. *J. Phys. Chem. B* **2013**, *117*, 9094–9105.

[14] Wulf, A.; Fumino, K.; Ludwig, R.; Taday, P. F. *ChemPhysChem* **2010**, *11*, 349–353.

[15] Yamamoto, K.; Tani, M.; Hangyo, M. *J. Phys. Chem. B* **2007**, *111*, 4854–4859.

[16] Buffeteau, T.; Grondin, J.; Danten, Y.; Lassègues, J.-C. *J. Phys. Chem. B* **2010**, *114*, 7587–7592.

[17] Grondin, J.; Lassègues, J.-C.; Cavagnat, D.; Buffeteau, T.; Johansson, P.; Holomb, R. *J. Raman Spectrosc.* **2011**, *42*, 733–743.

[18] Sarangi, S. S.; Reddy, S. K.; Balasubramanian, S. *J. Phys. Chem. B* **2011**, *115*, 1874–1880.

[19] Fumino, K.; Reichert, E.; Wittler, K.; Hempelmann, R.; Ludwig, R. *Angew. Chem. Int. Ed.* **2012**, *51*, 6236–6240.

[20] Hayes, R.; Imberti, S.; Warr, G. G.; Atkin, R. *Angew. Chem. Int. Ed.* **2013**, *52*, 4623–4627.

[21] Fumino, K.; Wulf, A.; Ludwig, R. *Angew. Chem. Int. Ed.* **2008**, *47*, 3830–3834.

[22] Wulf, A.; Fumino, K.; Ludwig, R. *J. Phys. Chem. A* **2010**, *114*, 685–686.

[23] Fumino, K.; Fossog, V.; Wittler, K.; Hempelmann, R.; Ludwig, R. *Angew. Chem. Int. Ed.* **2013**, *52*, 2368–2372.

[24] Fumino, K.; Ludwig, R. *J. Mol. Liq.* **2014**, *192*, 94–102.

[25] Frisch, M. J. et al. Gaussian 09 Revision D.01. Gaussian Inc. Wallingford CT **2009**.

[26] Dennington, R.; Keith, T.; Millam, J. GaussView Version 5. Semichem Inc., Shawnee Mission, KS, 2009.

[27] Hutter, J.; Ballone, J. P.; Bernasconi, M.; Focher, P.; Fois, E.; Goedecker, S.; Marx, D.; Parrinello, M.; Tuckerman, M. E. CPMD Version 3.13.2. Max Planck Institut fuer Festkoerperforschung and IBM Zurich Research Laboratory: Stuttgart, Germany, and Zurich, 1990.

[28] Troullier, N.; Martins, J. L. *Phys. Rev. B* **1991**, *43*, 1993–2006.

[29] Perdew, J. P.; Burke, K.; Ernzerhof, M. *Phys. Rev. Lett.* **1996**, *77*, 3865–3868.

[30] Grimme, S. *J. Comput. Chem.* **2006**, *27*, 1787–1799.

[31] Hockney, R. W. *J. ACM* **1965**, *12*, 95–113.

[32] Allen, F. H. *Acta Crystallogr., Sect. B: Struct. Sci* **2002**, *58*, 380–388.

[33] Bruno, I. J.; Cole, J. C.; Edgington, P. R.; Kessler, M.; Macrae, C. F.; McCabe, P.; Pearson, J.; Taylor, R. *Acta Crystallogr., Sect. B: Struct. Sci* **2002**, *58*, 389–397.

[34] Bruno, I.; Cole, J.; Lommerse, J.; Rowland, R.; Taylor, R.; Verdonk, M. *J. Comput. Aided Mol. Des.* **1997**, *11*, 525–537.

[35] Jones, P. G.; Fischer, A. K.; Vogt, H. *Z.Kristallogr.* **1994**, *209*, 834.

[36] Hartung, J.; Kopf, T.; Svoboda, I.; Fuess, H. *Acta Crystallogr. Sect. E: Struct. Rep. Online* **2006**, *62*, 570–572.

[37] Evans, D. J.; Hughes, D. L. *Acta Crystallogr.,Sect.C:Cryst.Struct.Commun.* **1990**, *46*, 1452–1454.

[38] Plimpton, S. *J. Comput. Phys.* **1995**, *117*, 1–19.

[39] Lopes, J. N. C.; Pádua, A. A. H. *J. Phys. Chem. B* **2004**, *108*, 16893–16898.

[40] Nosé, S. *J. Chem. Phys.* **1984**, *81*, 511–519.

[41] Nosé, S. *Mol. Phys.* **1984**, *52*, 255–268.

[42] Martyna, G. J.; Klein, M. L.; Tuckerman, M. *J. Chem. Phys.* **1992**, *97*, 2635–2643.

[43] Krishnan, M.; Balasubramanian, S. *Phys. Rev. B* **2003**, *68*, 064304.

[44] Macrae, C. F.; Edgington, P. R.; McCabe, P.; Pidcock, E.; Shields, G. P.; Taylor, R.; Towler, M.; van de Streek, J. *J. Appl. Crystallogr.* **2006**, *39*, 453–457.

[45] Humphrey, W.; Dalke, A.; Schulten, K. *J. Mol. Graphics* **1996**, *14*, 33–38.

[46] Jmol: an open-source Java viewer for chemical structures in 3D. http://www.jmol.org/.

[47] Sebastiani, D.; Parrinello, M. *J. Phys. Chem. A* **2001**, *105*, 1951–1958.

[48] Sebastiani, D.; Goward, G.; Schnell, I.; Parrinello, M. *Comput. Phys. Commun.* **2002**, *147*, 707–710.

[49] Sebastiani, D.; Parrinello, M. *ChemPhysChem* **2002**, *3*, 675–679.

[50] Goward, G. R.; Schuster, M. F. H.; Sebastiani, D.; Schnell, I.; Spiess, H. W. *J. Phys. Chem. B* **2002**, *106*, 9322–9334.

[51] Goward, G. R.; Sebastiani, D.; Schnell, I.; Spiess, H. W.; Kim, H.-D.; Ishida, H. *J. Am. Chem. Soc.* **2003**, *125*, 5792–5800.

[52] Manz, T. A.; Sholl, D. S. *J. Chem. Theory Comput.* **2010**, *6*, 2455–2468.

[53] Manz, T. A.; Sholl, D. S. *J. Chem. Theory Comput.* **2012**, *8*, 2844–2867.

[54] Fumino, K.; Wulf, A.; Ludwig, R. *Angew. Chem. Int. Ed.* **2009**, *48*, 3184–3186.

Chapter 4

Atomistic Simulations of Ammonium-based Protic Ionic Liquids: Steric Effects on Structure, Low Frequency Vibrational Modes and Electrical Conductivity

4.1 Introduction

Room temperature ionic liquids (ILs) have attracted tremendous interest as electrolytes or dopants in fuel cells, batteries, supercapacitors and solar cells due to their excellent thermodynamic, transport and electrochemical properties. [1–8] Improvement in thermal and electrochemical properties of fuel cells through the use of cost-effective ammonium based protic and aprotic ILs as electrolytes has spurred interest in them. [7, 9–15] Nakamoto and Watanabe synthesized a series of protic ILs (PILs) from Br∅nsted acid-base combination of aliphatic amines with oxoacids. They obtained remarkable electrolytic properties under anhydrous conditions for diethylmethylamine trifluoromethanesulfonic acid ([dema][TfO]) PIL. [10] Lee *et al.* [16] characterized composite polymer electrolyte membranes which were fabricated with [dema][TfO] IL under non-humidified conditions. The authors observed an excellent activity for fuel cell (H_2/O_2) reactions at Pt electrode and improved

Reprinted with permission from "Atomistic simulations of ammonium-based protic ionic liquids: steric effects on structure, low frequency vibrational modes and electrical conductivity" *Phys. Chem. Chem. Phys.* **2015**, *17*, 4625–4633. http://dx.doi.org/10.1039/C4CP05353B.

ionic conductivity using [dema][TfO] IL. Iojoiu and co-workers [17–22] analysed the nanostructuring and transport properties of ammonium based IL doped composite membranes as a function of temperature, hydration and concentration of doped IL. Apart from improved thermal and mechanical stability of the composite membrane, the presence of cationic and anionic clusters in the membrane matrix was shown to enhance long-range charge transfer. The strength of the Coulomb interactions and polarization forces are critical parameters in determining the orientational correlations of cations and anions as revealed in molecular dynamics study of imidazolium based ILs. [23–25] The sensitivity of cation-anion interactions, size and shape of cations in quaternary ammonium protic ILs is a crucial factor for electrochemical and charge transfer processes. Ludwig and co-workers [26–28] used far infrared and terahertz spectroscopy studies to probe molecular interactions in ILs. The authors characterized the low frequency region of various ILs and showed that structure of ILs is largely determined by Coulomb energy, hydrogen bonding and dispersion forces between the ion species. Koh *et al.* [29] analyzed the effect of cation size on the capacitance of electrochemical double layer capacitors using various quaternary ammonium cation based [BF_4^-] salts. They demonstrated that smaller crystallographic ionic radii of ions in trimethylethylammonium and trimethylpropylammonium cations lead to 10% higher capacitance compared to tetraethylammonium cations. Sunda and Venkatnathan [30] investigated the structure and dynamics of benzyltrialkylammonium trifluoromethanesulfonate ILs at varying hydration and demonstrated the strong influence of C–H/phenyl interactions on ionic conductivity. MD simulations on neat and hydrated [dema][TfO] IL by Chang *et al.* [31] showed that the ionic conductivity of IL increases with hydration due to enhanced translational and rotational motions of ions. Pulse field gradient stimulated echo NMR spectroscopy on triethylammonium methanesulfonate protic ILs by Blanchard *et al.* [32] suggested that proton decoupled transport was absent in the protic IL and diffusivity of the acidic proton was strongly influenced by the presence of water. Johnson *et al.* [33] studied Pt electrode kinetics as a function of temperature in [dema][TfO] IL for H_2 and O_2 fuels. The authors observed enhanced electrode kinetics in anhydrous IL above 100 °C. Ejigu and Walsh [34] characterized the effect of adsorbed ions on Pt electrodes for [dema][TfO] and dimethylethylammonium trifluoromethanesulfonate ([dmea][TfO]), and diethylmethylammonium bis-(trifluoromethanesulfonyl)imide ([dema][Tf_2N]) ILs. A slower O_2 reduction in [dema][Tf_2N] was observed due to adsorption of [Tf_2N^-] ions on Pt electrode compared to [dema][TfO] and [dmea][TfO] ILs.

The choice of alkyl group such as methyl, ethyl or *n*-propyl on trialkylammonium cation leads to a significant variation in proton conductivity and electrochemical properties. [10] Among the several alkyl group combinations, [dema][TfO] IL showed better electrochemical properties compared to other ILs. In the present work, MD simulations are employed

to characterize protic ILs (PILs) consisting of trialkylammonium cation and [TfO$^-$] anion. [TfO$^-$] anion based PILs with varying ammonium cation such as **a**) N,N-dimethyl-N-ethylammonium (dmea) triflate ([N112][TfO]), **b**) N,N-diethyl-N-methylammonium (dema) triflate ([N122][TfO]), **c**) N,N,N-triethylammonium (tea) triflate ([N222][TfO]), and **d**) N,N-di-*n*-propyl-N-methylammonium (dpma) triflate ([N133][TfO]) were chosen. This Chapter aims to investigate the influence of steric effects on hydrogen bond interactions due to the size of the alkyl group. Low frequency vibrational modes and dynamical properties of these PILs are also explored.

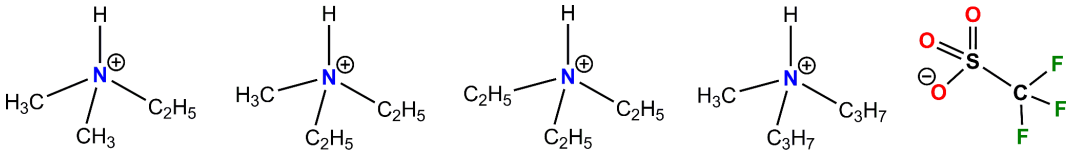

Figure 4.1: Ammonium cations a) N,N-dimethyl-N-ethylammonium ([N112]), b) N,N-diethyl-N-methylammonium ([N122]), c) N,N,N-triethylammonium ([N222]), d) N,N-di-*n*-propyl-N-methylammonium ([N133]), and e) triflate ([TfO$^-$]) anion.

4.2 Computational Section

Cation and the anion of PILs used in present study are shown in Figure 4.1. Classical MD simulations of these protic ILs were carried out using LAMMPS [35] program. Parameters for bonding interactions were taken from the OPLS-AA force-field. [36] For the non-bonding interactions, van der Waals parameters were taken from the work of Chang *et al.* [31] In Chapter 2A, based on condensed phase quantum calculations, we have shown that the ions in imidazolium based ILs realistically can be modelled with a fractional charge (less than unity). For instance, the charge on ions in such salts containing triflate ($CF_3SO_3^-$) as the anion was $\pm$ 0.78e. Assuming a similar charge transfer in PILs, the ion charges in the current simulations have been scaled down by a factor of 0.78 from the original values. [37, 38] Simulations with full atomic charges (at 300 K) slightly overestimate PILs density as shown in Table 4.1 and the diffusion coefficient (at 300 K) are found to be lower by an order of magnitude then either that of simulations with scaled charge or experiments (see Table 4.2).

All the systems were simulated using 256 ion pairs. Packmol [40] software package was used to set up the initial configurations. Particle-particle particle-mesh (PPPM) solver was used to compute the long-range electrostatic interactions with a precision of 10^{-5}. A distance cutoff of 11 Å was employed to calculate the pairwise interactions in real space. Equations of motion were integrated using the velocity Verlet algorithm with a time

Table 4.1: Density (ρ in g cm^{-3}) of ammonium-triflate PILs from NPT simulations. [a]ρ= 1.299 calculated using full atomic charges for [N122][TfO] at 300 K, and [b]ρ= 1.218 calculated using full atomic charges for [N133][TfO] at 300 K, and [c]experimental data from Ref. [39]

T(K)	[N112][TfO]	[N122][TfO]	[N222][TfO]	[N133][TfO]
300	-	1.262[a] (1.277[c])	-	1.192[b] (1.203[c])
313	-	1.251 (1.262[c])	-	1.184 (1.189[c])
393	1.236	1.184	1.139	1.118

Table 4.2: Self-diffusion coefficients ($\times 10^{-7}$cm^{2}s^{-1}) of PILs from MD simulations at 300 K.

System	Full charge model		Scaled charge model		Experiment[16]	
	D^+	D^-	D^+	D^-	D^+	D^-
[N122][TfO]	0.09	0.08	2.12	1.25	4.16	2.18
[N133][TfO]	0.04	0.03	0.43	0.28	-	-

step of 1 fs. All C–H covalent bonds were constrained using the SHAKE algorithm as implemented in LAMMPS. [35] Standard Lorentz-Berthelot rules were applied to derive the cross interactions between different atom types. Long-range corrections were applied while calculating the energy and pressure. The Nosé-Hoover thermostat [41, 42] and barostat were employed for constant temperature and constant pressure dynamics with a damping factor of 1 ps. MD simulations were performed at three different temperatures 300 K, 313 K and 393 K. The energy minimization of 256 ion-pairs was followed by an equilibration of 12 ns in NPT ensemble. Production run of 32 ns was generated in NVT ensemble and was further used to calculate the structural and dynamical properties of these protic ILs.

The computed densities from NPT simulations (see Table 4.1) were close to experiment, (within 2 % error) as reported for [N112][TfO] IL and [N133][TfO] IL. [39] Density decreases with increase in temperature from 300 K to 393 K. At 393 K, the density decreases with increase in molecular weight of ammonium cation or IL. Simulations were also carried out at 393 K, so as to compare with experimentally determined diffusion coefficients of ions and electrical conductivity of ILs.

A different set of simulations was performed for all the systems, each consisting 100 ion-pairs. The simulation temperature was 393 K. Each system was equilibrated for 5 ns in the NPT ensemble which was followed by a 10 ns production run in the NVT the ensemble. Atom coordinates were stored every 100 ps to obtain 100 snapshots for each PIL. Other details of the simulations are the same as discussed in previous section for 256 ion-pair systems.

An efficient conjugate gradient method as implemented in LAMMPS was employed to minimize the 100 configurations obtained from the classical MD trajectory for each ionic liquid. The Hessian matrix of the potential energy with respect to the atom coordinates was calculated using a normal-mode analysis (NMA) code developed earlier within our group. [43] The eigenvectors of the Hessian are related to atomic displacements in a mode and the eigenvalues corresponds to the frequencies. A 2 cm^{-1} bin width was used to calculate the frequency spectrum which was averaged over all the 100 quenched configurations.

The VDOS can also be obtained as the Fourier transform of time autocorrelation function of the atomic velocities (VACF). This can be defined as

$$I(\omega) = \frac{1}{k_B T} \sum_j m_j \left[\frac{1}{2\pi} \int_{-\infty}^{\infty} exp(-i\omega t) \langle \mathbf{v}_j(0).\mathbf{v}_j(t) \rangle dt \right] \tag{4.1}$$

where $\mathbf{v}_j(t)$ is the velocity of atom type j at time t. In order to calculate this VACF, a separate MD trajectory was generated for 100 ps and atomic velocities were stored at each time step.

VMD [44] and Jmol [45] were used to visualize all the systems. Atomic displacements were visualized in Jmol [45] for the assignment of different modes present in the systems.

The electrical conductivity was calculated through the equilibrium Green-Kubo relation using the time integral of electric-current autocorrelation function and using the Nernst-Einstein relation. [46, 47] A detailed description about these calculations is provided in Chapter 2A.

4.3 Results and Discussions

PILs used in the present study exhibit various inter-ionic interactions including hydrogen bonding due to the presence of the acidic site on ammonium cation. The steric effects of alkyl groups on cation center, cationic symmetry and hydrogen bond interactions play vital roles in determining the intermolecular structure and thus dynamics in PILs. We have calculated Radial Distribution Functions (RDFs), Spatial Distribution Functions (SDFs) and vibrational spectrum in the low frequency region to characterize these PILs.

4.3.1 Radial Distribution Functions

RDFs for various interionic interactions are shown in Figure 4.2 and Figure 4.3. The N-S RDF (see Figure 4.2a) show a bifurcated peak at 4 Å and 5.5 Å with a large solvation shell of 8 Å and a small shoulder with a lower rise around 7 Å. The first peak in N-S RDF at $\sim$ 4 Å is due to the strong hydrogen bond interaction between the acidic site of the quaternary ammonium cation (N-H) and oxygen atoms of anions within the first solvation

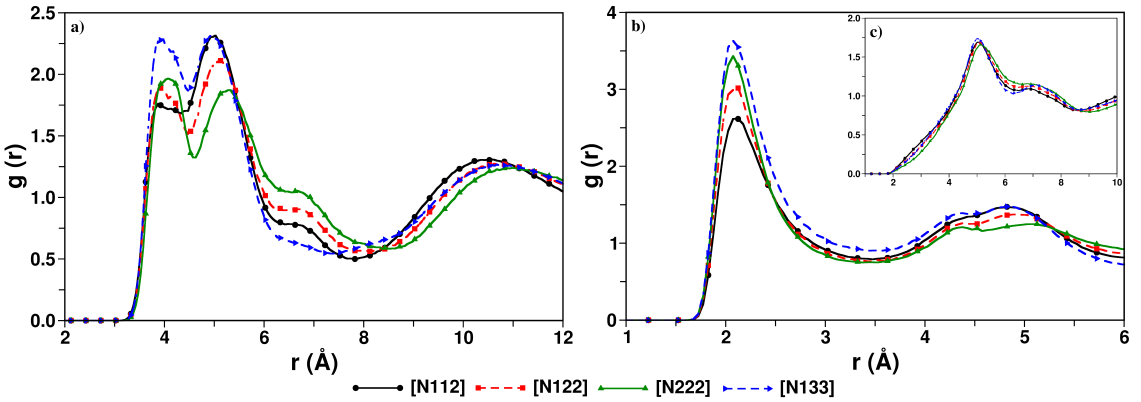

Figure 4.2: RDFs for cation-anion (a) N-S, and hydrogen bond interactions of acidic hydrogen (H_N) with [TfO^-] anion (b) H-O, and (c) H-F.

shell and the peak height is highest for [N133][TfO] IL. These cation-anion hydrogen bond interactions within $\sim$ 4 Å are revealed from the O-H RDF (see Figure 4.2b) which shows an intense peak around 2 Å. The peak height of O-H RDF increases with an increase in the

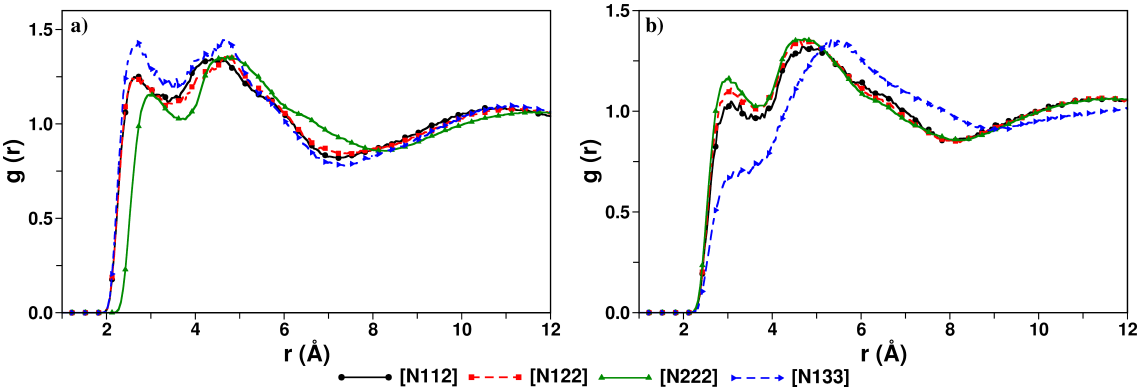

Figure 4.3: RDFs between (a) methyl/methylene hydrogen atoms, and (b) terminal alkyl (ethyl/propyl) hydrogen atoms of ammonium cation and anion oxygen atoms.

bulky nature of an alkyl group on the cation from the methyl to *n*-propyl group. This peak profile of O-H RDF for various PILs exhibits a qualitative similarity to the first peak of N-S RDF. Thus, the cation-anion hydrogen bond interactions within $\sim$4 Å distance suggest that anions prefer to approach from the top direction (i.e. along the N-H bond vector) of the cation. The second peak in N-S RDF at $\sim$ 5.5 Å is due to weak hydrogen bond interactions between terminal methyl hydrogen atoms and anion oxygen atoms which occur at larger distances. The peak height decreases from [N112][TfO] to [N222][TfO] but is found to be much higher for [N133][TfO]. Such an unusual peak profile can be understood by examining the RDFs between methyl/methylene hydrogen atoms of the quaternary ammonium cation and anion oxygen atoms (see Figure 4.3a). The interactions of anion

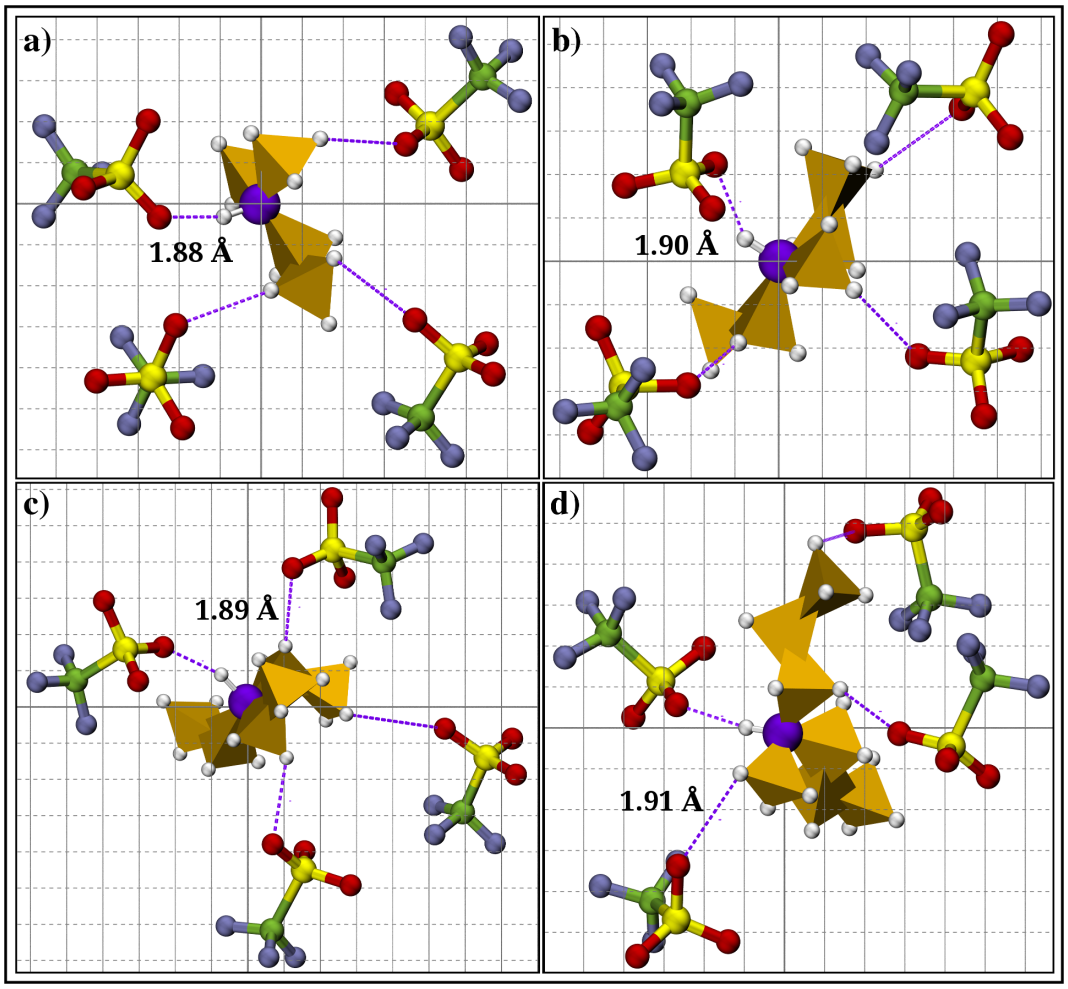

Figure 4.4: Snapshots for ammonium-triflate ILs from NVT production run showing cation-anion interactions; (a) [N112][TFO], (b) [N122][TFO], (c) [N222][TFO], and (d) [N133][TFO]. The N-H$\cdots$O hydrogen bond distance (in Å) is representative of the O-H distance. Snapshots are arbitrarily chosen based on the O-H distance and hence, the distance for the possible C$\cdots$O interaction (dashed line) is not displayed. Color scheme: nitrogen, violet; carbon, green; alkyl C, orange polyhedra; hydrogen, white; sulfur, yellow; oxygen, red; fluorine, iceblue.

oxygen atoms with methyl/methylene hydrogen atoms are strongest in [N133][TfO] and weakest in [N222][TfO]. A bifurcated peak at 5.5 Å is seen in the N-S RDF (Figure 4.2a). Thus, the approach of anions towards the cationic center from the methyl group side is restricted in [N222][TfO] IL due to the presence of more symmetric and bulky ethyl groups. However, such weak hydrogen bond interactions between terminal propyl H-atoms and anion oxygen atoms (in [N133][TfO]) are completely absent as seen from Figure 4.3b. The steric hindrance due to propyl chain limits the possibility of anion distribution over the propyl chain. Nevertheless, the weak hydrogen bond interactions between terminal ethyl H-atoms and anion oxygen atoms are highest in [N222][TfO] due to the presence

of more symmetric terminal hydrogen atoms. Hence, the RDF peak profile for terminal H-atoms of the ethyl/propyl tail and anion oxygen atoms reveals the characteristics of cation-anion interactions (seen from N-S RDF) at a larger distance of 7 Å. These hydrogen bond interactions between various sites of cation and anions can be seen from a snapshot of triflate anion clusters around the ammonium cation (see Figure 4.4). The hydrogen bond distance along the N-H bond vector is similar to that seen from the RDFs (Figure 4.2b). To summarize, the O-H hydrogen bonding (albeit a weak one) propensity increases with an increase in the alkyl tail length and depends critically on the symmetry of the cation as well. The coordination number for the N-S and O-H RDFs decreases with an increase in the length of the alkyl group on the cation from the methyl to *n*-propyl group (see Table 4.3). However, hydrogen bond interactions between acidic hydrogen (N-H) of the cation and fluorine atoms of the anion are not observed (see Figure 4.2c). The cation-cation interactions from N-N RDF (see Figure 4.5a) show a broad peak (5 to 9 Å). The peak

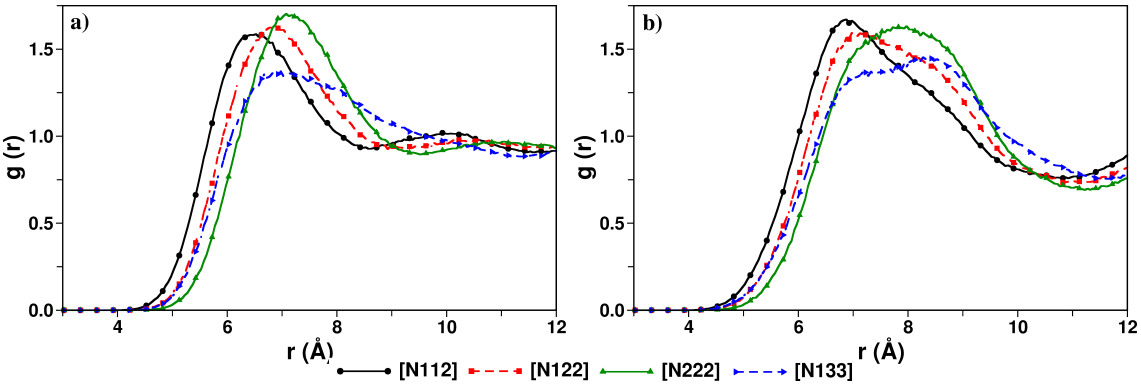

Figure 4.5: RDFs for a) N-N (cation-cation), and b) S-S (anion-anion interactions) at 393 K.

position is shifted towards larger distance with an increase in the length of the alkyl group on the cation. Similar to the cation-cation g(r), the S-S RDF (see Figure 4.5b) shows a broad peak (5 to 10 Å). Figure 4.6 shows that the structural correlations calculated for [N122][TfO] using the reduced charge model well reproduce those from the full charge model reported by Chang *et al.* [31] Although the O-H g(r) shows some difference, the running coordination number shows no change within the first shell from the results of the full charge simulations [31] as shown in the inset of Figure 4.6d. Thus, the trends seen in structural correlations for PILs are valid regardless of the use of a reduced charge model.

Furthermore, these structural observations are validated by calculating SDFs for these PILs. The SDFs calculated for the S-atom and the O-atom of anions around the N-atom of the cation are shown in Figure 4.7. The spatial density map of anions around the center of mass of the cation shows that the most preferred binding site of anions is opposite to the acidic proton. The distribution of anions along the N-H bond vector shows that the

Table 4.3: Coordination numbers for cation-anion and hydrogen bond interactions in the first solvation shell of PILs.

ILs	[N112][TfO]	[N122][TfO]	[N222][TfO]	[N133][TfO]
N–S (at 8.0 Å)	7.0	6.5	6.2	5.3
O–H (at 3.5 Å)	2.0	1.8	1.7	1.8

density map became more condensed and tapered over the quaternary ammonium acidic proton with an increase in the bulky nature of the cation. Whereas, the spatial density map of anions over alkyl terminals of the cation is highly diffused in [N112][TfO] IL which becomes scattered in [N122][TfO] and [N222][TfO] PILs respectively. In the case of [N133][TfO] IL, the steric-hindrance due to the propyl chain limits the anion distribution over the terminal propyl group of the cation. The spatial density map of anions around the quaternary ammonium cation is more symmetric in [N222][TfO] compared to other PILs.

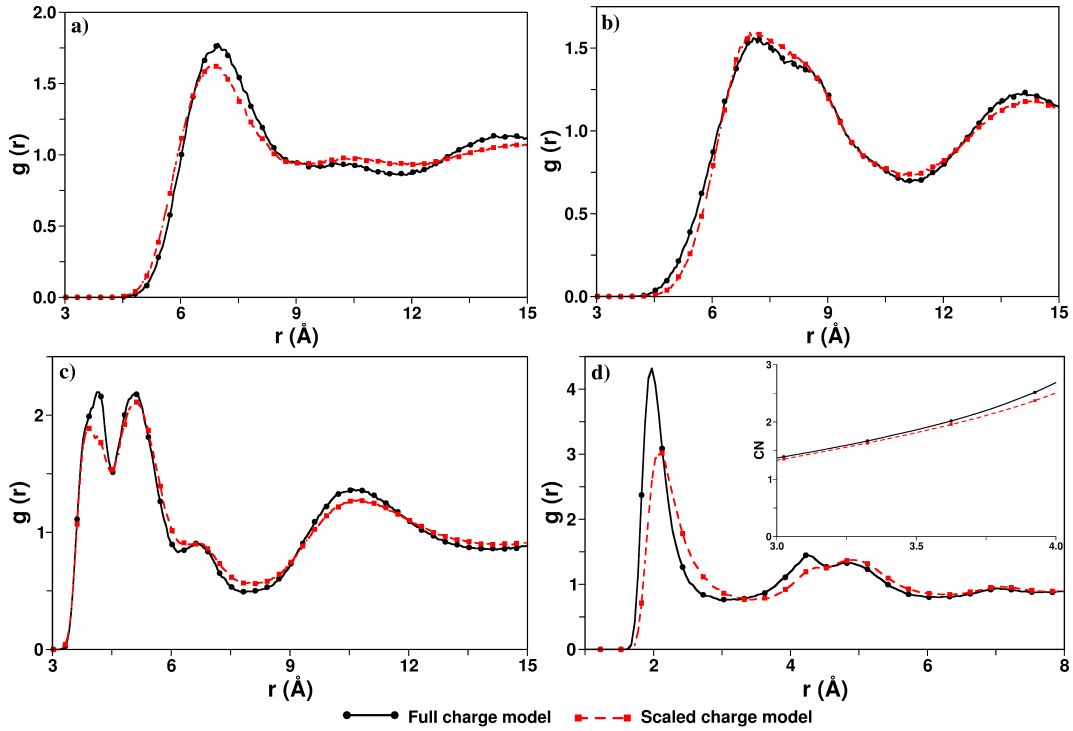

Figure 4.6: RDFs calculated for [N122][TfO] PIL using full charge model of Chang *et al.* [31] and scaled charge model at 393 K: a) N-N (cation-cation), b) S-S (anion-anion), c) N-S (cation-anion), and d) O-H (between anion oxygen atoms and acidic hydrogen attached to nitrogen of cation; inset shows coordination numbers).

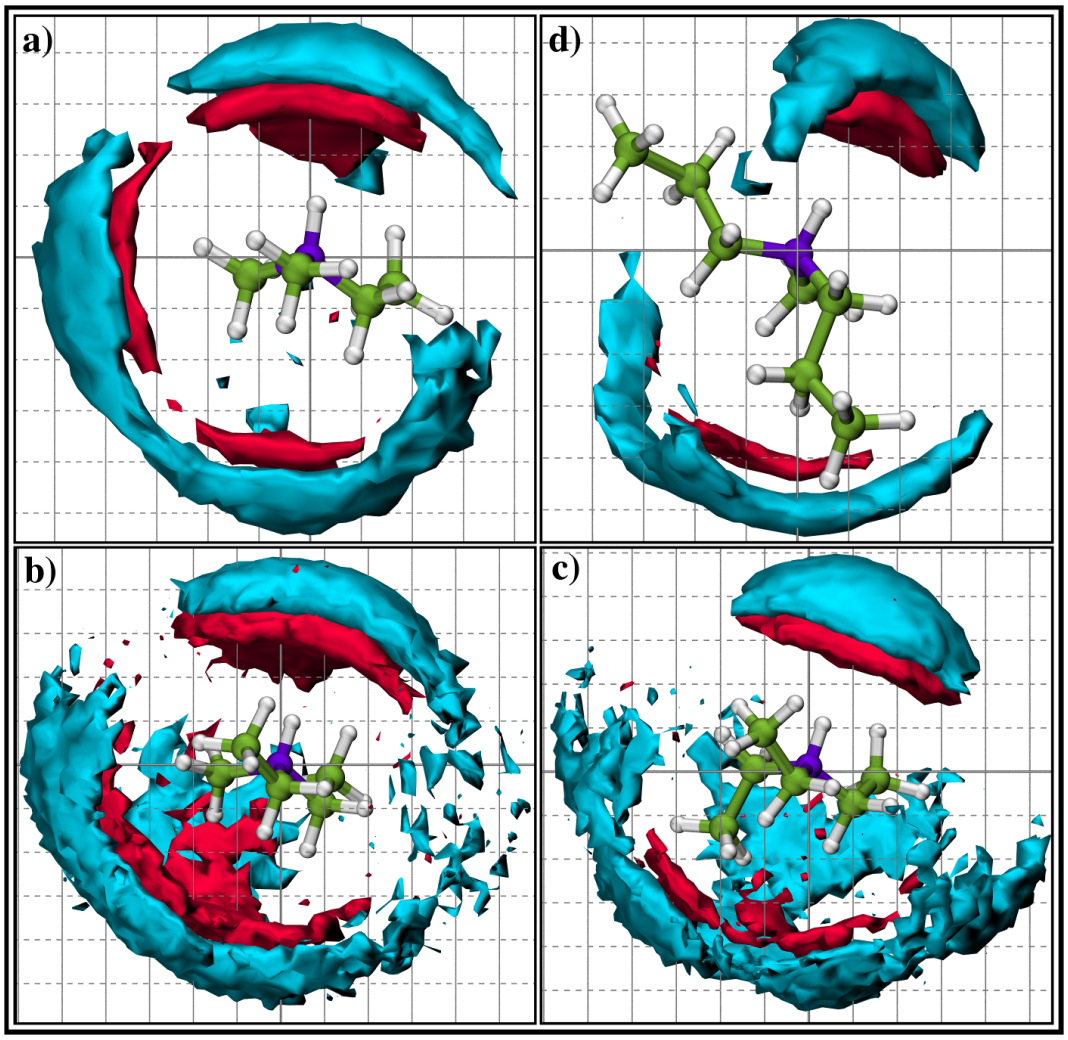

Figure 4.7: Spatial density map of anions (S-atom [cyan] and O-atoms [red]) around the center of mass of the ammonium cation calculated from MD simulation at 393 K for (a) [N112][TfO], (b) [N122][TfO], (c) [N222][TfO], and (d) [N133][TfO] PILs. Color scheme: nitrogen, violet; carbon, green; hydrogen, white. Iso-surface value is 0.005 $Å^{-3}$ for [N112][TfO], [N133][TfO], and 0.006 $Å^{-3}$ for [N122][TfO], [N222][TfO] respectively.]

4.3.2 Velocity Autocorrelation Function and Low Frequency Vibrational Modes

In order to characterize the dynamical processes in PILs, the center of mass velocity autocorrelation function (VACF) for cations and anions was calculated (see Figure 4.8). The first minimum is found to be deepest for the cation in [N112][TfO] (see inset of Figure 4.8a). The well depth decreases significantly with an increase in the bulkiness of alkyl tails on the quaternary ammonium cation and becomes insubstantial/or shallow in [N133][TfO] IL. The influence of the alkyl group attached to the quaternary ammonium ion on the exponential decay of the triflate anion VACF is minimal and found to be similar for all the

ILs. The variations in caging as seen from cation VACF suggests that the rattling motions are expected to be significant in [N112][TfO] IL.

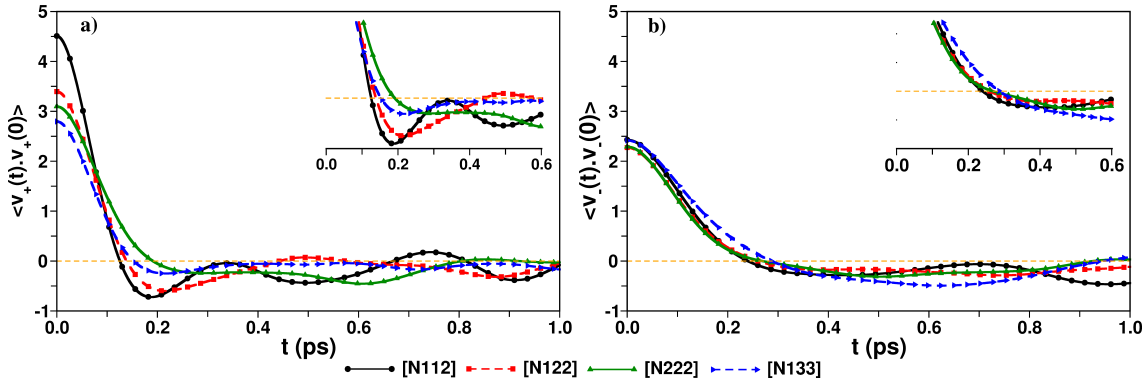

Figure 4.8: Center of mass velocity autocorrelation functions for (a) quaternary ammonium cations, and (b) triflate anions, respectively, at 393 K (insets show initial decay).

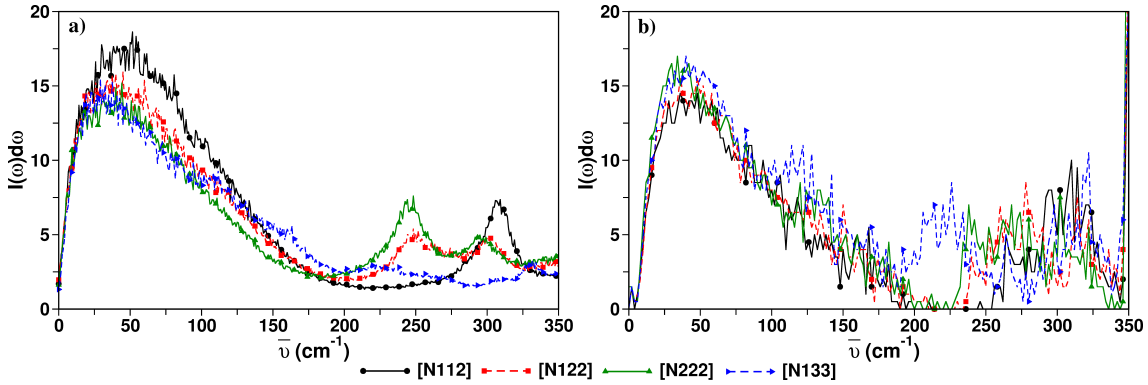

Figure 4.9: Vibrational density of states (VDOS) calculated for ILs at 393 K from (a) the power spectrum of the velocity autocorrelation function (VACF), and (b) normal-mode analysis (NMA) within the harmonic approximation.

The dynamics of PILs is further probed by examining the vibrational density of states (VDOS). The vibrational spectrum is calculated from the Fourier transform of the VACF (see Figure 4.9a). A broad peak in the low-frequency region corresponding to the collision frequency of inter-molecular modes is observed. As expected, the peak height is highest for [N112][TfO] IL. Additionally, low intensity peaks are also observed in the 200-350 cm^{-1} region of VDOS which show a red shift with an increase in the bulkiness of the alkyl group on the quaternary ammonium cation. Fumino *et al.* [26, 27] have characterized the low-frequency vibrational modes using far-infrared spectroscopy (FIR) for various quaternary ammonium based PILs with $[NO_3^-]$, $[CH_3SO_3^-]$, and $[CF_3SO_3^-]$ anions. They detected low-frequency vibrational bands (100âĂŞ400 cm^{-1}) due to the presence of inter-molecular interactions in PILs and assigned the vibrational bands at 100 cm^{-1}, 154–160 $cm^{-1}$and $\sim$

400 cm^{-1} region to unspecific librational motions, $^{+}$N–H$\cdots$anion interactions, and bending modes of cation respectively. To dissect the contribution of intermolecular interactions in the low-frequency vibrational band of PILs as seen from VDOS, we have carried out normal-mode analysis (NMA). Figure 4.9b displays atomic displacements (obtained from eigenvectors of the Hessian matrix) of a few modes in the PILs using the empirical force field. The atomic displacements obtained using NMA in the low frequency region of 40–100 cm^{-1} are mainly due to the rattling motions of anions. For example, the vibrational modes present in the [N133][TfO] at 51 cm^{-1} are shown in Figure 4.10a, where the [TfO^{-}] anions mainly contribute to the modes. The acidic protons (N-H) mainly contribute to the vibrational modes in the frequency range 155–165 cm^{-1}. For example, the N–H$\cdots$O stretching modes of the hydrogen bond in [N133][TfO] occurs at 161 cm^{-1} as depicted in Figure 4.10b. The low intensity peaks in the 200–350 cm^{-1} region (see Figure 4.9b) corresponds to the twisting modes of the quaternary ammonium ion. Similar to the VDOS of the cation, the peak intensity shows a red shift with an increase in the length of the alkyl group in the quaternary ammonium cation. For example, the twisting mode of the quaternary ammonium ion in [N133][TfO] occurs at 221 cm^{-1} as shown in Figure 4.10c. Results from MD simulations agree well with experimental observations of Fumino *et al.* [26, 27] on PILs.

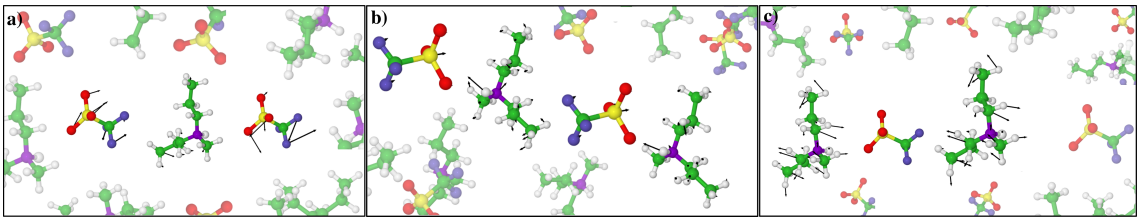

Figure 4.10: Atomic displacements in [N133][TfO] IL (a) interionic modes at 51 cm^{-1}, (b) stretching vibration of the N–H$\cdots$O hydrogen bond at 161 cm^{-1}, and (c) twisting modes of the cation center at 221 cm^{-1}. Here, only a few ions are highlighted out of the bulk liquid for the sake of clarity. Arrows represent atomic displacement vector and are scaled by an arbitrary factor for better visualization. Color scheme: nitrogen, violet; carbon, green; hydrogen, white; sulfur, yellow; oxygen, red; fluorine, iceblue.

4.3.3 Self-diffusion Coefficient and Electrical Conductivity

The influence of the quaternary ammonium triflate structure on the dynamical properties of PILs with varying alkyl groups on the cation is investigated by calculating the mean square displacement (MSD) and electrical conductivity. For all PILs, the MSD for cations and anions are calculated using the Einstein relationship. To identify the diffusive regime

Table 4.4: Self-diffusion coefficients ($\times 10^{-6}$cm^{2}s^{-1}) and electrical conductivity (Sm^{-1}) of ammonium-triflate ILs from MD simulations at 393 K.

System	D^+	D^-	σ_{NE}	σ_{GK}	$\sigma_{exp.}$ [12]	σ_{GK}/σ_{NE}
[N112][TfO]	2.9	2.2	4.8	1.9	5.60	0.39
[N122][TfO]	2.5	2.0	3.9	1.6	4.33	0.41
[N222][TfO]	2.2	1.7	3.0	0.9	2.76	0.29
[N133][TfO]	1.5	1.2	2.0	0.7	-	0.37

of ILs, the exponent β is determined using Eqn. 4.2[2, 48] as:

$$\beta(t) = \frac{d\ ln\langle \Delta r^2(t) \rangle}{d\ ln(t)} \tag{4.2}$$

where, $\beta(t)$ is the first derivative of log MSD versus log time plot. For diffusive behaviour, $\beta(t)$ = 1. The self-diffusion coefficients (D^+ and D^- for cations and anions respectively) are calculated from the diffusive regime (beyond 2 ns) of MSD.

The calculated D^+ and D^- values at 393 K are shown in Table 4.4. For all PILs, the diffusivity of cations (D^+) is higher compared to that of triflate anions in respective ILs. The self-diffusion coefficient (D^+) of the quaternary ammonium cation decreases with an increase in the bulkiness and molecular mass of the cation. A strong influence of the bulky nature of the cation is observed on the mobility of triflate anions. For example, the D^- in [N133][TfO] decreases by a factor of 0.6 compared to that in [N122][TfO]. The Nernst–Einstein conductivity calculated from D^+ and D^- decreases with an increase in the length of the alkyl group on the cation. The electrical conductivity calculated from the Green-Kubo relation shows large deviations (>60 %) with experimental values [12] and points to the necessity of refinement of the force field, particularly the non-bonded parameters. The difference between the conductivity obtained from the Green-Kubo relation compared to that obtained from the Nernst-Einstein relation indicates that the dynamics of these PILs is highly correlated. In summary, the self-diffusion coefficient and the electrical conductivity (σ_{NE} and σ_{GK}) from simulations is highest for [N112][TfO] and is lowest for [N133][TfO]. Although the σ_{GK} values are lower then $\sigma_{Exp.}$, [12] the trend among the PILs is captured from these simulations. A quantitative comparison can be expected with a refined force field.

4.4 Conclusions

A molecular level understanding of structure and dynamics in quaternary ammonium triflate PILs is presented using classical MD simulations. RDFs demonstrate that hydrogen bonding interactions between the ions increase with an increase in the bulkiness of the alkyl

group attached to the N-atom of the ammonium cation. Weak hydrogen bonding between ethyl hydrogen atoms and anion oxygen atoms lead to a more symmetric distribution of anions in [N222][TfO]. The spatial density map of anions over alkyl terminals of the cation varies from highly diffused (in [N112][TfO]), scattered (in [N122][TfO] and [N222][TfO]) to condensed (in [N133][TfO]), with an increase in size of the alkyl group from methyl to *n*-propyl. The depth at the first minimum of VACF is highest for [N112][TfO] and becomes insubstantial for [N133][TfO]. The VDOS calculated from the Fourier transform of VACFs clearly shows the presence of strong intermolecular interactions. Furthermore, normal-mode analysis (NMA) within the harmonic approximation distinctly reveals N–H$\cdots$O hydrogen bond stretching vibration in the low frequency region of 155–165 cm^{-1}. A red shift in twisting vibration modes of the quaternary ammonium cation is observed in the 200–350 cm^{-1} region with an increase in the bulkiness of the alkyl group from methyl to *n*-propyl. Anion rattling modes are present in the sub-100 cm^{-1} region.

The influence of steric effects on ionic mobility is examined by calculating the self-diffusion coefficient and electrical conductivity. A significant improvement in the prediction of self-diffusion coefficient is seen with the scaled charge model compared to the full charge model, which is compared for the case of [N122][TfO] to experimental values. The mobility of ions decreases with an increase in the size of the alkyl group. A large difference ($>60\%$) in electrical conductivity calculated from the Green-Kubo relation compared with that obtained from the Nernst-Einstein relation points to the correlated nature of ion transport in PILs. The force field for the simulations needs to be refined in order to quantitatively reproduce experimentally determined electrical conductivity values, although its trend upon changing the cation is well reproduced by the simulations. Furthermore, *ab initio* MD simulations and/or simulations using polarizable force fields too should be explored for these ammonium ion based protic ILs.

Bibliography

[1] Angell, C. A.; Byrne, N.; Belieres, J.-P. *Acc. Chem. Res.* **2007**, *40*, 1228–1236.

[2] Maginn, E. J. *Acc. Chem. Res.* **2007**, *40*, 1200–1207.

[3] MacFarlane, D. R.; Forsyth, M.; Howlett, P. C.; Pringle, J. M.; Sun, J.; Annat, G.; Neil, W.; Izgorodina, E. I. *Acc. Chem. Res.* **2007**, *40*, 1165–1173.

[4] Greaves, T. L.; Drummond, C. J. *Chem. Rev.* **2008**, *108*, 206–237.

[5] Bai, Y.; Cao, Y.; Zhang, J.; Wang, M.; Li, R.; Wang, P.; Zakeeruddin, S. M.; Grätzel, M. *Nat. Mater.* **2008**, *7*, 626–630.

[6] Armand, M.; Endres, F.; MacFarlane, D. R.; Ohno, H.; Scrosati, B. *Nat. Mater.* **2009**, *8*, 621–628.

[7] MacFarlane, D. R.; Tachikawa, N.; Forsyth, M.; Pringle, J. M.; Howlett, P. C.; Elliott, G. D.; Davis, J. H.; Watanabe, M.; Simon, P.; Angell, C. A. *Energy Environ. Sci.* **2014**, *7*, 232–250.

[8] Fedorov, M. V.; Kornyshev, A. A. *Chem. Rev.* **2014**, *114*, 2978–3036.

[9] Yoshizawa, M.; Xu, W.; Angell, C. A. *J. Am. Chem. Soc.* **2003**, *125*, 15411–15419.

[10] Nakamoto, H.; Watanabe, M. *Chem. Commun.* **2007**, 2539–2541.

[11] Belieres, J.-P.; Gervasio, D.; Angell, C. A. *Chem. Commun.* **2006**, 4799–4801.

[12] Belieres, J.-P.; Angell, C. A. *J. Phys. Chem. B* **2007**, *111*, 4926–4937.

[13] Luo, J.; Conrad, O.; Vankelecom, I. F. J. *J. Mater. Chem.* **2012**, *22*, 20574–20579.

[14] Kumar, M.; Venkatnathan, A. *J. Phys. Chem. B* **2013**, *117*, 14449–14456.

[15] Sarode, H. N.; Lindberg, G. E.; Yang, Y.; Felberg, L. E.; Voth, G. A.; Herring, A. M. *J. Phys. Chem. B* **2014**, *118*, 1363–1372.

[16] Lee, S.-Y.; Ogawa, A.; Kanno, M.; Nakamoto, H.; Yasuda, T.; Watanabe, M. *J. Am. Chem. Soc.* **2010**, *132*, 9764–9773.

[17] Noto, V. D.; Negro, E.; Sanchez, J.-Y.; Iojoiu, C. *J. Am. Chem. Soc.* **2010**, *132*, 2183–2195.

[18] Noto, V. D.; Piga, M.; Giffin, G. A.; Lavina, S.; Smotkin, E. S.; Sanchez, J.-Y.; Iojoiu, C. *J. Phys. Chem. C* **2011**, *116*, 1361–1369.

[19] Noto, V. D.; Piga, M.; Giffin, G. A.; Lavina, S.; Smotkin, E. S.; Sanchez, J.-Y.; Iojoiu, C. *J. Phys. Chem. C* **2011**, *116*, 1370–1379.

[20] Sood, R.; Iojoiu, C.; Espuche, E.; GouanvÃl', F.; Gebel, G.; Mendil-Jakani, H.; Lyonnard, S.; Jestin, J. *J. Phys. Chem. C* **2012**, *116*, 24413–24423.

[21] Langevin, D.; Nguyen, Q. T.; Marais, S.; Karademir, S.; Sanchez, J.-Y.; Iojoiu, C.; Martinez, M.; Mercier, R.; Judeinstein, P.; Chappey, C. *J. Phys. Chem. C* **2013**, *117*, 15552–15561.

[22] Sood, R.; Iojoiu, C.; Espuche, E.; Gouanvé, F.; Gebel, G.; Mendil-Jakani, H.; Lyonnard, S.; Jestin, J. *J. Phys. Chem. C* **2014**, *118*, 14157–14168.

[23] Chang, T.-M.; Dang, L. X. *J. Phys. Chem. A* **2009**, *113*, 2127–2135.

[24] Kohagen, M.; Brehm, M.; Thar, J.; Zhao, W.; Müller-Plathe, F.; Kirchner, B. *J. Phys. Chem. B* **2011**, *115*, 693–702.

[25] Schroder, C. *Phys. Chem. Chem. Phys.* **2012**, *14*, 3089–3102.

[26] Fumino, K.; Reichert, E.; Wittler, K.; Hempelmann, R.; Ludwig, R. *Angew. Chem. Int. Ed.* **2012**, *51*, 6236–6240.

[27] Fumino, K.; Fossog, V.; Wittler, K.; Hempelmann, R.; Ludwig, R. *Angew. Chem. Int. Ed.* **2013**, *52*, 2368–2372.

[28] Fumino, K.; Reimann, S.; Ludwig, R. *Phys. Chem. Chem. Phys.* **2014**, *16*, 21903–21929.

[29] Koh, A. R.; Hwang, B.; Chul Roh, K.; Kim, K. *Phys. Chem. Chem. Phys.* **2014**, *16*, 15146–15151.

[30] Sunda, A. P.; Dhavale, V. M.; Kurungot, S.; Venkatnathan, A. *J. Phys. Chem. B* **2014**, *118*, 1831–1838.

[31] Chang, T. M.; Dang, L. X.; Devanathan, R.; Dupuis, M. *J. Phys. Chem. A* **2010**, *114*, 12764–12774.

[32] Blanchard, J. W.; Belières, J.-P.; Alam, T. M.; Yarger, J. L.; Holland, G. P. *J. Phys. Chem. Lett.* **2011**, *2*, 1077–1081.

[33] Johnson, L.; Ejigu, A.; Licence, P.; Walsh, D. A. *J. Phys. Chem. C* **2012**, *116*, 18048–18056.

[34] Ejigu, A.; Walsh, D. A. *J. Phys. Chem. C* **2014**, *118*, 7414–7422.

[35] Plimpton, S. *J. Comput. Phys.* **1995**, *117*, 1–19.

[36] Jorgensen, W. L.; Maxwell, D. S.; Tirado-Rives, J. *J. Am. Chem. Soc.* **1996**, *118*, 11225–11236.

[37] Lopes, J. N. C.; Pádua, A. A. H. *J. Phys. Chem. B* **2004**, *108*, 2038–2047.

[38] Lopes, J. N. C.; Pádua, A. A. H. *J. Phys. Chem. B* **2004**, *108*, 16893–16898.

[39] Yasuda, T.; Kinoshita, H.; Miran, M. S.; Tsuzuki, S.; Watanabe, M. *J. Chem. Eng. Data* **2013**, *58*, 2724–2732.

[40] Martínez, L.; Andrade, R.; Birgin, E. G.; Martínez, J. M. *J. Comp. Chem.* **2009**, *30*, 2157–2164.

[41] Nosé, S. *J. Chem. Phys.* **1984**, *81*, 511–519.

[42] Hoover, W. G. *Phys. Rev. A* **1985**, *31*, 1695–1697.

[43] Krishnan, M.; Balasubramanian, S. *Phys. Rev. B* **2003**, *68*, 064304.

[44] Humphrey, W.; Dalke, A.; Schulten, K. *J. Mol. Graphics* **1996**, *14*, 33–38.

[45] Jmol: an open-source Java viewer for chemical structures in 3D. http://www.jmol.org/.

[46] Harada, M.; Yamanaka, A.; Tanigaki, M.; Tada, Y. *J. Chem. Phys.* **1982**, *76*, 1550–1556.

[47] Hansen, J.-P.; McDonald, I. R. *Theory of Simple Liquids, Third Edition*; Academic Press, 2006.

[48] Del Pópolo, M. G.; Voth, G. A. *J. Phys. Chem. B* **2004**, *108*, 1744–1752.

Chapter 5A

Thermal Phase Behavior and Ion Hopping in a Protic Organic Ionic Plastic Crystal

5A.1 Introduction

The thermal phase behavior of organic ionic plastic crystals (OIPCs) is crucial for their potential applicability as solid electrolytes in batteries, fuel cells and dye-sensitized solar cells. [1–17] The occurrence of one or more than one solid–solid phase transition in such plastic crystals is yet another reason that draws one's attention to investigate their structural characteristics. The varying dynamics of ions in different solid phases contribute critically to the electrolytic properties of pristine and alkali metal doped OIPCs. [18–23] Recently, Jin *et al.* [7] investigated the ion transport mechanism in diethyl(methyl)(iso-butyl)phosphonium hexafluorophosphate ($[P_{1224}][PF_6]$) OIPC and showed that the tumbling motion of ions in its plastic phase aids in faster ion diffusion. Further, molecular dynamics (MD) simulations by Forsyth and co-workers [24, 25] on $[P_{1224}][PF_6]$ showed the presence of dynamic heterogeneity in the solid phase and a crankshaft motion around the alkyl groups (methyl/ethyl group as head and the iso-butyl group as tail) in the plastic phase. Although plastic crystals exhibit long range translational order, orientational disorder can often set in at intermediate temperatures, which can enhance ion mobility.

Substantial progress has been made over the years in research on OIPCs to demonstrate their potential as solid-state anhydrous electrolytes. [4, 9] However, a molecular-level

Reprinted with permission from "Thermal Phase Behavior and Ion Hopping in 1,2,4-Triazolium Perfluorobutanesulfonate Protic Organic Ionic Plastic Crystal" *Phys. Chem. Chem. Phys.* **2016**, *18*, 2047–2053. http://dx.doi.org/10.1039/C5CP05701A.

understanding of the phase behavior, the temperature-dependent disordering phenomenon and transport mechanisms in Protic Organic Ionic Plastic Crystal (POIPC) materials is yet to be explored. While the dominant contribution to electrical conductivity is protonic, at moderate temperatures, ion motion too has been implicated. [11] Experiments on 1,2,4-triazolium perfluorobutanesulfonate ([TAZ][pfBu]) POIPC by Luo *et al.* [11] have revealed the following features: Up to 348 K, the crystal is stable, after which plastic deformation sets in. Ion rotation and likely diffusion happens in the range 350-375 K which is followed by a transition to a Phase-I (375-430 K) which exhibits high conductivity with an activation energy of 0.38 eV. In this phase, proton hopping via the Grotthuss mechanism is believed to be operative. Within a narrow range of temperature above 430 K, both cations and anions are also mobile which is followed by the melt phase. Given the above, details of the molecular motions of ions in the perfect crystal and of vacancies needs to be unravelled both by further experiments as well as microscopic simulations. While a study of proton transport is important, it will require *ab initio* MD simulations [26] and the likely inclusion of quantum effects on dynamics. Using empirical potential MD simulations, one can, however gain an understanding of the nature of phases as well as mechanisms of vehicular diffusion of ions. In this spirit, in the present work, we report results on the structure of different thermal phases of 1,2,4-triazolium perfluorobutanesulfonate ([TAZ][pfBu]) POIPC, obtained using such classical MD simulations. Significant changes in the cation-anion hydrogen bonding network [11] and a concomitant freedom from orientational order is seen in the plastic crystalline phase of this compound.

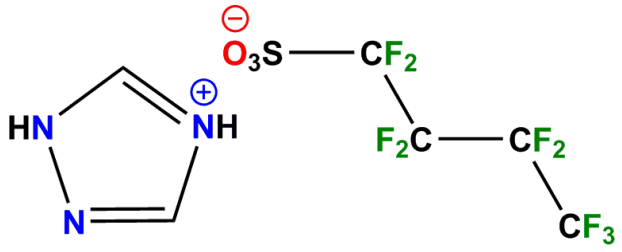

Figure 5A.1: The chemical structure of [TAZ][pfBu] POIPC.

5A.2 Simulation Details

The chemical structure of [TAZ][pfBu] is presented in Figure 5A.1. MD simulations of the perfect crystalline phase of this salt and a model containing one ion pair vacancy were performed using LAMMPS program. [27] Initial cell parameters and atomic positions were taken from the experimentally determined crystal structure. [11] The size of simulation cell was 6x4x1 unit cells (2496 atoms, see Table 5A.1). The interaction parameters to model the triazolium cation were taken from the work of Maginn and co-workers [28]

Table 5A.1: Summary of the cell parameters and supercell dimension for the perfect crystal and vacancy model simulations.

System	Cell parameter						Supercell	Number of atoms
	a(Å)	b(Å)	c(Å)	$\alpha(^o)$	$\beta\ (^o)$	$\gamma\ (^o)$		
Perfect Crystal	5.27	8.27	29.67	90.00	93.12	90.00	(6x4x1)	2496
Vacancy Model	5.27	8.27	29.67	90.00	93.12	90.00	(8x6x2)	9958

Table 5A.2: Simulated cell parameters and compared against the experimental data at 100 K. Uncertainty in simulated values were of the order of 0.002.

Supercell	Method	a (Å)	b (Å)	c (Å)	$\alpha\ (^o)$	$\beta\ (^o)$	$\gamma\ (^o)$	ρ (g/cm^3)
(6x4x1)	exp.	31.645	33.087	29.673	90.0	93.124	90.0	1.897
	sim.	31.877	33.238	29.886	89.73	92.657	89.87	1.899

and for the anion from the work of Goddard *et al.* [29] The latter force field did not have charges on sites which are crucial for the current study. Hence, the site charges on ions were determined via periodic density functional theory calculations performed using CP2K. [30] Results of such calculations yielded the valence electron density which was the input to the DDEC/c3 method to derive atomic site charges. [31, 32] A distance cutoff of 12 Å was employed to calculate the pairwise interactions in real space. The time-step used to integrate the equations of motion was 0.5 fs. The long-range interactions were evaluated using PPPM solver with a precision of 10^{-5}. The calculated cell parameters at 100 K differed by less than 0.7% of their experimental values (see Table 5A.2), which suggests that the crystal structure was stable in the simulations employing these force field parameters. Energy minimization was performed on the initial configuration. The configuration was then warmed to 300 K at a heating rate of 1 K/50 ps in the constant-NVT ensemble. It was followed by an equilibration of 5 ns at 300 K. The equilibrated configuration was further heated up to 500 K at a rate of 1 K/100 ps in the fully flexible isothermal-isobaric (NPT) ensemble. Coordinates were dumped each 10 K and a further equilibration of 4 ns was carried out in the fully flexible isothermal-isobaric (NPT) ensemble at each temperature. Cell parameters were taken from these runs. After the initial equilibration, a separate trajectory of 10 ns duration was generated at each temperature in the NVT ensemble to compute several equilibrium properties. The variation in cell parameters and change in cell volume with temperature (at different phases) are displayed in Figure 5A.2. We present a discussion on the identification of different phases on Figure 5A.2b later.

Vacancy model simulations. The vacancy model required a large supercell dimension (8x6x2) consisting of 384 ion pairs (9984 atoms). One pair of cation and anion was removed

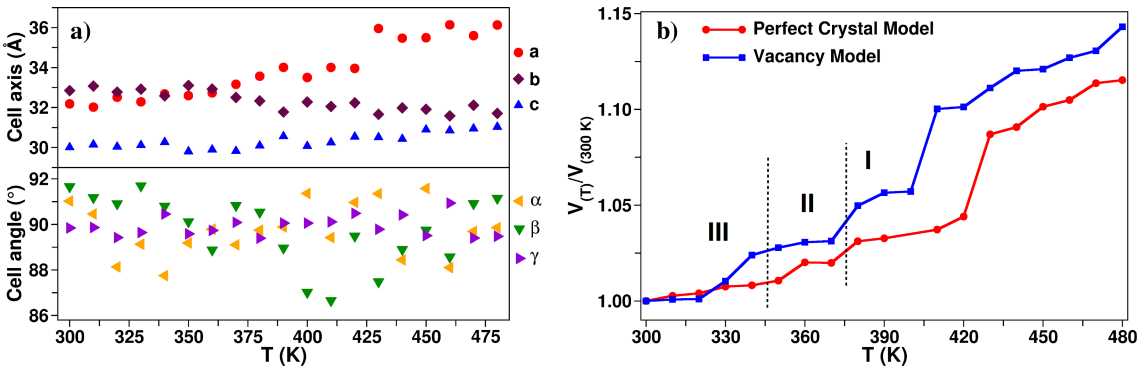

Figure 5A.2: (a) Cell parameters as a function of temperature in perfect crystalline model: cell axes (upper) and cell angles (lower). Standard deviations in cell lengths and angles are 0.15 Å and 0.62° respectively. (b) Variation in the volume of simulation cell with temperature.

in order to create vacancy sites. An energy minimized configuration was used to perform simulation in NVT ensemble with a heating rate of 1 K/50 ps to obtain a configuration at 500 K. It was followed by an another equilibration of 5 ns in a fully flexible NPT ensemble. The subsequent production trajectory was generated in NVT ensemble for 100 ns to compute dynamic properties. Other simulation details were kept similar to the perfect crystalline system.

Free energy calculations. To calculate the free energy barrier of hopping of an ion to a neighbouring vacancy site, a large supercell (8x6x2) from the experimental [11] crystal structure was considered. Following an energy minimization, MD simulation in the NVT ensemble was performed; later the system was warmed up to 500 K at a heating rate of 1 K/50 ps. At 500 K, the system was equilibrated for over 5 ns in the fully flexible NPT ensemble. A further equilibration was carried out in the NVT ensemble for 1 ns. From this equilibrated configuration, a pair (non-adjacent) of cation and anion was chosen whose time average center of mass (COM) positions were calculated over a duration of 500 ps. The selected pair of ions were then removed and a non-interacting dummy atom was placed at those average COM positions which acted as reference locations of the vacancy site. The COM of four ions (two cations and two anions) arbitrarily chosen such that they were situated far away from a chosen vacancy site were constrained such that the whole system cannot translate during the simulation. Colvar style “distance Z” was used in determining the free energy profile using the Adaptive Biasing Force (ABF) method. [33] Reaction coordinate (RC) was defined as the distance between the COM of an ion (cation or anion) and the COM of dummy atom (see Figure 5A.3a). Typically, the closest ion to the vacancy site was chosen as the “hopping” ion. ABF forces were applied every 500 steps with a bin

width of 0.2 Å. An average sampling ratio was around 4 after 5 ns between the highest and lowest points. The same procedure was applied to five different initial configurations for both the ion types. Free energy profiles were calculated from these five initial configurations and are presented in Figure 5A.3b. The mean free energy profile is presented and discussed later.

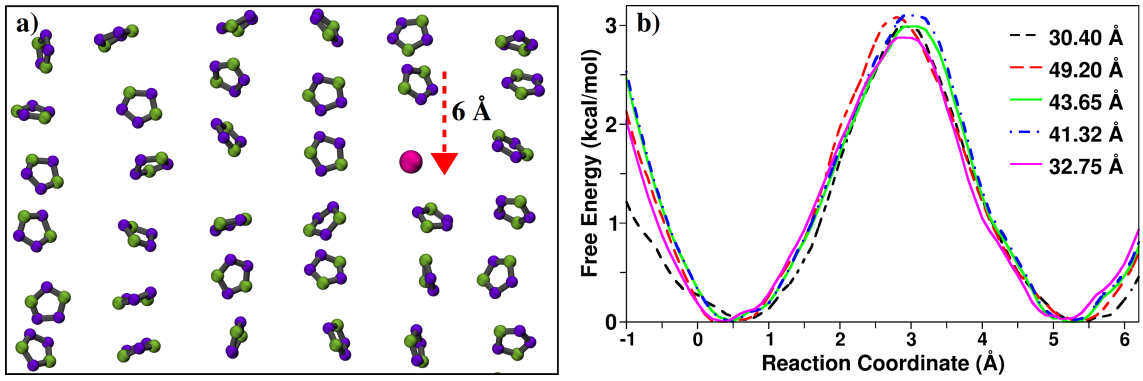

Figure 5A.3: (a) Snapshots show the reaction coordinate (RC) which is defined as the distance between the center of mass of dummy atom and center of mass of the cation. (b) Free energy profiles for the motion of cation obtained using different initial configurations. The distances mentioned in the legend correspond to that between the cation-anion vacancies in each initial configuration.

The effect of temperature on the vibrational spectrum was investigated through normal-mode analysis (NMA) at the harmonic level. For this, configurations collected from the classical MD trajectory at different temperatures were energy minimized in LAMMPS. [27] Later, the Hessian matrix (second derivative of the potential energy with respect to the atom coordinates) of such configurations was constructed using a normal-mode analysis code developed earlier in our group. [34] Within the harmonic approximation, diagonalization of this matrix yields eigenvectors which are proportional to atomic displacements of different modes. Complete details of charge calculations and normal-mode analysis (NMA) are described in Chapter 2A and Chapter 3, respectively.

5A.3 Results and Discussion

The structural characteristics of [TAZ][pfBu] at different temperatures were examined through cation-anion radial distribution functions (RDFs) and are displayed in Figure 5A.4. The H_N-O and H_C-O RDFs show that the strong N-H$\cdots$O and weaker C-H$\cdots$O hydrogen bonding interactions are not much influenced by temperature. The number of H_N atoms within the first solvation shell of oxygen atoms of anion decreases with increasing temperature, shown in Figure 5A.4d. As there are three hydrogen bonding sites on the anion and only two on the cation, the latter's rotation at intermediate temperatures allows the

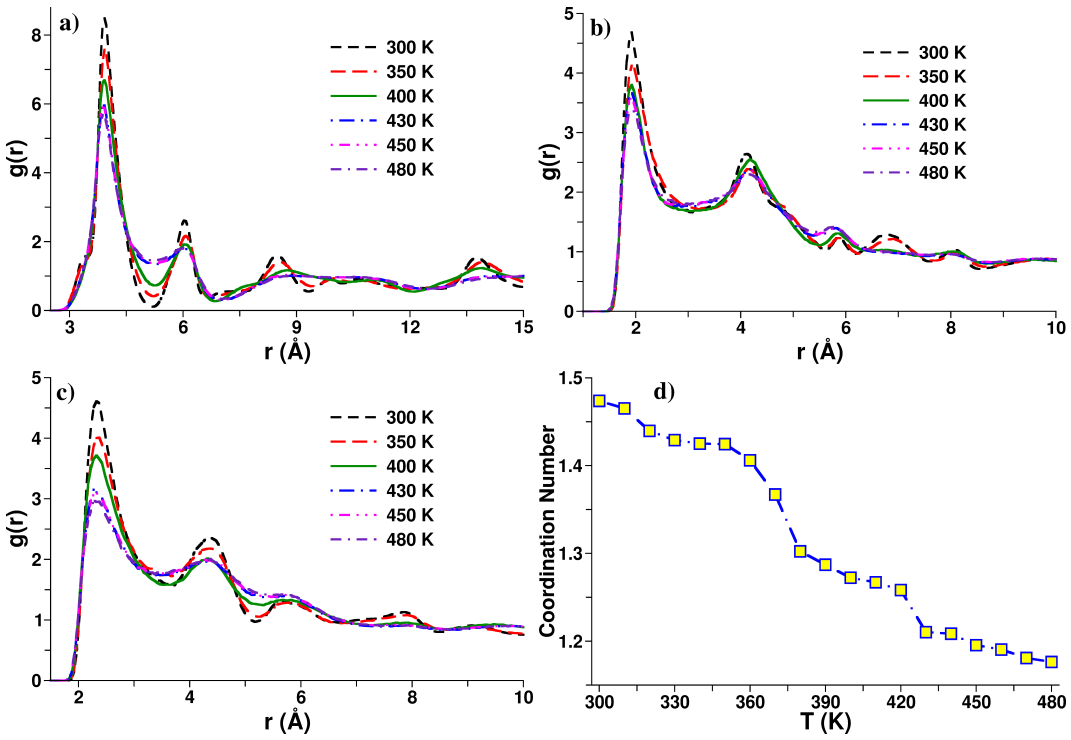

Figure 5A.4: RDFs for (a) cation–anion, (b) H_N-O, and (c) H_C-O pairs at various temperatures. (d) Coordination number of cation's N-H hydrogen (H_N) around anion's oxygen as a function of temperature.

breakage of existing H-bonds and formation of new ones. In this manner, every oxygen site on the anion participates in hydrogen bonding, creating a dynamic 3-dimensional hydrogen bonding network. The overall decrease in the coordination number suggests the presence of disorder at higher temperature. While the ion-ion RDFs at high temperature retain most features of those at low temperatures, a few critical shoulders (sub-peaks) are missing, pointing to a loss of certain degree of crystallinity. Crucially, the triazolium rings are seen to be misoriented with increasing temperature, although they retain their lattice positions (Figure 5A.5). Such an intermediate phase between 380 K and 430 K can thus be called as the rotator phase.

Ring plane rotational correlation (C(t)). The rotational dynamics of the cation was investigated using the time autocorrelation function of its ring normal, C(t) defined as,

$$C(t) = \langle \vec{R}_i(t).\vec{R}_i(0) \rangle \tag{5A.1}$$

where $\vec{R}_i(t)$ is the normal vector corresponding to each 1,2,4-triazolium ring plane at time t and the function is averaged over initial times and cation indices. Figure 5A.6a shows that C(t) does not decay much at 300 K. At low temperature (phase III, Figure 5A.2b), the

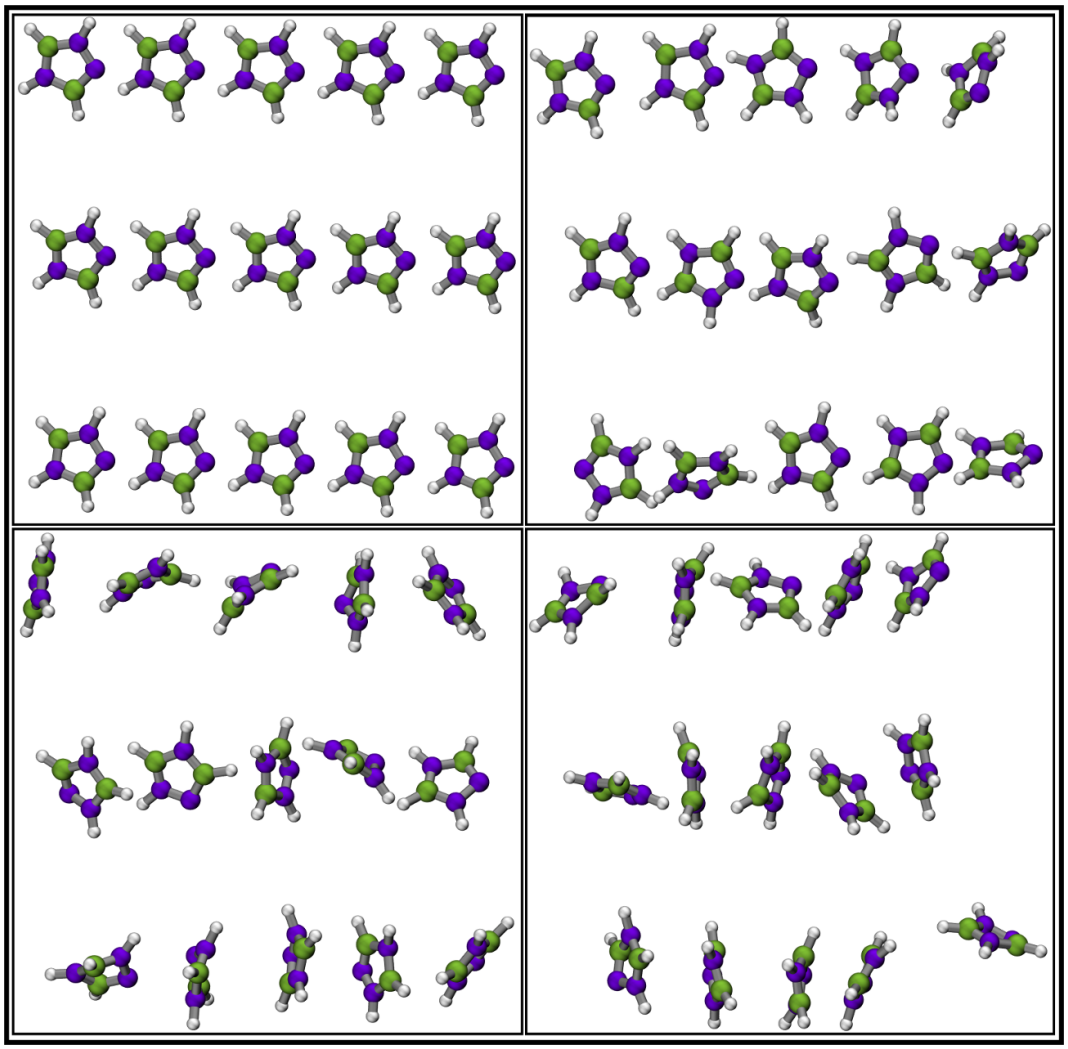

Figure 5A.5: Snapshots of 1,2,4-triazolium rings from MD simulation of the perfect crystal depicts ring plane rotational order & disorder at 330 K [top-left], 380 K [top-right], 430 K [bottom-left], and 470 K [bottom-right]. Color scheme: nitrogen, violet; carbon, green; hydrogen, white.

ring planes of cations are oriented in a perfect manner as shown in Figure 5A.6b. Between 360 K and 380 K, the rate of decay increases sharply (phase II, Figure 5A.2b). Above 430 K, (phase I, Figure 5A.2b) the correlation function decays to zero within 0.05 ns. Cations in the lattice lose their orientational rigidity in the temperature range of 330-380 K, above which they are free to rotate which is also seen in Figure 5A.6c and Figure 5A.5. Thus, the orientational order between 1,2,4-triazolium ring planes get decorrelated at higher temperature. The ring starts rotating above 350 K and tumbles at $\sim$ 430 K.

The distribution of the angle between the ring planes of neighboring cations was calculated at different temperatures. Figure 5A.7a shows it to be sharply peaked at low temperatures with values around ± 1, implying the parallel orientation of such planes.

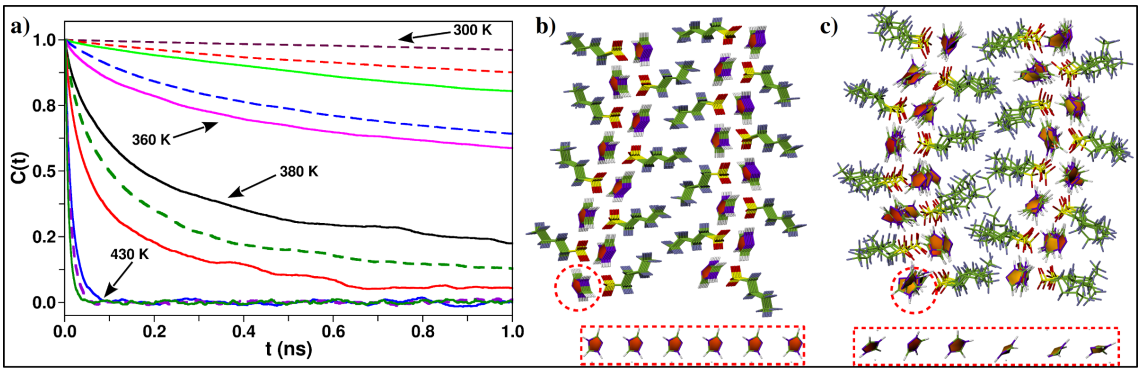

Figure 5A.6: (a) Auto time correlation function of ring plane normal of the cation at different temperatures. Only a few lines are marked with temperature for the sake of clarity, unmarked lines correspond to intermediate temperatures. Snapshots of [TAZ][pfBu] from NVT production runs at (b) 330 K, and (c) 380 K. Color scheme: nitrogen, violet; carbon, green; hydrogen, white; oxygen, red; sulfur, yellow; fluorine; iceblue.

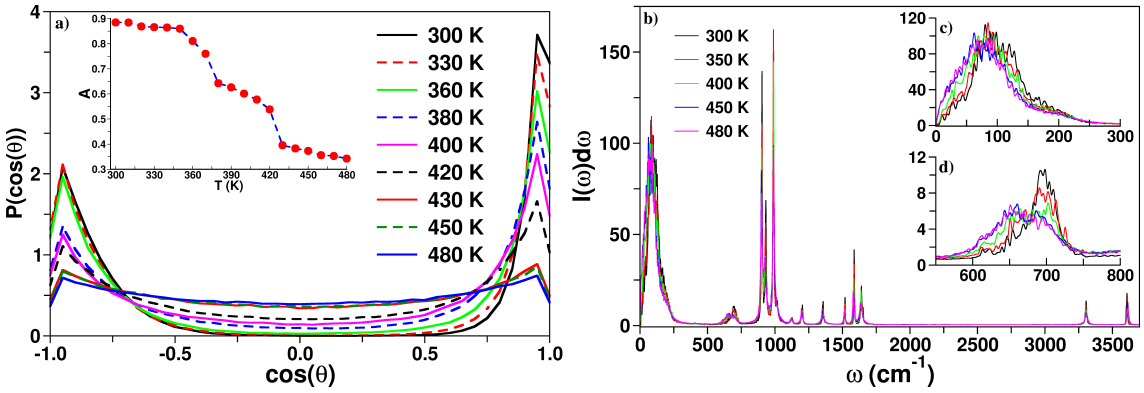

Figure 5A.7: (a) Distribution of the angle between ring planes of neighboring cations. Inset: Area under the distribution, for the regions $|\cos\theta| > 0.7$ versus temperature. (b) Vibrational density of states (VDOS) calculated for [TAZ][pfBu] from the power spectrum of the velocity autocorrelation function at different temperature. Inset: Region of spectrum (c) below 150 cm^{-1}, and (d) between 600-750 cm^{-1}.

At high temperatures, a nearly uniform distribution is seen which points to complete orientational disorder. The onset of this disorder can be captured by plotting the area under the curve (A) (between $cos(\theta)$ values of -1.0 to -0.7 and 0.7 to 1.0) against temperature as shown in inset of Figure 5A.7a. Its behavior is similar to that of the dependence of volume on T (see Figure 5A.2b), however the transitions are more evident. The observed discontinuities in both this area and the cell volume at the phase transitions are in excellent agreement with experiments [11], as expected for the three phases (phases III, II and I) of [TAZ][pfBu] POIPC, although the transition temperatures seen in simulations are higher, due to superheating effects. Thus, in the simulations, the crystal is in the rotator phase at

temperatures higher than 420-430 K too, and phase I of simulations is a metastable one.

Further, the vibrational density of states (VDOS) of [TAZ][pfBu] was calculated at various temperatures from the Fourier transform of the velocity time autocorrelation function of the ions (see Figure 5A.7b). An increase in temperature results in the softening of modes present below 100 cm^{-1} and around 700 cm^{-1}. The former can be assigned to librations of cations and the latter to out-of-plane motion of N–H protons in triazolium cation (see Figure 5A.8). Rotational disorder at higher temperature facilitates cation mobility and thus causes the change in spectral behavior. These observation reproduces the experimental results of Luo *et al.* [11] using [TAZ][pfBu] POIPC.

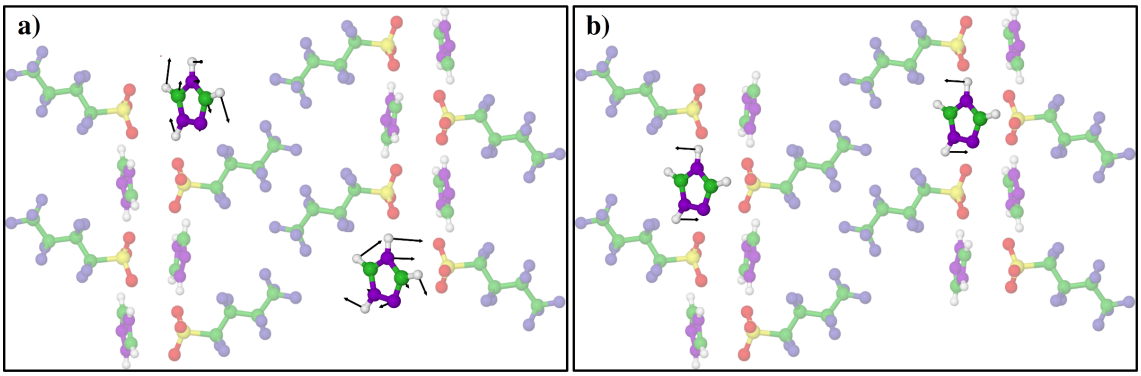

Figure 5A.8: Atomic displacements obtained from a normal mode analysis of crystalline POIPC. Two modes are shown for illustrative purposes. (a) librational mode of triazolium cation at 100 cm^{-1}, and (b) out-of-plane motion of N–H proton of triazolium cation at 715 cm^{-1}. Only a few ions from the modeled crystal are shown for the sake of clarity. Arrows are atomic displacements and are scaled by an arbitrary factor for better visualization. Color scheme: nitrogen, violet; carbon, green; hydrogen, white; oxygen, red; sulfur, yellow; fluorine; iceblue.

The dynamics of breakage and re-formation of cation-anion hydrogen bonds can be studied through time correlation functions. Two such TCFs, $S_{HB}(t)$ and $C_{HB}(t)$ can be defined, [35–38] the former providing a measure of the life time of a hydrogen bond while the latter measures the same, but allows for the reformation of hydrogen bond between the same donor-acceptor pair. The relaxation of H-bond lifetime was studied by $S_{HB}(t)$,

$$S_{HB}(t) = \frac{\langle h(0)H(t)\rangle}{\langle h\rangle} \tag{5A.2}$$

where $h(t)$ is unity when a particular H_N atom and an anion oxygen atom is hydrogen bonded at time t, and zero, otherwise. On the other hand, $H(t) = 1$ if the tagged pair of atoms remain continuously H-bonded till time t, else zero. The structural relaxation of

H-bonds was analysed by $C_{HB}(t)$,

$$C_{HB}(t) = \frac{\langle h(0)h(t)\rangle}{\langle h\rangle} \tag{5A.3}$$

The geometric definition of H-bonding (distance, angle conditions) was the same as used in previous report [37] and are provided below for the sake of completeness. A donor-acceptor (DA) pair is said to be hydrogen bonded, if the D-A distance is less than 3.5 Å, the H$\cdots$O distance less than 2.5 Å and the D-H$\cdots$O angle is greater than 140^o. The time resolutions used to obtain the $S_{HB}(t)$ and $C_{HB}(t)$ functions were 2.5 fs and 1 ps, respectively.

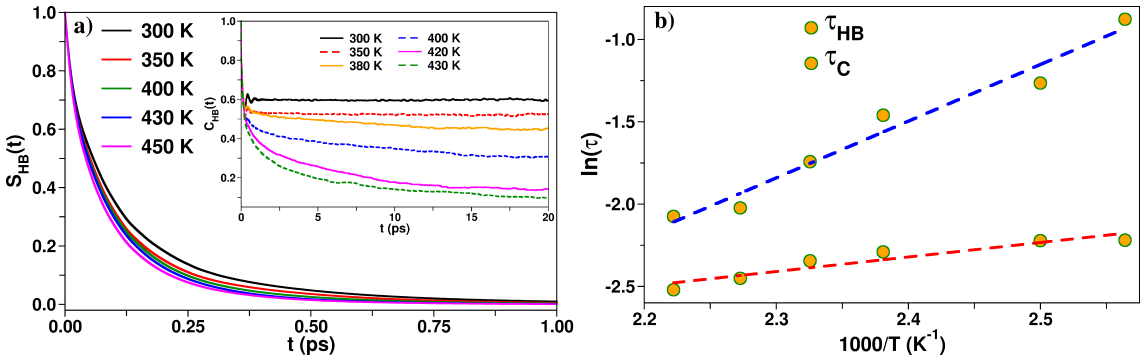

Figure 5A.9: (a) Relaxations of $S_{HB}(t)$ and $C_{HB}(t)$ (see inset) h-bond lifetime correlation function, for N-H$\cdots$O hydrogen bonding in POIPC. (b) Temperature dependence of hydrogen bond lifetime (τ_{HB}) and rotational time (τ_C). Dashed lines are best fits.

Figure 5A.9a displays the decay of $S_{HB}(t)$ and $C_{HB}(t)$ at different temperatures. $S_{HB}(t)$ relaxes quite fast even at 300 K due to the fast bond vibrational and librational motions of the ions. With increasing temperature, the decay rate increases. However, $C_{HB}(t)$ exhibits rapid oscillations at 300 K and decays to a constant value. The long time value of $C_{HB}(t)$ decreases with increasing temperature. At low temperatures, the probability for reformation of a H-bond is high and the non-zero asymptotic value of $C_{HB}(t)$ reflects this fact. At temperatures between 400 K and 430 K, this function decays slowly. The lifetime correlation functions were fitted to multi-exponential functions so as to obtain a mean relaxation time. We fit the $S_{HB}(t)$ function with a tri-exponential form,

$$S_{HB}(t) = \sum_{i=1}^{3} a_i e^{-t/\tau_i} \tag{5A.4}$$

whereas, a bimodal exponential decay and a constant term was used to fit the $C_{HB}(t)$ function

$$C_{HB}(t) = a_0 + \sum_{i=1}^{2} a_i e^{-t/\tau_i} \tag{5A.5}$$

Table 5A.3: Tri-exponential fit parameters for N-H$\cdots$O hydrogen bond lifetime correlation function ($S_{HB}(t)$) at various temperature.

Temp. (K)	a_1	$\tau_1(ps)$	a_2	τ_2 (ps)	a_2	τ_3 (ps)	$\langle\tau_S^{HB}\rangle$ (ps)
300	0.59	0.09	0.20	0.01	0.21	0.32	0.1223
350	0.63	0.10	0.18	0.01	0.19	0.30	0.1218
380	0.59	0.09	0.18	0.01	0.23	0.26	0.1147
390	0.60	0.08	0.19	0.01	0.21	0.28	0.1087
400	0.57	0.09	0.19	0.01	0.24	0.23	0.1084
420	0.63	0.09	0.20	0.01	0.17	0.25	0.1012
430	0.61	0.08	0.21	0.01	0.18	0.25	0.0959
440	0.55	0.08	0.22	0.01	0.20	0.20	0.0862
450	0.55	0.07	0.23	0.01	0.22	0.18	0.0804

Table 5A.4: Bi-exponential fit parameters for N-H$\cdots$O hydrogen bond structural relaxations ($C_{HB}(t)$) at various temperature.

Temp. (K)	a_0	a_1	$\tau_1(ps)$	a_2	τ_2 (ps)
400	0.60	0.39	0.12	0.24	2.56
420	0.55	0.39	0.08	0.21	1.98
430	0.49	0.34	0.07	0.19	1.36
440	0.39	0.19	0.05	0.17	0.16
450	0.23	0.17	0.04	0.10	0.11

where the constant a_0 is included to take into account the non-zero asymptotic value of $C_{HB}(t)$ at lower temperatures. The fit parameters are tabulated in Table 5A.3 and Table 5A.4, respectively. The mean lifetime obtained from $S_{HB}(t)$ is around 100 fs. Anion rotation has been suggested to assist proton hopping in POIPC crystal [11]. The short lifetime of the H-bond TCF in the plastic crystalline phase of this POIPC supports this mechanism. Further, the temperature dependence of hydrogen bond lifetime and rotational time are compared in Figure 5A.9b and interestingly, both of them were found to obey an Arrhenius behavior. A linear fit of the time constants to inverse temperature yields the associated activation energy of individual events. As expected, the faster hydrogen bond lifetime possess a lower activation barrier (1.75 kcal/mol) than the slower rotational time (6.78 kcal/mol).

In the IL crystal, each ion is surrounded by its counterions forming a cage. Time averaging of ion positions permits visualization of the underlying translational order in the crystal due to the effective "removal" of vibrational disorder. The same is shown in Figure 5A.10a. The average positions of the ring center at 300 K and 475 K are nearly

identical, implying the invariance of translational order with temperature over this range. The mean squared displacement (MSD) of cations is also shown (see Figure 5A.10b). After the initial ballistic motion ($\sim$ 0.2 - 0.7 ps), the MSDs of cations exhibit a plateau region (MSD $\sim$ 0.3 - 0.4 Å^2) due to the "cage". The plateau are very clearly seen at low temperatures. The time over which an ion is trapped inside a cage is different for cations and anions. Cations escape from the cage sooner due to their smaller size and rotational barrier, [24] compared to the anion.

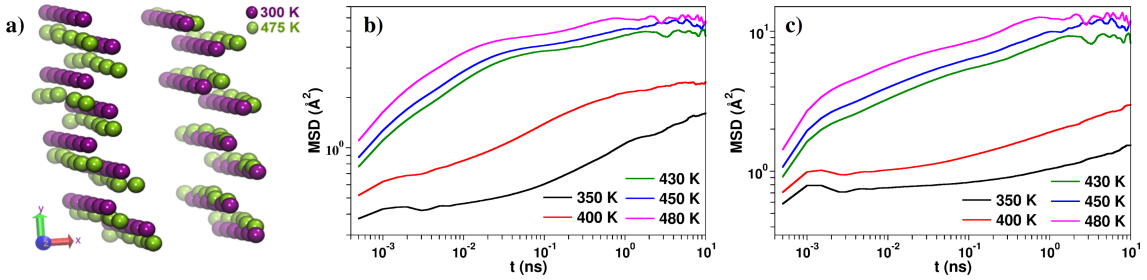

Figure 5A.10: (a) Time averaged positions of cation ring center at 300 K and 475 K, MSD of (b) cations and (c) anions calculated from MD simulations at various temperature.

The van Hove self-correlation functions identify the nature of translation of ions as either due to hopping or diffusion [39]. Even within the diffusive regime, they can aid in identifying dynamical heterogeneity. [25, 40–42] The same for the ions were calculated at 500 K, 550 K and 600 K between 0.25 to 1 ns time regime and are shown in Figure 5A.11. The first peak position for anions are slightly larger than that for cations. At 550 K, a short second peak at around 6 Å (first neighboring distance of ions) is seen at a time duration of 1 ns. The peak height grows gradually between 550 K and 600 K within 0.75 ns to 1 ns time scale. As discussed earlier, the translational motion of ions is restricted due to the formation of a cage by the counterion. The emergence of the second peak in $G_s(r,t)$ implies cation hopping. In a perfect crystal (as is the case studied here), migration of ions is possible only due to fluctuations in their environment. In the present instant, the latter is aided by rotational disorder discussed earlier. Rotational disorder aids in the migration of ions to their neighboring sites through the available free space due to structural relaxation. Cations attempting to hop to a neighboring site to later revert back to their original position, were also observed in movies of trajectories.

Ion transport in a crystalline solid state is primarily aided through defects, chief of which would be vacancies. Their concentration would increase with temperature. It is thus important to study the ion hopping phenomenon in the presence of vacancies. To this end, we have performed simulations of the crystal at 500 K which contained 384 ion pairs and one vacancy each of cation and anion. The van Hove correlation function calculated at 500 K for such a vacancy model shows the hopping of cation to take place within 1

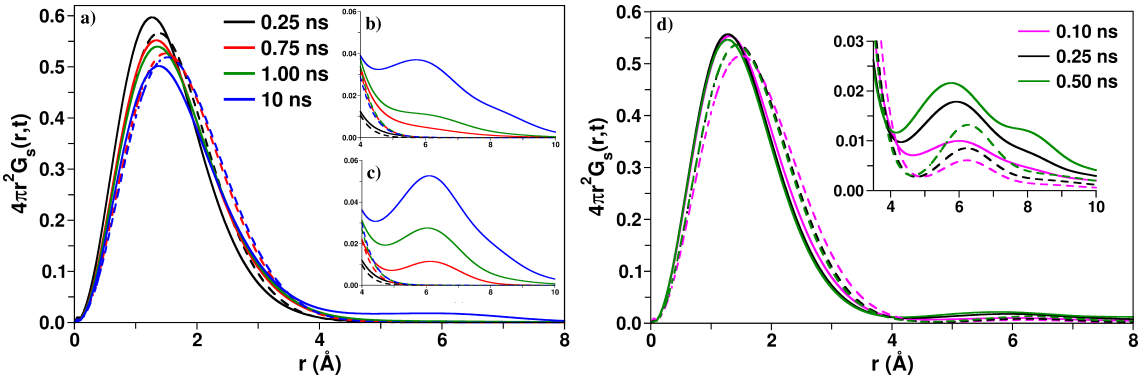

Figure 5A.11: Self part of van Hove correlation functions calculated for a perfect crystalline lattice from MD simulations at (a) 500 K, (b) 550 K, (c) 600 K, and using the vacancy model at (d) 500 K (solid line - for cation and dashed line - for anion).

ns time scale which was not observed in the perfect crystal (see Figure 5A.11). Thus, as expected, ion hopping occurs at a much lower temperature due to the presence of vacancies. The decay of the ring plane normal rotational correlation is much faster in the presence of vacancies compared to the perfect crystal (see Figure 5A.12) which suggests that the rotational disorder occurs at a lower temperature due to vacancies.

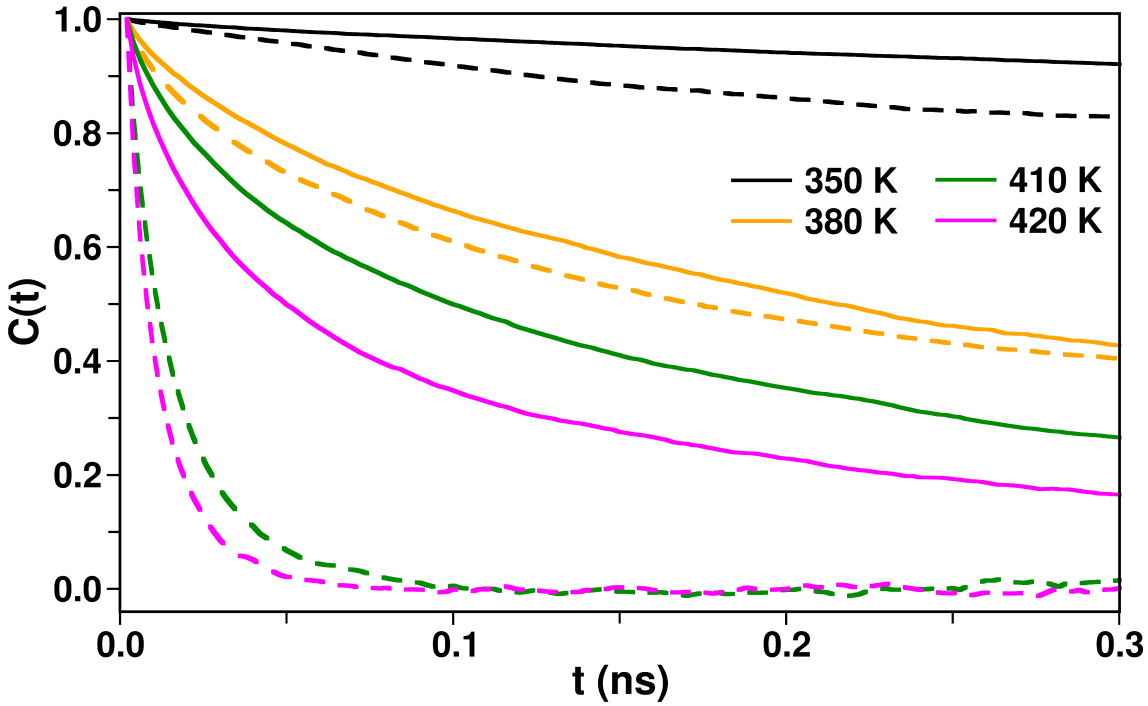

Figure 5A.12: Auto time correlation function of ring plane normal of the cation at different temperatures: solid line - perfect crystal and dashed line - vacancy model. Data for the perfect crystal was also presented in Figure 5A.6.

Figure 5A.13a-c is a pictorial view depicting the concerted hopping of cations which

results in a one-dimensional vacancy motion along the crystallographic *b*-axis. Qualitative observations showed that the hop rate for cations was higher than that for the anions. We have performed free energy calculations at 500 K to obtain the barrier associated with the hopping of ions. The calculated activation energy barrier are found to be 2.5 kcal/mol and 6.0 kcal/mol for cations and anions respectively (see Figure 5A.13d). Thus, a large energy barrier restricts the hopping of anions. Free energy calculations at a lower temperature of 400 K, but still within Phase I, yields larger barrier heights of 4.5 and 9.2 kcal/mol for the two ions. The activation (E_a) barrier obtained from ionic conductivity experiments in Phase I (373-430 K) was found to be 8.77 kcal/mol [11]. Although the results from simulations are able to predict the order of magnitude of E_a, there exists differences between the simulations and the experiment [11]. This could be due to the fact that the measured ionic conductivity in experiment is primarily protonic in nature, while the calculated activation energy from simulations is solely from individual ion motion i.e. cation and anion movement.

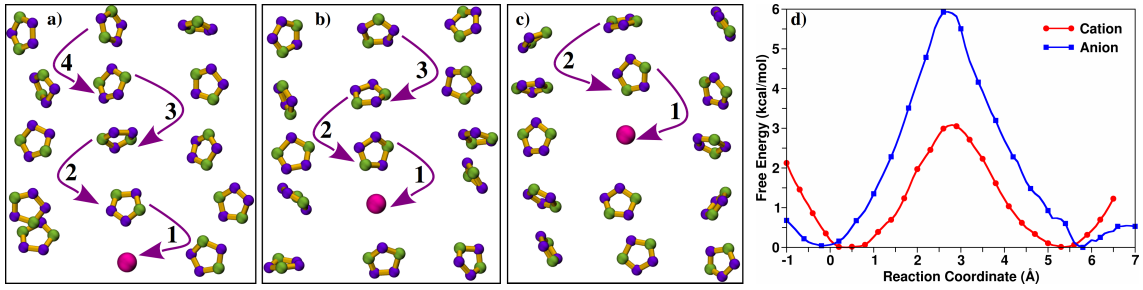

Figure 5A.13: (a-c) Concerted hopping of cations and (d) calculated free energy profiles for the motion of cation and anion at 500 K. Estimated standard error on the mean in the simulated free energy is around 0.22 kcal/mol.

The ion hopping frequency Γ can be estimated within the framework of transition state theory (TST) [43, 44]

$$\Gamma = \nu \, exp\left(\frac{-E_A}{k_B T}\right), \tag{5A.6}$$

where ν is the attempt frequency and is typically assumed to be 10^{13} Hz. [43–45] The resulting hopping frequency using Eq. 5A.6 for cations and anions are 8×10^{11} Hz and 2×10^{10} Hz, respectively. However, the number of hopping events in the MD simulations at 500 K over a duration of 1 ns were observed to be seven and two for cations and anions, respectively, which corresponds to jump frequencies of just 7×10^{9} and 2×10^{9} Hz. Thus, the hopping frequency in the vacancy based simulations are one to two orders of magnitude lesser than those obtained from the TST expression Eq. 5A.6. The reason for the difference is not far to seek; it can likely be accounted by barrier recrossing, a well established phenomenon which reduces the attempt frequency ν in Eq. 5A.6.

The jump diffusion coefficient (D_j) corresponding to an ion hopping to neighboring vacant site can be calculated as, [45]

$$D_j = \lambda^2 \Gamma / 6, \tag{5A.7}$$

where λ is a mean hopping distance. [45] The calculated jump diffusion coefficients (using Γ values obtained from Eq. 5A.6) for cations and anions are 5.7×10^{-4} cm^2 s^{-1} and 2.3×10^{-5} cm^2 s^{-1}, respectively. These are about two orders of magnitude larger than diffusion coefficients obtained from the MSD. The difference is expected as Γ via TST itself is overestimated, as discussed earlier.

5A.4 Conclusions

In conclusion, we have identified the existence of a rotator phase in [TAZ][pfBu] POIPC. It is characterized by the decorrelation of the orientation of cation ring planes. In the plastic crystalline phase, ion rotation leads to a short life-time of the N-H$\cdots$O hydrogen bond. The same has been characterized via H-bond lifetime correlation functions. The rotational disorder also allows for the hopping of ions at higher temperatures. The disorder and consequent ion hopping are accelerated due to vacancies in the crystal, and thus occur at lower temperatures (by at least 20 K) than in a perfect crystal. As the heating rates employed here are much higher than those used in experiments, superheating is likely; the same would be reflected in higher values of temperatures of phase transitions in simulations when compared to experiments. One-dimensional vacancy motion has been delineated and the free energy barrier for ion hopping has been estimated to 2.5 and 6.0 kcal/mol for cations and anions respectively. It will be interesting to extend these atomistic simulations to investigate the diffusion of additional ionic species like small alkali ions in such POIPC, as well as to study proton diffusion using *ab initio* MD methods. The latter forms the objective of Chapter 5B.

Bibliography

[1] MacFarlane, D. R.; Huang, J.; Forsyth, M. *Nature* **1999**, *402*, 792–794.

[2] Alarco, P.-J.; Abu-Lebdeh, Y.; Abouimrane, A.; Armand, M. *Nat. Mater.* **2004**, *3*, 476–481.

[3] Pas, S. J.; Pringle, J. M.; Forsyth, M.; MacFarlane, D. R. *Phys. Chem. Chem. Phys.* **2004**, *6*, 3721–3725.

[4] Pringle, J. M.; Howlett, P. C.; MacFarlane, D. R.; Forsyth, M. *J. Mater. Chem.* **2010**, *20*, 2056–2062.

[5] Armel, V.; Velayutham, D.; Sun, J.; Howlett, P. C.; Forsyth, M.; MacFarlane, D. R.; Pringle, J. M. *J. Mater. Chem.* **2011**, *21*, 7640–7650.

[6] Armel, V.; Forsyth, M.; MacFarlane, D. R.; Pringle, J. M. *Energy Environ. Sci.* **2011**, *4*, 2234–2239.

[7] Jin, L.; Nairn, K. M.; Forsyth, C. M.; Seeber, A. J.; MacFarlane, D. R.; Howlett, P. C.; Forsyth, M.; Pringle, J. M. *J. Am. Chem. Soc.* **2012**, *134*, 9688–9697.

[8] Li, Q.; Chen, X.; Zhao, J.; Qiu, L.; Zhang, Y.; Sun, B.; Yan, F. *J. Mater. Chem.* **2012**, *22*, 6674–6679.

[9] Pringle, J. M. *Phys. Chem. Chem. Phys.* **2013**, *15*, 1339–1351.

[10] Li, S.; Qiu, L.; Shi, C.; Chen, X.; Yan, F. *Adv. Mater.* **2014**, *26*, 1266–1271.

[11] Luo, J. et al. *Energy Environ. Sci.* **2015**, *8*, 1276–1291.

[12] Li, Q.; Zhao, J.; Sun, B.; Lin, B.; Qiu, L.; Zhang, Y.; Chen, X.; Lu, J.; Yan, F. *Adv. Mater.* **2012**, *24*, 945–950.

[13] MacFarlane, D. R.; Forsyth, M. *Adv. Mater.* **2001**, *13*, 957–966.

[14] Jin, L.; Howlett, P. C.; Pringle, J. M.; Janikowski, J.; Armand, M.; MacFarlane, D. R.; Forsyth, M. *Energy Environ. Sci.* **2014**, *7*, 3352–3361.

[15] Wang, P.; Dai, Q.; Zakeeruddin, S. M.; Forsyth, M.; MacFarlane, D. R.; ; Grätzel, M. *J. Am. Chem. Soc.* **2004**, *126*, 13590–13591.

[16] Golding, J.; Hamid, N.; MacFarlane, D. R.; Forsyth, M.; Forsyth, C.; Collins, C.; ; Huang, J. *Chem. Mater.* **2001**, *13*, 558–564.

[17] Patel, M.; Bhattacharyya, A. J. *Energy Environ. Sci.* **2011**, *4*, 429–432.

[18] Jin, L.; de Leeuw, S.; Koudriachova, M. V.; Pringle, J. M.; Howlett, P. C.; Chen, F.; Forsyth, M. *Phys. Chem. Chem. Phys.* **2013**, *15*, 19570–19574.

[19] Forsyth, M.; Chimdi, T.; Seeber, A.; Gunzelmann, D.; Howlett, P. C. *J. Mater. Chem. A* **2014**, *2*, 3993–4003.

[20] Chen, F.; Pringle, J. M.; Forsyth, M. *Chem. Mater.* **2015**, *27*, 2666–2672.

[21] Shi, C.; Li, S.; Zhang, W.; Qiu, L.; Yan, F. *J. Mater. Chem. A* **2013**, *1*, 13956–13962.

[22] Dai, Q.; MacFarlane, D. R.; Howlett, P. C.; Forsyth, M. *Angew. Chem. Int. Ed.* **2005**, *44*, 313–316.

[23] Romanenko, K.; Pringle, J. M.; O'Dell, L. A.; Forsyth, M. *Phys. Chem. Chem. Phys.* **2015**, *17*, 18991–19000.

[24] Chen, F.; Jin, L.; de Leeuw, S. W.; Pringle, J. M.; Forsyth, M. *J. Chem. Phys.* **2013**, *138*, 244503.

[25] Chen, F.; de Leeuw, S. W.; Forsyth, M. *J. Phys. Chem. Lett.* **2013**, *4*, 4085–4089.

[26] Vilčiauskas, L.; Tuckerman, M. E.; Bester, G.; Paddison, S. J.; Kreuer, K.-D. *Nat. Chem.* **2012**, *4*, 461–466.

[27] Plimpton, S. *J. Comput. Phys.* **1995**, *117*, 1–19.

[28] Cadena, C.; Maginn, E. J. *J. Phys. Chem. B* **2006**, *110*, 18026–18039.

[29] Jang, S. S.; Molinero, V.; Cagin, T.; Goddard, W. A. *J. Phys. Chem. B* **2004**, *108*, 3149–3157.

[30] Hutter, J.; Iannuzzi, M.; Schiffmann, F.; VandeVondele, J. *Wiley Interdiscip. Rev. Comput. Mol. Sci.* **2014**, *4*, 15–25.

[31] Manz, T. A.; Sholl, D. S. *J. Chem. Theory Comput.* **2010**, *6*, 2455–2468.

[32] Manz, T. A.; Sholl, D. S. *J. Chem. Theory Comput.* **2012**, *8*, 2844–2867.

[33] Darve, E.; Rodríguez-Gómez, D.; Pohorille, A. *J. Chem. Phys.* **2008**, *128*, 144120.

[34] Krishnan, M.; Balasubramanian, S. *Phys. Rev. B* **2003**, *68*, 064304.

[35] Rapaport, D. *Mol. Phys.* **1983**, *50*, 1151–1162.

[36] Luzar, A.; Chandler, D. *Nature (London)* **1996**, *379*, 53.

[37] Chandra, A. *Phys. Rev. Lett.* **2000**, *85*, 768–771.

[38] Balasubramanian, S.; Pal, S.; Bagchi, B. *Phys. Rev. Lett.* **2002**, *89*, 115505.

[39] Balasubramanian, S.; Rao, K. J. *J. Phys. Chem.* **1994**, *98*, 10871–10880.

[40] Sarangi, S. S.; Zhao, W.; Müller-Plathe, F.; Balasubramanian, S. *ChemPhysChem* **2010**, *11*, 2001–2010.

[41] Urahata, S. M.; Ribeiro, M. C. C. *J. Phys. Chem. Lett.* **2010**, *1*, 1738–1742.

[42] Liu, H.; Maginn, E. *J. Chem. Phys.* **2011**, *135*, 124507.

[43] Garcia-Belmonte, G.; Bisquert, J. *J. Chem. Phys.* **2005**, *123*, 074504.

[44] Van der Ven, A.; Ceder, G.; Asta, M.; Tepesch, P. D. *Phys. Rev. B* **2001**, *64*, 184307.

[45] Garcia-Belmonte, G.; García-Cañadas, J.; Bisquert, J.; Person, C. *Solid State Ionics* **2006**, *177*, 1635–1637.

Chapter 5B

Proton Hopping Mechanisms in a Protic Organic Ionic Plastic Crystal

5B.1 Introduction

Proton transfers and the consequent formation of protonic defects can lead to long range proton conduction, a key process in the function of polymer electrolyte membrane fuel cells (PEMFCs). [1, 2] PEMFCs are attractive electrochemical devices for use in transportation and portable power sources. [3, 4] A critical component of PEMFC is the electrolyte, which is a proton conductor. Often, a hydrated polymer electrolyte membrane is utilized to serve as the proton conducting material in a PEMFC, and thus it introduces a serious limitation in the operating temperature range of the cell through the boiling point of water. [5, 6]

In this regard, attempts have been made to develop water-free electrolyte materials which exhibit facile proton transport, e.g. imidazole in both solid and liquid phases, [7–10] imidazole derivatives, [6, 11, 12] proton conducting functionalized polymers, [13–24] etc. Recently, long-range proton transport phenomenon was also observed in framework materials consisting of suitable proton donor/acceptor sites, even at very low water concentrations. [25–27] Significant effort has also been focused on designing molecular crystals consisting of hydrogen-bonded network and which can act as water-free proton conductors. [28] However, it has been shown that systems with perfectly crystalline domains are not always conducive for proton transport [29, 30] and that the contribution of residual water molecules in the conduction process is non-negligible. [21, 31]

Organic ionic plastic crystals (OIPCs) composed of rotationally disordered mobile ions have emerged as solid-state ion conductors. [32–34] Although OIPCs have many positive attributes, [35, 36] inherently they are aprotic in nature and are therefore not proton conductors. In this regard, protic OIPCs (POIPCs) are promising solid-state proton conductors for fuel cell applications. [33, 37, 38] Recently, Luo *et al.* [38] explored 1,2,4-Triazolium Perfluorobutanesulfonate ([TAZ][pfBu]) POIPC, a novel electrolyte exhibiting

attractive features, such as intrinsic anhydrous proton conductivity and a wide plastic crystal phase (360–450 K). Their studies on [TAZ][pfBu] POIPC revealed high protonic conductivity in its plastic phase. In Chapter 5A, we studied the thermal phase behavior of [TAZ][pfBu] and ion transport mechanism in its perfect crystalline form and in one with an ion pair vacancy, through classical molecular dynamics simulations. However, proton diffusion, being a vital component of electrical conductivity in this system was not considered due to the lack of bond breaking and reforming capabilities in the simulation. This Chapter is focused on understanding the microscopic proton conduction mechanism in [TAZ][pfBu] under anhydrous conditions by means of *ab initio* molecular dynamics simulations. Proton shuttling between ion neighbors was observed on a significant number of occasions in the native crystal, whereas complete proton transfer was seen only in simulations of a defective crystal with a single proton-hole created in the cation. These observations delineate long-range proton conduction path in the plastic crystalline phase of this POIPC. Gas phase quantum chemical calculations of novel variants of the anion suggest the possibility of decreased barrier for proton transfer which can lead to enhanced electrical conductivities.

5B.2 Computational Details

In order to understand the mechanism of proton transport in the plastic crystalline phase of [TAZ][pfBu] POIPC (375–430 K as revealed from the experiments of Luo *et al.* [38]), the simulation temperature was set to 400 K. To obtain a pre-equilibrated configuration at 400 K, we first performed classical molecular dynamics (MD) simulations using the LAMMPS program package. [39] Details about the force field parameters and protocols are described in Chapter 5A. The initial configuration for the classical MD run was taken from the experimentally determined crystal structure [38] and contained $3\times2\times1$ unit cells, with 624 atoms. The energy minimized geometry was warmed to 400 K at a heating rate of 1 K per 100 ps in the fully flexible isothermal-isobaric (NPT) ensemble. A further equilibration of 5 ns was carried out in the NVT ensemble. A time-step of 0.5 fs was used to integrate the equations of motion. The atom labeling scheme used in the work is presented in Figure 5B.1.

An equilibrated supercell from the classical MD trajectory was used to set up Born-Oppenheimer MD simulations with the electronic structure code CP2K, [40] using the Quickstep module. [41] The electronic structure was computed on the level of Kohn–Sham density functional theory, [42, 43] utilizing the PBE exchange-correlation functional, [44] with empirical dispersion correction (D3) from Grimme. [45] All valence electrons were treated with triple-ζ polarized basis sets with an energy cutoff of 280 Ry. Goedecker–Teter–Hutter (GTH) [46, 47] pseudopotentials were applied to consider the effect of nuclei and

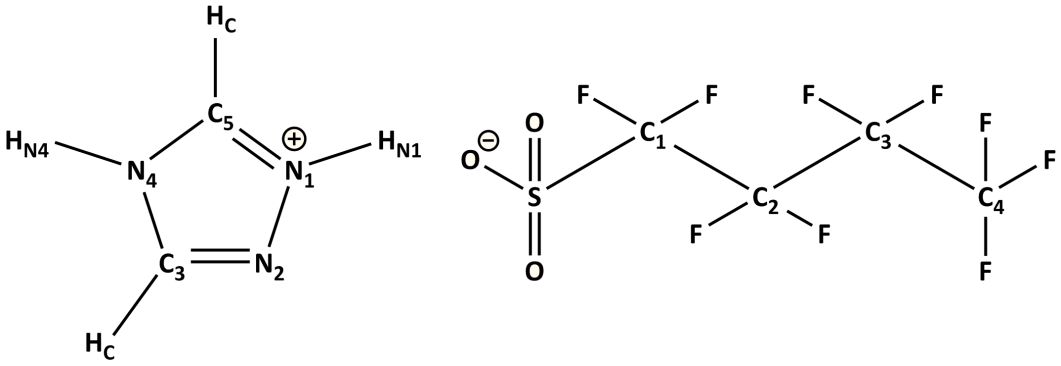

Figure 5B.1: Atom labeling in [TAZ][pfBu] used throughout in this article.

core electrons. The time-step to integrate the equations of motion was 0.4 fs. The system was equilibrated for 2 ps which was followed by a production run for 60 ps in canonical ensemble (NVT), with the temperature being maintained at 400 K using a Nosé-Hoover chain thermostat [48–50] with a coupling constant of 500 fs. The hydrogen bond network in [TAZ][pfBu] POIPC is shown in Figure 5B.2a.

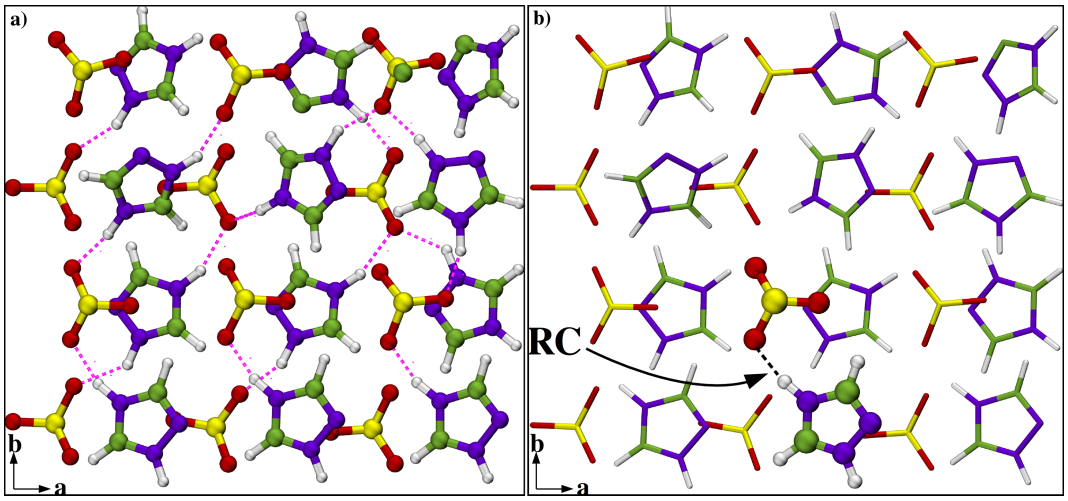

Figure 5B.2: (a) A part of simulation cell depicting the hydrogen bond network in the crystallographic *ab* plane. Alkyl tails are not shown for clarity. Color scheme: carbon, green; hydrogen, white; nitrogen, violet; sulfur, yellow; oxygen, red. (b) Reaction coordinate for proton shuttle events defined as the distance between acidic hydrogen (H_N) and sulfonate oxygen atom of anion. Reacting ions are shown in CPK presentation, while other ions are represented with licorice view.

Biased MD simulations were performed on the POIPC to calculate the free energy profile for the transfer of the acidic hydrogen of [TAZ^+] cation to the [$pfBu^-$] anion (see Figure 5B.2b). These were performed using the metadynamics method, [51] starting from configurations obtained from the equilibrium simulation described earlier. PLUMED-2.0.1

patched with CP2K-2.5.1 was employed to perform these metadynamics simulations. [52, 53] The distance between the sulfonate oxygen (O) and the acidic hydrogen (either H_{N1} or H_{N4}) (hydrogen bonded pair) was chosen to be the reaction coordinate, (RC, r_{O-H}) to calculate the potential of mean force (PMF). Each of these runs was performed for a duration of 8 ps. An initial bias potential of 0.05 kcal/mol was utilized. The sum_hills program [52] was used to compute the PMF along the reaction coordinate.

5B.3 Results and Discussion

Structural aspects: Radial distribution functions (RDFs) for the most relevant atom pairs (H_N-O and H_C-O) characterizing the properties of hydrogen bond network in [TAZ][pfBu] are shown in Figure 5B.3. C-H$\cdots$O hydrogen bonding interactions are distinctively weaker than the N-H$\cdots$O hydrogen bonds. The hydrogen bond geometry between different atom pairs was further analysed through combined probability distribution functions and the same are shown in Figure 5B.4. It is evident from Figure 5B.4 that the sulfonate oxygens form more linear and thus, stronger hydrogen bonds with the acidic hydrogen (H_N) atoms rather than with H_C atoms. The stronger hydrogen bonds usually result in much lower barriers for proton transfer [11] which can explain the facile intermolecular proton transfer events from [TAZ^+] cation to [$pfBu^-$] anion.

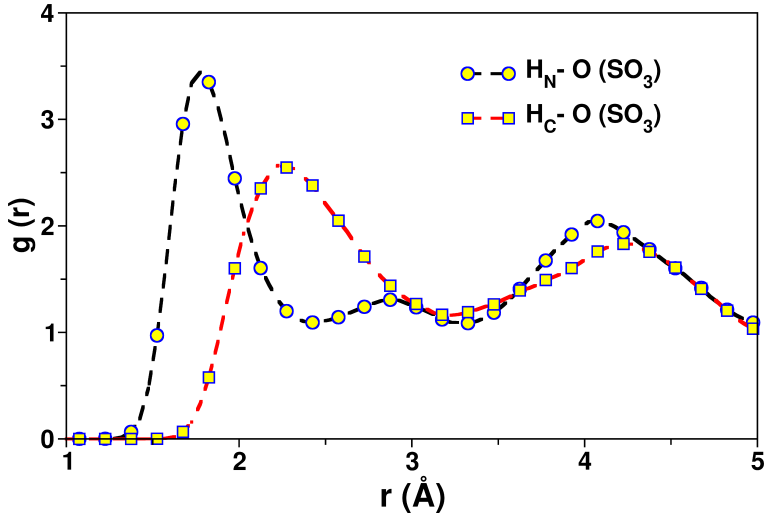

Figure 5B.3: Radial distribution functions between H_N and H_C atoms of cation with sulfonate oxygen atoms of anion in the native crystal obtained from AIMD simulations at 400 K.

The change in the geometry of species during proton transfer events was studied by calculating the instantaneous N-H_N and O-H_N distances and the N-$H_N\cdots$O angle, as shown in Figure 5B.5. Throughout the course of equilibrium simulation, there were instances where the acidic protons were found to shuttle between the cation's nitrogen and the anion's

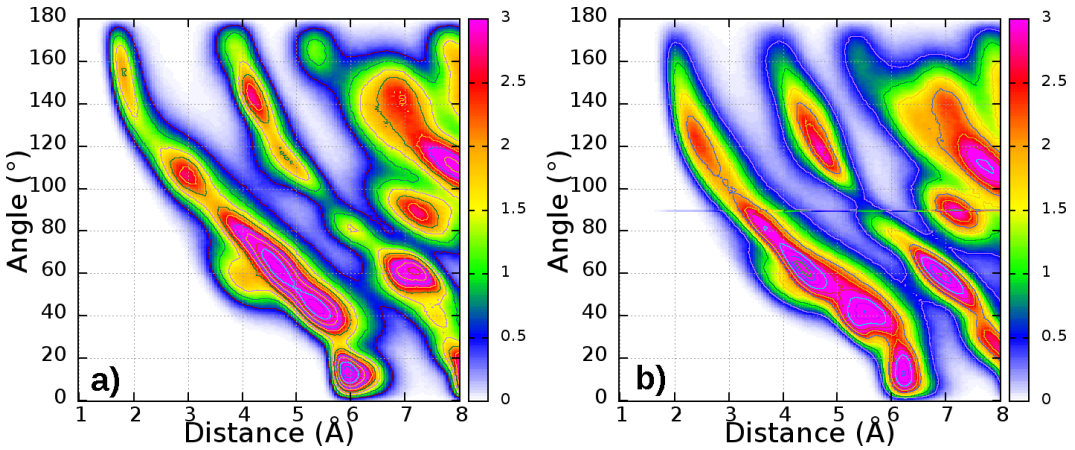

Figure 5B.4: Combined distribution functions depicting the hydrogen bond geometry between the oxygen atoms of [pfBu$^-$] anion and (a) H_N atoms of [TAZ$^+$] cation and (b) H_C atoms of [TAZ$^+$] cation.

oxygen. Figure 5B.5 shows the interatomic distances during such events (randomly chosen). In the figure, the covalent (∼1.0 Å) and hydrogen bond (∼1.8 Å) distances clearly show opposite behaviors at aroudn 100 fs timepoint. At the crossing point, the intermolecular angle also becomes more linear to facilitate the transfer process.

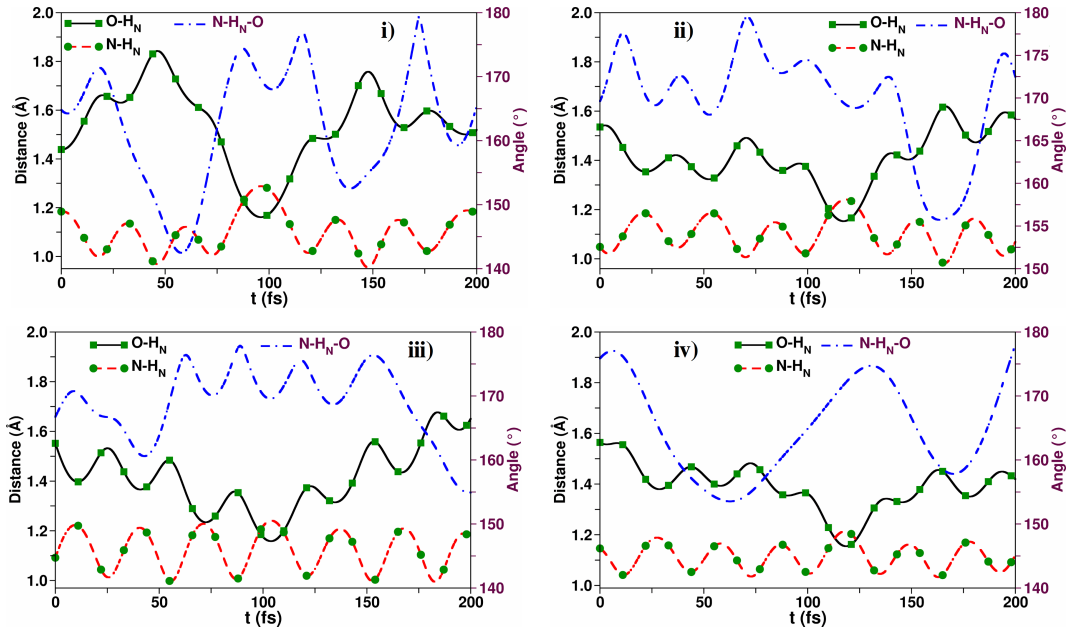

Figure 5B.5: N-H_N and O-H_N distances and N-$H_N\cdots$O angles during several proton transfer attempt event in [TAZ][pfBu] POIPC.

Ion rotation: There are three hydrogen bond acceptor sites (three oxygens) on the anion and two acidic hydrogens on cation. The libration of cations allows the breaking and

reformation of hydrogen bonds [38] and thus, in principle, every oxygen atom of an anion can hydrogen bond with a neighbouring cation i.e., it can participate in the proton transfer process. However, within the duration of the simulation, only a fraction of anion oxygens attempt to acquire a proton from the cation. We have calculated the S-O bond distance for oxygen atoms which participate in a proton transfer event and those which do not. The distribution of such distances are shown in Figure 5B.6. A clear distinction in sulfur-oxygen bond distance in two different instances is observed. The S-O bond distances for sulfonate groups in which one of the oxygen atoms participate in a proton transfer attempt event (such as the one depicted in Figure 5B.5) is shorter than those whose oxygens do not participate in such events in the entire simulation trajectory. When an oxygen atom takes up a proton, the specific S-O bond distance gets stretched making the other two S-O bonds (in the same sulfonate group) to contract. Thus, further examination of the role of the $–SO_3$ group in the proton transport mechanism is vital.

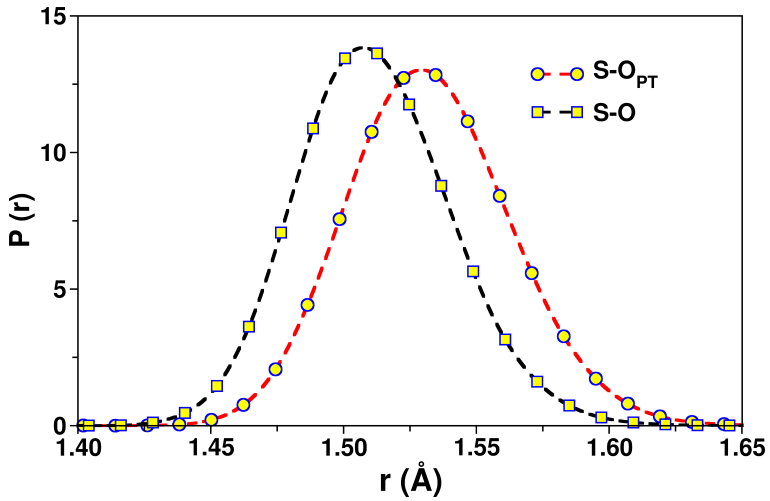

Figure 5B.6: Distribution of distance between sulfur and oxygen atoms in [pfBu$^-$] anion. O_{PT} differentiates oxygen atoms participating in proton shuttle events from those which do not (O)

.

The rotational dynamics of the cation and of the $–SO_3$ group are presented in Figure 5B.7a. At short times, the correlation functions decay sharply; that for the cation rotation is faster than that for the $–SO_3$ group. Thus, it is possible that a $–SO_3$ group can participate as a mediator in proton conduction process occurring along the hydrogen bond network in the crystallographic *ab* plane (see Figure 5B.8), also suggested by Luo *et al.* from experimental observations. [38] This process is further facilitated due to the smaller rotational barrier (6.78 kcal/mol) of triazolium cations (described in Chapter 5A). To further understand this plausible mechanism, we have calculated the distribution of residence times of acidic protons which are present within the covalent bond distance from the oxygen

atoms of the –SO_3 group (see Figure 5B.7b). From the mean value of this distribution, it is evident that the H_N protons stay in close proximity of –SO_3 oxygens (within 1.1 Å) for only 70–80 fs. Moreover, the time constant for –SO_3 group rotational time correlation function was found to be around 250 fs (obtained from classical MD simulation of [TAZ][pfBu] performed at 400 K in Chapter 5A). Thus, before a –SO_3 group can transfer a proton to another cation, the same proton hops back to its original cation. This phenomenon can be rationalized in terms of the strong ionic environment in the crystal which restricts the formation of such neutral moieties. Such events may be plausible in a real system due to the presence of finite number of defects. However, our simulations do not consider any such defects.

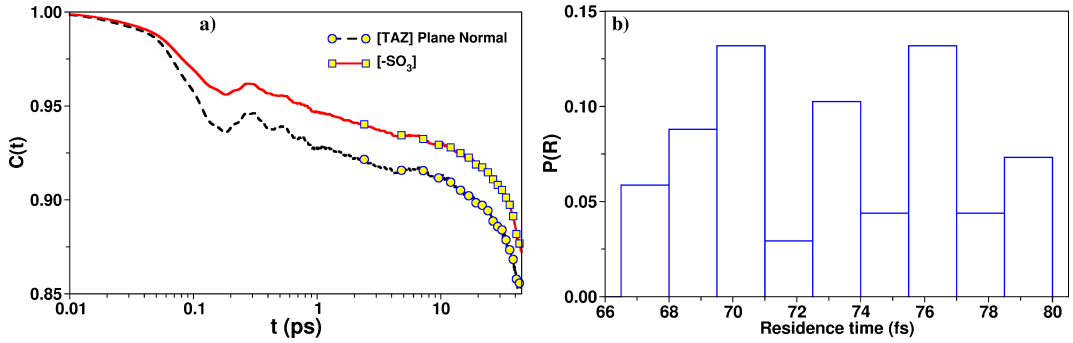

Figure 5B.7: (a) Auto time correlation function of the ring plane normal of [TAZ^+] cation and of the molecular orientation of –SO_3 group at 400 K. (b) Residence time distribution of H_N protons within the covalent bond distance from oxygen atoms in –SO_3 group.

Defect crystal simulations: In an earlier work, Eikerling *et al.* demonstrated the relevance of defects to proton transport in a triflic acid monohydrate solid using *ab initio* MD simulations. [54] Their simulations revealed the formation of a stable Zundel-ion ($H_5O_2^+$) in the defective crystal; followed by simultaneous rearrangement of neighboring $CF_3SO_3^-$ ions. They concluded that the intermediate state i.e., the Zundel-ion, functions as a mediator of proton transfer. In much the same spirit, we introduced a proton-hole defect into the equilibrated native crystal by removing a proton from one of the triazolium cation, resulting in a net charge of -1.0e of the system. Proton-holes in the cation were individually created by considering both the acidic hydrogen atoms i.e., H_{N1} and H_{N4} (see Figure 5B.1). Three independent simulations in each of which a H_{N1} atom was removed were performed. The same was done with respect to the H_{N4} atom as well. These six initial configurations were geometry optimized at the same level of theory as in BOMD simulations of native crystal. The gradient on the wave functions and on the nuclear positions were optimized with convergence criteria of 10^{-6} and 10^{-4} (au), respectively. Two such quenched geometries

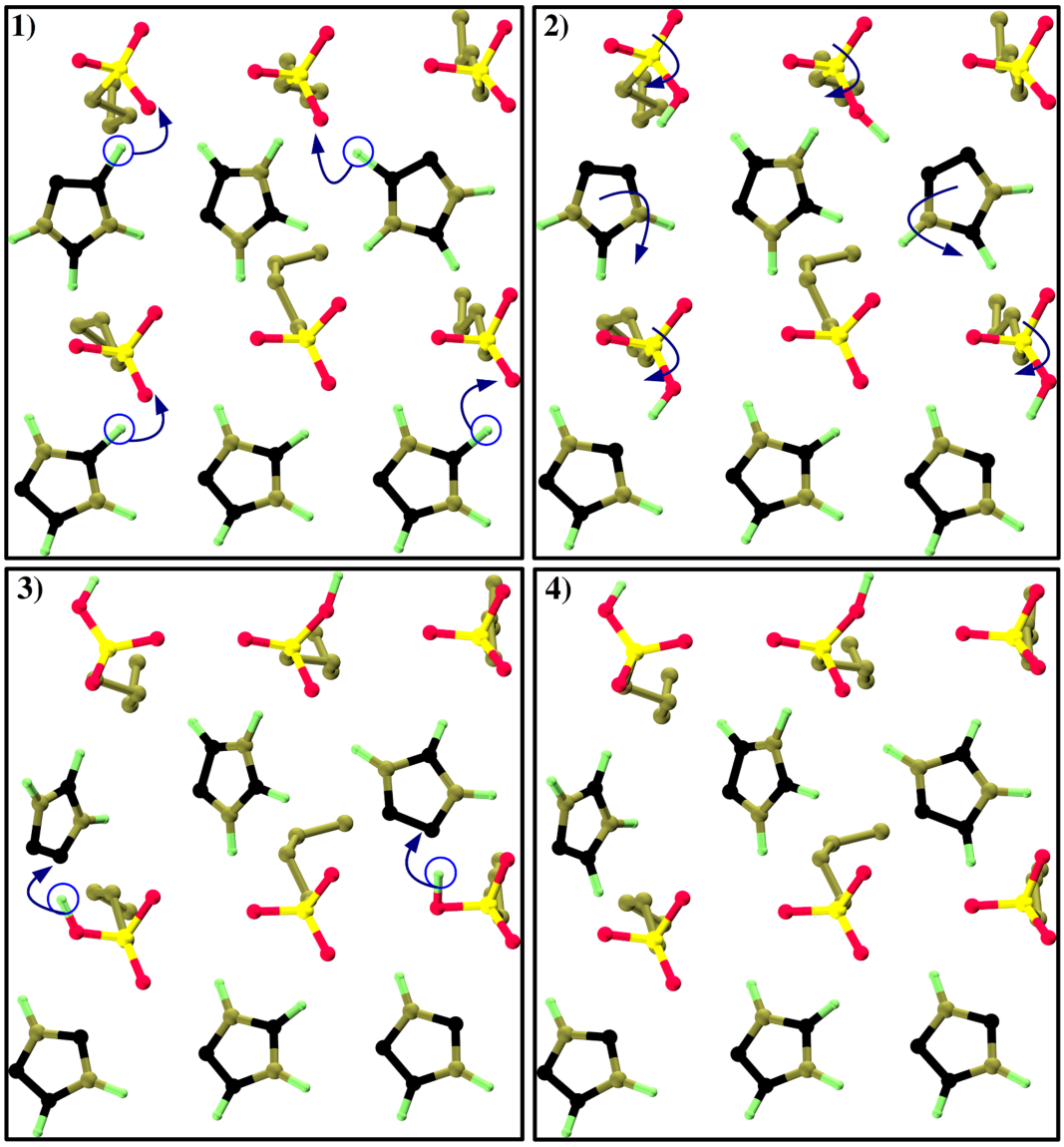

Figure 5B.8: Plausible mechanism for concerted hopping of acidic protons in [TAZ][pfBu] POIPC at 400 K. The proton transfer occurs via a series of molecular reorientation and autodissociation of H_N protons.

(one from each set) were selected and were further employed for BOMD simulations at 400 K. After an initial equilibration of 1 ps, an analysis trajectory for 9 ps was generated.

Geometry optimization of defective crystal with one proton-hole: The defective crystal (with one H_{N1} proton-hole) before and after the geometry optimization are shown in Figure 5B.9. In the following, the cation in which the proton-hole was created is referred to as "activated cation." Prior to geometry optimization, both the N_1 and N_2 sites in an activated cation are chemically equivalent and are capable of accepting protons from neighboring cations (left panel of Figure 5B.9). After optimization (right panel of Figure 5B.9),

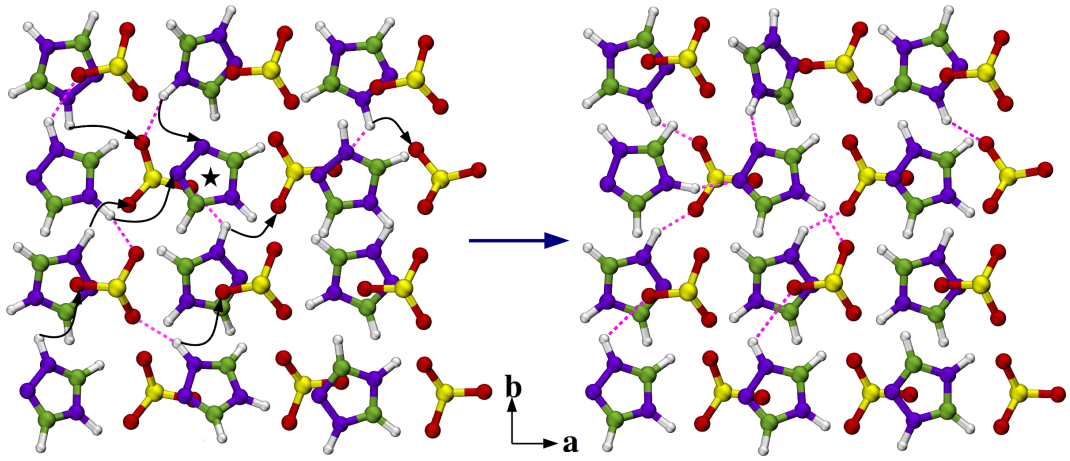

Figure 5B.9: Structure of defect crystal with H_{N1} proton-hole: before optimization (left panel) and after optimization (right panel). Only a part of the whole system has been shown and alkyl tails are not shown for the sake of clarity. Color scheme: nitrogen, violet; carbon, green; hydrogen, white, oxygen, red; sulfur, yellow. Only those hydrogen bonds which take part in break and reformation due to geometry optimization are shown. Other hydrogen bonds are intact and are not shown. Formation of new hydrogen bond is shown with curved arrow. Asterisk represents the activated cation.

both N_1 and N_2 sites of the activated cation are found to form strong hydrogen bond with a H_{N4} hydrogen of another [TAZ^+] cation. In the case of the N_2 site, the donor [TAZ^+] cation is located in the same layer (crystallographic *ab* plane) of the activated cation, while for the N_1 site, it was from a different layer. The initial and final distances between the N_1 and H_{N4} hydrogen atom were 3.83 Å and 1.89 Å, respectively, while the same for N_2 and H_{N4} hydrogen were 3.01 Å and 1.73 Å, respectively. As a consequence of this rearrangement due to facile rotation of triazolium cation, there were instances of breaking of existing hydrogen bond and subsequent formation of new hydrogen bonds. This phenomenon can be rationalized in terms of local charge imbalance around the $–SO_3$ group created by the proton-hole. When a [TAZ^+] cation rotates to act as a donor for a newly formed N_4-H$\cdots N_{1/2}$ hydrogen bond, its existing hydrogen bond with a $–SO_3$ group is broken and thus, the $–SO_3$ group is short of one hydrogen bond, i.e. slightly more electron rich than the other anions. As a result, breakage and formation of hydrogen bonds propagate in the whole system, and the same is depicted in Figure 5B.9. Similar observations were made in the case of H_{N4} proton-hole system and are shown in Figure 5B.10. This phenomenon has been observed in simulations started from all the six different initial configurations. Hydrogen bond network has been reconfigured although no proton transfer takes place after geometry optimization.

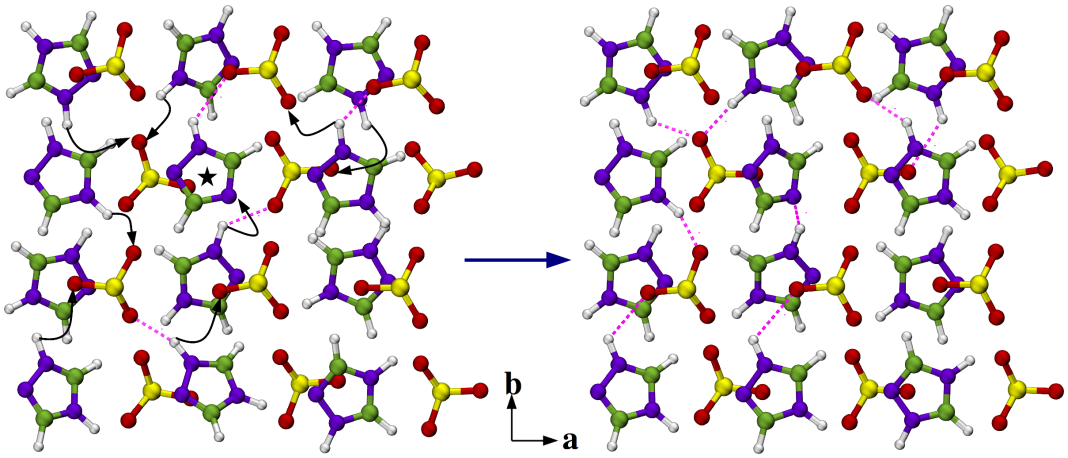

Figure 5B.10: Structure of defect crystal with H_{N4} proton-hole; before optimization (left panel) and after optimization (right panel). Other details are same as Figure 5B.9.

BOMD simulations of defective crystal with one proton-hole: Figure 5B.11 displays interatomic distances during a proton exchange between triazolium cations from BOMD simulations of a defective crystal (H_{N1} proton-hole). Within 5 ps of the trajectory, H_{N4} hydrogen of a neighboring cation that is located in another layer of the activated cation was found to be completely transferred to the N_1 site of the activated cation. During this period, the distance between the N_2 site of activated cation and the H_{N4} hydrogen of a cation from the same layer increased by a significant amount. The proton was found to be covalently attached to the N_1 site of the activated cation for over 4 ps time duration. These observations suggest that intrinsic proton defects present in the plastic crystal can facilitate sequential proton conduction.

Simulations in which the H_{N4} atom was covalently (manually) attached to the $-SO_3$ group to which it was H-bonded in the native crystal were also carried out. Post this addition, geometry optimization resulted in the restoration of the native crystal. However, addition of the same H^+ to a sulfonate group which is far from the activated cation, followed by quenching and a BOMD simulation at 400 K produced a similar kind of proton shuttling as was observed in a native crystal.

***Ab initio* Metadynamics simulations:** In order to characterize the energetics of proton transfer in this POIPC, we have performed *ab initio* metadynamics simulations along the proton transfer path. The free energy profiles obtained from three different runs were averaged and are presented in Figure 5B.12a. A minimum in the free energy profile was observed at around 1.8 Å, which is the typical hydrogen bond distance between the acidic proton and the sulfonate oxygen. The free energy barrier to dissociate the proton from the sulfonate oxygen is around 7.0 kcal/mol. Thus, the system with the protonated

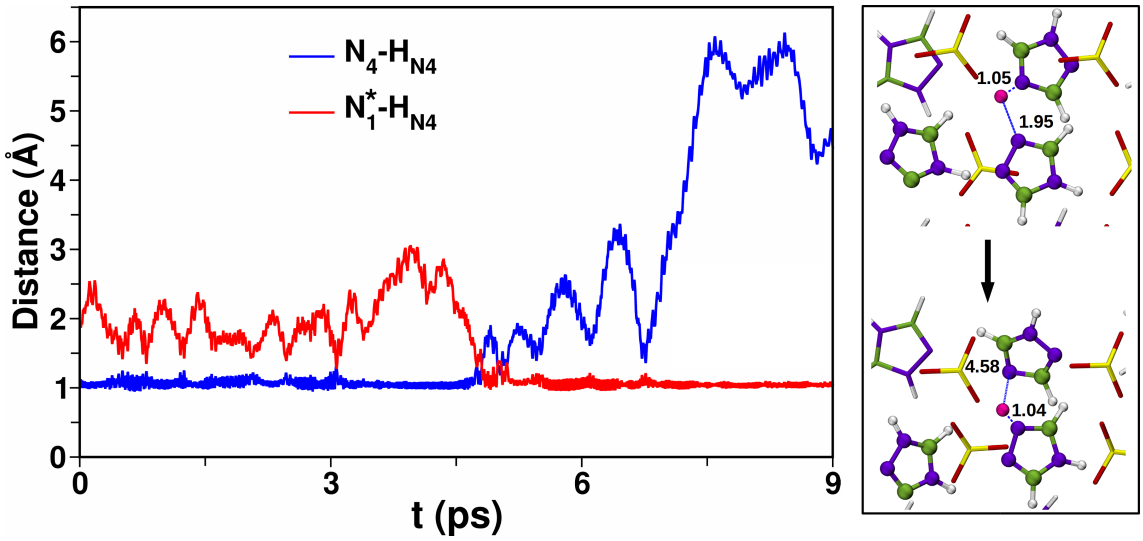

Figure 5B.11: Interatomic distances during the BOMD simulation of defect crystal with H_{N1} proton-hole (left panel). Here, N_1^* and N_4 sites belong to the activated cation and a normal cation from another layer, respectively. Right panel shows the initial and final snapshot of a small part of simulation cell where the proton transfer event takes place.

[TAZ^+] cation and [$pfBu^-$] anion is more stable than a pair of neutral species by about 7 kcal/mol. Note that both the states are located in a matrix of ions in the crystalline environment, which obviously would prefer the two molecular species to be ionic rather than to be neutral. Experimental ionic conductivity data [38] on this POIPC in the plastic crystal region (373–430 K) show an activation energy barrier of 8.8 kcal/mol. Further, the measured experimental conductivity was reported to be mainly protonic in nature. [38] It is thus evident that the calculated free energy barrier for proton transfer process is in good agreement with experimental activation energy. For the sake of comparison, we have performed a similar calculation where the distance between the sulfonate oxygen (O) and the acidic hydrogen (H_{N1}) (hydrogen bonded pair) was chosen as the reaction coordinate. The free energy profile was quite similar to that shown in Figure 5B.12a and the free energy barrier was around 7.5 kcal/mol.

Furthermore, the free energy barrier for proton transfer in a defective crystal (H_{N1} proton-hole) was determined in a similar fashion as described above. The distance between the N_1 site of the activated cation and the H_{N4} hydrogen of a cation from same layer (hydrogen bonded pair) was chosen as the reaction coordinate. The free energy profile is displayed in Figure 5B.12b and the barrier was around 6.2 kcal/mol.

Gas phase calculations: To substantiate the energetics of proton transfer in [TAZ][pfBu], we have performed gas phase calculations using an ion-pair in Gaussian 09 program. [55]

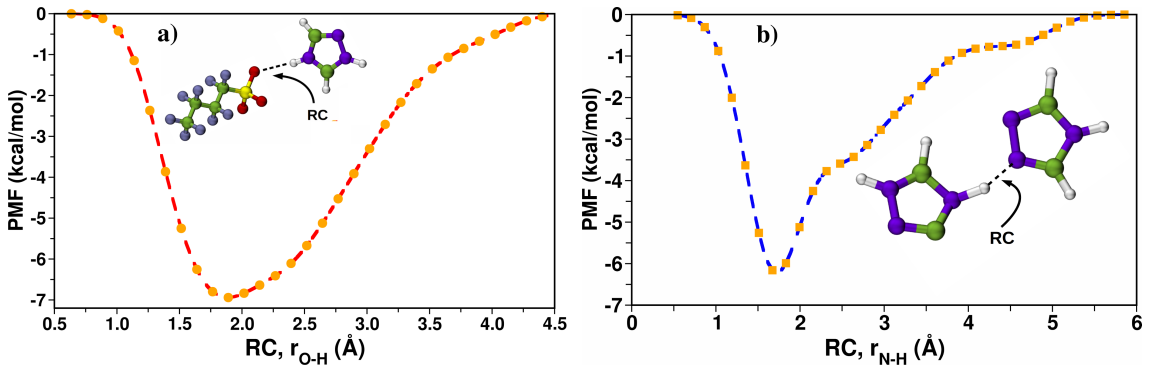

Figure 5B.12: Free energy profile along the proton transfer coordinate in the plastic crystal phase of [TAZ][pfBu] POIPC at 400 K (a) native crystal and (b) defect crystal with H_{N1} proton hole.

Starting configurations were constructed using GaussView package [56]. Geometry optimization was performed at M06/aug-cc-pVDZ level of theory. Frequency analysis within the harmonic approximation was carried out to confirm that the optimized geometry is a minimum. Further, the transition state was validated by performing intrinsic reaction coordinate (IRC) calculations which could able to connect the transition state to both reactant and the product. The energy barrier obtained from IRC calculation (see Figure 5B.13) was 6.8 kcal/mol which is in good agreement with the free energy barrier obtained from *ab initio* metadynamics simulations. IRC calculation was also performed considering proton transfer from N_4 site to sulfonate oxygen and the energy barrier was found to be around 6.5 kcal/mol. Thus, the transfer of either of the acidic protons to the anion is equally probable, consistent with results obtained from *ab initio* metadynamics simulations.

Gas phase calculations on an ion pair (see Figure 5B.13) show that the neutral species is stable over the ionic one by just 1.1 kcal/mol. The crystalline form though, is stabilized by multiple hydrogen bond networks and long range electrostatic interactions, which are absent in the gas phase calculation. At this point, we are interested to explore ways to decrease the energy barrier for proton transfer in POIPC (which could enhance proton conduction), without altering the plastic crystallinity much. Towards this purpose, we adopted two simple procedures to increase the anion basicity: i) reduction of the alkyl tail length in the anion and ii) partial substitution of fluorine atoms on different carbons in the anion by hydrogens. IRC calculations on several ion pairs have been carried out following the same protocol as discussed above. The barrier for proton transfer reduced from a value of 6.8 kcal/mol to 5.1 kcal/mol upon changing the [$pfBu^-$] anion to [$CF_3SO_3^-$] (see Figure 5B.13). In this process, the van der Waals interaction between the alkyl tails may get compromised by a large amount, which in turn can destabilize the crystal and/or reduce the temperature range of the plastic crystal phase. On the other hand, either the

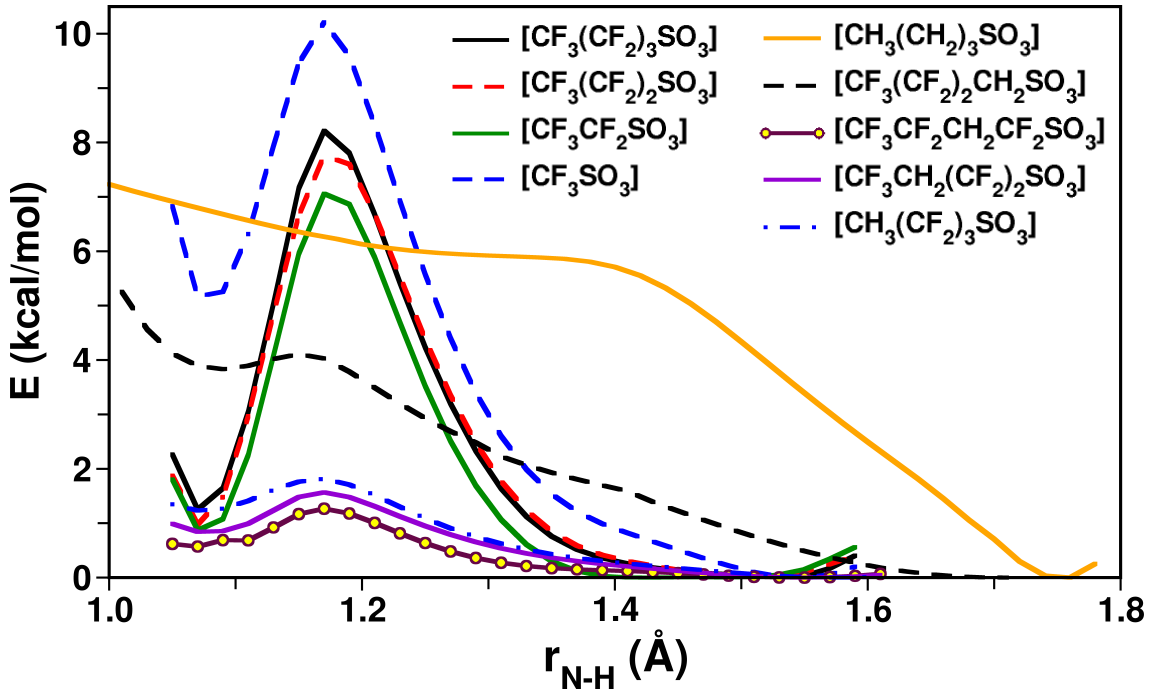

Figure 5B.13: Energy barrier associated with proton transfer reaction obtained from gas-phase calculations at M06/aug-cc-pVDZ level of theory. The common cation is [TAZ$^+$].

complete or partial substitution at C_1 site of the fluorine atoms by hydrogens resulted in a barrierless process (see Figure 5B.13), which indicates that the ionic species is not stable when compared to the neutral one. However, substitution at other carbon sites, e.g. C_2, C_3 or C_4 produced reasonable profiles which balanced both the energy barrier and the stability of ionic state. Considering all the profiles obtained from IRC calculations, an anion with a perfluorobutyl tail where the fluorine atoms at C_2 position alone are substituted by hydrogens yields a low barrier (0.6 kcal/mol) for proton transfer and will likely not affect the crystal stability much. Thus, we believe [TAZ][$CF_3CF_2CH_2CF_2SO_3$] POIPC could be a promising candidate for high proton conductivity with wide plastic crystal phase as compared to [TAZ][pfBu].

5B.4 Conclusions

The details of proton transport in the plastic crystalline phase of [TAZ][pfBu] POIPC have been investigated using Born-Oppenheimer molecular dynamics simulations. The ions pack in layers perpendicular to the crystallographic *c* axis and this results in the formation of a hydrogen bond network along the crystallographic *ab* plane (see Figure 5B.2). *Ab initio* molecular dynamics simulations detect spontaneous autodissociation of the acidic proton (H_N), in the absence of any water molecule. No significant conduction of proton along the hydrogen bond network was seen and the back transfer of a proton from the anion

back to the cation always occurred in a few tens of femtoseconds in the native crystal. The rotational correlation for both the cation and the $–SO_3$ group decay sharply at short times, which suggest the importance of molecular reorientation in the proton transport process.

However, complete proton transfers were observed in simulations of a defective crystal where one proton-hole was created by removing one of the acidic proton in a triazolium cation. The optimized structure demonstrated the formation of strong hydrogen bond between N_1 and N_2 sites of the "activated cation" and the H_{N4} of another cation.

The energy barrier for proton transfer was determined by free energy calculations and the estimated barrier was found to be around 7.0 kcal/mol against the experimentally determined activation barrier of 8.77 kcal/mol obtained from conductivity measurements. [38] The current simulations treat the proton as a classical particle. However, nuclear quantum effects can affect the barrier for its transfer and need to be taken into account. This is beyond the scope of the current manuscript. Gas phase IRC calculations on ion pairs suggest [TAZ][$CF_3CF_2CH_2CF_2SO_3$] to be a promising material for proton conducting membrane. These observations illustrate that high temperature dry fuel cell membrane materials are not very far from our reach and this would remarkably enhance the efficiency of all hydrogen full cell systems.

Bibliography

[1] Kreuer, K.-D. *Chem. Mater.* **1996**, *8*, 610–641.

[2] Kreuer, K.-D.; Paddison, S. J.; Spohr, E.; ; Schuster, M. *Chem. Rev.* **2004**, *104*, 4637–4678.

[3] Gasteiger, H. A.; Marković, N. M. *Science* **2009**, *324*, 48–49.

[4] Debe, M. K. *Nature* **2012**, *486*, 43–51.

[5] Nimmanpipug, P.; Laosombat, T.; Lee, V. S.; Vannarat, S.; Chirachanchai, S.; Yana, J.; Tashiro, K. *Chem. Eng. Sci.* **2015**, *137*, 404–411.

[6] Eisbein, E.; Joswig, J.-O.; Seifert, G. *Microporous Mesoporous Mater.* **2015**, *216*, 36 – 41.

[7] Iannuzzi, M. *J. Chem. Phys.* **2006**, *124*, 204710.

[8] Münch, W.; Kreuer, K.-D.; Silvestri, W.; Maier, J.; Seifert, G. *Solid State Ionics* **2001**, *145*, 437–443.

[9] Chen, H.; Yan, T.; Voth, G. A. *J. Phys. Chem. A* **2009**, *113*, 4507–4517.

[10] Li, A.; Cao, Z.; Li, Y.; Yan, T.; Shen, P. *J. Phys. Chem. B* **2012**, *116*, 12793–12800.

[11] Vilčiauskas, L.; Tuckerman, M. E.; Melchior, J. P.; Bester, G.; Kreuer, K.-D. *Solid State Ionics* **2013**, *252*, 34–39.

[12] Thisuwan, J.; Sagarik, K. *RSC Adv.* **2014**, *4*, 61992–62008.

[13] Roy, S.; Ataol, T. M.; Müller-Plathe, F. *J. Phys. Chem. B* **2008**, *112*, 7403–7409.

[14] Schuster, M.; Rager, T.; Noda, A.; Kreuer, K. D.; Maier, J. *Fuel Cells* **2005**, *5*, 355–365.

[15] Joswig, J.-O.; Seifert, G. *J. Phys. Chem. B* **2009**, *113*, 8475–8480.

[16] Vilčiauskas, L.; Paddison, S. J.; Kreuer, K.-D. *J. Phys. Chem. A* **2009**, *113*, 9193–9201.

[17] Vilčiauskas, L.; Tuckerman, M. E.; Bester, G.; Paddison, S. J.; Kreuer, K.-D. *Nat. Chem.* **2012**, *4*, 461–466.

[18] Steininger, H.; Schuster, M.; Kreuer, K. D.; Kaltbeitzel, A.; Bingol, B.; Meyer, W. H.; Schauff, S.; Brunklaus, G.; Maier, J.; Spiess, H. W. *Phys. Chem. Chem. Phys.* **2007**, *9*, 1764–1773.

[19] Kreuer, K.-D.; Wohlfarth, A. *Angew. Chem. Int. Ed.* **2012**, *51*, 10454–10456.

[20] Vuilleumier, R.; Borgis, D. *Nat. Chem.* **2012**, *4*, 432–433.

[21] Ludueña, G. A.; Kühne, T. D.; Sebastiani, D. *Chem. Mater.* **2011**, *23*, 1424–1429.

[22] Kabbe, G.; Wehmeyer, C.; Sebastiani, D. *J. Chem. Theory Comput.* **2014**, *10*, 4221–4228.

[23] Weber, J.; Kreuer, K.-D.; Maier, J.; Thomas, A. *Adv. Mater.* **2008**, *20*, 2595–2598.

[24] Wehmeyer, C.; Schrader, M.; Andrienko, D.; Sebastiani, D. *J. Phys. Chem. C* **2013**, *117*, 12366–12372.

[25] Umeyama, D.; Horike, S.; Inukai, M.; Itakura, T.; Kitagawa, S. *J. Am. Chem. Soc.* **2012**, *134*, 12780–12785.

[26] Pardo, E.; Train, C.; Gontard, G.; Boubekeur, K.; Fabelo, O.; Liu, H.; Dkhil, B.; Lloret, F.; Nakagawa, K.; Tokoro, H.; ichi Ohkoshi, S.; Verdaguer, M. *J. Am. Chem. Soc.* **2011**, *133*, 15328–15331.

[27] Sadakiyo, M.; Ōkawa, H.; Shigematsu, A.; Ohba, M.; Yamada, T.; Kitagawa, H. *J. Am. Chem. Soc.* **2012**, *134*, 5472–5475.

[28] Maly, K. E.; Gagnon, E.; Maris, T.; ; Wuest, J. D. *J. Am. Chem. Soc.* **2007**, *129*, 4306–4322.

[29] Lee, Y. J.; Bingöl, B.; Murakhtina, T.; Sebastiani, D.; Meyer, W. H.; Wegner, G.; ; Spiess, H. W. *J. Phys. Chem. B* **2007**, *111*, 9711–9721.

[30] Lee, Y. J.; Murakhtina, T.; Sebastiani, D.; ; Spiess, H. W. *J. Am. Chem. Soc.* **2007**, *129*, 12406–12407.

[31] Siwick, B. J.; ; Bakker, H. J. *J. Am. Chem. Soc.* **2007**, *129*, 13412–13420.

[32] MacFarlane, D. R.; Forsyth, M. *Adv. Mater.* **2001**, *13*, 957–966.

[33] Pringle, J. M. *Phys. Chem. Chem. Phys.* **2013**, *15*, 1339–1351.

[34] Jin, L.; Nairn, K. M.; Forsyth, C. M.; Seeber, A. J.; MacFarlane, D. R.; Howlett, P. C.; Forsyth, M.; Pringle, J. M. *J. Am. Chem. Soc.* **2012**, *134*, 9688–9697.

[35] Armel, V.; Forsyth, M.; MacFarlane, D. R.; Pringle, J. M. *Energy Environ. Sci.* **2011**, *4*, 2234–2239.

[36] Jin, L.; Howlett, P. C.; Pringle, J. M.; Janikowski, J.; Armand, M.; MacFarlane, D. R.; Forsyth, M. *Energy Environ. Sci.* **2014**, *7*, 3352–3361.

[37] Luo, J.; Conrad, O.; Vankelecom, I. F. J. *J. Mater. Chem. A* **2013**, *1*, 2238–2247.

[38] Luo, J. et al. *Energy Environ. Sci.* **2015**, *8*, 1276–1291.

[39] Plimpton, S. *J. Comput. Phys.* **1995**, *117*, 1–19.

[40] Hutter, J.; Iannuzzi, M.; Schiffmann, F.; VandeVondele, J. *Wiley Interdiscip. Rev. Comput. Mol. Sci.* **2014**, *4*, 15–25.

[41] VandeVondele, J.; Krack, M.; Mohamed, F.; Parrinello, M.; Chassaing, T.; Hutter, J. *Comput. Phys. Commun.* **2005**, *167*, 103–128.

[42] Hohenberg, P.; Kohn, W. *Phys. Rev.* **1964**, *136*, 864–871.

[43] Kohn, W.; Sham, L. J. *Phys. Rev.* **1965**, *140*, 1133–1138.

[44] Perdew, J. P.; Burke, K.; Ernzerhof, M. *Phys. Rev. Lett.* **1996**, *77*, 3865–3868.

[45] Grimme, S.; Antony, J.; Ehrlich, S.; Krieg, H. *J. Chem. Phys.* **2010**, *132*, 154104.

[46] Goedecker, S.; Teter, M.; Hutter, J. *Phys. Rev. B* **1996**, *54*, 1703–1710.

[47] Hartwigsen, C.; Goedecker, S.; Hutter, J. *Phys. Rev. B* **1998**, *58*, 3641–3662.

[48] Nosé, S. *J. Chem. Phys.* **1984**, *81*, 511–519.

[49] Nosé, S. *Mol. Phys.* **1984**, *52*, 255–268.

[50] Martyna, G. J.; Klein, M. L.; Tuckerman, M. *J. Chem. Phys.* **1992**, *97*, 2635–2643.

[51] Laio, A.; Gervasio, F. L. *Rep. Prog. Phys.* **2008**, *71*, 126601–126623.

[52] Bonomi, M.; Branduardi, D.; Bussi, G.; Camilloni, C.; Provasi, D.; Raiteri, P.; Donadio, D.; Marinelli, F.; Pietrucci, F.; Broglia, R. A.; Parrinello, M. *Comput. Phys. Commun.* **2009**, *180*, 1961–1972.

[53] Tribello, G. A.; Bonomi, M.; Branduardi, D.; Camilloni, C.; Bussi, G. *Comput. Phys. Commun.* **2014**, *185*, 604 – 613.

[54] Eikerling, M.; Paddison, S. J.; Pratt, L. R.; Jr., T. A. Z. *Chem. Phys. Lett.* **2003**, *368*, 108–114.

[55] Frisch, M. J. et al. Gaussian 09 Revision D.01. Gaussian Inc. Wallingford CT **2009**.

[56] Dennington, R.; Keith, T.; Millam, J. GaussView Version 5. Semichem Inc., Shawnee Mission, KS, 2009.

Chapter 6A

Understanding SO_2 Capture by Ionic Liquids

6A.1 Introduction

Sulfur dioxide (SO_2), a dominant air pollutant, is released into the atmosphere through the combustion of fossil fuels for energy conversion. For instance, the gas emission from coal plants contains 0.3–5% of SO_2. [1] It is extremely important to control and minimize this outflow, as it is harmful to environment and causes health hazards. [1]

Another important aspect concerning SO_2 is its use as a component in lithium-sulfur dioxide ($Li-SO_2$) batteries. [2] $Li-SO_2$ system is a class of primary battery which is longer-lasting than alkaline ones, metal-air batteries etc., with high energy density, wherein the inexpensive SO_2 can be used as the active cathode material. [3] Also, $Li-SO_2$ battery has some inherent advantages in contrast to other primary batteries, such as alkaline batteries, [4] and metal-air batteries; [5] for instance, $Li-SO_2$ battery has a high energy density (up to 330 Wh kg^{-1}, i.e. 2-4 times higher than those of alkaline batteries) and good discharge performance with working voltage around 3.0 V. [2] These unique characteristics have made $Li-SO_2$ batteries to be useful for applications requiring long service life which is beyond the reach of conventional primary batteries.

In spite of these positive attributes, safety issues associated with $Li-SO_2$ batteries restrict its applications; [3] the cell is comprised of liquefied SO_2 under pressure, and this constrains the upper limit of pressure that it can resist without leaking toxic SO_2, being 3.4 atm at 294 K. [2] Moreover, the electrolyte, acetonitrile being used in a $Li-SO_2$ battery is volatile in nature and can lead to an uncontrolled increase in pressure, resulting in the risk

Reprinted with permission from "Understanding SO_2 Capture by Ionic Liquids" *J. Phys. Chem. B* **2016**, *120*, 4457–4466.

of fire. A great deal of effort has focused on the search for electrolyte solvents which have low vapor pressure, and are less reactive too. [6, 7]

In light of these facts, there is general interest to develop new materials for the efficient, reversible, and economical capture of SO_2 which can also function as electrolytes. Traditional technologies developed over the years for flue-gas desulfurization (FGD) includes limestone scrubbing, ammonia scrubbing, and absorption by organic solvents. [8, 9] As an alternative, ionic liquids (ILs) have manifested their efficacy as better absorbents for acidic gases such as SO_2, [10–13] and CO_2, [14–18] owing to their properties such as low vapor pressure, high thermal and chemical stability, wide liquid temperature range, non-flammability, and tunable properties. [19–21] Three types of interactions such as physical, chemical or hybrid (physical and chemical), play important roles in the solubility of SO_2 in ILs. [12, 16, 22–24] However, an effective capture of SO_2 from flue gases entails chemical absorption because of low partial pressure in flue gases. [25] Han *et al.* demonstrated the first example of SO_2 capture by chemisorption in a functionalized IL, namely, tetramethylguanidinium lactate ([TMG][L]). [10] Subsequently, several other functionalized ILs were explored for effective SO_2 capture, including hydroxyl ammonium ILs, [26] imidazolium ILs, [22, 23, 27–29] TMG-based ILs, [12] phenolate-based ILs, [30] and supported ionic liquid membranes (SILMs). [31–33] In general, the chemisorption of SO_2 is based on strong interactions between SO_2 with the electronegative oxygen atom or nitrogen atom in the anion. [24, 34, 35] Recently, a new strategy was developed for improving SO_2 capture through multiple-site absorption by tunable ILs. [36–40] In the current manuscript, we examine the physical adsorption of SO_2 in imidazolium ILs.

The observed trend of SO_2 solubility in ILs from experimental measurements are not entirely conclusive. Jiang *et al.* reported the solubility of SO_2 in imidazolium based ILs in the order $[BMIM][BF_4] > [BMIM][NTf_2] > [BMIM][PF_6]$ at 298 K and 1 bar. [31] In another study, the order in SO_2 solubility in $[BMIM]^+$ based ILs was seen to be $[OAc]^- > [NTf_2]^- > [BF_4]^- > [PF_6]^-$. [41] In a recent work, Dai and co-workers reported the SO_2 solubility in imidazolium ILs in the following order, $[SCN]^- > [Cl]^- > [NTf_2]^-$ at 296 K and 1 atm. [2]

Molecular simulations are frequently employed to understand microscopic interactions. In recent years, several molecular simulation studies to understand gas absorption in ILs have been undertaken. [42–57] Maginn *et al.* explored the effect of anion on the high solubility of CO_2 in imidazolium based ILs by molecular dynamics (MD) simulations. [42] Ribeiro *et al.* investigated the structure and dynamics of 1-butyl-3-methylimidazolium bromide ([BMI][Br]) IL on addition of SO_2 using MD simulations and Raman spectroscopy. [58] Wick and co-workers employed a polarizable force field to examine the

binding of CO_2 and SO_2 at the air/liquid interface of 1-butyl-3-methylimidazolium tetrafluoroborate ([BMIM][BF_4]). [59] A minimum in free energy was observed at the interface. The nature of interactions between acidic gases at the interface of ILs was further studied using Gibbs free energy of solvation by many research groups. [60, 61]

As mentioned above, most studies have focused on interactions in CO_2-IL mixtures, while only a few have been devoted to SO_2-IL mixtures. [59, 61, 62] Furthermore, a systematic study of interactions of SO_2 at IL interface and its anion dependence is lacking. Needless to state, a fundamental understanding of interactions between ILs and SO_2 is extremely important for the further design of new ILs for SO_2 absorption. The present work is aimed in this direction and examines the anion dependence of SO_2 capture in eight ionic liquids using MD simulations and quantum chemical calculations. Based on the solvation free energy and binding energies of SO_2 in ILs, we find the IL with the thiocyanate anion to be the most suited for SO_2 absorption.

6A.2 Computational Details

ILs, all having 1-butyl-3-methylimidazolium ($[BMIM]^+$) as the cation, and the following anions, Chloride ($[Cl]^-$), Nitrate ($[NO_3]^-$), Tetrafluoroborate ($[BF_4]^-$), Hexafluorophosphate ($[PF_6]^-$), Triflate ($[CF_3SO_3]^-$), Bis(trifluoromethanesulfonyl)imide ($[NTf_2]^-$), Acetate ($[OAc]^-$), and Thiocyanate ($[SCN]^-$) were studied. These are displayed in Figure 6A.1. The atom labeling in $[BMIM]^+$ cation is the as shown in Figure 2A.1 in Chapter 2A. Three different approaches were utilized to study SO_2-IL interactions: (i) Quantum Chemical (QM) calculations, (ii) Classical Molecular Dynamics (MD) simulations, and (iii) Free Energy (FE) calculations based on (ii).

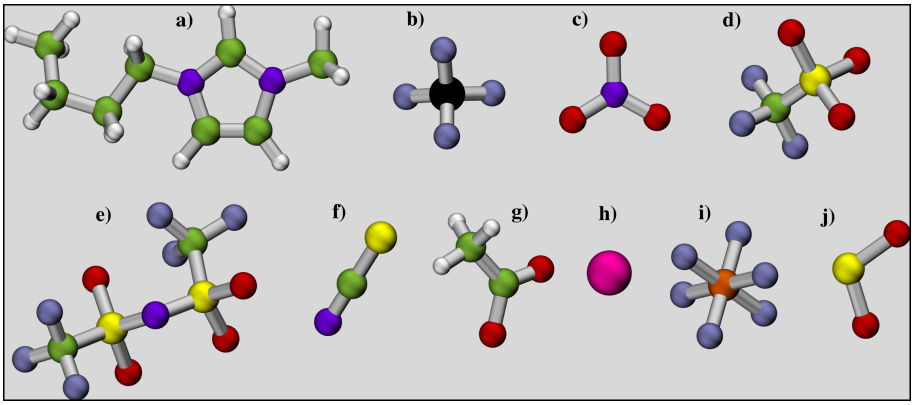

Figure 6A.1: Molecular structure of (a) $[BMIM]^+$, (b) $[BF_4]^-$, (c) $[NO_3]^-$, (d) $[CF_3SO_3]^-$ or $[TFO]^-$, (e) $[NTf_2]^-$ or $[TFSO]^-$, (f) $[SCN]^-$, (g) $[CH_3COO^-]$ or $[OAc]^-$, (h) $[Cl]^-$, (i) $[PF_6]^-$, and (j) $[SO_2]$ used in simulations. Color scheme: nitrogen, violet; carbon, green; hydrogen, white; oxygen, red; sulfur, yellow; boron, black; fluorine, iceblue; phosphorus, orange; chlorine, magenta.

QM Calculations. Systems, each of isolated IL ion pair, SO_2 molecule, and SO_2-IL complex (one SO_2 molecule and one IL ion pair) were geometry optimized at MP2/aug-cc-pVDZ level of theory. Five different initial configurations were constructed using GaussView software, [63] wherein the SO_2 molecule was kept near H_A, H_B or H_1 sites. Optimized minima on the potential energy surface were confirmed via frequency analysis. Binding energy (BE) was estimated as the energy difference between the complex and the sum of the energy of components.

$$BE = E_{SO_2-IL} - (E_{IL} + E_{SO_2}) \tag{6A.1}$$

where E_{SO_2-IL}, E_{IL}, and E_{SO_2} represent energy of SO_2-IL complex, isolated IL ion pair with lowest energy and SO_2, respectively. Counterpoise corrections for basis set superposition error (BSSE) were added to the computed interaction energy. [64] The calculations were performed using Gaussian 09 program. [65] In rest of the discussion, we limit ourselves to that optimized configuration which had the best binding energy for SO_2.

To quantify the charge transfer in these SO_2-IL complexes, atomic site charges were computed using the DDEC/c3 method in gas phase. [66, 67] To this end, minimum energy configurations were utilized to calculate the valence electron density of these systems and the same was employed as an input to DDEC/c3.

Classical Simulations. MD simulations were carried out with the LAMMPS program. [68] ILs were modeled using a non-polarizable all-atom force field developed and discussed in Chapter 2A and Chapter 2B. Interaction parameters for SO_2 were adopted from the work of Potoff *et al.* [69] which was used previously to simulate SO_2 in ILs. [61] The parameters for cross-terms were computed by Lorentz-Berthelot rules. Particle-particle particle mesh solver was employed to evaluate the long-range electrostatic interactions. Equations of motion were integrated using velocity Verlet algorithm with a time step of 1 fs. Tail corrections to energy and pressure were applied. All C-H covalent bonds were constrained using SHAKE algorithm as implemented in LAMMPS. [68] The temperature and pressure in simulations were controlled using Nosé-Hoover thermostat [70, 71] and barostat.

The initial configurations were generated with the program, Packmol. [72] Experimental observations suggest that SO_2 is soluble in all ILs studied here up to at least 0.5 mole fraction at 298 K. Thus, the simulations of bulk solutions were performed in a cubic box containing 256 cations, 256 anions and 128 SO_2 molecules to obtain a molar ratio of 0.5. Simulations were carried out at 298 K in order to compare the results against reported experimental properties (although [BMIM][Cl] is solid at 298 K, the simulations for SO_2 loaded [BMIM][Cl] system was also performed at 298 K for the sake of comparison). All

the systems were equilibrated in the NPT ensemble for 10 ns duration. It was followed by another 5 ns equilibration in the NVT ensemble. Finally, a 48 ns production run was generated in the NVT ensemble. The simulated box dimensions for all SO_2-IL mixtures are tabulated Table 6A.1. For purpose of comparison, a separate simulation was performed with CO_2 loaded ionic liquid system at 298 K. The systems were visualized in VMD. [73]

Table 6A.1: Simulation box length of pure IL and SO_2-IL mixtures in bulk, at 298 K.

System	Box Length (Å)	
	Pure IL	SO_2-IL
[BMIM][SCN]	42.58	44.22
[BMIM][Cl]	41.07	42.83
[BMIM][OAc]	43.04	44.64
[BMIM][CF_3SO_3]	44.43	45.60
[BMIM][BF_4]	43.01	44.62
[BMIM][NO_3]	41.82	43.51
[BMIM][PF_6]	44.16	45.70
[BMIM][NTf_2]	49.74	51.32

Transport properties such as self-diffusion coefficient, shear viscosity and electrical conductivity were calculated using equilibrium Green-Kubo relations discussed in Chapter 2A.

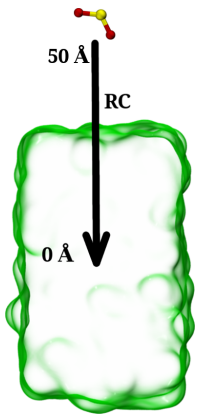

Figure 6A.2: Reaction coordinate for solvation free energy calculation of SO_2 in ILs.

Free Energy Calculations. All the FE simulations were carried out employing the colvars module [74] as implemented in LAMMPS. [68] The solvation free energy (SFE) can be defined as the energy required to bring one SO_2 molecule into bulk IL from the gas phase. A simulation cell containing 256 ion pairs was equilibrated in the NPT ensemble

at 298 K for 8 ns ([BMIM][Cl] at 353 K, as it is a solid at room temperature). To create a liquid-vapor interface, the cell length along z-axis was stretched to 200 Å, and then the system was further equilibrated in the NVT ensemble for 2 ns. This was followed by FE calculations in the NVT ensemble. Colvar style "distance Z" was employed in determining the free energy profile using the Adaptive Biasing Force (ABF) method. [75] The distance between the center of mass (COM) of IL molecules and the center of mass of SO_2 molecule was used to define the reaction coordinate (RC) (see Figure 6A.2). Four nonoverlapping windows along Z direction were created to divide the whole reaction coordinate, spanning from 0 to 50 Å. The first and last window represents SO_2 to be completely submerged in bulk IL and completely in gas phase, respectively. ABF forces were applied every 500 steps with a bin width of 0.1 Å. In each window, an average sampling ratio of 5 between the highest and lowest point was achieved, after running for at least 40 ns.

6A.3 Results and Discussion

6A.3.1 Quantum Chemical Analysis

The computed binding energies (BE) at MP2/aug-cc-pVDZ level of theory for SO_2-IL complexes are tabulated in Table 6A.2. Aparicio *et al.* investigated the interaction strength in a pool of SO_2-IL systems by decomposing the total BE into cation-anion, SO_2-cation, and SO_2-anion contributions. [51] They observed SO_2-anion interactions to be the major contribution to total BE for SO_2-IL systems. In our calculations, BE varies between -31.38 kJ/mol ([BMIM][NTf_2]) and -82.19 kJ/mol ([BMIM][SCN]) (see Table 6A.2).

Table 6A.2: BSSE corrected binding energies (B.E.) of SO_2-Ion pair systems at MP2/aug-cc-pVDZ level of theory.

SO_2-IL System	B.E. (kJ mol^{-1})
[BMIM][SCN]	-82.19
[BMIM][Cl]	-72.17
[BMIM][OAc]	-59.12
[BMIM][CF_3SO_3]	-57.78
[BMIM][NO_3]	-54.68
[BMIM][BF_4]	-49.51
[BMIM][PF_6]	-40.05
[BMIM][NTf_2]	-31.38

Among the systems studied, there appears to be more than one approach for the SO_2 molecule to interact with the IL ions. Anions such as $[Cl]^-$ or $[SCN]^-$, prefer to be located above the imidazolium ring plane whereas SO_2 interacts along the C_1 site on cation.

However, anions like $[BF_4]^-$, $[NO_3]^-$ and $[TFO]^-$, interact along the most acidic site on cation (C_R) and SO_2 prefers to stay above the ring plane, interacting with H_1 hydrogens. In the acetate system, both the anion as well as SO_2 prefer to be in the same plane as that of the imidazolium ring; while acetate anion shows very strong interaction with the acidic proton (H_A), SO_2 interacts with H_1 sites. But, in systems such as $[PF_6]^-$ and $[TFSO]^-$, SO_2 and the anion are located on either side of the imidazolium ring, resulting in minimal SO_2-anion interaction among all SO_2-IL system examined here. The same can be seen in the BE values for SO_2-IL system having either $[PF_6]^-$ or $[TFSO]^-$. The minimum energy structures of SO_2-IL complexes are displayed in Figure 6A.3.

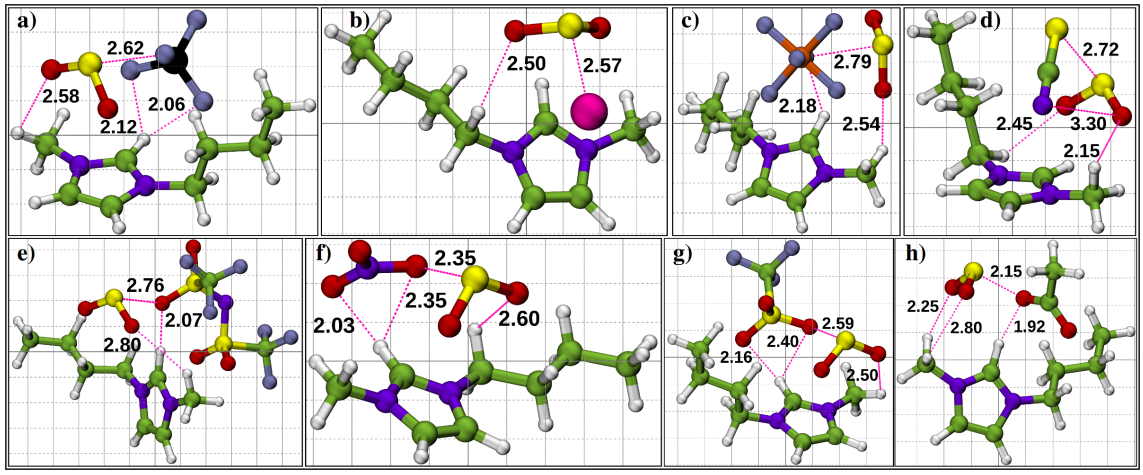

Figure 6A.3: Minimum energy structures of SO_2-IL complexes at MP2/aug-cc-pVDZ level of theory; (a) [BMIM][BF_4], (b) [BMIM][Cl], (c) [BMIM][PF_6], (d) [BMIM][SCN], (e) [BMIM][NTf_2], (f) [BMIM][NO_3], (g) [BMIM][CF_3SO_3], and (h) [BMIM][OAc]. The dotted line represents interatomic distances in angstrom.

Charge transfer between SO_2 and IL has been reported earlier [51] which can be used to understand the gas absorption capacity. The charge transfer between the ion pair and SO_2 molecule is calculated as the difference in total charge on SO_2 molecule in the isolated state and in the SO_2-IL complex and the same is tabulated in Table 6A.3. In all the systems studied here, the total charge on SO_2 molecule is negative; this implies that charge is transferred to the SO_2 molecule from the ion pair. A linear relationship between the BE and charge transfer in these complexes is observed (Figure 6A.4). The trend in observed experimental solubility [2, 31, 41] ties with that of the BE and points to the enthalpic nature of SO_2 solvation in ILs.

6A.3.2 Liquid Structure

To obtain an insight into the effect of SO_2 on the structure of ILs, we compared cation-anion and anion-H_A radial distribution functions (RDFs) in the pure IL and in SO_2 loaded

Table 6A.3: Charge transfer in SO_2-Ion pair complexes obtained from DDEC/c3 method [66, 67] based on MP2/aug-cc-pVDZ calculations.

SO_2-IL System	Charge Transfer (e)
[BMIM][SCN]	-0.239
[BMIM][Cl]	-0.227
[BMIM][OAc]	-0.199
[BMIM][CF_3SO_3]	-0.053
[BMIM][BF_4]	-0.029
[BMIM][NO_3]	-0.119
[BMIM][PF_6]	-0.018
[BMIM][NTf_2]	-0.010

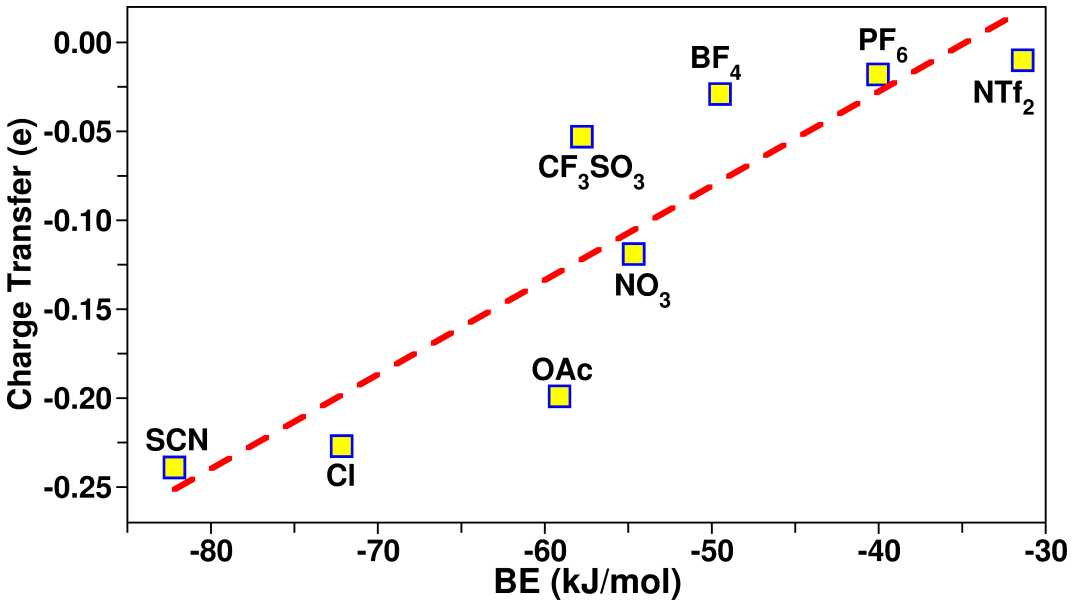

Figure 6A.4: Binding energies versus charge transfer to SO_2 upon complexation with IL ion pairs in gas phase. $[BMIM]^+$ is the common cation.

ILs (see Figure 6A.5). No significant changes were observed in these pair correlation functions upon SO_2 inclusion, which is consistent with previous MD simulations of SO_2 loaded ILs. [56, 57, 76] SO_2 solvation in ILs was further investigated through RDFs between the center of mass (COM) of the ions and that of SO_2 and the same are shown in Figure 6A.6. Anions interact with the solute better than cations do. Within its first coordination sphere, SO_2 molecule is surrounded by around 1.5 anions and 5.5 cations (see Table 6A.4). The presence of such high cation to anion ratio (which was also seen in many instances for CO_2 solvation in ILs [77, 78], as well as for SO_2 solvation in [EMIM][SCN] from an *ab initio* MD study [57]) suggests a possible formation of "cation cage" around

SO_2. Thus, it is worth investigating in more detail the role of contributing sites and compare them against results for CO_2 solvation by ILs.

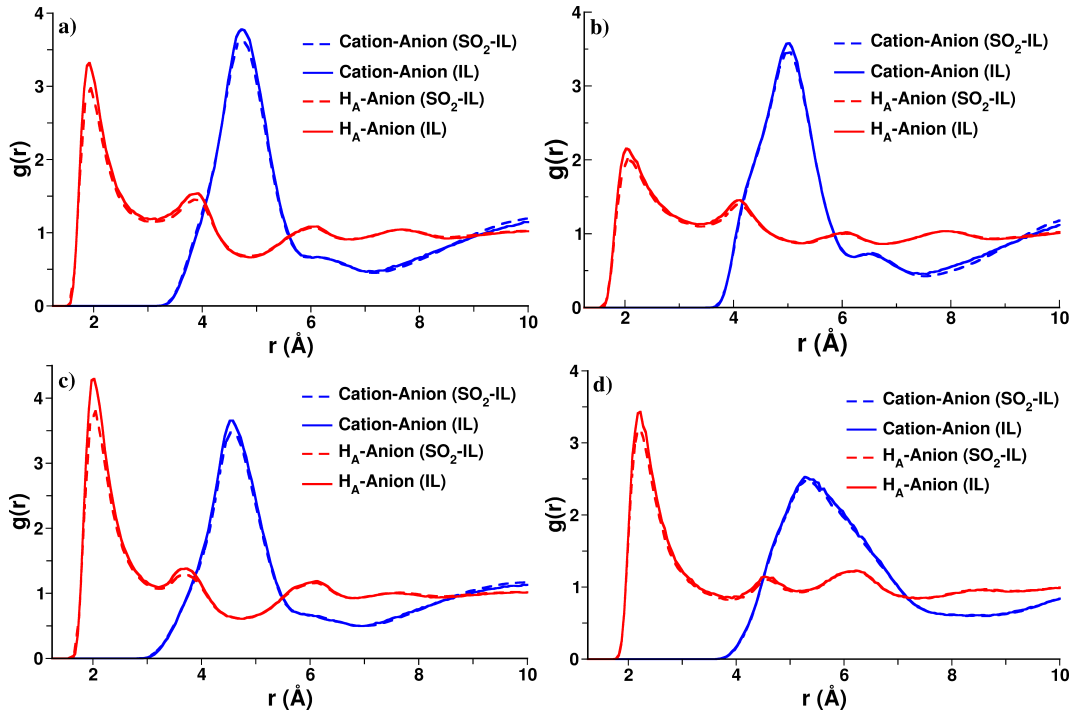

Figure 6A.5: Radial distribution functions in pure IL and SO_2-IL mixtures; (a) [BMIM][BF_4], (b) [BMIM][PF_6], (c) [BMIM][NO_3], (d) [BMIM][NTf_2].

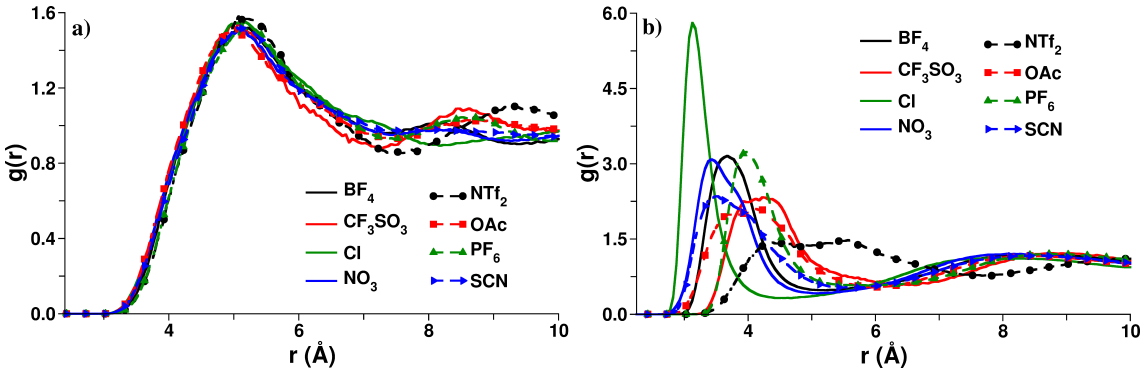

Figure 6A.6: Radial distribution functions between (a) center of mass (SO_2) - center of ring (cation) and (b) center of mass (SO_2) - center of anion in SO_2-IL mixtures. $[BMIM]^+$ is common cation.

We have examined various site-site RDFs to unveil the role of specific interactions in SO_2 solvation and these are displayed in Figure 6A.7. The cation hydrogen atoms e.g. H_B and H_1 possess a stronger interaction with SO_2 (than H_A as is evident from the well defined and sharp peak around 2.6–2.7 Å in Figure 6A.7). The coordination numbers

Table 6A.4: Coordination number (integrated RDF up to distance provided in parenthesis, in Å) of cations (N_C) and anions (N_A) around SO_2 in SO_2-IL mixtures.

SO_2-IL System	N_C	N_A
[BMIM][SCN]	5.81 (7.50)	1.64 (5.50)
[BMIM][Cl]	5.92 (7.60)	1.57 (4.60)
[BMIM][OAc]	5.53 (7.50)	1.62 (5.90)
[BMIM][CF_3SO_3]	5.64 (7.40)	1.66 (6.50)
[BMIM][BF_4]	5.72 (7.50)	1.56 (5.25)
[BMIM][NO_3]	6.04 (7.45)	1.61 (5.00)
[BMIM][PF_6]	5.24 (7.55)	1.54 (5.75)
[BMIM][NTf_2]	4.02 (7.65)	1.48 (7.50)

(integrated RDFs up to 3.5 Å) suggest that SO_2 molecule is surrounded by more H_1 atoms (1.65) than H_B atoms (0.75), which is consistent with the preference seen in gas phase quantum chemical calculations. Interestingly, the acidic hydrogen (H_A) atom having a strong interaction with anion, also shows notable contact with SO_2, indicated by a sharp rise at short distance of 2.2 Å in Figure 6A.7c, but its peak height is lower than that with either the H_B or H_1. It is followed by a small hump at around 4.2 Å, and broad peak around 6 Å. On the contrary, the interaction of CO_2 with IL cation is primarily driven by the dispersion between solute and alkyl side chain, as no such direct contact between oxygen of CO_2 and the acidic hydrogen atom (H_A) on imidazolium ring was observed in a simulation of CO_2-IL solution (Figure 6A.8a) and in previous reports as well. [77, 78] Thus, the considerably higher solubility of SO_2 than CO_2 in ILs might be a consequence of the crucial contrast in their structure of the solvation shell.

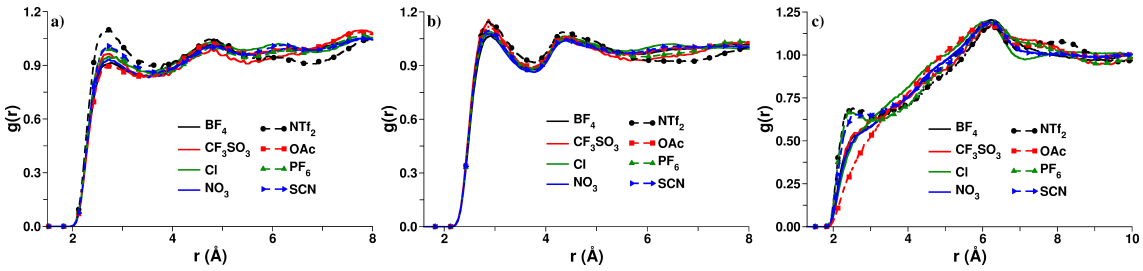

Figure 6A.7: Radial distribution functions between (a) SO_2-H_B, (b) SO_2-H_1, and (c) SO_2-H_A in SO_2-IL mixtures. $[BMIM]^+$ is common cation.

Spatial distribution functions (SDFs) were examined to validate these structural correlations. Figure 6A.9 displays the computed SDFs of the anion and SO_2 molecule around the center of ring of the imidazolium cation, at isosurface values of 0.006 $Å^{-3}$ and 0.003 $Å^{-3}$,

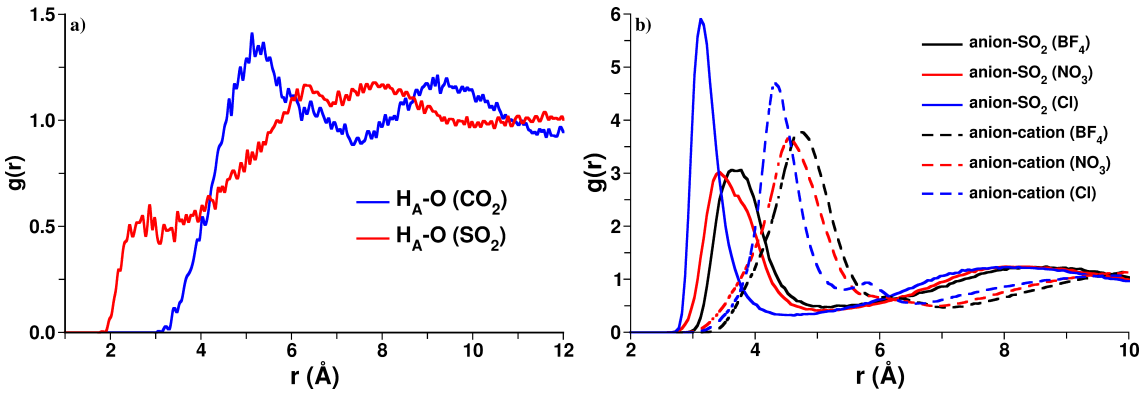

Figure 6A.8: (a) Radial distribution functions between oxygen atoms of CO_2 and of SO_2 with the cation's acidic hydrogen atom (H_A) in [BMIM][NTf_2]. The mole fraction of either solute in the ionic liquid was 0.2. The simulations were carried out at 298 K and 1 atm. TraPPE force field with LJ and charge sites was considered for CO_2. [79] (b) Radial distribution functions in SO_2-IL mixtures. $[BMIM]^+$ is common cation.

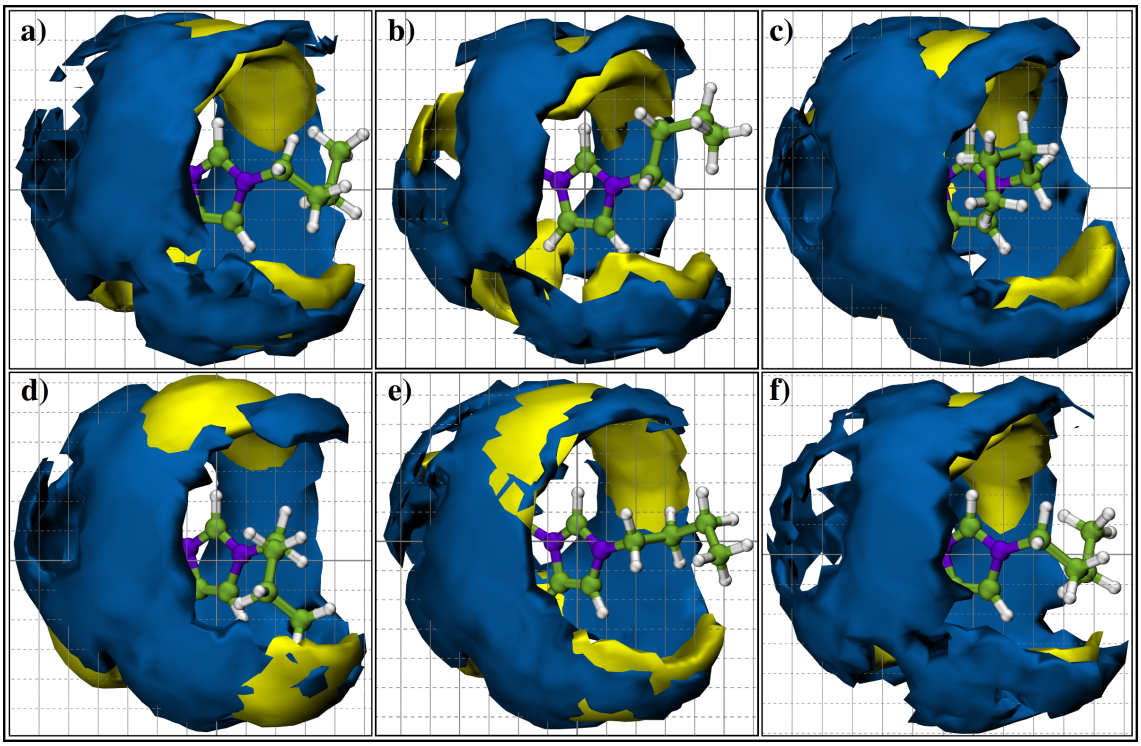

Figure 6A.9: Spatial density map of anion (yellow) and SO_2 (blue) around the center of ring of the cation for (a) $[Cl]^-$, (b) $[NO_3]^-$, (c) $[OAc]^-$, (d) $[BF_4]^-$, (e) $[PF_6]^-$, and (f) $[SCN]^-$. Isosurface density: 0.006 $Å^{-3}$ (anion) and 0.003 $Å^{-3}$ (SO_2). Color scheme: violet, nitrogen; green, carbon; white, hydrogen.

respectively. It is evident from Figure 6A.9 that there is a hole in the density map of SO_2 exactly on top of the H_A atom. Instead, the density map of SO_2 is condensed around sites

such as H_B and H_1, indicating binding preferences for SO_2 with these sites. Anions show stronger binding towards the most acidic hydrogen atom (H_A) located on the cation ring (see anion density map in Figure 6A.9) than the neutral SO_2 molecules do. Consequently, SO_2 interacts with the other hydrogen atoms on cation i.e., H_B and H_1. These observations are in agreement with the RDF analysis and gas phase quantum chemical calculations. Spatial distributions of cation ring center and of SO_2 molecule around the center of mass of the anion are displayed in Figure 6A.10. Although both cation and SO_2 share the same space around the anion, the latter interacts from a shorter distance than the former. A similar phenomenon was also observed in their respective radial distribution functions (see Figure 6A.8b). The more electron rich centers in anion e.g. oxygens of $[OAc]^-$, $[NO_3]^-$, $[TFO]^-$ etc. are more preferred over the other sites by the cation and SO_2.

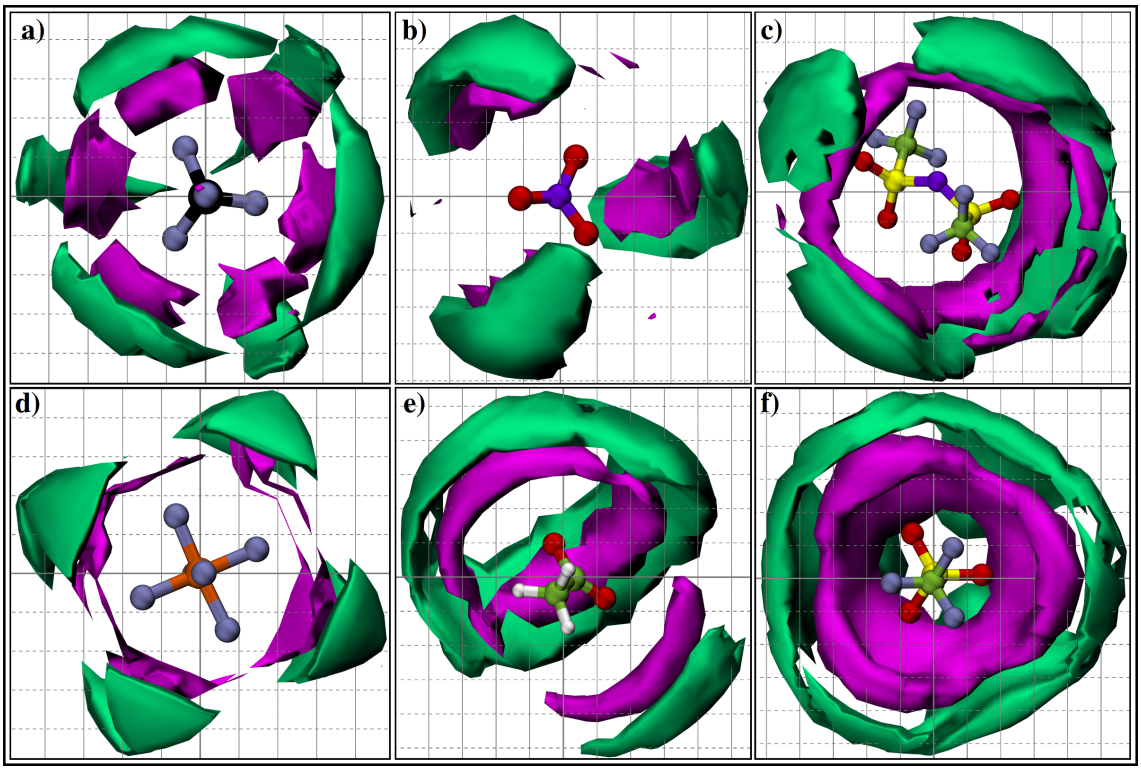

Figure 6A.10: Spatial density map of cation (magenta) and SO_2 (green) around the center of mass of the anion for (a) $[BF_4]^-$, (b) $[NO_3]^-$, (c) $[NTf_2]^-$, (d) $[OAc]^-$, (e) $[TFO]^-$, and (f) $[PF_6]^-$. Isosurfaces are at a density of 0.006 $Å^{-3}$ for the cation and 0.003 $Å^{-3}$ for SO_2. Color scheme: nitrogen, violet; carbon, green; hydrogen, white; oxygen, red; sulfur, yellow; boron, black; fluorine, iceblue; phosphorus, orange.

In order to quantify the arrangement of the anion and SO_2 around the cation ring plane, combined distribution functions (CDFs) were calculated [80, 81] and the same are displayed in Figure 6A.11. As described earlier, the acidic hydrogen atom H_A exhibits pronounced interaction with the anion rather than with the SO_2 molecule. The first and

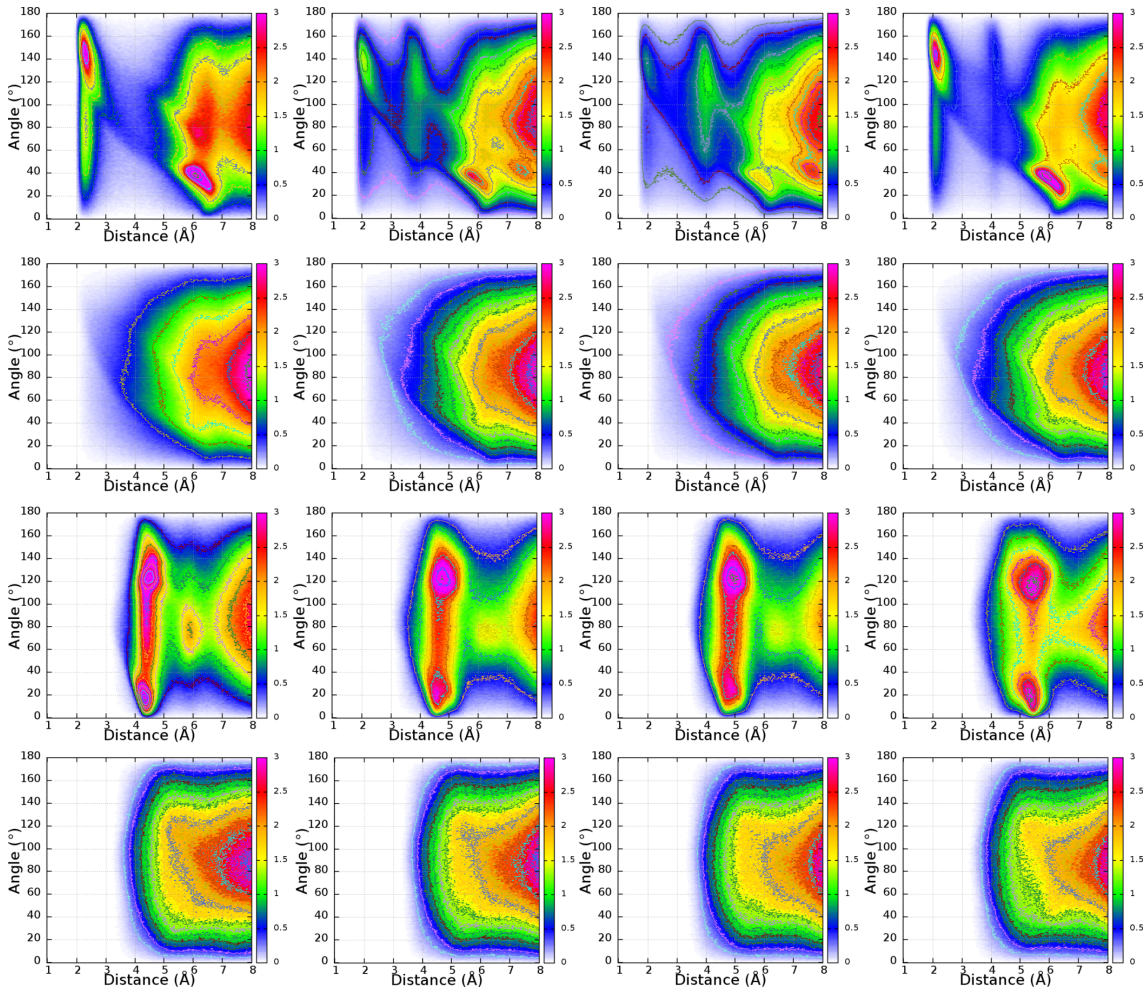

Figure 6A.11: Combined distribution functions depicting the in-plane and on-top distribution with relative intensity color coding. The distance is H_A-anion [first panel], H_A-SO_2 [second panel], CoR-CoM (anion) [third panel] and CoR-CoM (SO_2) [fourth panel]. The angle is C_R-H_A-anion [first panel], C_R-H_A-SO_2 [second panel], CoR-C_R-CoM (anion) [third panel] and CoR-C_R-CoM (SO_2) [fourth panel]. CoR indicates the center of the imidazolium ring and CoM indicates the center of mass of either anion or SO_2. The anions are $[Cl]^-$ (first column), $[NO_3]^-$ (second column), $[BF_4]^-$ (third column) and $[OAc]^-$ (fourth column).

second panel of Figure 6A.11 indicate that the probability for anions to be located closer to this acidic hydrogen and more linear to the C_R-H_A bond is higher than that for SO_2. The CDFs depicting the coordination at acidic hydrogen atom reveal that the anion interacts directly toward the H_A atom (in-plane arrangement) and this directionality is most intense in [BMIM][Cl] and least in [BMIM][TFSO]. This trend can be justified based on the reduced acceptor probability due to larger charge delocalization in anions such as $[PF_6]^-$, $[TFSO]^-$ etc. However, the orientation of SO_2 molecule toward the acidic hydrogen atom is independent of the anion. It is evident from third and fourth panel of Figure 6A.11 that

the anion is likely to be present on-top of the imidazolium ring too at short distances when compared to that of SO_2 distribution. These observations further substantiate the fact that SO_2 is more likely to be found near the methyl hydrogen atoms (H_1) which was also seen in RDF analysis and gas phase DFT calculations.

6A.3.3 Thermodynamics of SO_2 Absorption

The potential of mean force (PMF) for bringing the solute, SO_2, from its vapor phase into the bulk IL was calculated. The free energy profiles for SO_2 solvation in various ILs consisting $[BMIM]^+$ as the common cation combined with different anions are displayed in Figure 6A.12a. Solvation free energy (SFE) is the difference in the free energies between the vapor phase and the solvated state of the solute in the IL. The SFE profiles become zero around 42 Å in most ILs, except in [BMIM][Cl]. This is due to the smaller thickness of the [BMIM][Cl] liquid slab (see Figure 6A.12b). As the SO_2 approaches the liquid region, the PMF displays a monotonic decay and it become most negative at the air-IL interface. The PMF increases in value in the bulk region, before converging to a constant value. Similar kind of PMF profiles were observed in earlier gas absorption studies in ILs. [59, 60] The occurrence of the minimum near the air-IL interface in the SO_2 PMF clearly reveals a preference for the solute to be at the interface.

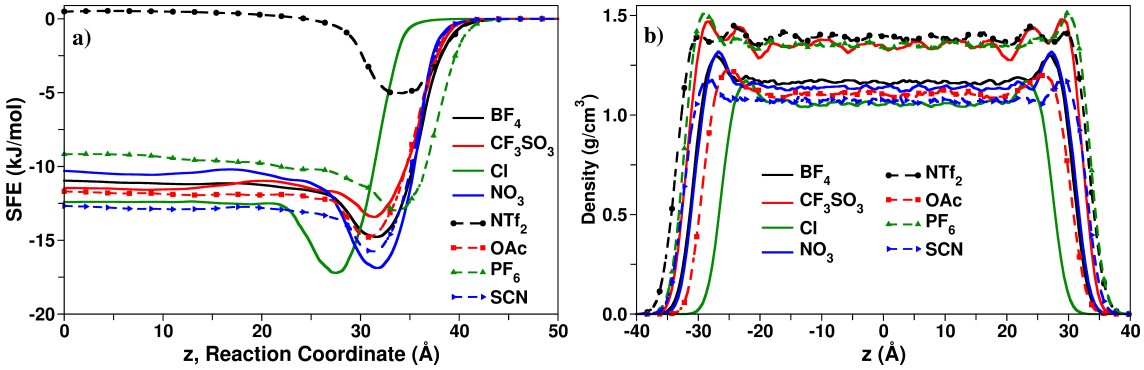

Figure 6A.12: (a) Solvation free energy profile of SO_2 in various ionic liquids ($[BMIM]^+$ as common cation). $z = 0$ is the center of mass of IL (bulk) and $z > 45$ is SO_2 in vapor phase. (b) Mass density profile for various ILs from the liquid-vapor simulations.

Further, Figure 6A.13 presents the PMF along with the number density profile of various sites on cation and anion in [BMIM][NO_3] and [BMIM][BF_4]. It is evident that the minimum in SO_2 PMF coincides with the maximum in C_1 number density at the interface, which confirms the preferable interaction of SO_2 with H_1 atoms over other sites of the cation. The cation alkyl chain is oriented normal to the liquid-vapor interface [82], which can enhance the gas solubility through dispersion interaction with SO_2 (also seen from the bulk liquid structure). In addition, this may also lead to the formation of an adsorbed SO_2

layer at the interface, which indeed was found for CO_2 in a recent study. [83]

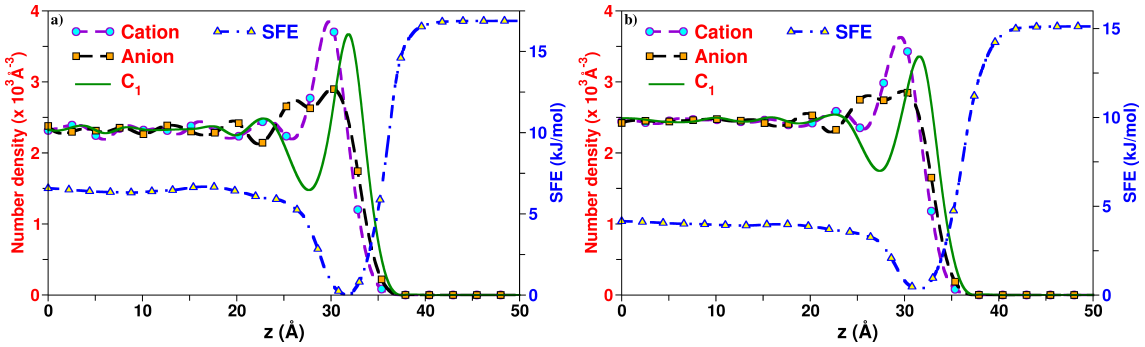

Figure 6A.13: Number density profile of cation ring center, anion center of mass and C_1 atom of butyl tail, compared against SO_2 PMF in (a) [BMIM][NO_3] and (b) [BMIM][BF_4].

In a liquid system which is in equilibrium with its vapor phase, the change in potential energy across the vapor-liquid interface is presumed to be the same as the enthalpy change. Thus, the relative solubility of SO_2 in different ILs can be understood in terms of enthalpy and entropy contributions. The trend in SFE determined using an empirical force field can be correlated to the binding energy of one ion pair with a SO_2 molecule (computed at MP2/aug-cc-pVDZ level of theory) and a linear correlation is displayed in Figure 6A.14a. This observation suggests that the SO_2 solvation in ILs is largely enthalpy driven. In

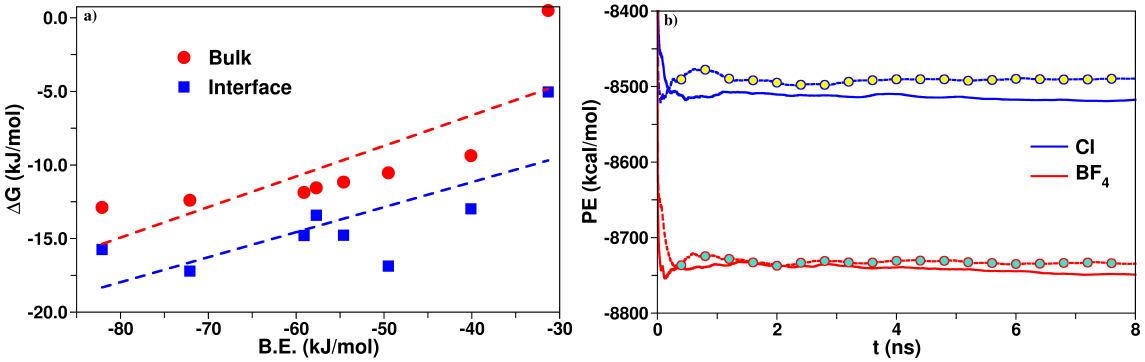

Figure 6A.14: (a) Binding energy (BE) of SO_2 with IL ion pair versus the solvation free energy (SFE) of SO_2 in bulk IL and in IL-vapor interface. BE is obtained from gas phase quantum chemical calculation while the SFE are determined from bulk MD simulations with an empirical force field. Dashed lines are best fits to data. Red (blue) circles are ΔG between SO_2 in vapor and in the bulk (interface) of IL. (b) Running average of potential energy of SO_2 in $[BMIM]^+$ ionic liquids. The solid line shows SO_2 present inside the bulk IL, while the dashed-symbol line is for SO_2 kept at 40 Å away from the center of bulk ionic liquid, i.e., far away from the IL-vapor interface.

addition, the energetic and entropic contributions to SFE were determined through two additional simulations. In one, a solute SO_2 molecule was kept 40 Å away from the bulk IL

region i.e., clearly in the vapor phase. The other one contained the SO_2 molecule submerged inside the bulk IL. The simulation box dimensions, temperature etc. were kept the same as in those described in the Free Energy Calculation section. Both the systems were equilibrated in the NVT ensemble for 8 ns duration (see Figure 6A.14b). The difference in potential energy between these two equilibrated systems was taken as the enthalpy change (ΔH) for SO_2 solvation. The entropy contribution to the dissolution process is obtained as the difference between the solvation free energy and the potential energy and the same is tabulated in Table 6A.5. In most of the ILs, the change in entropy with respect to the energy difference is moderate. However, in the case of [BMIM][NTf_2], the relative entropy contribution is much higher than in rest of the ILs, resulting in it becoming a poor solvent for SO_2 solvation. Further investigation suggests that the addition of solute SO_2 in the bulk ionic liquids stretches the cation marginally (see Figure 6A.15). For the smaller anions such as $[SCN]^-$, $[OAc]^-$, $[CF_3SO_3]^-$, $[BF_4]^-$, $[PF_6]^-$ etc. there is no conformational change and thus no change in geometry, upon addition of SO_2. However, $[NTf_2]^-$ being larger in size, can be rotationally excited and thus have different conformational preferences with and without SO_2. Figure 6A.15d displays the distribution of distances between the terminal fluorine atoms in $[NTf_2]^-$ anion in pure [BMIM][NTf_2] and in 50% SO_2 loaded [BMIM][NTf_2]. It is evident that the distribution becomes narrower on addition of SO_2 in bulk IL. The increased width of this distribution consequently expands its conformational space, increasing the entropy of SO_2 dissolved [BMIM][NTf_2] and decreasing the free energy of dissolution. Among the ILs studied here, [BMIM][SCN] appeared to be the best solvent for SO_2 capture, which is consistent with the experimental observation. [2]

Table 6A.5: Changes in free energy ($\Delta G = G_{liq} - G_{gas}$), enthalpy ($\Delta H = H_{liq} - H_{gas}$), and entropy ($T\Delta S = S_{liq} - S_{gas}$) for SO_2 solvation in various ILs. ΔS is a derived quantity from ΔG and ΔH. $[BMIM]^+$ is the cation.

IL	ΔG (kJ/mol)	ΔH (kJ/mol)	$T\Delta S$(kJ/mol)
$[SCN]^-$	-12.84	-53.68	-40.84
$[Cl]^-$	-12.38	-89.41	-77.03
$[OAc]^-$	-11.84	-75.35	-63.51
$[CF_3SO_3]^-$	-11.55	-35.23	-23.68
$[BF_4]^-$	-11.13	-81.46	-70.33
$[NO_3]^-$	-10.50	-60.21	-49.71
$[PF_6]^-$	-9.330	-59.99	-50.66
$[NTf_2]^-$	0.502	-43.89	-44.39

The gas solubility in a liquid at infinite dilution can be measured via Henry's law

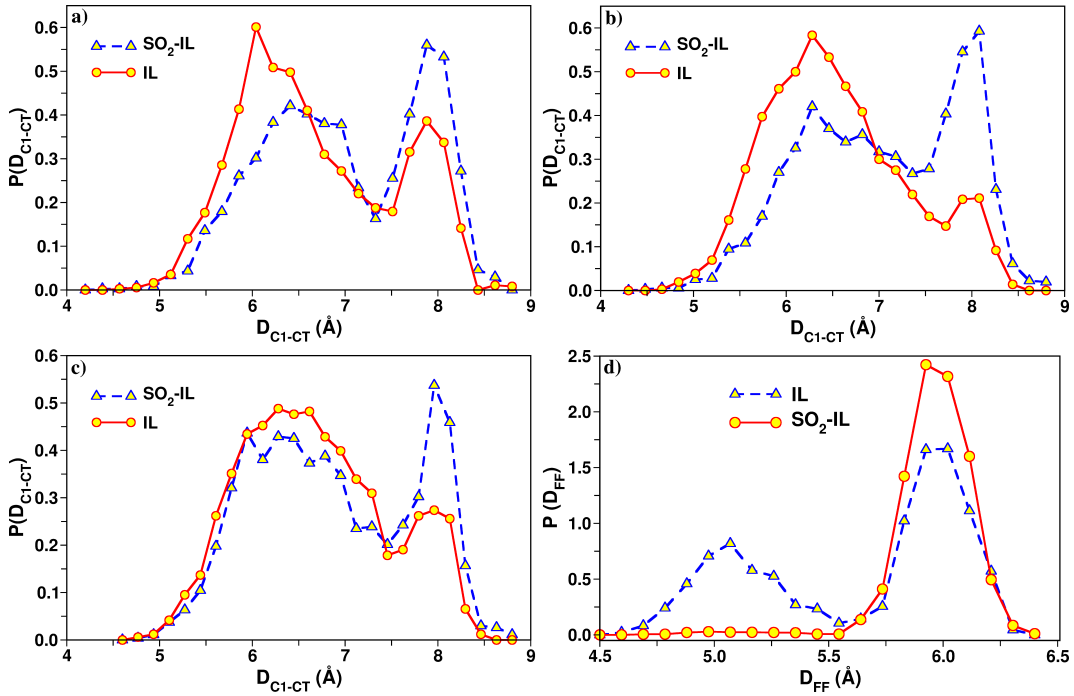

Figure 6A.15: Distribution of distances between C_1 and C_T atoms of imidazolium cation in pure ionic liquid and in SO_2-IL mixtures; (a) $[OAc]^-$, (b) $[PF_6]^-$ and (c) $[NTf_2]^-$. $[BMIM]^+$ is common cation. (d) Distribution of distance between the terminal fluorine atoms of $[NTf_2]^-$ anion in pure $[BMIM][NTf_2]$ and in 50% SO_2 loaded $[BMIM][NTf_2]$ mixture.

constant, K_H. It is defined using the standard thermodynamic relation as,

$$K_H = \frac{RT\rho}{M} exp\left(\frac{\Delta G_{Sol}}{RT}\right) \tag{6A.2}$$

where, ΔG_{Sol} is the free energy of solvation, ρ is the density, and M is the molecular weight of the pure IL. Henry's constant is indirectly proportional to gas solubility. The Henry's law constant of SO_2 in all the IL systems studied here is summarized in Table 6A.6. Although there exists some differences in the solubility order reported in literature from simulations (e.g. solubility order, $[BMIM][NTf_2] > [BMIM][BF_4] > [BMIM][PF_6]$ by Elliott and co-workers [55] and $[BMIM][PF_6] > [BMIM][NTf_2] > [BMIM][BF_4]$ by Aparicio *et al.* [51]), we would like to discuss this matter in the light of our observations. As can be seen from Table 6A.6, SO_2 is soluble in all ILs investigated here. The obtained K_H values showed the following solubility order: $[BMIM][SCN] > [BMIM][Cl] > [BMIM][OAc] > [BMIM][TFO] > [BMIM][BF_4] > [BMIM][NO_3] > [BMIM][PF_6] > [BMIM][NTf_2]$.

Thus, [BMIM][SCN] is the most preferred solvent for SO_2 solvation, while $[BMIM][NTf_2]$ fares the worst. It is interesting to note that the solubility of SO_2 is more in ILs with smaller molar volumes. [55] Enthalpic contributions as captured through gas phase calculations

Table 6A.6: Henry's law constant (K_H) of SO_2 in studied ILs at 298 K and P = 1 atm. †The temperature is 353 K.

IL	K_H (atm)
[BMIM][SCN]	0.77
[BMIM][Cl]†	1.01
[BMIM][OAc]	1.09
[BMIM][CF_3SO_3]	1.21
[BMIM][BF_4]	1.49
[BMIM][NO_3]	2.08
[BMIM][PF_6]	2.80
[BMIM][NTf_2]	5.72

and bulk MD simulations largely determine SO_2 solubility in ILs. These observations are important in further design of functional ionic liquids for SO_2 capture.

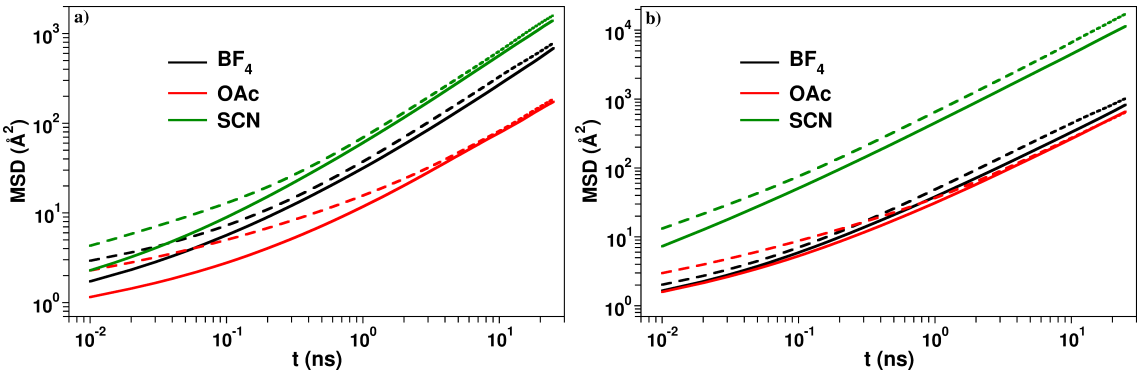

Figure 6A.16: Mean square displacement (MSD) of ions as a function of time in (a) pure ionic liquid and (b) SO_2-IL mixture at 298 K. The solid and dashed lines are for cation and anion, respectively.

6A.3.4 Dynamics in SO_2-IL Mixtures

Ion self diffusion coefficients in pure IL and SO_2-IL mixtures are computed from mean square displacement (see Figure 6A.16) and are compared in Table 6A.7. Ionic diffusion in SO_2-IL mixture is higher than in pure ILs, which was also seen in previous MD simulations. [53, 56, 58, 61] Likewise, shear viscosity and ionic conductivity are affected by the dissolution of SO_2 in ILs. Computed viscosity and electrical conductivity are presented in Table 6A.8. In accordance with both experimental and simulation results, [2, 13, 53, 56, 58] the dissolution of SO_2 reduces the viscosity and enhances the electrical conductivity of the liquid. The transport coefficient values obtained from Green-Kubo relations for ILs, [BMIM][NTf_2] and [BMIM][SCN] showed adequate agreement with experimental

Table 6A.7: Ion Self-diffusion Coefficients ($\times 10^{-7} cm^2 s^{-1}$) in Pure IL and SO_2-IL Mixtures Calculated from Bulk Simulations at 298 K. † Temperature is 300 K.

IL	D_+		D_-		D_{SO_2}
	Pure†	Mix.	Pure†	Mix.	
[BMIM][SCN]	9.48	16.1	9.97	20.2	57.98
[BMIM][OAc]	1.27	4.23	1.32	4.43	24.59
[BMIM][CF_3SO_3]	2.08	3.52	1.41	2.85	22.65
[BMIM][BF_4]	2.30	7.89	1.83	7.92	34.26
[BMIM][NO_3]	1.65	6.24	1.51	5.04	27.62
[BMIM][PF_6]	1.05	4.80	0.74	4.17	33.79
[BMIM][NTf_2]	2.70	7.73	2.10	5.98	33.82

Table 6A.8: Shear Viscosity, η (mPa.s) and Electrical Conductivity, σ ($S.m^{-1}$) in Pure IL and SO_2-IL Mixtures at 298 K. † The Temperature is 300 K.

IL	η		σ	
	Pure†	Mix.	Pure†	Mix.
[BMIM][SCN]	35.20	14.05	0.62	1.34
[BMIM][OAc]	191.5	62.19	0.07	0.31
[BMIM][CF_3SO_3]	65.00	32.21	0.25	0.66
[BMIM][BF_4]	71.00	26.39	0.42	1.06
[BMIM][NO_3]	129.0	50.38	0.31	0.76
[BMIM][PF_6]	185.0	72.19	0.17	0.51
[BMIM][NTf_2]	42.00	18.27	0.29	0.79

measurements available at low SO_2 loading. [2] Although SO_2 has been reported to be reactive with some ionic liquids, [10, 28] its effect on the IL viscosity is unknown. However, the viscosity of ionic liquids increases drastically upon chemisorption of CO_2. [84, 85] In the present work, we assume the physisorption of SO_2 in ILs and thus the viscosity of the solution decreases with respect to the neat IL.

6A.4 Conclusions

A microscopic understanding behind the solvation of SO_2 is important to obtain in order to interpret its solubilities in different ionic liquids. In this Chapter, we have employed molecular dynamics simulations and *ab initio* calculations to provide a detailed understanding of the dissolution of SO_2 in ionic liquids and consequent changes in their structure and transport coefficients.

Gas phase quantum chemical calculation results indicated the propensity of both the

cation and anion to interact with the SO_2 molecule. Strong charge transfer interaction between the anion and SO_2 molecule was also observed. A linear correlation between the binding energy of SO_2 with the ion pair and the net charge transfer (primarily from the anion to the SO_2 molecule) evidenced the anion$\cdots SO_2$ interaction as the major contribution in SO_2 capture in ILs. Binding energy values ranged from -31.38 kJ/mol ([BMIM][NTf_2]) to -82.19 kJ/mol ([BMIM][SCN]). Thus, $[SCN]^-$ emerged as the best anion to provide high SO_2 capture efficiency. [2]

Condensed phase MD simulations of SO_2-IL mixtures revealed the significant role of both cations and anions in the SO_2 dissolution process. SO_2 molecule was found to be surrounded by the cations through dispersion interaction, mainly with the alkyl group which leads to the formation of a "cation cage" around SO_2. On the other hand, less than a pair of anions were present within the first coordination shell of the solute. Thus, SO_2 shares favorable interactions with both the cation and the anion. The dynamical consequences of the dissolution of SO_2 in IL are the significant decrease in the shear viscosity and a resultant increase in diffusion coefficient and electrical conductivity.

The free energy profiles for SO_2 dissolution obtained from MD simulations demonstrate the preference for the solute to be located at the IL-vapor interface relative to the bulk liquid; the same can be rationalized from the richness of the cation alkyl groups at the interface. A nearly linear relationship between the solvation free energy and the gas phase binding energy of SO_2 with the ions is observed which points to the enthalpic nature of SO_2 dissolution in ILs. Thus, a good solvent for SO_2 capture must possess good hydrogen bond donor ability in the cation and a strong interaction with the anion. The calculated solubility order based on the Henry's law constant of SO_2 in various ILs, indicates [BMIM][SCN] to be the best solvent for SO_2 dissolution which was also reported earlier experimentally. [2]

Bibliography

[1] Smith, S. J.; van Aardenne, J.; Klimont, Z.; Andres, R. J.; Volke, A.; Delgado Arias, S. *Atmos. Chem. Phys.* **2011**, *11*, 1101–1116.

[2] Xing, H.; Liao, C.; Yang, Q.; Veith, G. M.; Guo, B.; Sun, X.-G.; Ren, Q.; Hu, Y.-S.; Dai, S. *Angew. Chem. Int. Ed.* **2014**, *53*, 2099–2103.

[3] Ratnakumar, B. V.; Smart, M. C.; Ewell, R. C.; Whitcanack, L. D.; Kindler, A.; Narayanan, S. R.; Surampudi, S. *J. Electrochem. Soc.* **2007**, *154*, A715–A724.

[4] Paik, Y.; Osegovic, J. P.; Wang, F.; Bowden, W.; Grey, C. P. *J. Am. Chem. Soc.* **2001**, *123*, 9367–9377.

[5] Zhang, H.; Zhong, X.; Shaw, J. C.; Liu, L.; Huang, Y.; Duan, X. *Energy Environ. Sci.* **2013**, *6*, 2621–2625.

[6] Kilroy, W. P.; Ebner, W.; Chua, D. L.; Venkatasetty, H. V. *J. Electrochem. Soc.* **1985**, *132*, 274–281.

[7] Dey, A. N.; Kuo, H. C.; Piliero, P.; Kallianidis, M. *J. Electrochem. Soc.* **1988**, *135*, 2115–2120.

[8] Zheng, Y.; Kiil, S.; Johnsson, J. E. *Chem. Eng. Sci.* **2003**, *58*, 4695–4703.

[9] Ma, X.; Kaneko, T.; Tashimo, T.; Yoshida, T.; Kato, K. *Chem. Eng. Sci.* **2000**, *55*, 4643 – 4652.

[10] Wu, W.; Han, B.; Gao, H.; Liu, Z.; Jiang, T.; Huang, J. *Angew. Chem. Int. Ed.* **2004**, *43*, 2415–2417.

[11] Cui, G.; Wang, C.; Zheng, J.; Guo, Y.; Luo, X.; Li, H. *Chem. Commun.* **2012**, *48*, 2633–2635.

[12] Huang, J.; Riisager, A.; Wasserscheid, P.; Fehrmann, R. *Chem. Commun.* **2006**, 4027–4029.

[13] Ren, S.; Hou, Y.; Wu, W.; Liu, Q.; Xiao, Y.; Chen, X. *J. Phys. Chem. B* **2010**, *114*, 2175–2179.

[14] Wang, C.; Luo, X.; Luo, H.; Jiang, D.-e.; Li, H.; Dai, S. *Angew. Chem. Int. Ed.* **2011**, *50*, 4918–4922.

[15] Wang, C.; Luo, H.; Jiang, D.-e.; Li, H.; Dai, S. *Angew. Chem. Int. Ed.* **2010**, *49*, 5978–5981.

[16] Bara, J. E.; Camper, D. E.; Gin, D. L.; Noble, R. D. *Acc. Chem. Res.* **2010**, *43*, 152–159.

[17] Bates, E. D.; Mayton, R. D.; Ntai, I.; Davis, J. H. *J. Am. Chem. Soc.* **2002**, *124*, 926–927.

[18] Zhang, Y.; Zhang, S.; Lu, X.; Zhou, Q.; Fan, W.; Zhang, X. *Chem. Eur. J.* **2009**, *15*, 3003–3011.

[19] Huang, J.-F.; Luo, H.; Liang, C.; Sun, I.; Baker, G. A.; Dai, S. *J. Am. Chem. Soc.* **2005**, *127*, 12784–12785.

[20] Merrigan, T. L.; Bates, E. D.; Dorman, S. C.; Davis Jr., J. H. *Chem. Commun.* **2000**, 2051–2052.

[21] Bara, J. E.; Carlisle, T. K.; Gabriel, C. J.; Camper, D.; Finotello, A.; Gin, D. L.; Noble, R. D. *Ind. Eng. Chem. Res.* **2009**, *48*, 2739–2751.

[22] Anderson, J. L.; Dixon, J. K.; Maginn, E. J.; Brennecke, J. F. *J. Phys. Chem. B* **2006**, *110*, 15059–15062.

[23] Shiflett, M. B.; Yokozeki, A. *Energy Fuels* **2010**, *24*, 1001–1008.

[24] Hong, S. Y.; Im, J.; Palgunadi, J.; Lee, S. D.; Lee, J. S.; Kim, H. S.; Cheong, M.; Jung, K.-D. *Energy Environ. Sci.* **2011**, *4*, 1802–1806.

[25] Boniface, J.; Shi, Q.; Li, Y. Q.; Cheung, J. L.; Rattigan, O. V.; Davidovits, P.; Worsnop, D. R.; Jayne, J. T.; Kolb, C. E. *J. Phys. Chem. A* **2000**, *104*, 7502–7510.

[26] Yuan, X. L.; Zhang, S. J.; Lu, X. M. *J. Chem. Eng. Data* **2007**, *52*, 1150–1150.

[27] Yokozeki, A.; Shiflett, M. B. *Energy Fuels* **2009**, *23*, 4701–4708.

[28] Shiflett, M. B.; Yokozeki, A. *Ind. Eng. Chem. Res.* **2010**, *49*, 1370–1377.

[29] Yang, D.; Hou, M.; Ning, H.; Ma, J.; Kang, X.; Zhang, J.; Han, B. *ChemSusChem* **2013**, *6*, 1191–1195.

[30] Shang, Y.; Li, H.; Zhang, S.; Xu, H.; Wang, Z.; Zhang, L.; Zhang, J. *Chem. Eng. J.* **2011**, *175*, 324 – 329.

[31] Jiang, Y.-Y.; Zhou, Z.; Jiao, Z.; Li, L.; Wu, Y.-T.; Zhang, Z.-B. *J. Phys. Chem. B* **2007**, *111*, 5058–5061.

[32] Luis, P.; Neves, L.; Afonso, C.; Coelhoso, I.; Crespo, J.; Garea, A.; Irabien, A. *Desalination* **2009**, *245*, 485–493.

[33] Hu, X.-B.; Li, Y.-X.; Huang, K.; Ma, S.-L.; Yu, H.; Wu, Y.-T.; Zhang, Z.-B. *Green Chem.* **2012**, *14*, 1440–1446.

[34] Yang, Z.-Z.; He, L.-N.; Song, Q.-W.; Chen, K.-H.; Liu, A.-H.; Liu, X.-M. *Phys. Chem. Chem. Phys.* **2012**, *14*, 15832–15839.

[35] Wang, C.; Zheng, J.; Cui, G.; Luo, X.; Guo, Y.; Li, H. *Chem. Commun.* **2013**, *49*, 1166–1168.

[36] Chen, K.; Lin, W.; Yu, X.; Luo, X.; Ding, F.; He, X.; Li, H.; Wang, C. *AIChE Journal* **2015**, *61*, 2028–2034.

[37] Wang, C.; Cui, G.; Luo, X.; Xu, Y.; Li, H.; Dai, S. *J. Am. Chem. Soc.* **2011**, *133*, 11916–11919.

[38] Cui, G.; Lin, W.; Ding, F.; Luo, X.; He, X.; Li, H.; Wang, C. *Green Chem.* **2014**, *16*, 1211–1216.

[39] Wang, C.; Zheng, J.; Cui, G.; Luo, X.; Guo, Y.; Li, H. *Chem. Commun.* **2013**, *49*, 1166–1168.

[40] Cui, G.; Zhang, F.; Zhou, X.; Li, H.; Wang, J.; Wang, C. *Chem. Eur. J.* **2015**, *21*, 5632–5639.

[41] Lei, Z.; Dai, C.; Chen, B. *Chem. Rev.* **2014**, *114*, 1289–1326.

[42] Cadena, C.; Anthony, J. L.; Shah, J. K.; Morrow, T. I.; Brennecke, J. F.; Maginn, E. J. *J. Am. Chem. Soc.* **2004**, *126*, 5300–5308.

[43] Huang, X.; Margulis, C. J.; Li, Y.; Berne, B. J. *J. Am. Chem. Soc.* **2005**, *127*, 17842–17851.

[44] Bhargava, B. L.; Balasubramanian, S. *J. Phys. Chem. B* **2007**, *111*, 4477–4487.

[45] Shah, J. K.; Maginn, E. J. *J. Phys. Chem. B* **2005**, *109*, 10395–10405.

[46] Wang, Y.; Pan, H.; Li, H.; Wang, C. *J. Phys. Chem. B* **2007**, *111*, 10461–10467.

[47] Bhargava, B. L.; Krishna, A. C.; Balasubramanian, S. *AIChE Journal* **2008**, *54*, 2971–2978.

[48] Zhang, X.; Huo, F.; Liu, Z.; Wang, W.; Shi, W.; Maginn, E. J. *J. Phys. Chem. B* **2009**, *113*, 7591–7598.

[49] Deschamps, J.; Gomes, M. F. C.; Pádua, A. A. H. *ChemPhysChem* **2004**, *5*, 1049–1052.

[50] Urukova, I.; Vorholz, J.; Maurer, G. *J. Phys. Chem. B* **2005**, *109*, 12154–12159.

[51] Garcia, G.; Atilhan, M.; Aparicio, S. *Phys. Chem. Chem. Phys.* **2015**, *17*, 13559–13574.

[52] Zhang, X.; Liu, X.; Yao, X.; Zhang, S. *Ind. Eng. Chem. Res.* **2011**, *50*, 8323–8332.

[53] Monteiro, M. J.; Ando, R. A.; Siqueira, L. J. A.; Camilo, F. F.; Santos, P. S.; Ribeiro, M. C. C.; Torresi, R. M. *J. Phys. Chem. B* **2011**, *115*, 9662–9670.

[54] Yu, G.; Chen, X. *J. Phys. Chem. B* **2011**, *115*, 3466–3477.

[55] Ghobadi, A. F.; Taghikhani, V.; Elliott, J. R. *J. Phys. Chem. B* **2011**, *115*, 13599–13607.

[56] Mohammadi, M.; Foroutan, M. *J. Mol. Liq.* **2014**, *193*, 60 – 68.

[57] Firaha, D.; Kavalchuk, M.; Kirchner, B. *J Solution Chem* **2015**, *44*, 838–849.

[58] Siqueira, L. J. A.; Ando, R. A.; Bazito, F. F. C.; Torresi, R. M.; Santos, P. S.; Ribeiro, M. C. C. *J. Phys. Chem. B* **2008**, *112*, 6430–6435.

[59] Wick, C. D.; Chang, T.-M.; Dang, L. X. *J. Phys. Chem. B* **2010**, *114*, 14965–14971.

[60] Dang, L. X.; Chang, T.-M. *J. Phys. Chem. Lett.* **2012**, *3*, 175–181.

[61] Morganti, J. D.; Hoher, K.; Ribeiro, M. C. C.; Ando, R. A.; Siqueira, L. J. A. *J. Phys. Chem. C* **2014**, *118*, 22012–22020.

[62] Prasad, B. R.; Senapati, S. *J. Phys. Chem. B* **2009**, *113*, 4739–4743.

[63] Dennington, R.; Keith, T.; Millam, J. GaussView Version 5. Semichem Inc., Shawnee Mission, KS, 2009.

[64] Boys, S.; Bernardi, F. *Mol. Phys.* **1970**, *19*, 553–566.

[65] Frisch, M. J. et al. Gaussian 09 Revision D.01. Gaussian Inc. Wallingford CT **2009**.

[66] Manz, T. A.; Sholl, D. S. *J. Chem. Theory Comput.* **2010**, *6*, 2455–2468.

[67] Manz, T. A.; Sholl, D. S. *J. Chem. Theory Comput.* **2012**, *8*, 2844–2867.

[68] Plimpton, S. *J. Comput. Phys.* **1995**, *117*, 1–19.

[69] Ketko, M. H.; Kamath, G.; Potoff, J. J. *J. Phys. Chem. B* **2011**, *115*, 4949–4954.

[70] Nosé, S. *J. Chem. Phys.* **1984**, *81*, 511–519.

[71] Hoover, W. G. *Phys. Rev. A* **1985**, *31*, 1695–1697.

[72] Martínez, L.; Andrade, R.; Birgin, E. G.; Martínez, J. M. *J. Comp. Chem.* **2009**, *30*, 2157–2164.

[73] Humphrey, W.; Dalke, A.; Schulten, K. *J. Mol. Graphics* **1996**, *14*, 33–38.

[74] Fiorin, G.; Klein, M. L.; Hénin, J. *Mol. Phys.* **2013**, *111*, 3345–3362.

[75] Darve, E.; Rodríguez-Gómez, D.; Pohorille, A. *J. Chem. Phys.* **2008**, *128*, 144120.

[76] Zeng, S.; Gao, H.; Zhang, X.; Dong, H.; Zhang, X.; Zhang, S. *Chem. Eng. J.* **2014**, *251*, 248–256.

[77] Hollóczki, O.; Kelemen, Z.; Könczöl, L.; Szieberth, D.; Nyulászi, L.; Stark, A.; Kirchner, B. *ChemPhysChem* **2013**, *14*, 315–320.

[78] Hollóczki, O.; Firaha, D. S.; Friedrich, J.; Brehm, M.; Cybik, R.; Wild, M.; Stark, A.; Kirchner, B. *J. Phys. Chem. B* **2013**, *117*, 5898–5907.

[79] Potoff, J. J.; Siepmann, J. I. *AIChE* **2001**, *47*, 1676–1682.

[80] Malberg, F.; Hollóczki, O.; Thomas, M.; Kirchner, B. *Struct. Chem.* **2015**, *26*, 1343–1349.

[81] Weber, H.; Salanne, M.; Kirchner, B. *J. Phys. Chem. C* **2015**, *119*, 25260–25267.

[82] Bhargava, B. L.; Balasubramanian, S. *J. Am. Chem. Soc.* **2006**, *128*, 10073–10078.

[83] Perez-Blanco, M. E.; Maginn, E. J. *J. Phys. Chem. B* **2011**, *115*, 10488–10499.

[84] Zhang, J.; Zhang, S.; Dong, K.; Zhang, Y.; Shen, Y.; Lv, X. *Chem. Eur. J.* **2006**, *12*, 4021–4026.

[85] Goodrich, B. F.; de la Fuente, J. C.; Gurkan, B. E.; Zadigian, D. J.; Price, E. A.; Huang, Y.; Brennecke, J. F. *Ind. Eng. Chem. Res.* **2011**, *50*, 111–118.

Chapter 6B

Molecular Dynamics Investigation of Efficient SO_2 Absorption by Anion-Functionalized Ionic Liquids

Designing novel materials and processes for the efficient removal and possible recovery of SO_2 is of paramount importance. It was observed (in Chapter 6A) that SO_2 has an optimistic solubility in conventional ILs through physical interactions, [1–3] and the anion plays a crucial role in SO_2 capture. [4, 5] Therefore, a new strategy was developed to enhance the absorption capacity of SO_2 at low partial pressure by introducing different weak basic anions to form anion-functionalized ILs that absorbs an equimolar amount of SO_2 through chemical absorption. [1, 3, 6–19]

In chemisorption, the electronegative oxygen or nitrogen site in the anion of task-specific ILs possesses very strong interaction (Lewis acid-base type) with the SO_2 molecule. [2, 20, 21] Thus, chemical absorption process always results in a high uptake of SO_2. However, desorption gets difficult due to high enthalpy of absorption, making the regeneration process expensive. [22, 23] To reduce absorption enthalpy, several techniques were developed, such as tuning the basicity [24] and introduction of an electron-withdrawing group on the anion. [25–27] However, these approaches most often result in reduced absorption capacity, due to diminished interaction strength between the gas and the IL.

Recently, Wang *et al.* demonstrated a new strategy for efficient absorption followed by easy desorption of SO_2 by introducing an electron withdrawing site on the anion in anion-functionalized ILs. [16, 21, 22, 28–34] The motivation behind this strategy was three-fold: a) increase in the SO_2 absorption capacity, b) reducing the absorption enthalpy for easy desorption and c) efficient capture of SO_2 at very low concentration (about 2000 ppm). The electron-withdrawing group diminishes the absorption enthalpy which in turn improves the desorption and subsequently, it acts as an added interaction site that increases

the absorption capacity. These ILs exhibited very high absorption capacity, ~ 4.5 mol SO_2 per mole of IL through multiple-site interactions.

Molecular simulations have been critical to address the microscopic picture behind gas absorption in ILs. [35–49] Discerning the mechanism of multiple-site interactions between the anion and SO_2, which results in a dramatic increase in absorption capacity with low absorption enthalpies is of extreme importance. In this spirit, the present Chapter is devoted to understand the microscopic interactions and consequent effect of SO_2 capture by six anion-functionalized ILs using MD simulations and quantum chemical calculations.

6B.1 Computational Details

Task-specific ILs consisting of various functionalized anions were employed in this Chapter. Experiments on SO_2 solubility in ILs have been carried out with $[P(C_6H_{13})_3C_{14}H_{29}]^+$ as the cation. [29, 31, 32] In order to reduce computational cost, the present Chapter utilizes $[P(C_2H_5)_3CH_3]^+$ or $[P_{2221}]^+$ as the common cation in combination with anions such as, $[4-BrC_6H_4O]^-$, $[4-BrC_6H_4COO]^-$, $[4-CNC_6H_4O]^-$, $[4-CNC_6H_4COO]^-$, $[Tetz]^-$, and $[N(CN)_2]^-$. These are displayed in Figure 6B.1. Wang *et al.* reported the solubility of SO_2 in $[P(C_6H_{13})_3C_{14}H_{29}]^+$ based functionalized ILs to be in the order $[BrPhCOO]^- > [CNPhCOO]^- > [Tetz]^- > [CNPhO]^- > [BrPhO]^- > [DCA]^-$. [29, 31, 32]

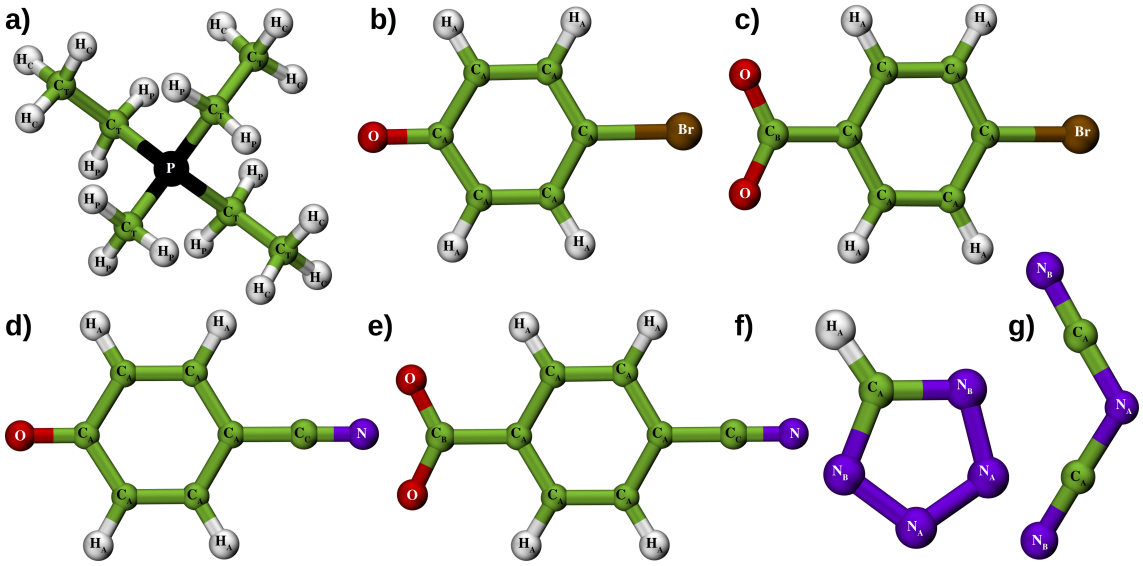

Figure 6B.1: Molecular structure of (a) $[P_{2221}]^+$, (b) $[BrPhO]^-$, (c) $[BrPhCOO]^-$, (d) $[CNPhO]^-$, (e) $[CNPhCOO]^-$, (f) $[Tetz]^-$, and (g) $[DCA]^-$ used in simulations. Color scheme: phosphorus, black; carbon, green; hydrogen, white; oxygen, red; nitrogen, blue; bromine, ochure.

Quantum Chemical Calculations: DFT calculations are performed with Gaussian 09 program [50] at M06/aug-cc-pVDZ level of theory. Geometry optimization of isolated IL

ion pair, SO_2 molecule, and SO_2-IL complex (one SO_2 molecule and one IL ion pair) were carried out. GaussView software [51] was utilized to construct the initial configurations, wherein SO_2 molecule was placed at different locations around the IL ion pair such as phenolate oxygen, carboxylate oxygen, bromine, cyano group, N_A, N_B, H_A, etc. Frequency analysis confirmed the minimum energy configuration. Binding energy (BE) was computed as

$$BE = E_{SO_2-IL} - (E_{IL} + E_{SO_2}) + E_{BSSE} \tag{6B.1}$$

where E_{SO_2-IL}, E_{IL}, E_{SO_2}, and E_{BSSE} represent the energy of SO_2-IL complex, IL ion pair, SO_2, and the counterpoise correction for basis set superposition error (BSSE), [52] respectively.

Further, to gain better insight on the contributions to the interaction energy of the SO_2-IL complexes, we performed Symmetry Adapted Perturbation Theory (SAPT) calculations [53] using PSI4 software. [54] Minimum energy configurations at M06/aug-cc-pVDZ level were exploited in the SAPT2 [55] calculations.

Classical Simulations: MD simulations were performed with the LAMMPS program. [56] Force field parameters for $[P_{2221}]^+$ cation were adopted from the work of Wang *et al.* [57] while, anions were modeled using the all-atom TraPPE parameters. [58, 59] Atomic site charges for these functionalized ILs were obtained following the protocol described in Chapter 6A. The fully flexible SO_2 molecule was modeled with parameters previously used in simulation of neat SO_2 and of SO_2 in ILs. [60, 61] Other details of the calculations are the same as those discussed in Chapter 6A. Additionally, simulations were performed for systems such as $[P(C_6H_{13})_3C_{14}H_{29}]$[BrPhO] and $[P(C_6H_{13})_3C_{14}H_{29}]$[BrPhCOO] to validate the force field. The density of these two IL (as the experimental density values for other ILs are not available) computed at 298 K are compared with the experimental values [29] in Table 6B.1. A satisfactory agreement between experimental and simulated data is observed with a maximum deviation of 1.01%.

Table 6B.1: Density (ρ) of ionic liquids (g/cm^3) obtained from MD simulations at 298 K and 1 atm, compared against experiment. [29] $\Delta\rho = (\rho^{Sim} - \rho^{Exp})/\rho^{Exp}$.

System	ρ^{Exp}	ρ^{Sim}	$\Delta\rho(\%)$
[P66614][BrPhO]	0.993	0.983	-1.01
[P66614][BrPhCOO]	1.021	1.008	-1.27

Experimental measurements suggest that the solubility of SO_2 in these ILs is higher than one mol per mol of IL. [29, 31, 32] Thus, in the case of bulk simulations, 256 cations,

256 anions and 256 SO_2 molecules were placed in a cubic box to attain equimolar concentration. The starting configurations were generated with the program Packmol. [62] For all the mixtures considered, starting configurations were subjected to energy minimization followed by 10 ns equilibration in the isothermal-isobaric (NPT) ensemble at 1 atm and 298 K. Temperature and pressure were maintained via Nosé-Hoover thermostat and barostat. [63, 64] Subsequently, all the systems were equilibrated in NVT ensemble for 5 ns, followed by a 40 ns production run in the NVT ensemble. The box lengths for pure IL and SO_2-IL mixtures are provided in Table 6B.2.

Table 6B.2: Simulation box length of pure IL and equimolar SO_2-IL mixtures in bulk, at 298 K.

System	Box Length (Å)	
	Pure IL	SO_2-IL
$[P_{2221}][BrPhO]$	46.52	49.02
$[P_{2221}][BrPhCOO]$	47.76	50.12
$[P_{2221}][CNPhO]$	46.72	49.40
$[P_{2221}][CNPhCOO]$	47.66	49.94
$[P_{2221}][Tetz]$	43.08	46.16
$[P_{2221}][DCA]$	43.82	46.65

Free Energy Calculations: Free energy (FE) profiles were obtained using the "colvars" module [65] as implemented in LAMMPS. [56] Adaptive Biasing Force (ABF) [66] method was employed to determine the FE profiles. Other details of the free energy calculations are the same as those discussed in Chapter 6A. The RC spanned from 0 Å (center of IL box) to 60 Å and was divided into four nonoverlapping windows. The colvar style of "distanceZ" was used to determine the free energy profiles. ABF forces were applied every 500 steps with a bin width of 0.1 Å.

6B.2 Results and Discussion

6B.2.1 Quantum Chemical Analysis

An investigation of various intermolecular interactions between the gas and the ILs can be utilized to understand SO_2 uptake in these ILs. Figure 6B.2 displays the minimum energy structures of the SO_2-IL complexes. The molecular structure of SO_2 was seen not to be perturbed by its interactions with IL ions.

Ion pair-SO_2 structure: The interaction of SO_2 with these functionalized ILs can be broadly classified into two categories: a) strong Lewis acid-base interaction with the anion,

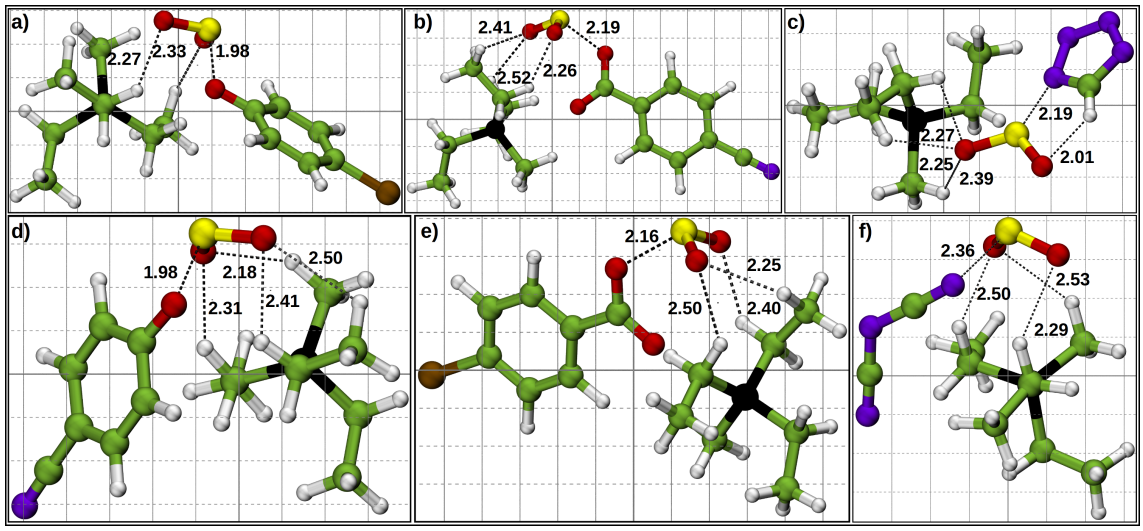

Figure 6B.2: Minimum energy structures of the complexes of SO_2 with (a) $[P_{2221}][BrPhO]$, (b) $[P_{2221}][CNPhCOO]$, (c) $[P_{2221}][Tetz]$, (d) $[P_{2221}][CNPhO]$, (e) $[P_{2221}][BrPhCOO]$, and (f) $[P_{2221}][DCA]$. Dotted lines are interatomic distances in Å.

where the most electron rich sites on anion (either oxygen or nitrogen) share their electron density with the sulfur atom in SO_2 and b) weak hydrogen bond interactions with various C-H hydrogens in the cation. Anions with high basicity, such as $[BrPhO]^-$ and $[CNPhO]^-$, interact strongly with SO_2, as is evident from the shortest S–O (anion) distance (1.98 Å) in the respective SO_2-IL complexes (see Figure 6B.2). Less basic anions, e.g. $[BrPhCOO]^-$ and $[CNPhCOO]^-$ are slightly farther away from sulfur (2.16 Å and 2.19 Å, respectively). However, in the case of $[Tetz]^-$, the gas molecule not only interacts with the electron rich nitrogen center (S–N_B distance; 2.19 Å) in the anion, but also possesses a strong hydrogen bond with anion H_A atom (O–H_A distance; 2.01 Å). On the other hand, $[DCA]^-$, the least basic among these anions, interacts with the gas molecule from the farthest distance (S–N_B distance; 2.36 Å). In each of these SO_2-IL complexes, the oxygen atom of SO_2 was involved in hydrogen bond interaction with cation hydrogen atoms e.g., H_P or H_C, irrespective of the basicity of the anions. This reflects the role of cations in SO_2 dissolution in these functionalized ILs.

Interaction energy: The computed binding energies (BE) at M06/aug-cc-pVDZ level of theory for SO_2-IL complexes were evaluated to reaffirm the order of the strength of SO_2 interaction with ILs. These energies are tabulated in Table 6B.3. Among all the ILs, $[P_{2221}][BrPhO]$ exhibits the highest affinity in binding to SO_2, followed by $[P_{2221}][CNPhO]$ and $[P_{2221}][Tetz]$. The highly basic nature of the phenoxide anions allows them to form stronger SO_2-IL complex that results in a large value of absorption enthalpy, whereas in $[P_{2221}][Tetz]$, the presence of both Lewis acid-base interaction and strong hydrogen bond

Table 6B.3: Binding energies (BE, kcal/mol) at M06/aug-cc-pVDZ level of theory and energy decomposition of the interaction energy (kcal/mol) in SAPT2/aug-cc-pVDZ level of theory of SO_2-IL complexes.

SO_2-IL complex	BE	E_{SAPT2}	E_{elst}	E_{exch}	E_{ind}	E_{disp}
$[P_{2221}]$[BrPhO]	-54.18	-58.54	-137.81	216.27	-105.12	-31.88
$[P_{2221}]$[BrPhCOO]	-41.75	-43.81	-100.47	153.61	-67.20	-29.75
$[P_{2221}]$[CNPhO]	-50.03	-52.39	-111.46	172.88	-86.70	-27.11
$[P_{2221}]$[CNPhCOO]	-38.62	-40.34	-82.19	119.77	-52.55	-25.37
$[P_{2221}]$[Tetz]	-48.27	-50.62	-118.06	187.75	-89.21	-31.10
$[P_{2221}]$[DCA]	-29.88	-31.92	-61.77	93.76	-39.73	-24.18
$[P_{2221}]$[PhO]	-65.89	—	—	—	—	—
$[P_{2221}]$[PhCOO]	-47.48	—	—	—	—	—

with anion contribute to the higher binding energy. Due to the more electron withdrawing nature of cyano group than bromine, the electron density at phenoxide oxygen atom is less in the presence of the former group and thus, resulting in higher BE for SO_2-$[P_{2221}]$[BrPhO] complex. Moreover, the lower basicity of benzoate anions and $[DCA]^-$ manifested in their lower BE values for SO_2-IL complex.

In phenoxide and benzoate anions, minimum energy configuration was the one where SO_2 molecule interacts with the anion oxygen atom (see Figure 6B.2). In principle, the SO_2 molecule can also interact with either the bromine or cyano group in these anions. The optimized geometry obtained when the SO_2 molecule was kept near those groups was found to be 3-4 kcal/mol less stable than the minimum energy configuration. For the sake of comparison, we have also computed the binding energy of SO_2-$[P_{2221}]$[PhO] and SO_2-$[P_{2221}]$[PhCOO] complexes at the same level of theory. It is evident from Table 6B.3, that in the absence of any functionalization at para position, both phenoxide and benzoate anions exhibit much stronger interaction with the solute SO_2 molecule. However, both bromine and cyano group reduce the binding energy by a significant amount. Thus, on the one hand, these electron withdrawing groups act as an additional site for SO_2 binding (which increases the SO_2 absorption capacity), while on the other hand, they result in lower interaction energy i.e. diminished absorption enthalpy.

Energy decomposition analysis: In order to discern the nature of interaction of SO_2 with the ILs, the total interaction energy for each of these SO_2-IL complex was decomposed into individual contributions and these are summarized in Table 6B.3. Dispersion (E_{disp}) contributes more than 50% towards the total interaction energy. Contribution from the electrostatic energy (E_{elst}) is significant in the complexes with highly basic anions, while

dispersion energy (E_{disp}) contributes maximum (75%) in complex with weak basic $[DCA]^-$ anion. Thus, dispersion forces are of immense importance for the efficient absorption of SO_2 in these ILs.

6B.2.2 Liquid Structure

The influence of SO_2 on the bulk liquid structure was elucidated by the structural correlations between cations and anions computed from the trajectories obtained from the MD simulations of pure IL and SO_2-IL mixtures. The radial distribution functions (RDFs) between cation-anion, H_P–anion, and H_C–anion in the pure IL and SO_2 loaded ILs are displayed in Figure 6B.3. It is evident that the structure of these ILs remain unaltered even in the presence of solute. [42, 43]

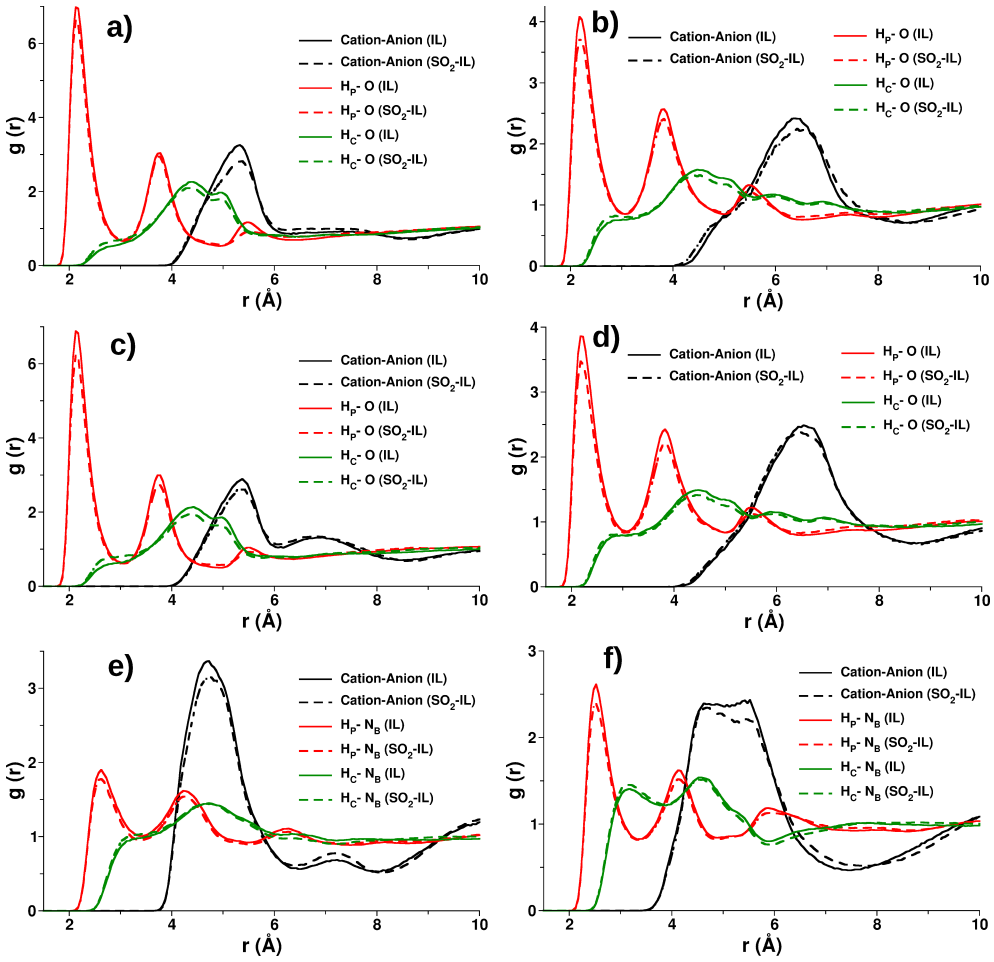

Figure 6B.3: Radial distribution functions in pure IL and SO_2-IL mixtures; a) $[P_{2221}][BrPhO]$, b) $[P_{2221}][BrPhCOO]$, c) $[P_{2221}][CNPhO]$, d) $[P_{2221}][CNPhCOO]$, e) $[P_{2221}][Tetz]$, and f) $[P_{2221}][DCA]$.

Several experiments [29, 31, 32, 67] and molecular simulation [4, 5] studies have shown that the nature of anions has a profound effect on the interaction between SO_2 and ILs.

Figure 6B.4 shows the RDFs between the center of mass (COM) of the ions and that of SO_2. As shown in Figure 6B.4b, SO_2 is predominantly located near the anion as evidenced by the short peak around 3.8 Å, followed by small hump around $\sim$ 5.1 Å in $[P_{2221}]$[DCA] system. Similarly, we can see a clear shoulder at 3.7 Å, which is followed by a sharp peak near 4.1 Å in $[P_{2221}]$[Tetz]. However, in the case of phenoxide and benzoate based anions, the first peak in SO_2–anion $g(r)$ is present at a slightly large distance (due to their bigger size). These RDFs also exhibit a hump at small distances (3.5 Å). Thus, it is evident that SO_2 interacts with multiple sites of the anions in these SO_2-IL complexes. To dissect this aspect further, we have examined various site-site RDFs.

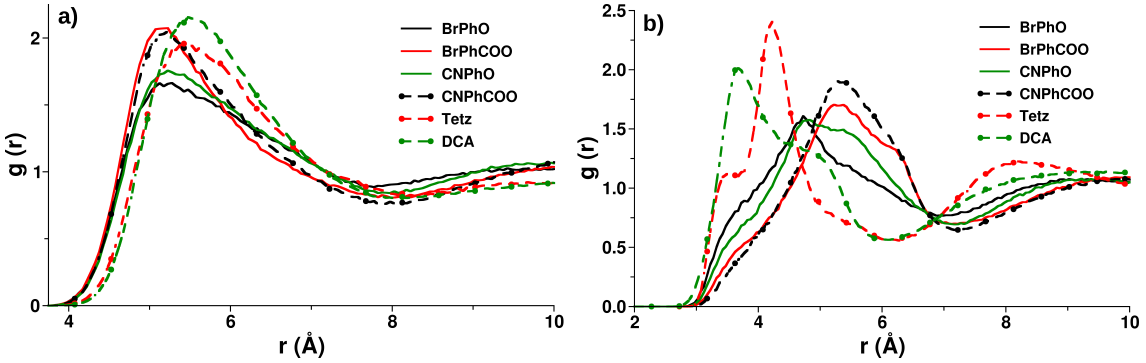

Figure 6B.4: Radial distribution functions between a) center of mass (SO_2) - center of mass (cation) and b) center of mass (SO_2) - center of mass (anion) in SO_2-IL mixtures.

Figure 6B.5 displays RDFs between the sulfur atom of SO_2 and two electron rich centers in the anion, such as O and N/Br site in phenoxide and benzoate anions; and N_A and N_B sites in $[Tetz]^-$ and $[DCA]^-$ (see Figure 6B.1). Electron rich oxygen centers in phenoxide and benzoate anion (higher basicity) interact strongly with SO_2 at shorter distances than the relatively less electron rich nitrogen sites present in either $[Tetz]^-$ or $[DCA]^-$ anion (lower basicity) (see Figure 6B.5a). The coordination numbers (integrated $g(r)$ up to first solvation shell) suggest that SO_2 is surrounded by more number of oxygen atoms in benzoate anions (2.3) than in phenoxide anions (0.70), whereas more number of N_B atoms are observed around SO_2 in $[P_{2221}]$[DCA] (3.9) than in $[P_{2221}]$[Tetz](3.5). On the other hand, the cyano group exhibits stronger interaction with the solute SO_2 than bromine, as is evident from Figure 6B.5b. Phenoxide anion is more basic than benzoate and cyano group has more electron withdrawing capability than bromine; thus, the electron density at para substituted group in $[CNPhO]^-$ is maximum, followed by $[CNPhCOO]^-$, $[BrPhO]^-$, and $[BrPhCOO]^-$. A similar order is observed in the first peak position in RDFs of these groups with SO_2 and their corresponding coordination numbers. Moreover, the N_A sites in $[Tetz]^-$ and $[DCA]^-$ also possess significant interaction with SO_2, as can be seen from peaks present between 3–3.5 Å distance, although the coordination numbers suggest SO_2

is surrounded by very few N_A atoms. Thus, SO_2 prefers to bind more towards the more electron rich oxygen centers in phenoxide and benzoate anions and N_B sites in $[Tetz]^-$ and $[DCA]^-$, consistent with the preference seen in gas-phase quantum chemical calculations.

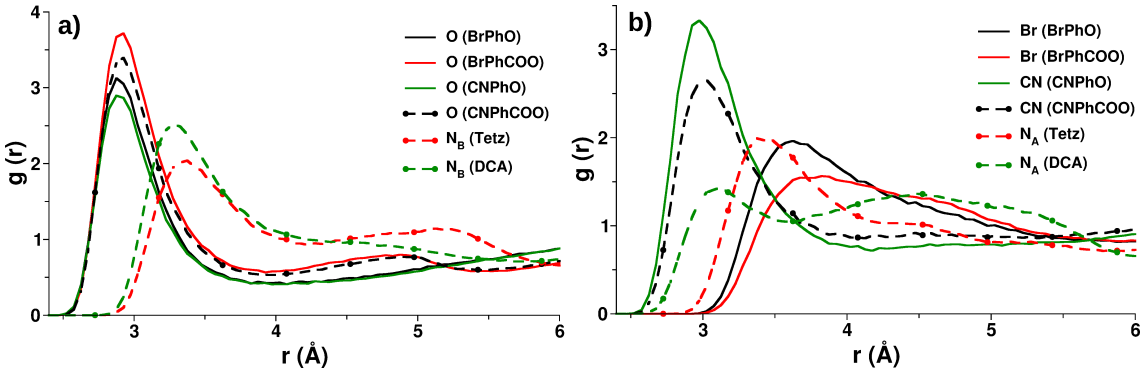

Figure 6B.5: Radial distribution functions between various sites in anion and SO_2 in SO_2-IL mixtures. $[P_{2221}]^+$ is the common cation.

Further, we have examined RDFs between various hydrogen atoms on cation and anion with SO_2 oxygens to demonstrate the contribution of specific interactions in SO_2 dissolution and these are presented in Figure 6B.6 and Figure 6B.7. The H_C atoms on the cation exhibit

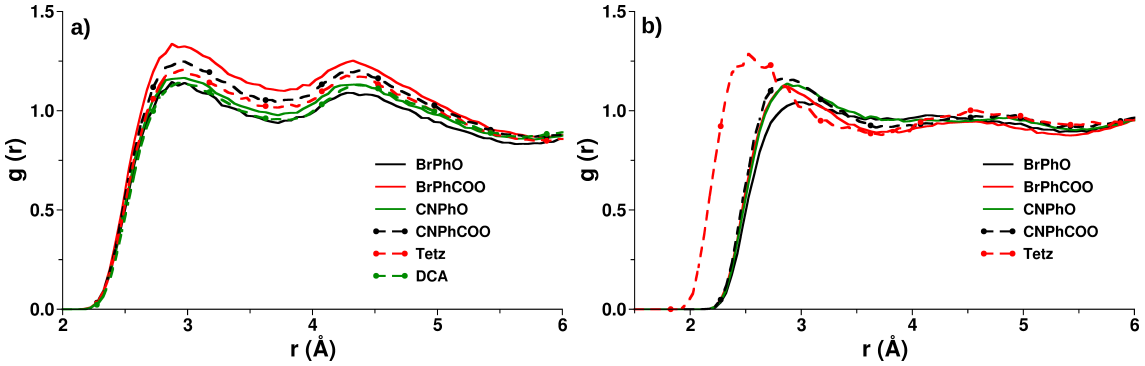

Figure 6B.6: Radial distribution functions between (a) $O(SO_2)$-H_C and (b) $O(SO_2)$-H_A in SO_2-IL mixtures. $[P_{2221}]^+$ is the common cation.

stronger interaction with SO_2 than H_P atoms as is evident from well defined and sharp peak around 2.8 Å, Figure 6B.6a. Moreover, the first peak height in SO_2-H_P $g(r)$ (2.7 Å, see Figure 6B.7a) is lower than that of SO_2-H_C $g(r)$. The coordination numbers indicate that SO_2 is surrounded by more number of H_C atoms (1.6) than H_P atoms (0.95). Thus, SO_2 interacts with the alkyl H_C atoms of the cation and consequently, it highlights the importance of dispersion forces in SO_2 solubility in these ILs as seen in SAPT calculations and previous studies. [43] Figure 6B.6b presents the RDFs between anion hydrogen atoms (H_A) and SO_2 oxygen atoms. Similar to H_C atoms, H_A sites also possess a strong interaction

with SO_2, indicated by the well defined peak around 2.85 Å in phenoxide and benzoate based ILs. Interestingly, a very strong interaction at much shorter distance (2.4 Å) is observed between H_A and SO_2 in $[P_{2221}]$[Tetz], which was also seen in the gas phase DFT calculations (O(SO_2)-H_A distance, 2.0 Å). H_A atom in $[Tetz]^-$ is covalently bonded to a carbon atom which sits in between two electronegative nitrogen atoms. Thus, the acidic nature of the H_A atom is more in $[Tetz]^-$ than in phenoxide or benzoate anions. As a result, among all the anions studied here, SO_2 exhibits stronger hydrogen bond interaction with $[Tetz]^-$. In summary, the multiple-site interactions between the anion and SO_2 explain the extremely high SO_2 absorption capacity in these anion-functionalized ILs.

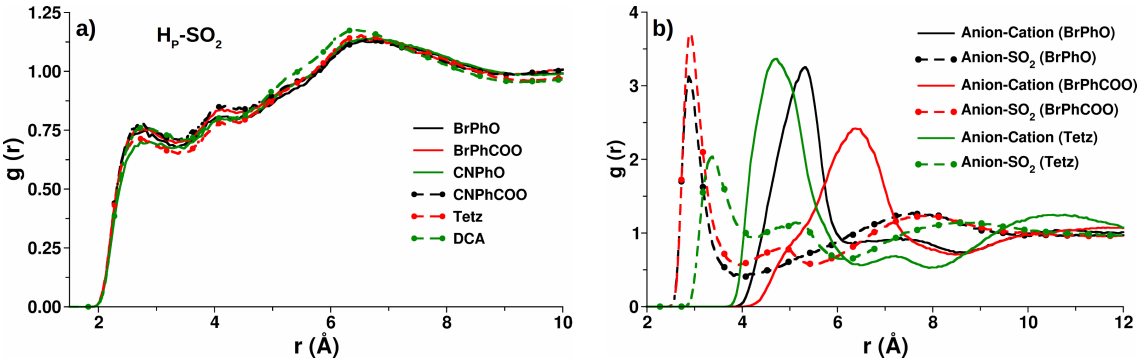

Figure 6B.7: Radial distribution functions in SO_2-IL mixtures. $[P_{2221}]^+$ is the common cation.

Furthermore, these structural correlations were validated by computing spatial distribution functions (SDFs) in SO_2 loaded ILs. The SDFs calculated for the anion and SO_2 around the center of mass (COM) of the $[P_{2221}]^+$ cation are shown in Figure 6B.8. The density map of anions around the COM of cation shows that anions tend to bind to the H_P hydrogen atoms located on the first carbon in alkyl chain rather than to H_C sites. A similar preference for H_P atoms over H_C atoms was also observed in their respective RDFs (see Figure 6B.3). Moreover, the distribution of SO_2 around cation shows that the density map to be more condensed over the H_C atoms with some scattered density around H_P sites too. These observations are agreement with RDF analysis and gas phase DFT calculations.

Figure 6B.9 displays the computed SDFs of the cation and SO_2 molecule around the center of mass of the anion, at an isosurface value of 0.006 $Å^{-3}$. It is evident that SO_2 is closer to the anion than to the cation, an observation which is consistent with the RDFs as well (see Figure 6B.7b). SO_2 shows stronger binding preference towards the more electron rich centers in the anion, e.g. oxygens in phenoxide or benzoate anions and nitrogens in others. Besides this, significant interactions are observed between SO_2 and other additional sites in the anion such as bromine, cyano group, and H_A atoms. The strength of this additional interaction can be rationalized in terms of available electron

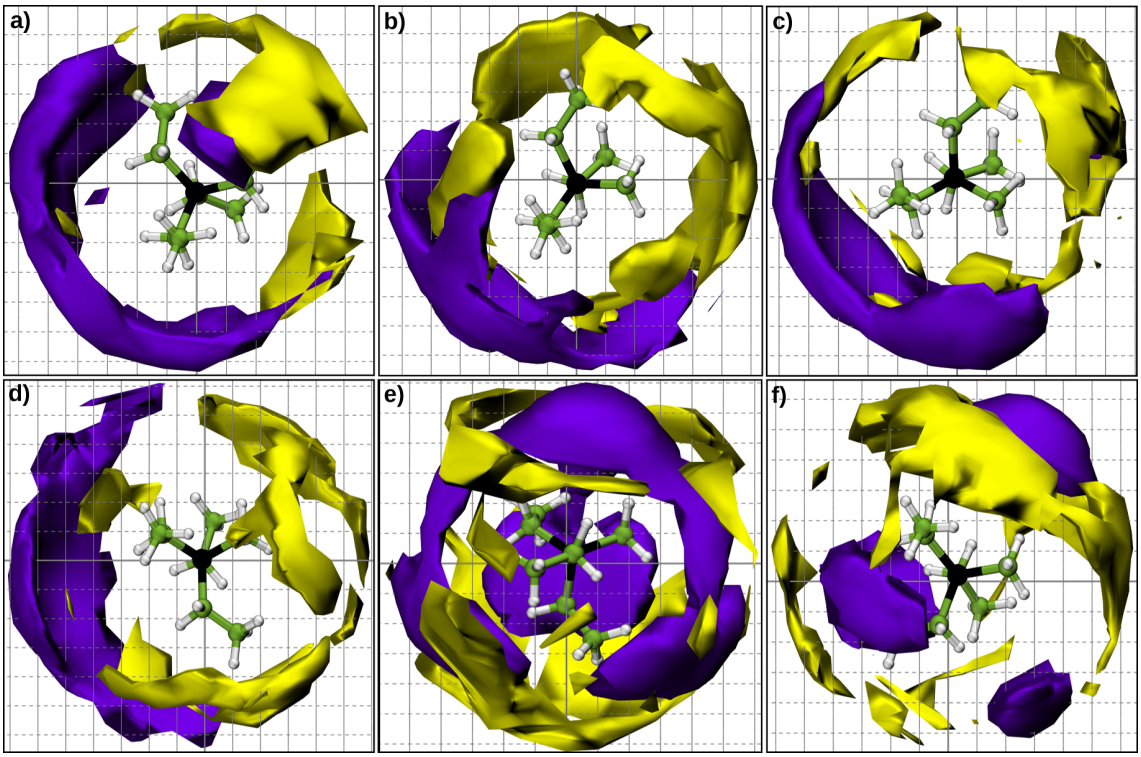

Figure 6B.8: Spatial density map of anion (purple) and SO_2 (yellow) around the center of mass of the cation for (a) $[BrPhO]^-$, (b) $[BrPhCOO]^-$, (c) $[CNPhO]^-$, (d) $[CNPhCOO]^-$, (e) $[Tetz]^-$, and (f) $[DCA]^-$. Isosurface density: 0.006 $Å^{-3}$. Color scheme: black, phosphorus; green, carbon; white, hydrogen.

density at those additional sites. In this regard, phenoxide group is more basic in nature than the benzoate group; and while bromine is a moderate electron withdrawing group, cyano group exhibits a strong electron withdrawing nature. Thus, electron density at the para substituted group can be ordered as, $[P_{2221}][CNPhO]$, $[P_{2221}][CNPhCOO]$, $[P_{2221}][BrPhO]$ and $[P_{2221}][BrPhCOO]$. As a consequence, SO_2 binds more strongly to the cyano group in $[P_{2221}][CNPhO]$ or $[P_{2221}][CNPhCOO]$, than to the bromine sites in $[P_{2221}][BrPhO]$ or $[P_{2221}][BrPhCOO]$, as evident from a more condensed density of SO_2 near the cyano group. Also, SO_2 density was found near the H_A atoms, indicating a binding preference for SO_2 with this site. Especially, in $[P_{2221}][Tetz]$, the density map of SO_2 is highly condensed around H_A atom. These observations further substantiate the conclusions drawn from RDF analysis and gas phase quantum chemical calculations and demonstrate the importance of multiple site interactions in the high uptake of SO_2 in these task-specific ILs.

Combined distribution functions (CDFs) were computed to demonstrate the arrangement of cations and SO_2 around the anion ring plane and the same are shown for $[P_{2221}][CNPhO]$ and $[P_{2221}][Tetz]$ in Figure 6B.10 and Figure 6B.11, respectively. As discussed earlier, H_P atom exhibits predominant interaction with anion while SO_2 prefers to bind near the H_C

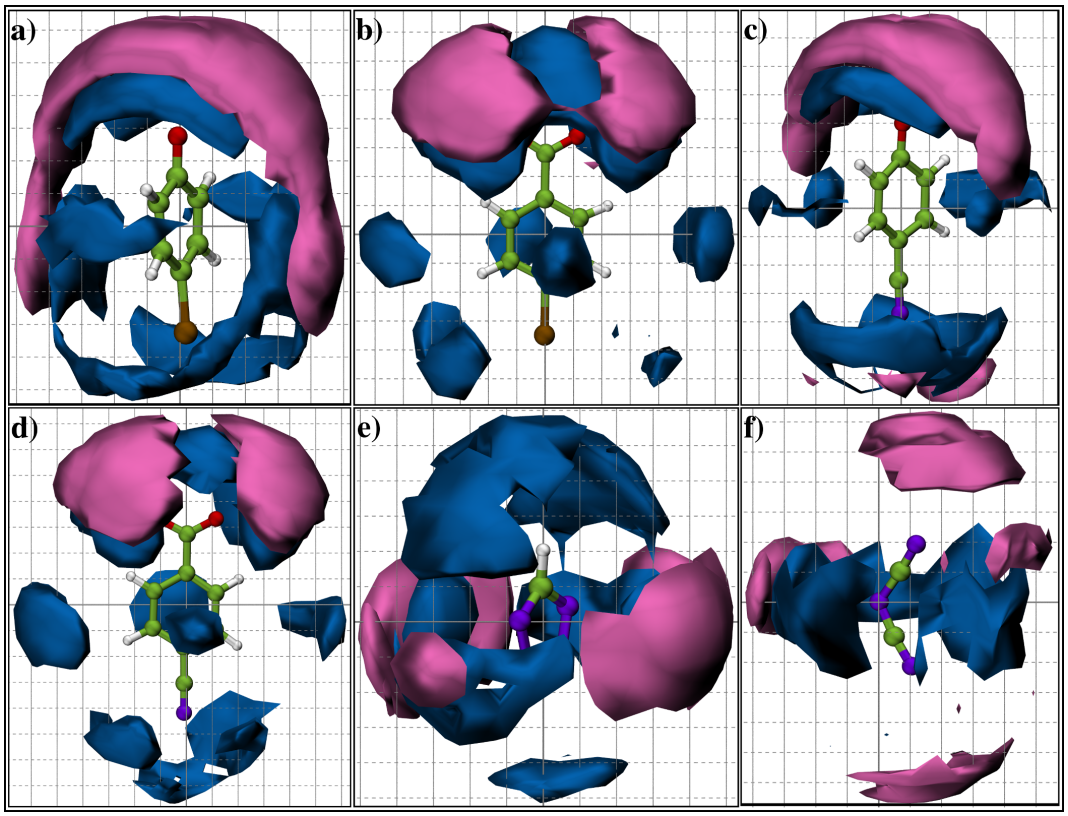

Figure 6B.9: Spatial density map of cation (pink) and SO_2 (blue) around the center of mass of the anion for (a) $[BrPhO]^-$, (b) $[BrPhCOO]^-$, (c) $[CNPhO]^-$, (d) $[CNPhCOO]^-$, (e) $[Tetz]^-$, and (f) $[DCA]^-$. Isosurface density: 0.006 $Å^{-3}$. Color scheme: green, carbon; white, hydrogen; red, oxygen; violet, nitrogen; ochure, bromine.

atom. Figure 6B.10a and Figure 6B.11a shows the strong interaction of anion with the H_P site, while preferable interaction of SO_2 with the H_C atoms is evident from Figure 6B.10c and Figure 6B.11c, in these ILs. The CDF (Figure 6B.10b) exhibits that $[P_{2221}]^+$ cation prefers an in-plane arrangement with the anion ring rather than a on-top arrangement in $[P_{2221}][CNPhO]$ (similar orientation was also observed for other phenoxide- and benzoate-based ILs). However, in $[P_{2221}][Tetz]$, the cation is observed to be both at in-plane and on-top arrangements (Figure 6B.11b). This observation can be understood in terms of cation's preference to bind at electronegative oxygen sites in phenoxide- and benzoate-based ILs. However, the orientation of SO_2 molecule around the anion ring plane is independent of the anion, as the SO_2 molecule is seen at both on-top and in-plane locations (Figure 6B.10d and Figure 6B.11d). These observations further validate the multiple-site interactions of SO_2 with anions which was also seen in RDF and SDF analyses.

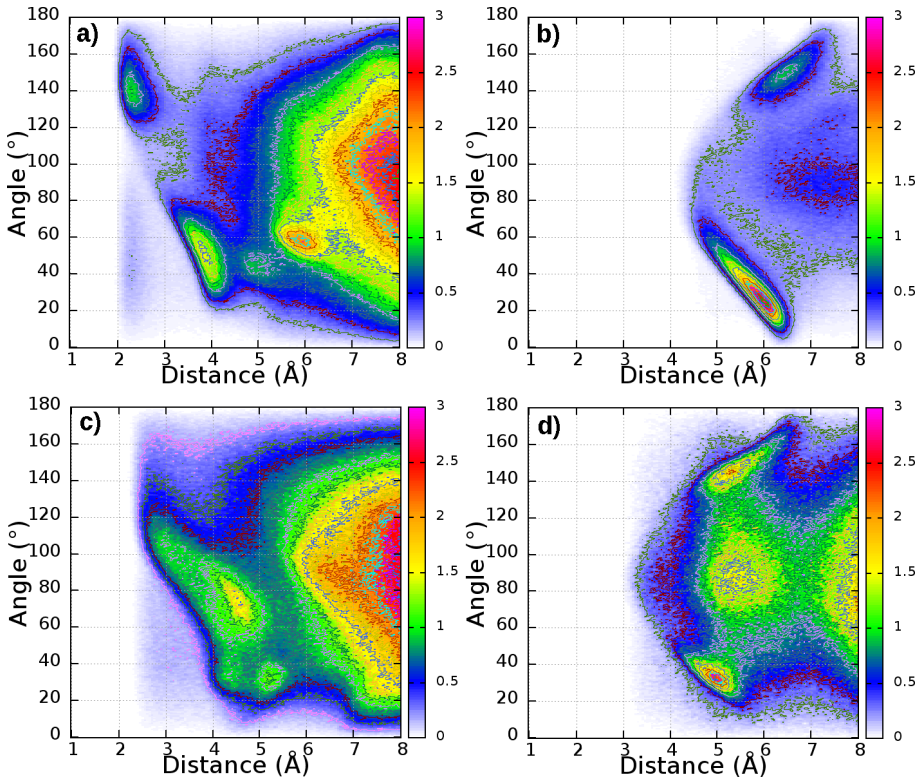

Figure 6B.10: Combined distribution functions depicting the in-plane and on-top distribution with relative intensity color coding. The distance is (a) H_P-anion, (b) CoR-CoM (cation), (c) H_C-SO_2, and (d) CoR-CoM (SO_2). The angle is (a) C_T-H_P-anion, (b) CoR-C_A-CoM (cation), (c) C_T-H_C-SO_2, and (d) CoR-C_A-CoM (SO_2). CoR indicates the center of the benzene ring and CoM center of mass of either cation or SO_2. The anion is $[CNPhO]^-$.

6B.2.3 Solvation Free Energy

The structural correlations observed in SO_2 loaded ILs have shown strong anion-SO_2 binding through multiple-site interactions. Thus, it is time to address the question of relative solubility of SO_2 in different anion-functionalized ILs. The free energy profiles for bringing one SO_2 molecule from its vapor phase into the bulk IL have been determined. Figure 6B.12a displays the same for SO_2 solvation in various ILs containing $[P_{2221}]^+$ as the common cation but different anions. In an IL, the solvation free energy is the difference in free energies between the gas phase and the solvated state of SO_2. Moving in from the vapor phase, the SFE profiles become nonzero at around 52 Å in most ILs. However, in the case of $[P_{2221}][BrPhO]$, due to its smaller width of density profile at the liquid-vapor interface (see Figure 6B.12b), such changes occur at 48 Å. The potential of mean force (PMF) attains a minimum around the interface and later starts to increase towards the bulk region. After crossing a barrier, it eventually converges to a constant value. Dang *et al.* observed similar features in the PMF profile for CO_2 molecules across the air-IL interface. [45, 68, 69] In all the systems studied here, the PMF is most negative at the vapor-IL interface; thus, at

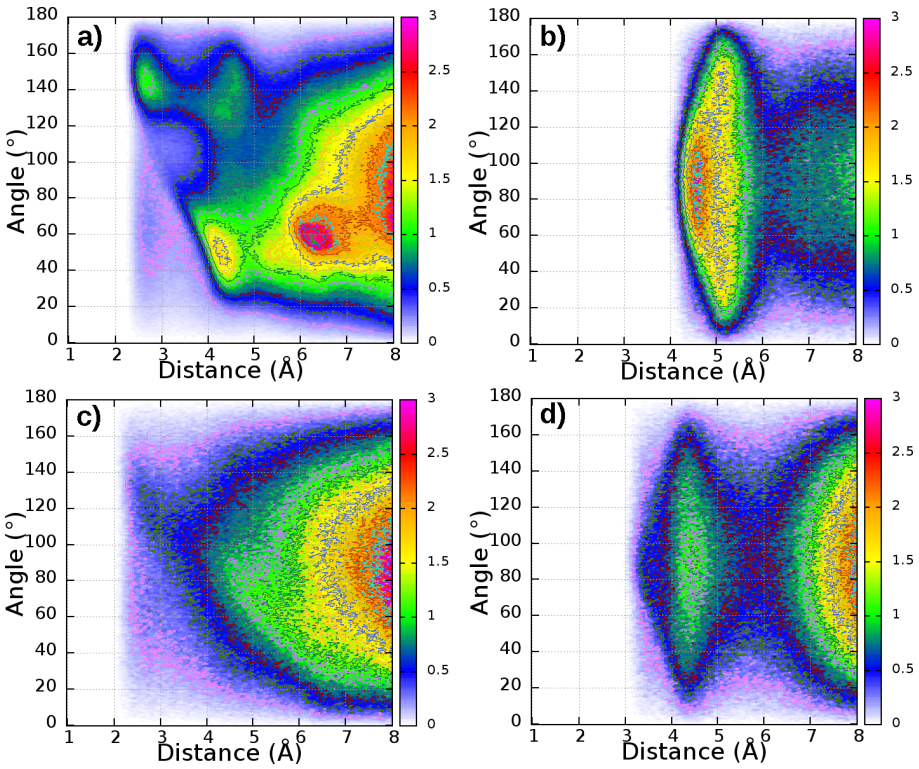

Figure 6B.11: Combined distribution functions depicting the in-plane and on-top distribution with relative intensity color coding. The distance is (a) H_P-anion, (b) CoR-CoM (cation), (c) H_C-SO_2, and (d) CoR-CoM (SO_2). The angle is (a) C_T-H_P-anion, (b) CoR-C_A-CoM (cation), (c) C_T-H_C-SO_2, and (d) CoR-C_A-CoM (SO_2). CoR indicates the center of the triazole ring and CoM center of mass of either cation or SO_2. The anion is $[Tetz]^-$.

low concentrations, SO_2 prefers to be located at the interface than elsewhere. A similar phenomenon has been reported for CO_2 by Perez-Blanco and Maginn. [70] The behavior of PMF across the air-IL interface has been compared with the number density profile of various sites on cation and anion in Figure 6B.13a. The preferred interaction of SO_2 with H_C and H_P atoms of the cation is confirmed by the occurrence of the minimum in SO_2 PMF and maximum in C_T number density at the interface.

The decomposition of solvation free energy into its enthalpic and entropic contributions is crucial to interpret its anion dependence. Towards this purpose, we have performed two addition simulations and details of such calculations are described in Chapter 6A. The entropy change due to solvation is moderate compared to the change in energy in these ILs (see Table 6B.4). However, in ILs such as $[P_{2221}]$[BrPhCOO] and $[P_{2221}]$[CNPhCOO], the relative entropic contribution is slightly lower than in rest of the ILs; as a result, the net solvation free energy is little high.

Further, Figure 6B.13b displays the correlation between the computed SFE using

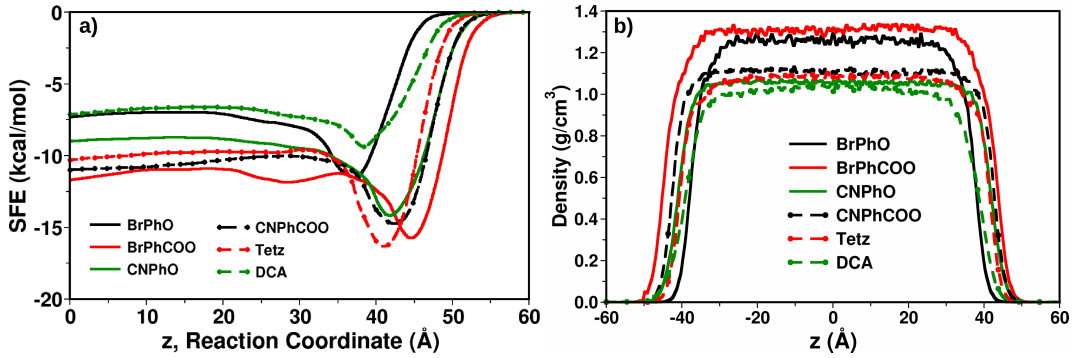

Figure 6B.12: (a) Solvation free energy profile of SO_2 in various IL ($[P_{2221}]^+$ as common cation). z= 0 is the center of mass of IL (bulk) and $z > 45$ is SO_2 in vapor phase. (b) Mass density profile for various ionic liquids from the liquid-vapor simulations.

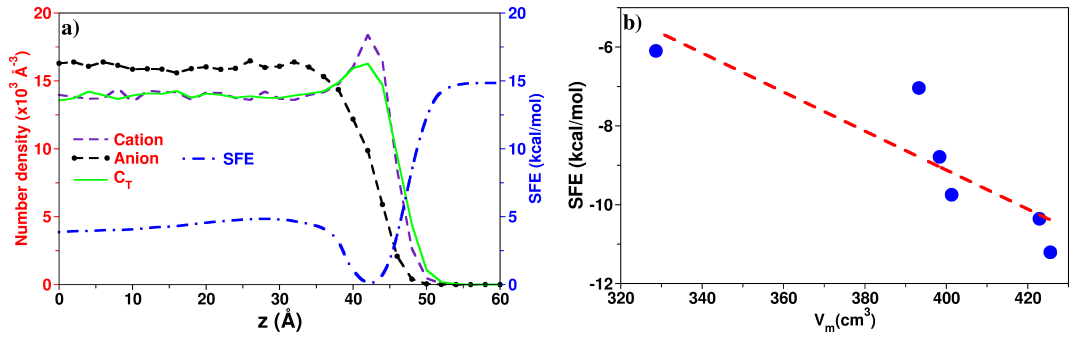

Figure 6B.13: (a) Number density profile of cation center of mass, anion center of mass and C_T atom of cation, compared against SO_2 PMF in $[P_{2221}]$[CNPhCOO]. (b) Molar volume of pure IL versus the solvation free energy (SFE) of SO_2 in bulk IL. Dashed line is best fits to data.

Table 6B.4: Changes in Free Energy ($\Delta G = G_{liq} - G_{gas}$), Enthalpy ($\Delta H = H_{liq} - H_{gas}$), and Entropy ($T\Delta S = S_{liq} - S_{gas}$) for SO_2 Solvation in Various ILs. ΔS is a Derived Quantity from ΔG and ΔU. $[P_{2221}]^+$ is the Cation.

IL	ΔG (kcal/mol)	ΔH (kcal/mol)	$T\Delta S$ (kcal/mol)
$[BrPhO]^-$	-7.04	-45.38	-38.34
$[BrPhCOO]^-$	-11.21	-32.75	-21.54
$[CNPhO]^-$	-8.79	-41.42	-32.63
$[CNPhCOO]^-$	-10.36	-35.16	-34.80
$[Tetz]^-$	-9.75	-46.28	-36.53
$[DCA]^-$	-6.10	-40.16	-34.06
$[PhO]^-$	-6.35	—	—
$[PhCOO]^-$	-9.45	—	—

Table 6B.5: Henry's Law Constant (K_{H}) of SO_2 in Studied ILs at 298 K and P = 1 atm.

IL	$K_{\mathrm{H}} \times 10^3$ (atm)
$[P_{2221}]$[BrPhO]	0.6989
$[P_{2221}]$[BrPhCOO]	0.0006
$[P_{2221}]$[CNPhO]	0.0366
$[P_{2221}]$[CNPhCOO]	0.0024
$[P_{2221}]$[Tetz]	0.0092
$[P_{2221}]$[DCA]	4.1450

empirical force field and the molar volume of the respective ILs. For the sake of completeness, SO_2 solvation free energy has also been calculated in two other ILs, $[P_{2221}]$[PhO] and $[P_{2221}]$[PhCOO] and is tabulated in Table 6B.4. It is evident from Table 6B.4 that an inclusion of additional electronegative site at the para position not only reduces the binding energy (see Table 6B.3) but also increases the net solvation free energy. This observation reaffirms the dual characteristics of the additional electron withdrawing groups (bromine or cyano) in phenolate- and benzoate-based ILs. Among the ILs investigated here, $[P_{2221}]$[BrPhCOO] turned out to be the best solvent for SO_2 dissolution, consistent with experimental results.

Further, Henry's law constant was calculated to obtain a quantitative measure of gas solubility in these ILs. It is defined as,

$$K_{\mathrm{H}} = \frac{RT\rho}{M} exp\left(\frac{\Delta G_{Sol}}{RT}\right) \tag{6B.2}$$

where, ρ and M are the density, and molecular weight of pure IL and ΔG_{Sol} is the free energy change due to solvation. The gas solubility in a liquid at infinite dilution is inversely proportional to the Henry's constant. Table 6B.5 summarizes the computed Henry's law constant of SO_2 in all the IL systems studied here. From Figure 6B.12 and Table 6B.5, it is evident that SO_2 is very much soluble in these anion-functionalized ILs. The calculated K_{H} values demonstrate the following solubility order:

$[BrPhCOO]^- > [CNPhCOO]^- > [Tetz]^- > [CNPhO]^- > [BrPhO]^- > [DCA]^-$

Hence, it is obvious that the obtained solubility order from free energy calculations is in very well agreement with experimentally measured SO_2 absorption capacities in these ILs ($[BrPhCOO]^- > [CNPhCOO]^- > [Tetz]^- > [CNPhO]^- > [BrPhO]^- > [DCA]^-$). [29, 31, 32]

6B.3 Conclusions

In summary, we have provided detailed insights into the SO_2 solubility in anion-functionalized task-specific ILs from *ab initio* calculations and molecular dynamics simulations. Gas phase quantum chemical calculations show that in the presence of electron-withdrawing moiety such as, bromine or cyano group, the negative charge on oxygen atom (in phenoxide or benzoate anion) get dispersed which results in a reduction in the interaction between oxygen atoms and SO_2, and thus, the binding energy (or absorption enthalpy) decreases. Moreover, due to the flow of negative charge from oxygen atoms to these additional sites, the negative charge on cyano nitrogen or bromine atom increases, which leads to enhanced CN/Br$\cdots SO_2$ interaction. In the case of $[Tetz]^-$, besides $\mathrm{N_B}\cdots SO_2$ interaction, oxygen atoms of SO_2 molecule form a strong hydrogen bond with the $\mathrm{H_A}$ site. Thus, an improved absorption capacity at much lower desorption cost is a consequence of the dual role of the added interaction site on the anion.

MD simulations of bulk SO_2-IL mixtures indicated the propensity of both cation and anion to interact with the solute SO_2 molecule. The SO_2 molecule was found to interact with cations via dispersion forces, mainly with $\mathrm{H_C}$ and $\mathrm{H_P}$ hydrogens on the alkyl group. The cyano group exhibited stronger interaction with SO_2 molecule than the bromine site. The PMF profiles for SO_2 solvation obtained from ABF calculations manifested the air-IL interface to be a preferable location for the solute SO_2 molecule. The experimentally determined solubility of SO_2 in ILs varies as $[BrPhCOO]^- > [CNPhCOO]^- > [Tetz]^- > [CNPhO]^- > [BrPhO]^- > [DCA]^-$. [29, 31, 32] SFE values computed in this work are consistent with the experimental observations.

Bibliography

[1] Huang, J.; Riisager, A.; Wasserscheid, P.; Fehrmann, R. *Chem. Commun.* **2006**, *38*, 4027–4029.

[2] Hong, S. Y.; Im, J.; Palgunadi, J.; Lee, S. D.; Lee, J. S.; Kim, H. S.; Cheong, M.; Jung, K.-D. *Energy Environ. Sci.* **2011**, *4*, 1802–1806.

[3] Anderson, J. L.; Dixon, J. K.; Maginn, E. J.; Brennecke, J. F. *J. Phys. Chem. B* **2006**, *110*, 15059–15062.

[4] Prasad, B. R.; Senapati, S. *J. Phys. Chem. B* **2009**, *113*, 4739–4743.

[5] Garcia, G.; Atilhan, M.; Aparicio, S. *Phys. Chem. Chem. Phys.* **2015**, *17*, 13559–13574.

[6] Wu, W.; Han, B.; Gao, H.; Liu, Z.; Jiang, T.; Huang, J. *Angew. Chem. Int. Ed.* **2004**, *43*, 2415–2417.

[7] Yuan, X. L.; Zhang, S. J.; Lu, X. M. *J. Chem. Eng. Data* **2007**, *52*, 1150–1150.

[8] Yokozeki, A.; Shiflett, M. B. *Energy Fuels* **2009**, *23*, 4701–4708.

[9] Shiflett, M. B.; Yokozeki, A. *Energy Fuels* **2010**, *24*, 1001–1008.

[10] Shiflett, M. B.; Yokozeki, A. *Ind. Eng. Chem. Res.* **2010**, *49*, 1370–1377.

[11] Yang, D.; Hou, M.; Ning, H.; Ma, J.; Kang, X.; Zhang, J.; Han, B. *ChemSusChem* **2013**, *6*, 1191–1195.

[12] Shang, Y.; Li, H.; Zhang, S.; Xu, H.; Wang, Z.; Zhang, L.; Zhang, J. *Chem. Eng. J.* **2011**, *175*, 324 – 329.

[13] Jiang, Y.-Y.; Zhou, Z.; Jiao, Z.; Li, L.; Wu, Y.-T.; Zhang, Z.-B. *J. Phys. Chem. B* **2007**, *111*, 5058–5061.

[14] Luis, P.; Neves, L.; Afonso, C.; Coelhoso, I.; Crespo, J.; Garea, A.; Irabien, A. *Desalination* **2009**, *245*, 485 – 493.

[15] Hu, X.-B.; Li, Y.-X.; Huang, K.; Ma, S.-L.; Yu, H.; Wu, Y.-T.; Zhang, Z.-B. *Green Chem.* **2012**, *14*, 1440–1446.

[16] Wang, J.; Zeng, S.; Bai, L.; Gao, H.; Zhang, X.; Zhang, S. *Ind. Eng. Chem. Res.* **2014**, *53*, 16832–16839.

[17] Zeng, S.; He, H.; Gao, H.; Zhang, X.; Wang, J.; Huang, Y.; Zhang, S. *RSC Adv.* **2015**, *5*, 2470–2478.

[18] Sun, S.; Niu, Y.; Xu, Q.; Sun, Z.; Wei, X. *RSC Adv.* **2015**, *5*, 46564–46567.

[19] Han, G.-Q.; Jiang, Y.-T.; Deng, D.-S.; Ai, N. *RSC Adv.* **2015**, *5*, 87750–87757.

[20] Yang, Z.-Z.; He, L.-N.; Song, Q.-W.; Chen, K.-H.; Liu, A.-H.; Liu, X.-M. *Phys. Chem. Chem. Phys.* **2012**, *14*, 15832–15839.

[21] Wang, C.; Zheng, J.; Cui, G.; Luo, X.; Guo, Y.; Li, H. *Chem. Commun.* **2013**, *49*, 1166–1168.

[22] Wang, C.; Cui, G.; Luo, X.; Xu, Y.; Li, H.; Dai, S. *J. Am. Chem. Soc.* **2011**, *133*, 11916–11919.

[23] Huang, J.; Rüther, T. *Aust. J. Chem.* **2009**, *62*, 298–308.

[24] Wang, C.; Luo, X.; Luo, H.; Jiang, D.-e.; Li, H.; Dai, S. *Angew. Chem. Int. Ed.* **2011**, *50*, 4918–4922.

[25] Gurkan, B.; Goodrich, B. F.; Mindrup, E. M.; Ficke, L. E.; Massel, M.; Seo, S.; Senftle, T. P.; Wu, H.; Glaser, M. F.; Shah, J. K.; Maginn, E. J.; Brennecke, J. F.; Schneider, W. F. *J. Phys. Chem. Lett.* **2010**, *1*, 3494–3499.

[26] Wang, C.; Luo, H.; Li, H.; Zhu, X.; Yu, B.; Dai, S. *Chem. Eur. J.* **2012**, *18*, 2153–2160.

[27] Teague, C. M.; Dai, S.; en Jiang, D. *J. Phys. Chem. A* **2010**, *114*, 11761–11767.

[28] Cui, G.; Wang, C.; Zheng, J.; Guo, Y.; Luo, X.; Li, H. *Chem. Commun.* **2012**, *48*, 2633–2635.

[29] Cui, G.; Zheng, J.; Luo, X.; Lin, W.; Ding, F.; Li, H.; Wang, C. *Angew. Chem. Int. Ed.* **2013**, *52*, 10620–10624.

[30] Cui, G.; Lin, W.; Ding, F.; Luo, X.; He, X.; Li, H.; Wang, C. *Green Chem.* **2014**, *16*, 1211–1216.

[31] Cui, G.; Zhang, F.; Zhou, X.; Li, H.; Wang, J.; Wang, C. *Chem. Eur. J.* **2015**, *21*, 5632–5639.

[32] Chen, K.; Lin, W.; Yu, X.; Luo, X.; Ding, F.; He, X.; Li, H.; Wang, C. *AIChE Journal* **2015**, *61*, 2028–2034.

[33] Cui, G.; Huang, Y.; Zhang, R.; Zhang, F.; Wang, J. *RSC Adv.* **2015**, *5*, 60975–60982.

[34] Cui, G.; Zhang, F.; Zhou, X.; Huang, Y.; Xuan, X.; Wang, J. *ACS Sustainable Chem. Eng.* **2015**, *3*, 2264–2270.

[35] Huang, X.; Margulis, C. J.; Li, Y.; Berne, B. J. *J. Am. Chem. Soc.* **2005**, *127*, 17842–17851.

[36] Wang, Y.; Pan, H.; Li, H.; Wang, C. *J. Phys. Chem. B* **2007**, *111*, 10461–10467.

[37] Bhargava, B. L.; Krishna, A. C.; Balasubramanian, S. *AIChE Journal* **2008**, *54*, 2971–2978.

[38] Zhang, X.; Liu, X.; Yao, X.; Zhang, S. *Ind. Eng. Chem. Res.* **2011**, *50*, 8323–8332.

[39] Monteiro, M. J.; Ando, R. A.; Siqueira, L. J. A.; Camilo, F. F.; Santos, P. S.; Ribeiro, M. C. C.; Torresi, R. M. *J. Phys. Chem. B* **2011**, *115*, 9662–9670.

[40] Yu, G.; Chen, X. *J. Phys. Chem. B* **2011**, *115*, 3466–3477.

[41] Ghobadi, A. F.; Taghikhani, V.; Elliott, J. R. *J. Phys. Chem. B* **2011**, *115*, 13599–13607.

[42] Mohammadi, M.; Foroutan, M. *J. Mol. Liq.* **2014**, *193*, 60–68.

[43] Firaha, D.; Kavalchuk, M.; Kirchner, B. *J Solution Chem* **2015**, *44*, 838–849.

[44] Siqueira, L. J. A.; Ando, R. A.; Bazito, F. F. C.; Torresi, R. M.; Santos, P. S.; Ribeiro, M. C. C. *J. Phys. Chem. B* **2008**, *112*, 6430–6435.

[45] Wick, C. D.; Chang, T.-M.; Dang, L. X. *J. Phys. Chem. B* **2010**, *114*, 14965–14971.

[46] Cadena, C.; Anthony, J. L.; Shah, J. K.; Morrow, T. I.; Brennecke, J. F.; Maginn, E. J. *J. Am. Chem. Soc.* **2004**, *126*, 5300–5308.

[47] Bhargava, B. L.; Balasubramanian, S. *J. Phys. Chem. B* **2007**, *111*, 4477–4487.

[48] Shah, J. K.; Maginn, E. J. *J. Phys. Chem. B* **2005**, *109*, 10395–10405.

[49] Zhang, X.; Huo, F.; Liu, Z.; Wang, W.; Shi, W.; Maginn, E. J. *J. Phys. Chem. B* **2009**, *113*, 7591–7598.

[50] Frisch, M. J. et al. Gaussian 09 Revision D.01. Gaussian Inc. Wallingford CT **2009**.

[51] Dennington, R.; Keith, T.; Millam, J. GaussView Version 5. Semichem Inc., Shawnee Mission, KS, 2009.

[52] Boys, S.; Bernardi, F. *Mol. Phys.* **1970**, *19*, 553–566.

[53] Jeziorski, B.; Moszynski, R.; Szalewicz, K. *Chem. Rev.* **1994**, *94*, 1887–1930.

[54] Turney, J. M. et al. *WIREs Comput. Mol. Sci.* **2012**, *2*, 556–565.

[55] Hohenstein, E. G.; Sherrill, C. D. *J. Chem. Phys.* **2010**, *133*, 014101–014113.

[56] Plimpton, S. *J. Comput. Phys.* **1995**, *117*, 1–19.

[57] Wang, Y.-L.; Shah, F. U.; Glavatskih, S.; Antzutkin, O. N.; Laaksonen, A. *J. Phys. Chem. B* **2014**, *118*, 8711–8723.

[58] Rai, N.; Siepmann, J. I. *J. Phys. Chem. B* **2007**, *111*, 10790–10799.

[59] Rai, N.; Siepmann, J. I. *J. Phys. Chem. B* **2013**, *117*, 273–288.

[60] Ketko, M. H.; Kamath, G.; Potoff, J. J. *J. Phys. Chem. B* **2011**, *115*, 4949–4954.

[61] Morganti, J. D.; Hoher, K.; Ribeiro, M. C. C.; Ando, R. A.; Siqueira, L. J. A. *J. Phys. Chem. C* **2014**, *118*, 22012–22020.

[62] Martínez, L.; Andrade, R.; Birgin, E. G.; Martínez, J. M. *J. Comp. Chem.* **2009**, *30*, 2157–2164.

[63] Hoover, W. G. *Phys. Rev. A* **1985**, *31*, 1695–1697.

[64] Nosé, S. *J. Chem. Phys.* **1984**, *81*, 511–519.

[65] Fiorin, G.; Klein, M. L.; Hénin, J. *Mol. Phys.* **2013**, *111*, 3345–3362.

[66] Darve, E.; Rodríguez-Gómez, D.; Pohorille, A. *J. Chem. Phys.* **2008**, *128*, 144120.

[67] Xing, H.; Liao, C.; Yang, Q.; Veith, G. M.; Guo, B.; Sun, X.-G.; Ren, Q.; Hu, Y.-S.; Dai, S. *Angew. Chem. Int. Ed.* **2014**, *53*, 2099–2103.

[68] Dang, L. X.; Wick, C. D. *J. Phys. Chem. B* **2011**, *115*, 6964–6970.

[69] Dang, L. X.; Chang, T.-M. *J. Phys. Chem. Lett.* **2012**, *3*, 175–181.

[70] Perez-Blanco, M. E.; Maginn, E. J. *J. Phys. Chem. B* **2010**, *114*, 11827–11837.

Chapter 7

Future Outlook

The present thesis sheds light on four major aspects: (i) Development of an all-atom nonpolarizable force field for 1,3-dialkylimidazolium based ionic liquids, (ii) Examination of the nature of hydrogen bonds and its effect on low frequency vibrational modes and electrical conductivity in ammonium-based ionic liquids, (iii) Investigation of a protic ionic plastic crystal as a solid-state electrolyte, a role in which it can contribute both by its ionic as well as protonic transport, and (iv) Understanding SO_2 capture by ionic liquids.

In Chapters 2A and 2B, a robust protocol to obtain atomic site charges from the crystal or from the liquid has been described. It has been shown that these procedures are much less expensive than performing a full-blown *ab initio* MD simulation and are thus attractive. A transferable force field for ILs has been derived and validated by comparing computed physical properties against experimental data. In principle, this protocol can be extended to develop force field for ILs based on other cations, such as pyridinium, pyrrolidinium, ammonium, phosphonium, etc. In the current framework, charges on the same cation in two pure ILs (with different anions) can be different. As a result, the current approach shows a limitation in modeling mixtures of ILs having same cation but different anions. Further efforts are needed to overcome this issue.

In Chapter 3, the signature and strength of cation-anion hydrogen bonding in ammonium-based bromide salts has been probed by vibrational spectra, which show a blue shift in the far-IR mode with increase in number of cation-anion hydrogen bonds. Further, enhancement in hydrogen bonding interactions and consequent reduction in ion mobility due to steric hindrance has been demonstrated in Chapter 4. The effect of steric hindrance in analogous salts composed of phosphonium cation should be explored. Furthermore, *ab initio* MD simulations should be performed to shed light on proton conduction in ammonium/phosphonium salts.

Phase transitions and significant insights into the mechanism of ion/proton conduction occurring through hopping have been demonstrated for a protic ionic plastic crystal here.

Atomistic simulations should be performed to investigate the diffusion of additional alkali ions in such systems. Effect of an external electric field in ion/proton conduction can be explored. Similar protocol can be extended to study phase transitions and ion transport mechanism in ionic liquid crystals.

Absorption of SO_2 by ILs has been explored to shed light on designing task-specific ILs as electrolytes for efficient SO_2 capture. It is shown that multiple-site interactions between solute and functionalized anion results in both enhancement of SO_2 capture and reduction in absorption enthalpy. Effects of cation functionalization on SO_2 absorption can be investigated. The interactions of SO_2 with functionalized zwitterionic salts should be explored.

To summarize, the present thesis illustrates chemically realistic modeling of molecular interactions in ionic liquids and mechanism of ion/proton transport in such salts.

List of publications

- Quantitative Prediction of Physical Properties of Imidazolium based Room Temperature Ionic Liquids Through Determination of Condensed Phase Site Charges: A Refined Force Field
  Mondal, A.; Balasubramanian, S. *J. Phys. Chem. B* **2014**, 118, 3409-3422.

- Intermolecular Structure in tri-*n*-butyl phosphate/*n*-octane Mixtures: A Molecular Dynamics Simulation Study
  Mondal, A.; Balasubramanian, S. *Current Science* **2014**, 106, 1235-1242.

- A Molecular Dynamics Study of Collective Transport Properties of Imidazolium Based Room Temperature Ionic Liquids
  Mondal, A.; Balasubramanian, S. *J. Chem. Eng. Data* **2014**, 59, 3061-3068.

- Dissolution of Cellulose in Room Temperature Ionic Liquids: Anion Dependence
  Payal, R. S.; Bejagam, K. K.; **Mondal, A.**; Balasubramanian, S. *J. Phys. Chem. B* **2015**, 119, 1654-1659.

- Atomistic Simulations of Ammonium-based Protic Ionic Liquids: Steric Effects on Structure, Low Frequency Vibrational Modes and Electrical Conductivity
  Sunda, A. P.*; **Mondal, A.***; Balasubramanian, S. *Phys. Chem. Chem. Phys.* **2015**, 17, 4625-4633. (*Equal Contribution).

- Vibrational Signatures of Cation-Anion Hydrogen Bonding in Ionic Liquids: A Periodic Density Functional Theory and Molecular Dynamics Study
  Mondal, A.; Balasubramanian, S. *J. Phys. Chem. B* **2015**, 119, 1994-2002.

- A Refined All-Atom Potential for Imidazolium-Based Room Temperature Ionic Liquids: Acetate, Dicyanamide and Thiocyanate Anions
  Mondal, A.; Balasubramanian, S. *J. Phys. Chem. B* **2015**, 119, 11041-11051.

- Thermal Phase Behavior and Ion Hopping in 1,2,4-Triazolium Perfluorobutanesulfonate Protic Organic Ionic Plastic Crystal

Mondal, A.; Sunda, A. P.; Balasubramanian, S. *Phys. Chem. Chem. Phys.* **2016**, 18, 2047-2053.

- Understanding SO_2 Capture by Ionic Liquids
  Mondal, A.; Balasubramanian, S. *J. Phys. Chem. B* **2016**, 120, 4457-4466.

- Proton Hopping Mechanism in a Protic Organic Ionic Plastic Crystal
  Mondal, A.; Balasubramanian, S. (Submitted).

- Molecular Dynamics Investigation of Efficient SO_2 Absorption by Anion-Functionalized Ionic Liquids
  Mondal, A.; Balasubramanian, S. (To be submitted).